Ultrasound-enhanced delivery of therapeutic agents to tumours using submicron cavitation nuclei

Rachel Myers

Wadham College

University of Oxford

Supervised by

Prof. Constantin Coussios and Prof. Robert Carlisle

Submitted: 12th February 2016

Submitted to the Department of Engineering Science, University of Oxford, in fulfilment of the requirements for the degree of Doctor of Philosophy

Abstract

Cancer therapy is severely hampered by the poor delivery of agents out of the blood vessels and into tumours. This is due to the irregular vasculature, high interstitial pressure and dense extracellular matrix associated with tumour tissue. As a consequence, high doses of agents must be administered intravenously for effective accumulation in the tumour. This leads to a low therapeutic index, necessitates multiple administrations of the same drug, and for many cancer drugs, also leads to toxic side-effects. Increasingly complex therapeutics, such as antibodies and viruses, only exacerbate this delivery problem as their greater size leads to lower coefficients of diffusion and, consequently, even greater portions of the tumour remain untreated.

There have been studies aimed at improving therapeutic outcomes using microbubble-nucleated, ultrasound-induced cavitation, which provides a mechanical impetus to drive drugs out of the vasculature and into tumours. However, microbubbles are limited by their large size, their instability in the blood and their destruction upon cavitation. This thesis details the formulation of two alternative cavitation nuclei to overcome the limitations of microbubbles: mesoporous carbon particles and polymer cups. These are solid, submicron particles that contain crevices into which nanobubbles can be stabilised. Initial studies of their biocompatibilty have indicated that these formulations may be safe for intravenous administration.

A tumour mimicking phantom was first used to quantify drug delivery caused by cavitation. Both polymer cups and mesoporous carbon particles were found to significantly enhance delivery of a model therapeutic agent by this method.

In vivo the polymer cups were used to enhance the delivery of an oncolytic vaccinia virus: intravenous administration of $1x10^5$ pfu vaccinia virus, polymer cups and ultrasound treatment was shown to cause a 780-fold increase in genome copies in the tumours of a SKOV-3 tumour model, and 5,700-fold, in the tumours of a HEPG2 tumour model 20 days after the treatment. In mice treated with $1x10^6$ pfu of virus cavitation caused by cups and ultrasound was shown to cause regression in 7 of the 8 tumours in comparison to just 1 of the 8 tumours that were treated with virus alone.

Declaration

I declare this thesis is entirely my own work and, except where otherwise stated, describes my own research

Rachel Myers

Wadham College

Acknowledgements

This thesis would not have been possible without the support of a great number of people. First, I would like to thank my supervisors Professor Constantin Coussios and Professor Robert Carlisle. They supplied encouragement and advice when necessary but also provided me with the freedom to make my own mistakes and become an independent researcher.

I would like to thank the entire BUBBL lab for being a source of both assistance and friendship. Within the lab Susan Graham supplied indispensable enthusiasm and support while Dr. Jamie Collin provided seemingly endless patience tutoring me about ultrasound. Dr. Christian Coviello and Dr. James Kwan contributed expertise whenever needed while Dr. Tracey King, Jim Fisk and David Salisbury managed to keep the lab standing.

I am grateful to my friends and family outside of the BUBBL lab with particular thanks to those willing to read this thesis. Finally, I would like to thank my parents for not being too upset when I quit my job and decided to write this thesis. They have always encouraged me to do what I want as long as it wasn't nothing.

My research was supported by RCUK (Digital Economy Programme grant number EP/G036861/1 Oxford Centre for Doctoral Training in Healthcare Innovation), the Wellcome Trust and EPSRC (under grant number WT088877/Z/09/Z) and Transgene SA, France.

Table of Contents

List of Figures

List of Tables

Abbreviations

°C	Degrees Celsius
5-FC	5-Fluorocytosine
5-FU	5-Fluorouracil
Ad	Adenovirus
AFM	Atomic force microscopy
ALCAM	A leukocyte cell adhesion molecule
ALP	Alkaline phosphatase
ALT	Alanine aminotransferase
ANOVA	Analysis of variance
AST	Aspartate aminotransferase
AT-CNP	Acid treated carbon nanoparticles
BUN	Blood urea nitrogen
C3	Complement component 3
CMP	Carbon macroparticles
CNP	Carbon nanoparticles
CTLA-4	Cytotoxic T-lymphocyte-associated protein 4
DC	Duty cycle
DLS	Dynamic light scattering
DMEM	Dulbecco's Modified Eagle media
DMSO	Dimethyl sulfoxide
DNA	Deoxyribonucleic acid
DTT	DL-dithiothreitol
ECM	Extracellular matrix
EDC	1-Ethyl-3-[3-dimethylaminopropyl] carbodiimide hydrochloride
EDTA	Ethylenediaminetetraacetic acid
EEV	Extracellular enveloped virus
EGFR	Epidermal growth factor receptor
ELISA	Enzyme-linked immunosorbent assay
EPR	Enhanced permeability and retention
FBS	Foetal bovine serum
Fc	Fragment crystallisable
FDA	US Food and Drug Administration
FITC	Fluorescein isothiocyanate
g	Standard acceleration of gravity
GM-CSF	Granulocyte-macrophage colony-stimulating factor
HCl	Hydrochloric acid
HEPES	4-(2-Hydroxyethyl)-1-piperazineethane-sulfonic acid
HER2	human epidermal growth factor receptor 2
HIFU	High intensity focused ultrasound
HPF	High pass filter
HPMA	N-(2-hydroxypropyl) methacrylamide
hr	Hours
i.p.	Intra peritoneal
i.t.	Intra tumoural
i.v.	Intravenous
IgG	Immunoglobulin G
IgM	Immunoglobulin M
IL	Interleukin
IMV	Intracellular mature virus
I_{SPPA}	Spatial peak pulse average intensity
I_{SPTA}	Spatial peak temporal average intensity

LPS	Lipopolysaccharide
M	Molar
MBL	Mannose binding lectin
MDR	Multi drug resistance
MES	2-(N-morpholino)ethane-sulfonic acid
mg	Milligram
MI	Mechanical index
mins	Minutes
mL	Millilitre
mM	Millmolar
MPS	Mononuclear phagocyte system
mTorr	Millitorr
MTS	3-(4,5-dimethylthiazol-2-yl)-5-(3-carboxymethoxyphenyl) -2-(4-sulfophenyl)-2H-tetrazolium
MWCNT	Multi-walled carbon nanotubes
NaOH	Sodium hydroxide
NCI	National Cancer Institute
NIST	National Institute of Standards and Technology
NK cells	Natural killer cells
nm	Nanometer
PAM	Passive acoustic mapping
PBS	Phosophate buffered saline
PCD	Passive cavitation detector
PD-1	Programmed death 1
PDI	Polydispersity index
PEG	Poly ethylene glycol
pfu	Plaque forming units
PI	Propidium iodide
PK/PD	Pharmacokinetics/ pharmacodynamics
PRF	Pulse repetition frequency
PVC	Poly vinyl chloride
qPCR	Quantitative polymerase chain reaction
RBC	Red blood cells
ROS	Reactive oxygen species
RPMI	Roswell Park Memorial Institute-1680
s.c.	Subcutaneous
SDS	Sodium dodecyl sulphate
SDS-PAGE	Sodium dodecyl sulphate polyacrylamide gel electrophoresis
sec	Seconds
sulfo-NHS	N-hydroxysulfosuccinimide
SV	SonoVue™
SWCNT	Single-walled carbon nanotubes
T-VEC	Talimogene laherparepvec
TEM	Transmission electron microscopy
TI	Thermal index
TLR-2	Transient toll like receptor 2
TMB	3,3',5,5'-Tetramethylbenzidine
TNF-α	Tumour necrosis factor-α
TRITC	Tetramethylrhodamine
UCA	Ultrasound contrast agent
VEGF	Vascular endothelial growth factor
VV	Vaccinia virus
µL	Microlitres
µm	Micron

1 Introduction

Cancer is any type of malignant growth or tumour, caused by abnormal and uncontrolled cell division. In 2008 cancer was the main cause of death in developed countries and accounted for approximately 7.6 million deaths worldwide[1,2]. It has been estimated that the number of cancer-related deaths in 2030 will have increased to 13.1 million[3]. However, cancer is a very broad term encompassing a range of pathologies that can affect any part of the body. As a consequence, there is unlikely to be one universal curative approach, but instead a variety of strategies that will produce greater understanding of the mechanisms involved in cancer and, consequently, gradual advances in its diagnosis and treatment[4,5]. These advances may originate from: identification of gene mutations present in cancers, discovery of markers that are expressed either by the body in response to cancer or by cancer tissue itself, improvements to drug delivery or from a better understanding of how to utilise the immune system[6-17].

At present, however, the majority of conventional chemotherapeutic drugs have an extremely low therapeutic ratio (the lethal or toxic dose divided by the effective dose)[18]. This is because of a number of factors including low potency caused by reduced susceptibility of cancer cells to drug induced apoptosis, multi-drug resistance, poor specificity of the therapeutic, and limited selectivity of accumulation in tumour deposits compared to normal tissue[19-23].

To address the challenge of poor delivery this thesis explores the use of submicron cavitation nuclei to mechanically drive therapeutics into tumours. This introduction will discuss how cancer therapies are advancing and why delivery is becoming a more critical issue, what therapeutic effects can be achieved with ultrasound and the ideal properties a cavitation nuclei would have to best improve drug distribution.

1.1 Cancer therapeutics

Standard cancer treatment is typically a combination of surgery, radiotherapy and chemotherapy. Surgery and radiotherapy can be effective forms of treatment of solid localised disease but once a tumour has metastasised, location and treatment of all of the secondary tumours becomes unfeasible.

Conventional chemotherapy uses small molecules that target specific phases within cell cycle growth and proliferation commonly targeting rapidly dividing cells. It is typically used systemically and does not require knowledge of the location of all tumour deposits but has a very narrow therapeutic index. The cytotoxicity of these agents to both cancerous and healthy tissue makes identifying the correct dose a challenging task. Whilst careful control of dosing regimens and recovery periods can help alleviate some of these toxicities it is clear that to fully optimise the potential of chemotherapeutic drugs and reduce the risk of multi-drug resistance the targeting of their delivery must be improved[24].

Biological therapeutics, such as antibodies, are being increasingly used as a form of cancer treatment, either to replace or to combine with conventional chemotherapeutics, as they can be much more tumour site specific. They

typically rely on a combination of activating the anti-tumour immune response and changing signalling pathways within a cell[25]. Between 1984 and 2013, 36 monoclonal antibodies gained FDA approval, 15 of which were for cancer[26]. A further 4 antibodies were approved in 2014[27]. Bevacizumab, cetuximab and trastuzumab are the most commonly used antibody based therapeutics and they target the vascular endothelial growth factor (VEGF), epidermal growth factor receptor (EGFR) and human epidermal growth factor receptor 2 (HER2) respectively. A more recent antibody strategy has been to target receptors on immune cells that are responsible for the immune suppression within tumours, rather than targeting the cancer cells directly. Cytotoxic T-lymphocyte-associated protein 4 (CTLA-4) and programmed death 1 (PD-1) are two such receptors found on the surface of T cells[28]. Furthermore programmed death ligand 1 (PD-L1), a ligand specific to PD-1, is selectively expressed on tumour cells[29]. These checkpoint inhibitors are thought to be key to the regulation and suppression of the immune system inside tumours. Concurrent administration of anti-CTLA-4 and anti-PD-1 antibodies caused an objective response in 40% of patients with stage III or IV melanoma. Of those patients 76% showed tumour regression of more than 80% at 12 weeks[30]. Meanwhile, categorising a cohort with urothelial bladder cancer by upregulation of PD-L1 it was shown that 50% of patients with more than 10% of cancer cells expressing PD-L1 showed an objective response when treated with anti-PD-L1 antibodies[31]. The systemic auto-immune effects of these agents remains an issue and employing strategies to try and ensure that a greater proportion of the antibody dose enters into the tumour would address this limitation.

Unfortunately, antibodies have an even more limited distribution within the tumour than conventional small molecule drugs[32,33]. This is, in part, due to the difference in size of the molecules: for example trastuzumab has a molecular weight of 146 kg/mol while doxorubicin only has a molecular weight of 544 g/mol[22,23]. In addition their binding affinity, the rate at which they are cleared and their non-specific interactions with the extracellular matrix (ECM), all affect their delivery into and throughout tumours[34-37]. If the distribution of antibody therapeutics could be improved, it would be expected that their efficacy could also be improved.

Oncolytic viruses are another cancer therapeutic that provide the opportunity to more specifically target tumours. Viruses encompass a broad spectrum of infectious agents ranging in size from 18 – 750 nm that are capable of replicating inside living cells[38,39]. They each carry genetic material that, depending on the virus, may integrate into the cells DNA. This genetic material is surrounded by a protein coat and, in some cases, a further lipid envelope[40]. Obligate pathogenic viruses have been forced to evolve highly efficient cell entry mechanisms and once within the host cell they can utilise the cell's infrastructure to build and release progeny virions. This process can be non-pathogenic or lead to the violent lysis and necrotic death of the cell. The rapid growth, loss of apoptotic control and immunocompromised environment of cancer cells means that some viruses have a natural tumour tropism[41-43].

The therapeutic benefit of first generation oncolytic viruses was derived from the lysis of infected cells, destruction of the vasculature caused by inflammation and the stimulation of an immune response[42,44]. Subsequent

generations of oncolytic viruses have been genetically engineered to be more selective and the newest wave of oncolytic viruses are now 'armed' with transgenes that can either directly impact upon the tumour, produce an enzyme to convert a pro-drug to an active chemotherapeutic or stimulate the immune response to target cancer cells[45-48].

Examples of viruses that have been repurposed as oncolytics are herpes simplex virus, adenovirus, measles virus, retrovirus, lentivirus, Newcastle virus, Seneca valley virus, poliovirus, vesicular stomatitis virus and vaccinia virus[40,49]. Sheridan briefly reviewed the 15 oncolytic viruses in clinical trials in 2015[50].

In October 2015 the US Food and Drug Administration (FDA) approved the use of Talimogene laherparepvec (T-VEC), a herpes simplex virus genetically modified to selectively replicate within cancer cells and produce the cytokine granulocyte-macrophage colony-stimulating factor (GM-CSF), for the treatment of inoperable melanoma tumours. Phase III trials had shown complete responses in 11% of patients with unresectable Stage IIIb, IIIc and IV melanoma disease (the control arm of subcutaneous (s.c.) injection of GM-CSF alone showed a complete response in just 6% of patients)[51-54].

A frequent difficulty with oncolytic virus treatment has been delivery. Not only does their size cause them to have limited penetration into tumours but they are typically quickly cleared in the blood[55]. As a consequence most viruses, thus far, have been administered intra-tumourally (i.t.). This severely limits their ability to treat tumour metastases. There have been attempts to 'stealth' the virion either by coating them in polymers or injecting pre-infected cells[56].

Another approach is to carefully select the virus for systemic delivery: for example instead of using the common Adenovirus (Ad) serotype Ad5, Di et al. used a virus with the Ad11p capsid, which resulted in it retaining its ability to kill cancer cell lines in the presence of human plasma[57].

Alternatively, Vaccinia virus (VV) has naturally evolved to have 2 virion forms: intracellular mature virus (IMV) and extracellular enveloped virus (EEV). IMV are immunogenic and are released as the cell lyses whereas EEV are IMV particles enveloped by lipids present in the host cell and are released before cell death. This means that the EEV particles are theoretically capable of traversing the blood stream and infecting distant cancer cells.

By overcoming this significant hurdle of stability in blood it is likely that oncolytic viruses will be able to treat a greater range of cancers with an improved probability of success. The size of the viruses, however, means that their dissemination in tumours is even more hampered than that of antibody therapeutics leading to heterogeneous treatment of tumours[58]. An understanding of tumour biology is important in comprehending the difficulties in cancer therapeutic delivery and developing a strategy to improve distribution.

1.2 Tumour microenvironment

Tumours trigger angiogenesis/neovascularisation (the 'angiogenic switch') to acquire their own blood supply thereby providing a source of nutrients and a waste removal route. However these vessels grow so rapidly that they lack organisation, leading to abnormalities in their structure such as poor pericyte coverage and large gaps between neighbouring endothelial cells[59]. The

disorganisation and leakiness of this vasculature leads to temporal and spatial irregularities in blood flow. The unimpeded influx of blood components through leaky vasculature raises pressure within the interstitial space and contributes to the collapse of the lymphatics within the tumour. With ineffective drainage and uncontrolled influx the pressure of the interstitial fluid within the tumour rises until it matches that within capillaries[60]. Ultimately convective forces across the tumour are lost and the movement of drugs becomes reliant on diffusion alone. The dense and disorganised ECM within tumours makes this an extremely inefficient process especially for therapeutics with a large molecular weight[61-63]. Figure 1-1 illustrates the difficulties faced in the delivery of drugs into a tumour.

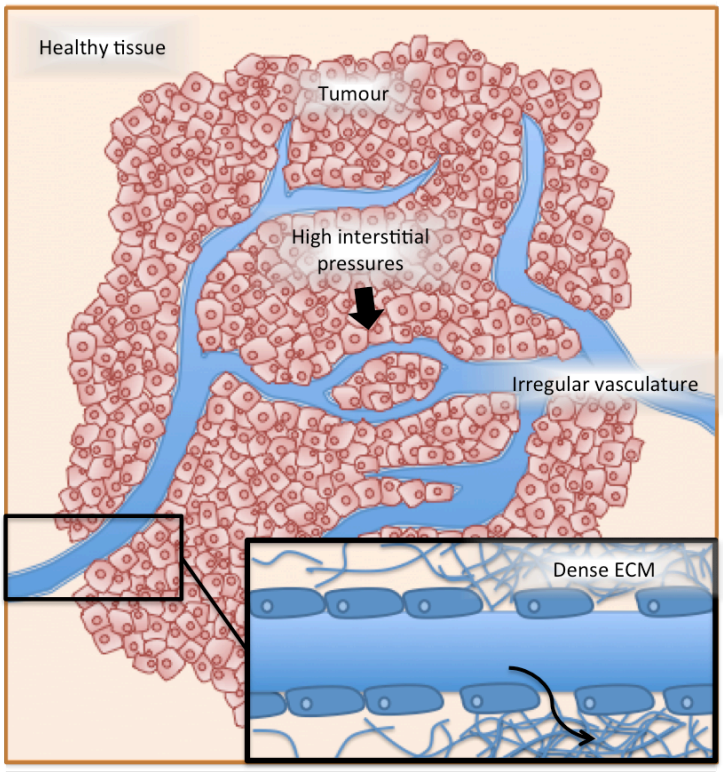

a

Figure 1-1: Schematic of the tumour microenvironment
Poor delivery of cancer drugs is due to the disorganised blood supply, high interstitial pressures due to the collapse of the lymphatic drainage system and the permeable blood vessels and a stiff, fibrous extracellular matrix (ECM).

However, the irregular vasculature of a tumour can impart some benefit: the presence of leaky vasculature provides a means by which therapeutics of a specific size can be selectively deposited within a tumour. The gaps between endothelial cells supplying cancerous tissue can range from 100 to 700 nm as opposed to a range of 2 to 10 nm in typical healthy tissue[62,64-67]. The passive accumulation of long-circulating therapeutics in the 100-700 nm size range into tumours is known as the enhanced permeability and retention (EPR) effect[68,69]. In this thesis, the terms 'nanoparticles' and 'submicron particles' refer to particles of a size range that can selectively accumulate in tumours, as opposed to the more standard definition of particles that have at least one dimension in the size range 1 nm to 100 nm[70].

1.3 Nanoparticles as cancer therapeutics

The chemotherapy drug doxorubicin encapsulated in 100 nm liposomes causes the maximum concentration of the drug in the tumour to be 4-15 times greater than if the same amount of free drug was injected[71]. The time that the peak concentration within tumours is reached changes from just 0.5 hours with free drug to between 48 and 72 hours for the encapsulated drug[72]. Not only can nanoencapsulation of a drug enhance pharmacokinetics and reduce off-target toxicity but it can offer a more hospitable environment to the drug than the bloodstream protecting and stabilising it following intravenous (i.v.) administration[18,73].

A range of materials and structures have been used to formulate nano-sized systems for cancer therapeutics and diagnostics: metalic, polymeric, ceramic and magnetic nanoparticles as well as quantum dots, lipids, dendrimers and

micelles. The choice of nanoparticle type is typically a compromise between price, stability, ease of manipulation, biocompatibility, drug loading capacity and biodegradability[74,75]. For example, the morphology and surface properties of polymer nanoparticles are relatively easy to manipulate but they tend to degrade quickly[76].

In 2013, Etheridge et al. identified 789 current clinical trials using nanomedicines including 141 unique nanomedicine products, 38 of which had already been approved[77]. The majority of the nanoparticles were formulated as drug carriers but some were formulated to enhance standard treatment e.g. radiation[78].

1.3.1 Biocompatibility of nanoparticles

It is critical to understand how the body may respond to nanoparticles in order to understand the likely pharmacokinetics of the particles and potential side-effects of the treatment. Nanoparticles are not a new phenomena: they are a natural by-product of bacteria and a waste product from the degradation of industrial products. Their use in cosmetics, an industry where safety limitations are less rigid, have not revealed any obvious toxic side effects[70,79,80]. For the biocompatibility of nanoparticles introduced into the body Naahidi et *al.* and Dobrovolskaia and McNeil both provided in depth reviews[81,82]. In general most particles show limited to no toxicity but the majority of studies are performed over the short term and so only assess acute responses[83-86].

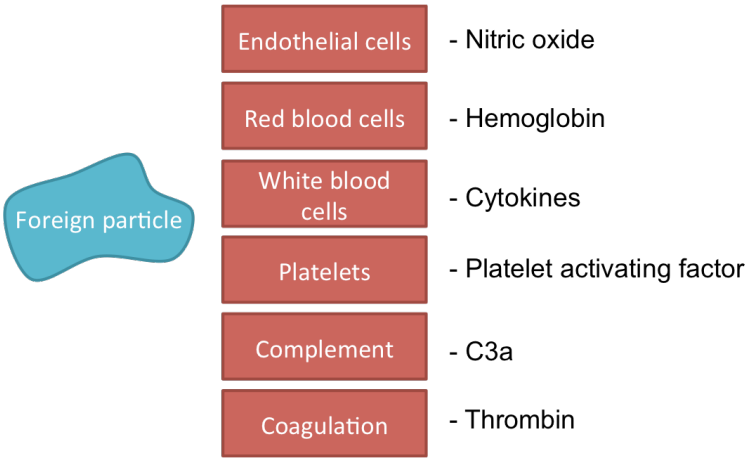

Figure 1-2: Examples of how components of blood may interact with particles
A list of the key components of the blood that a nanoparticle will interact with if systemically administered. Examples of the mediators that each component can release in order to stimulate an inflammatory response are provided on the right which will, in turn, lead to the rapid clearance of the particle.

If nanoparticles are to be injected i.v. the primary focus of biocompatibility studies should be with the blood. Blood is a complex composition of white blood cells, red blood cells, platelets and proteins surrounded by vasculature, each of which may interact with nanoparticles (see Figure 1-2)[87]. With careful engineering a particle can have a long blood circulation time and avoid sequestration by the liver, kidneys and spleen[88]. Particle size distribution, chemical composition, surface reactivity, surface area, charge and concentration are all critical to the length of time a particle will circulate before being cleared[73,87,89].

Hemolysis is the most obvious and extreme toxic response in the blood whereby the red blood cells rupture[90]. In addition to the clear loss of utilisable haemoglobin content in the blood, haemolysis can also lead to extensive oxidative stress, as well as prothrombitic and proinflammatory response[91]. A strong positive charge of a particle has been linked with red blood cell toxicity

as positive silica nanoparticles caused greater cell death than their negative counterparts[92,93].

White blood cells are a key component of the immune system and, consequently, can be the root of a strong cytotoxic or inflammatory response. A simple sign of an immune response can be a change in the composition of the blood as there may be increased recruitment of leukocytes caused by the secretion of GM-CSF. The shape and size of a particle is critical to how macrophages interact with it. For example if the tangential angle at which a macrophage comes into contact with a particle is large enough the macrophage will spread around the particle instead of internalising it and, consequently, cylindrical nanoparticles have a longer blood circulation time than spheres[94-98]. Meanwhile, Hutter et al. demonstrated that irregularly contoured nanoparticles cause the upregulation of transient toll like receptor 2 (TLR-2), a pattern recognition receptor linked with synthesis and secretion of pro-inflammatory cytokines such as tumour necrosis factor−α (TNF−α), Interleukin-6 (IL-6), IL-8, IL-10, IL-12 that will stimulate an immune response. The composition of the nanoparticle also impacts on how a particle will interact with white blood cells. For example, silica zeolites containing aluminium compared to non-aluminium containing particles were much more cytotoxic to macrophages while both polymer and iron particles caused leukocyte cell death[97,99,100].

Nanoparticles may also trigger a complement system cascade - a primary inflammatory response mediated by components which can directly bind to and neutralise particulate material, as well as instigate signalling to activate and recruit white blood cells. The alternative pathway is activated by non-

specific opsonisation of the particle more likely to occur if the particle has a strong surface charge[81,101-107]. The surfaces of particles are frequently modified with long polymer chains such as poly ethylene glycol (PEG) and N-(2-hydroxypropyl)methacrylamide (HPMA) in order to provide steric shielding from blood components, prevent agglomeration, increase the hydrophilicity of the particle and optimise the surface charge[55,104,105,108-114]. However, modification of the surface is frequently to the detriment of the efficacy of the particle and there is evidence emerging that some of the polymers used may trigger immune responses when re-dosing is performed[71,112,115,116]. The classical complement pathway is activated by the binding of immunoglobulin M (IgM) or immunoglobulin G (IgG) antibodies to the nanoparticles. The ultimate result is the same, with recognition by complement, fragment crystallisable (Fc) region receptors and particle receptors on hepatic Kupffer cells and splenic macrophages leading to the removal of the nanoparticles from the blood by the mononuclear phagocytosis system (MPS). Lipid nanoparticles have been reported to stimulate a complement response[117].

The plasma coagulation system regulates the concentrations of thrombin, plasmin and kallikein. The combination of system with tissue factors secreted by leukocytes leads to blood coagulation, thrombosis and platelet adhesion[118].

Platelets are key to maintenance of vasculature integrity and are equipped with many receptors to activate and inhibit agonists able to change the cytosketetal organisation[119]. Carbon nanotubes have been shown to activate platelets while dendrimers impair the functionality of platelets[120].

Finally, endothelial cells may respond to stress by altering the production of ECM, collagen and fibronectin thus changing both their morphology and their environment to encumber or ease diffusion[121].

Provided stability in the bloodstream can be achieved, the liver is a primary organ for the metabolism of nanoparticles and a high percentage of most i.v. injected nanoparticles smaller than 100 nm are sequestered on their passage through the liver[95,122,123]. Bloodstream concentrations of enzymes such as alanine aminotransferase (ALT), aspartate aminotransferase (AST) and alkaline phosphatase (ALP) are used as biomarkers for liver function and liver toxicity in in vivo tests[124], as their release into the bloodstream is indicative of damage to the integrity of membranes of cells within the liver. Some materials that have caused liver toxicity in their nanoparticle form are titanium dioxide, copper, iron oxide, lipids, aluminium and cadmium[124-126].

As the size of particles increases above 100 nm they become increasingly sequestered by the spleen[127]. Consequently particles of a hydrodynamic diameter between 100 and 200 nm have the longest circulation time but, may not localise as ideally dependent on the purpose of the nanoparticles[128]. A month after i.v. administration of 110 nm silver nanoparticles, the spleens of rats had significantly grown and contained much greater numbers of B and T cells, but natural killer (NK) cells were almost completely suppressed.

The kidneys may also be exposed to high concentrations of foreign material if the nanoparticles are metabolised into their constituent parts. For example, despite cadmium selenide quantum dots not being toxic as an entity they become toxic as they are metabolised into their elemental cadmium

form[129,130]. In addition to standard cell death experiments, creatinine concentrations can be used as a measure of renal function[131]. Blood urea nitrogen (BUN) tests can be used as an indicator of either kidney or liver damage[126].

1.3.2 Approaches to enhance pharmacokinetics

Alternatively, instead of modifying the particle to improve its distribution, the environment can be altered to lower the immune response using an MPS blockade or modification of the target site to make it more accessible[41]. To extend blood circulation times of a nanoparticle, pre-treatment with cobra venom factor or cyclophosamide depletes complement while i.v. injection of clodronate suppresses Kupffer cells thereby reducing liver sequestration[132-134]. Otherwise, pre-treatment with interleukin-2 (IL-2), histamine, tumour necrosis factor (TNF−α) and bradykinin have all been used to increase vasculature permeability[135-139]. Meanwhile, the high interstitial pressure and dense collagen matrix within the tumour can be reduced by using anti-VEGF antibodies and losartan respectively[140].

Conversely, depending on the purpose of the particle, the administration route can be chosen to improve delivery to the target site. By i.t., s.c. or intra peritoneal (i.p.) injection the standard physical barriers such as serum factors and irregular vasculature can be avoided. I.t. injections can reduce interactions with serum factors, cause much less off target toxicity and lead to greater concentrations of the therapeutic in the tumour[141,142]. However, the distribution within the tumour is much more variable and high insterstitial fluid pressures within the tumour can cause doses to flow back through the needle

tract thus reducing the overall efficacy[143]. I.p. injection may accumulate in tumours via the interstitium, leading to higher stomach and intestine accumulation although a higher proportion of the dose resides in the injection site longer when compared to alternative injection locations. S.c. injections would also accumulate in the tumour via the interstitium although there is delayed accumulation in both the kidney and the stomach[12]. Alternatively, if particles are delivered via inhalation or orally they interact with negatively charged mucin to enhance transportation across the mucus but can still experience mucociliary and macrophage mediated clearance[123].

The eventual removal pathway of long-lasting nanoparticles is very poorly understood. Some nanoparticles have been shown to be retained in the body for longer than 2 years and, as of yet, the long term effects of nanoparticles within the system are unclear[144-146]. Many polymer nanoparticles are biodegradable but gold and other metal nanoparticles could remain intact within the body indefinitely. It has been demonstrated that magnetic nanoparticles retained in the urinary tract can cause bladder spasms and pain but these symptoms were treatable[147]. Nanoparticles that are inhaled, due to their size, are capable of travelling deep into the lungs and into the alveoli where they can remain for up to two months causing granulomatous inflammation[147-149].

1.4 Active targeting of nanoparticles

Of the current carrier systems in clinical use, Doxil provides a good example of how the regulation of all these physicochemical factors have provided a long circulating vector capable of benefiting from the EPR effect[150,151].

However, even with the EPR effect, only 1-2% of the total injected dose achieves tumour accumulation[152]. In addition, despite the encapsulation of the drug offering a more hospitable environment to the drug than the bloodstream the stability these carriers require to survive the bloodstream often limits the release of their payload once at the target site[71,153]. In an attempt to increase the accumulation of drugs into tumours and release the drug, nanoparticles can be made sensitive to the microenvironment of the tumour or, alternatively, an external stimulus can be applied to direct and destroy the nanoparticles.

Targeting of therapeutics with antibodies or other targeting ligands has been demonstrated to accelerate uptake into target cells and reduce clearance, although there is some dispute as to whether targeting improves localization of nanoparticles[83,154-157]. However, it is agreed that enhancing internalisation of a therapeutic into a cell increases its efficacy and that this approach is particularly useful for non-soluble drugs[62,158]. As we gain greater understanding of fundamental cancer mechanisms at the genetic and protein level the list of potential targets increases[4,115,159]. Some targets are expressed by the cancer cells themselves while others are targeted at the microenvironment that supports the tumour e.g. new blood vessels[160-162]. Just a few of the moieties that have been targeted are E-selectin, EGFR, VEGF, folate receptor, transferrin, a leukocyte cell adhesion molecule (ALCAM), αvβ3 and αvβ5 integrins[11,62,83,159,163-170]. The choice of receptor target is determined by the therapeutic strategy being employed, the level and specificity of the expression of the receptor, and the availability of suitable ligands. The conjugation of the targeting ligand to the nanoparticle is critical to

the specificity of the targeting, the stability of the nanoparticles and its pharmacokinetics. There are extremely comprehensive texts available covering different chemistry techniques to optimise the conjugation of the two elements[171-174]. Polymer chains, such as those mentioned in Section 1.3.1 for the improvement of the pharmacokinetics of nanoparticles, can act as a chain linker to better orientate the targeting moiety[175,176].

Magnetic force is an example of an external stimuli used to direct magnetic nanoparticles in the body to deposit at specific sites. This approach has the additional advantage of providing a means of monitoring their accumulation by magnetic resonance imaging[177].

Different strategies have been tried to trigger release either in response to exposure to the unique tumour environment or to externally applied stimuli[178,179]. Naturally occurring biological conditions associated with the tumour environment, such as a drop in pH, the presence of enzymes or a change in the redox potential can act as triggers to release an encapsulated drug[180,181]. However drug carriers that respond to biological triggers have been difficult to create due to the requirement that they be very responsive to small changes in their surroundings that may not even be present across the entire heterogeneous tumour mass. For example hypoxia caused by heterogeneous vasculature within tumours is correlated with the pH of tumours being mildly acidic (pH 6.4 - 7.0). However, the central, most hypoxic regions that have the lowest pH are the least accessible to therapeutics[182-184]. This typically leads to large proportions of the drug not being released once within the tumour[185]. Alternatively a change to the environment can be caused externally[108]. For example heat can be used to trigger release from

thermosensitive drug carriers[170,186,187]. The heat can be locally applied using ultrasound, electromagnetic waves, perfusion (either drugs or blood is warmed and pumped into the patient) or thermal chambers[188,189]. The main limitation of hyperthermia triggered release is premature leakage of the drug into the blood[190].

The mechanical effects of ultrasound have been demonstrated both to improve the distribution of therapeutic agent and to be able to release liposomes containing a drug[152,191]. Alternatively, the heating effects of ultrasound can be used to release the payload of a liposome[192].

1.5 Ultrasound in medicine

Ultrasound is a pressure wave with a frequency above 20 kHz. Ultrasound B-mode scanners have been used as a diagnostic tool in hospitals since the early 1960s[193]. Since then ultrasound has mainly been used as an imaging tool due to its ability to focus deep into the body whilst being non-invasive, non-ionising and inexpensive. As an imaging tool it is a well understood modality ubiquitous in the clinic, however, by varying the pressure, frequency and duty cycle of the acoustic wave it can also be used as a therapeutic tool[194]. At low intensities it can induce mild hyperthermia to aid healing, while at high intensities it can both be used to ablate tissue by heating areas of the body to between 60°C and 80°C and create shockwaves to disintegrate tissue such as kidney and gall stones[195,196]. Typically imaging ultrasound has an intensity range of 0.0001 - 0.5 W/cm^2, ultrasound therapy uses 0.5 - 3 W/cm^2 and high intensity focused ultrasound (HIFU) uses more than 10 W/cm^2[197].

1.5.1 Diagnostic ultrasound

As ultrasound propagates through tissue, the change in acoustic impedance of different tissues causes waves to be partially reflected and scattered. The reflected signal in time can be converted into distance through knowledge of the speed of sound to identify the location of these interfaces relative to the probe. B-mode imaging is the most recognizable form of sonography and is frequently used to monitor fetal development. It uses a linear array of transducers to produce a 2 dimensional image. Since its introduction there has been a great deal of research to enhance the spatial resolution of the images, improve the signal to noise ratio and achieve 3 dimensional imaging. A number of technologies and techniques have been used to achieve this: improved quality of transducers, using a 2 dimensional array of transducers, incorporating the Doppler effect to measure velocities within the tissue, using computer power and programming to better reconstruct and render images, and the injection of microbubbles that act as contrast agents by causing ultrasound reflections off the gas they contain[198-200].

1.5.2 Therapeutic ultrasound treatments

Typically the therapeutic effects of ultrasound are not achieved directly by the pressure oscillations of the wave, but by its secondary effects of heating and cavitation. These effects are typically achieved by using frequencies that are slightly lower for therapy (0.5 – 3 MHz) than for diagnostic applications (2 – 10 MHz) and higher duty cycles. Heating occurs due to viscous absorption of the incident ultrasound wave, and typically requires very long pulses of ultrasound

involving thousands of acoustic cycles rather than the 1-10 acoustic cycles used for diagnostic applications.

A lead thermal application of therapeutic ultrasound is HIFU, which can directly ablate tissue as an alternative to surgery or radiotherapy[201]. Tissue is typically destroyed by thermal necrosis induced by viscous absorption of the incident wave at temperatures exceeding 55^{o}C for several seconds[202]. At the high intensities and long propagation path lengths typically employed, non-linear propagation of the wave through tissue leads to the pulse becoming distorted to form a shockwave, which further enhances local heat deposition. Destruction can be further compounded by both boiling and cavitation[203].

HIFU treatment is relatively non-invasive with patients able to leave hospital the day of the treatment and, as a consequence, it has a much lower morbidity than treatments such as surgery. However, extended exposure durations are required, with difficulties in imaging caused by heterogeneity of the tissue leading to the risk of failing to treat the entire target region. As a consequence the safety margins on the treatment volume are high and a large portion of surrounding healthy tissue is treated as well[204].

An alternative or complimentary heat-based therapeutic ultrasound treatment involves the temperature sensitive liposomes mentioned in Section 1.4, which can readily release encapsulated doxorubicin following HIFU-induced mild hyperthermia in the range of 40 – 43 °C[205]. The ability to reduce the ultrasound intensities required for treatment reduces the risk of off-target cell death whilst subsequent diffusion of the cytotoxic drug potentially removes the need to expose the whole tumour to ultrasound[192].

Thus far, heating has been considered to be the predominant secondary medical effect of ultrasound, but the ultrasound induced phenomenon known as cavitation can provide a powerful and targetable stimulus either to directly destroy tissue or to improve the delivery of therapeutics. Cavitation is a process whereby ultrasound-induced changes in pressure cause the oscillation of a gas or vapour inclusion in a liquid (Figure 1-3). Stable cavitation describes the linear or non-linear oscillation of a bubble for several acoustic cycles under the effect of the pressure gradients imposed by the ultrasound wave on the surrounding fluid. Inertial cavitation describes the unstable growth of a bubble during the rarefaction half-cycle, followed by violent collapse during the compressional half-cycle of the ultrasound wave under the effects of the inertia of the surrounding fluid[206,207].

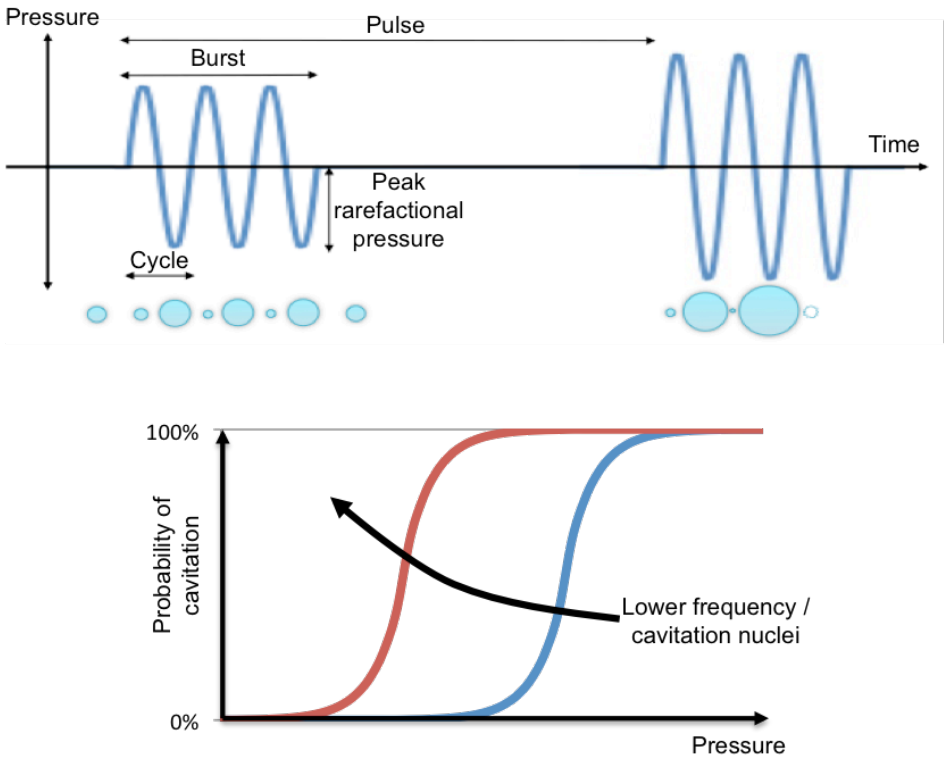

Figure 1-3: Diagram to illustrate stable and inertial cavitation
The cavitation of an ultrasound contrast agent (UCA) caused by ultrasound can cause periodic oscillation of the bubble, stable cavitation, or can lead to the unstable collapse of the bubble, inertial cavitation. The probability of inertial cavitation is dependent on peak rarefactional pressure, driving frequency and the choice of cavitation nuclei.

The type of cavitation that occurs is dependent on the ultrasound parameters and whether artificially introduced gas nuclei, known as ultrasound contrast agents (UCA) or cavitation nuclei, are present. By lowering the driving frequency of the ultrasound the probability of inertial cavitation increases: the growth stage of the ultrasound contrast agent UCA is extended and, consequently, the inertial forces acting on the gas pocket during the compressional phase are greater leading to unstable collapse. Alternatively increasing the pressure or extending the duty cycle (proportion or burst length over pulse length) of the ultrasound will increase the likelihood of cavitation. UCA are not essential to inertial cavitation but they substantially reduce the cavitation threshold of a liquid.

Stable or inertial cavitation can be distinguished by the spectral content of acoustic emissions associated with each type of cavitation. ‘Stable cavitation’ typically produces acoustic emissions at subharmonics, harmonics and ultraharmonics of the excitation frequency. In contrast, ‘inertial cavitation’ typically returns broadband emissions. A third type of emission caused by boiling vapour can be seen in the kilohertz frequency range[208,209]. It should also be noted that combinations of these different behaviours are possible: for example a bubble collapsing inertially and periodically can produce both broadband and harmonic emissions due to period doubling or period tripling[206]. The collapse of a bubble causes microstreaming, microjets, localised high temperatures and pressure shockwaves[210-213]. In the body these effects can fractionate tissue and disrupt nearby cells as well as increase delivery of therapeutics and aid the thrombolysis of blood clots[214-220].

By increasing the intensity of the ultrasound and shortening the pulse length lithotripsy and histotripsy are treatments that use pulsed HIFU to disintegrate either solid masses such as urinary stones or tissue[196]. The ultrasound tends to have a low frequency of between 0.1 MHz to 1 MHz, a high spatial peak pressure of 20 to 100 MPa, a peak rarefactional pressure of between 3 MPa and 10 MPa and a low pulse repetition frequency of approximately 1 Hz[221].

1.5.3 Ultrasound safety

Originally developed to ensure the safety of diagnostic ultrasound, the mechanical index (MI, see Equation 1-1) and the thermal index (TI, see Equation 1-2) are used to indicate the potential tissue damage that ultrasound will cause through either cavitational or thermal mechanisms[222,223].

Equation 1-1: Mechanical index (MI) is a function of peak rarefactional pressure (P) as measured in MPa and driving frequency (F) as measured in MHz[224].

$$MI = \frac{P}{\sqrt{F}}$$

Equation 1-2: Thermal index (TI) is a function of the power parameter (W_P) and the estimated power to increase the tissue by 1° C (W_{deg}) where power is measured as a function of power output, depth from the transducer and absorption and attenuation coefficients of the tissue[225].

$$TI = \frac{W_P}{W_{deg}}$$

The FDA limit diagnostic levels of ultrasound to an MI of 1.9 and TI of 1 in soft tissue or bone, but with initial specifications on the spatial peak pulse average intensity (I_{SPPA}, see Equation 1-3) of 190 W/cm^2 or the spatial peak temporal average intensity (I_{SPTA}, see Equation 1-4) of 720 mW/cm^2 [226].

Equation 1-3: Spatial peak pulse average intensity (I_{SPPA}) is a function of peak rarefactional pressure (P), density of the tissue (ρ) and the speed of sound in the tissue (c).

$$I_{SPPA} = \frac{P^2}{2\rho c}$$

Equation 1-4: Spatial peak temporal average intensity (I_{SPTA}) is the spatial peak pulse average intensity (I_{SPPA}) multiplied by the duty cycle (DC)

$$I_{SPTA} = DC \times I_{SPPA}$$

These equations do not take into account the presence of UCA. If present capillary damage can be observed above a MI of 0.4 and can also cause haemolysis within these limits[225,227,228].

1.5.4 Cavitation-enhanced drug delivery

Beyond surgical applications, cavitation can also play a key role in drug and gene therapies. Sonoporation and sonophoresis are processes that permeabilise either cells or skin[229]. The underlying cause of this phenomena is not well understood: It has been hypothesised to be mediated by the shear stresses caused by microstreaming and microjets, although there is some debate as to whether this creates pores in the membrane or if it reduces the thickness of the boundary layer around the cells; an alternative hypothesis is that temporary membrane pores are formed by the ultrasound stimulation of the endocytosis pathway[213,223,230,231]. Notably, within 24 hours the ultrasound-induced changes to the permeability of the cells have returned to their original levels. Sonophoresis raises the possibility of achieving vaccination through the skin by delivering to and utilizing the immune cells present in the dermis, while sonoporation enables improved transfection of genes or enhanced delivery of drugs into tumour cells[135,232-235].

In terms of drug delivery for cancer, cavitation can provide a driving force to counter the positive pressure gradient and enhance transport distances within tumours[236]. The microstreaming caused by cavitation of microbubbles is hypothesized to be capable of driving therapeutics out of the vasculature and to enable transport to cells that lie more than 100 microns from the nearest blood vessel. Cavitation enhanced delivery has been shown to improve the efficacy of therapeutics ranging in size from small molecules up to viruses and to enable extended survival in mice without the need to modify the therapeutic agent[187,189,191,197,237-239].

With very high negative pressures inertial cavitation can be induced in water or tissue; Wang et al. achieved enhanced penetration of an antibody using HIFU with frequency 1 MHz, pressure of 8.7 MPa, 5% duty cycle and 1Hz pulse repetition frequency (PRF)[240]. However, these ultrasound parameters are similar to those used for lithotripsy and consequently are likely to cause damage to tissue regardless of the delivery of therapeutic. As discussed in Section 1.5.2, UCA or cavitation nuclei lower the cavitation threshold, which reduce the risk of collateral tissue damage away from the target site[241]. Gas nuclei formulations are typically microbubbles. By virtue of having pre-existing stabilised gas pockets present, the cavitation event does not require the extreme rarefactional pressures required to create a void in the liquid. The combination of an i.v. injected UCA and focused ultrasound has been show to work as a cancer treatment without any addition of a drug due to cavitation causing destruction of the tumour vasculature and cells[242]. However, by optimising the ultrasound parameters, drug delivery can be improved without damaging the surrounding environment.

By providing greater flexibility to the ultrasound parameters usable UCA also enable more of the body to be treated safely: higher frequencies have a greater spatial resolution but are unable to penetrate as far into the body, while high pressures, due to non-linear propagation of the ultrasound wave into the body, also limit the depth of treatment. Ultrasound with lower pressures and frequencies can be used in combination with UCA without causing cavitation in undesired locations.

The mechanical impetus derived from cavitation has been shown to increase small drug accumulation between 2- and 5-fold[243,244]. However, as the therapeutic agent increases in size, the reliance on diffusion to deliver a drug into a tumour will be further hampered. As a consequence the impact of cavitation enhanced extravasation will be more pronounced – Bazan-Peregrino et al. demonstrated a 50-fold increase in virus delivery to a tumour when combined with a UCA and ultrasound[245]. Furthermore the distribution of the therapeutic may no longer be limited to the perivascular regions and thus a greater proportion of the tumour is treated[246].

The destruction of the UCA during this delivery could be detectable on standard B-mode imaging, and thus a reduction in contrast could be equated with drug delivery[199]. However, passive acoustic mapping (PAM) offers a real-time imaging method by which to monitor cavitation. It uses a linear transducer array to map the location of broadband emissions and overlays them on top of a B-mode image[247]. PAM may then act as a metric for delivery whereby the location and degree of delivery can be estimated[248].

By combining UCAs with a therapeutic agent and applying focused ultrasound it is possible to achieve targetable, controllable, non-invasive delivery of drugs thereby offering a true theranostic solution. The fact that ultrasound is such a commonly used clinical modality means that the equipment required for such an approach is relatively inexpensive, clinically available and acceptable to the public.

1.6 Cavitation nuclei at the nanoscale

The six commercially available UCAs are Echovist, Levovist, Optison, SonoVue, Definity and Imagent. All of these are microbubbles with a hydrodynamic diameter range between 1 and 10 μm. Alter et al. compared each of them to determine which factors were critical to deliver a plasmid DNA *in vivo*[249]. These studies demonstrated that cavitation response was determined by the stability of the microbubble formulation rather than size or shell composition. It is also notable that the process of cavitation destroys these microbubble formulations, meaning they provide only a short-lived response typically not exceeding 2 minutes in vivo[245].

This thesis addresses the hypothesis that gas nuclei stabilised on the surface of nanoparticles may provide cavitation nuclei more suited to the role of enhancing drug delivery. Firstly, altering the size of the cavitation nuclei to be smaller than the gaps found between neighbouring endothelial cells in the tumour should enable the drug and the nuclei to be driven into the tumour. This would not rely on the passive accumulation of the EPR effect (discussed in Section 1.2) as the effect seems to only cause minimal improvement in biodistribution of the particles. Instead, the size of the particles will simply

enable the nuclei to extravasate alongside a therapeutic agent when 'pushed' by the cavitation. Provided an extended cavitation response could be achieved, this would subsequently allow a chain reaction of cavitation to provide a continuous mechanical impetus into the tumour and so treatment would be achieved beyond the perivascular regions. It is even possible that sonoporation effects would then be able to enhance the cytotoxicity of the delivered drug.

Previous attempts to formulate nanoscale cavitation nuclei have typically relied upon the temperature sensitive phase change of an encapsulated liquid to a gas[190,250-253]. In the past these vectors struggled with stability and responsiveness to ultrasound. This lead to concerns that the phase change may occur before reaching the tumour, that results may be difficult to replicate and that the ultrasound parameters required to cause cavitation may be too damaging to surrounding tissue[251,254254-257]. However, Sheeran et al. demonstrated nanodroplets that were stable at 37°C and which required low intensity ultrasound to cause the droplets to vaporise[258]. Couture et al. produced nanodroplets with a diameter of 400nm containing both isohexane (56°C boiling point) and fluorescein which were demonstrated to deliver the payload of the droplet at the ultrasound foci both *in vitro* and *in vivo*[259,260]. However, the purpose of the ultrasound in both cases is to temporarily destabilise the droplet rather than provide a sustained mechanical impetus to the surrounding microenvironment. In addition, the purpose of the droplets is to utilise the EPR effect and then change size once at the desired location. Conversely, the aim of the nano-scale cavitation nuclei in this thesis would be

to remain co-localised with therapeutic agents as both agents are propelled into the tumour.

Shapiro et al. demonstrated that gas nanobubbles produced by biological organisms were able to act as UCA in vivo[261]. The ultrasound pressures used were for the benefit of imaging rather than therapeutic applications and, as such, it is not possible to know what ultrasound parameters would be required to cause inertial cavitation. However, it is an exciting technology that may have a use as a therapeutic ultrasound agent in the future.

Atomic force microscopy (AFM) has shown that bubbles are stable at the nanoscale on a solid surface without a stabilising lipid layer[262-264]. This is in contravention to the Young-Laplace equation (Equation 1-5), a model that considers the force balance of surface tension and pressure difference between the inside and outside of a droplet. It predicts that the extremely high pressure differentiation expected from such small bubbles would quickly lead to their dissolving into the liquid phase as per Henry's Law (Equation 1-6). This is a model that directly correlates partial pressure of a gas and the concentration of the gas in the liquid.

Equation 1-5: Young-Laplace equations: ΔP = pressure difference between bulk liquid and gas within the bubble; γ = surface tension; R = bubble radius of curvature[265]

$$\Delta P = \frac{2\gamma}{R}$$

Equation 1-6: Henry's Law: p = partial pressure of the gas; k_H = Henry's constant of the gas in the liquid; c = concentration of the gas dissolved in the liquid[266]

$$\boldsymbol{p = k_H . c}$$

To explain this discrepancy, Brenner and Lohse have suggested a model whereby the constant influx of gas at the interface at which the gas, liquid and solid meet is in equilibrium with the Laplacian pressures, i.e. the dissolving of

the gas at the bubble liquid interface caused by surface tension is compensated for by gas enriching at the gas, liquid, solid interface[239,265,267]. Unlike at the macro-scale, hydrophobicity is determined by surface roughness rather than the material of the solid at the nano-scale[268,269].

There are multiple models used to estimate the oscillation and collapse of bubbles upon stimulation by ultrasound. They typically rely on a modified Rayleigh-Plesset equation, which takes into account external and internal pressures, variable surface tension, viscosity, density and radiation forces, to calculate the dynamics of a spherical bubble[224,262-264,270]. Applying these models suggests that gas entrained in a cavity with a radius of curvature of 100 nm will cavitate at a frequency of 0.5 MHz and pressures less than 1.5 MPa[271,272]. At these parameters there will be limited spatial resolution but the depth of penetration will not be restricted. As the intention is to use low duty cycles, cavitation occurring outside of a tumour should not cause irreversible damage and consequently precision is not critical. The gaps already present in the endothelial wall should mean that only in the tumour will the nuclei and a therapeutic be driven out of the blood vessels.

1.7 Thesis objectives

1.7.1 Hypotheses

The hypothesis that nanobubbles stabilised upon solid particles of a size smaller than 500 nm should act as cavitation nuclei will be addressed. It is expected that this cavitation should lead to the same mechanical forces as achieved by UCA, but with the added capability of being able to be propelled

out of the blood vessels of the tumour alongside nano-scale therapeutics due to the gaps in the endothelial wall. By being able to co-localise both the therapeutic and the cavitation nuclei, more widespread deposition within the tumour is predicted, with improved efficacy as a result.

1.7.2 Aims

1) Formulate particulate cavitation nuclei that:
    a. Are of a size that will be able to escape the vasculature of a tumour through the endothelium.
    b. Have a cavitation threshold that will enable the use of ultrasound parameters that are non-damaging to the surrounding tissue.
    c. Use ultrasound of a frequency that will not restrict the depth of tissue it is capable of treating
2) Characterise their ultrasound properties in a tumour-like environment.
3) Characterise the biocompatibility of these particles.
4) Measure whether cavitation still causes enhanced drug delivery in comparison to a clinically approved contrast agent *in vitro.*
5) Optimise the ultrasound conditions to then examine whether delivery of a therapeutic can be enhanced *in vivo.*

2 Materials and methods

This chapter details the materials and methods used in the formulation of cavitation nuclei and their subsequent in vitro and in vivo characterisation. Two novel types of nanoscale, solid cavitation nuclei were manufactured: polymer nanocups and carbon nanoparticles. These particles were characterised and their ability to enhance delivery of cancer therapeutics was assessed using the methodologies described hereafter.

2.1 Formulation of ultrasound responsive polymer cups

Cups were prepared as previously described by Hui *et al*, with modifications made by James Kwan[273,274]. Latex polystyrene beads with a diameter of either 100 nm or 300 nm (Sigma, LB1 or LB3 respectively) were used as template particles with the size of the beads determining the eventual size of the cups. The particles were diluted in filtered and deionised water (Elix 3 UV Milli-Q Water Purification System, Merck Millipore) to have a concentration of 8.9×10^{12} particles/mL, for the 100 nm beads, or 3.8×10^{11}, for the 300 nm beads, to have a final volume of 36 mL. This dilution was chosen such that the total polystyrene weight remained approximately constant at 0.2 g. The solutions were then deoxygenated in a two neck round bottom flask (Wilmad-LabGlass, ML-1120-800) by saturating the liquid with nitrogen before placing in a water bath heated to 80°C with a magnetic stirrer positioned to produce

unstable mixing. A Liebig condenser (Wilmad-LabGlass, ML-560-714) was attached to one neck to prevent evaporation, whilst the second was stoppered (Wilmad-LabGlass, LG-10330-102) except when adding reagents. Methyl methacrylate (Sigma, M55909), 2-hydroxyethyl methacrylate (Sigma, 477028) and divinylbenzene (Sigma, 414565) were added to have a final concentration of 203 mM, 18 mM and 96 mM respectively. Potassium persulfate (Sigma, 216224) was then added at a final concentration of 560 μM in order to initiate the reaction. The solution was reacted for 5 hours then transferred to a centrifuge tube. Once cooled to room temperature excess monomers were removed by centrifugation at 20,000 g for 30 minutes, the supernatant was discarded and the pellet resuspended in 35 mL of water. This centrifugation and resuspension step was repeated twice more to give a total of 3 washing steps.

The entrapment of gas onto the surface of the cups was achieved by the drying of the suspension overnight on a hot plate at 50°C and then reconstituting in water or buffer. Magnetic stirring was used to break apart agglomerates in the solution before size separation using sieves of 106 μm and 32 μm (Endecotts) and syringe filters of 10 μm and 2.7 μm (VWR, 516-1001 and 514-0526).

To fluorescently label the cups, fluorescein O-methacrylate (Sigma, 568864) was introduced at a ratio of 1:9 with methyl methacrylate such that their combined concentration in the round bottom flask summed to 203 mM.

2.2 Conjugation Chemistry

2.2.1 Oxidation and freeze drying of carbon nanoparticles

Inside a fume cupboard 25 mL of 70% nitric acid (Sigma, 438073) was added to 300 mg mesoporous carbon (Sigma, 699632) in a 50 mL glass round bottom flask. The mixture was refluxed in an oil bath at 121°C with the carbon particles being stirred using a magnetic stirrer.

583 µL aliquots of the mixture were washed of nitric acid by dilution of the sample in 50 mL water and centrifugation at 20,000g for 1 hour followed by resuspension of the pellet in fresh water. Samples to be freeze dried were pipetted into glass vials (Adelphi, VCDIN2R) which were snap frozen in liquid nitrogen for 30 minutes. They were then transferred to a VirTis AdVantage 2.0 benchtop freeze dryer with shelves pre-cooled to -40°C. VirTis Lyophilization Control Software was used to adjust the temperatures as described in Table 2-1 while maintaining 100 mTorr pressure.

Table 2-1: Freeze drying protocol

Temperature (°C)	Time (mins)	Ramp/Hold
-40	20	Ramp
-40	10	Hold
-20	50	Ramp
-20	2160	Hold
20	180	Ramp
20	720	Hold

Ramp indicates a linear adjustment in temperature in the time prescribed from the temperature stated in the previous row to the temperature in the same row. Hold indicates the temperature was maintained at the set temperature for the allocated time.

2.2.2 Carbodiimide conjugation

For fluorescent labelling 42 mg of freeze dried, nitric acid treated carbon nanoparticles (AT-CNP) were dispersed in 1 mL of 50 mM 2-(N-morpholino)ethanesulfonic acid (MES, Sigma, M3671) buffer pH 4.5 (pH was adjusted using sodium hydroxide (Fisher, 10020340)). The solution was mixed with 10 µL of 5 mg/mL BODIPY® TR Cadaverine (Life Technologies, D6251) in dimethyl sulfoxide (DMSO, Sigma, D8418), 3.5 µL of 2 mg/mL 1-Ethyl-3-[3-dimethylaminopropyl]carbodiimide hydrochloride (EDC, Pierce, 77149) and 0.8 µL of 10 mg/mL N-hydroxysulfosuccinimide (sulfo-NHS, Pierce, 24520) and incubated at room temperature on a shaker for 2 hours. The solution was diluted in 1x phosphate buffered saline (PBS, Sigma, P4417) to a have a final volume of 50 mL. The samples were then centrifuged at 14,000 g for 30 minutes and re-dispersed in PBS. This washing step was repeated 3 times and in the final washing step the pellet was dispersed in 3.5 mL PBS.

2.2.3 Purification

Dialysis was performed using 10 cm of 13 kDa cut-off dialysis tubing (Spectra/Por, 132274) that had been pre-soaked in water for 30 minutes. One end of the tubing was fastened with a clip before 1.5 mL of sample was pipetted in. The open end was then sealed using a second clip. The dialysis tubing was suspended in a flask containing 300 mL of PBS and stirred using a magnetic stirrer. The PBS solution was replaced after 2 hours and 6 hours. The sample was removed from the dialysis tubing after 24 hours.

Gel filtration was performed using a pre-fabricated PD-10 column containing Sephadex G-75 (GE Healthcare, 17-0050-01). 10 mL PBS was run through the gel and, once there was no more liquid above the frit at the top of the gel, 1 mL of the sample was added. After this had passed into the column PBS was added continuously with 1 mL aliquots of eluate being collected from the bottom of the column.

Microspin gel columns, an intermediate between washing by centrifugation and gel filtration, were also used. Microspin S-200 HR columns (GE Healthcare) containing a gel matrix (a mixture of allyl dextran and N, N'-methylenebisacrylamide) were prepared by removal of storage buffer by centrifugation at 725 g for 2 minutes. 100 µL of sample was then added to the top of the column and the eluent from centrifugation at 725 g for 1 minute was collected.

2.3 *In vitro* ultrasound experimental setup

2.3.1 Single element cavitation detection

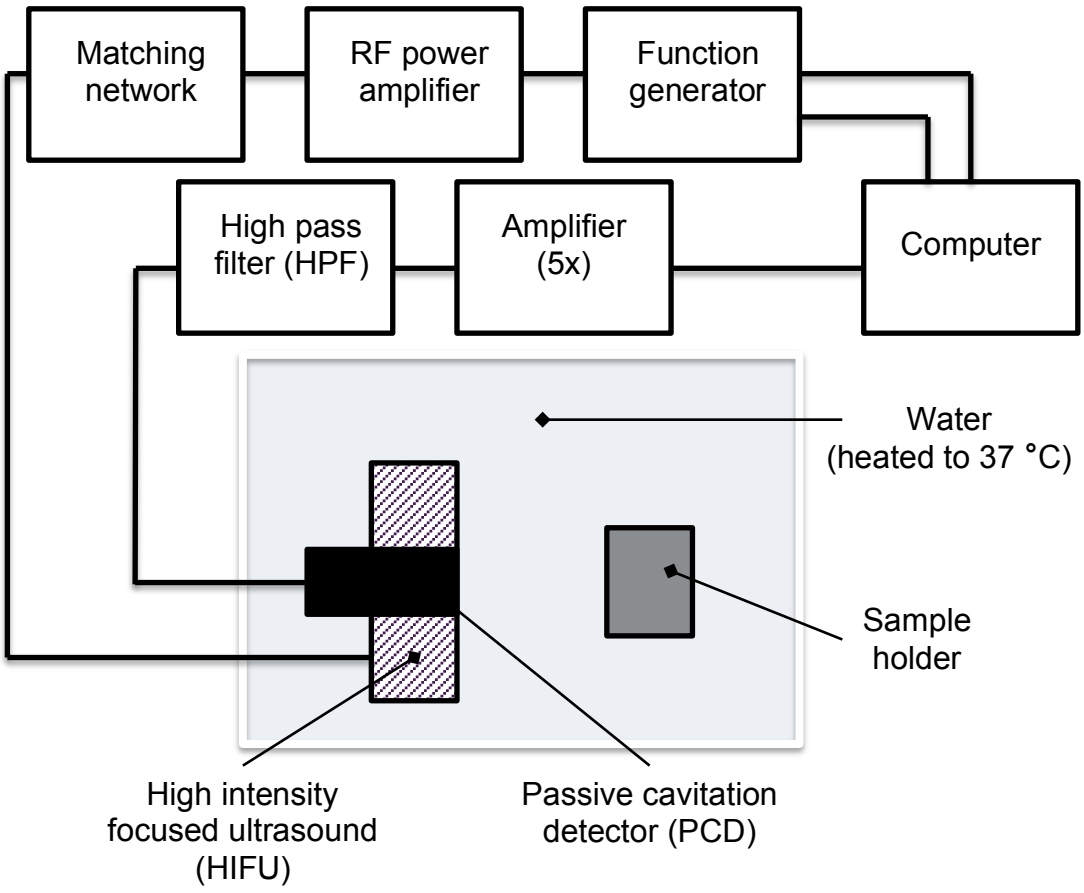

Figure 2-1: Experimental set up used to apply ultrasound and measure the pressure response caused by cavitation nuclei

A computer was used, via a function generator (Agilent, 33250A), a 300 W RF power amplifier (Electronics and Innovation, A-300) and a matching network (Sonic Concepts), to trigger a 0.5 MHz high intensity focused ultrasound (HIFU) device (H107D, Sonic Concepts), to apply ultrasound of either 0.5 MHz or 1.6 MHz to particles contained within a sample holder. A single element 7.5 MHz passive cavitation detector (PCD, Panametrics, SN 671678) was positioned coaxially and confocally with the HIFU transducer in order to

detect acoustic emissions emanating from the HIFU focus, which were then filtered using either a 2 MHz (for 0.5 MHz excitation) or 5 MHz (for 1.6 MHz excitation) high pass filter (HPF, Allen Avionics, FILT-HP2-A or FILT-HP5-A), amplified (Stanford Research Systems, SR445A) and recorded. All measurements were performed in a tank containing filtered water heated to 37°C. A schematic of the setup can be seen in Figure 2-1.

Custom LabView software (National Instruments) was used to both control HIFU input and record voltage data. This data was subsequently processed using custom Matlab (MathWorks) code written by Susan Graham.

2.3.2 Sample holders

Static sample holder

A custom cylindrical sample chamber was made out of Delrin® with a Mylar® film on the front and back face to allow ultrasound to penetrate into the holder. This static chamber was 20 mm diameter and could contain 6.7 mL liquid. A port in the Delrin® enabled sample to be injected into the holder. The holder was then sealed using an O-ring and a screw.

Capillary flow channel

To characterise particles in a setup where they were continually being replenished a setup with a flow channel was used as described by Kwan et al.[275]. 200 µm capillary tubing (Cuprophan, RC55 8/200) was connected to poly vinyl chloride (PVC) tubing with inner diameter 2 mm (Fisher, 13173503) using a combination of barbed to female and barbed to male luer connectors (Cole-Parmer, WZ-45511-00) held in a custom made Delrin structure. Flow

was controlled using the NE-1000 syringe pumps (World Precision Instruments) and was set to 300 µL/min. Ultrasound with a driving frequency of 0.5 MHz focused on the capillary channel caused there to be an activated volume of 20 nL. Figure 2-2 shows both a photograph and a basic schematic of this flow system.

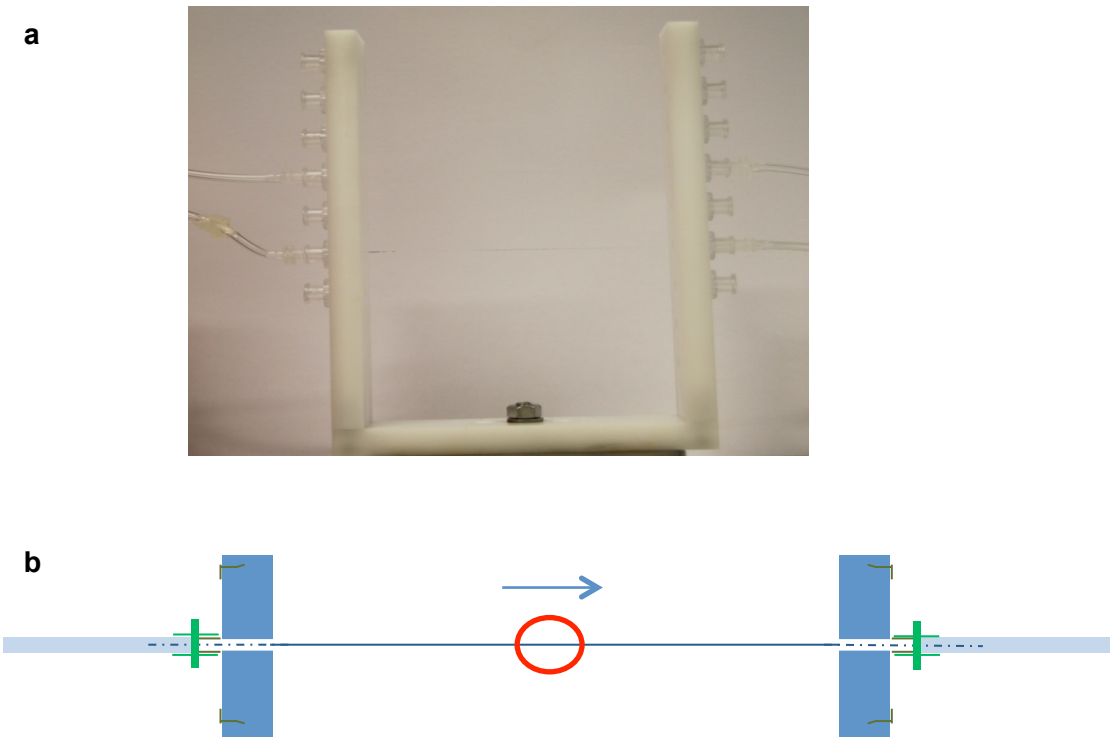

Figure 2-2: Capillary tubing flow model
Sample was flowed through capillary tubing at 300 µL/min and insonated using the same ultrasound setup as shown in Figure 2-1. The flow channel can be seen as a (a) photograph and (b) schematic.

Tissue mimicking phantom

A flow phantom holder filled with agar was used to model particle and drug extravasation (Figure 2-3). The acoustically transparent film allows the flow channels to be exposed to ultrasound and the acoustic emissions of the nuclei to be measured. Whilst its optical transparency allows the delivery of fluorescently labelled molecules out of a flow channel and into surrounding matrix to be imaged.

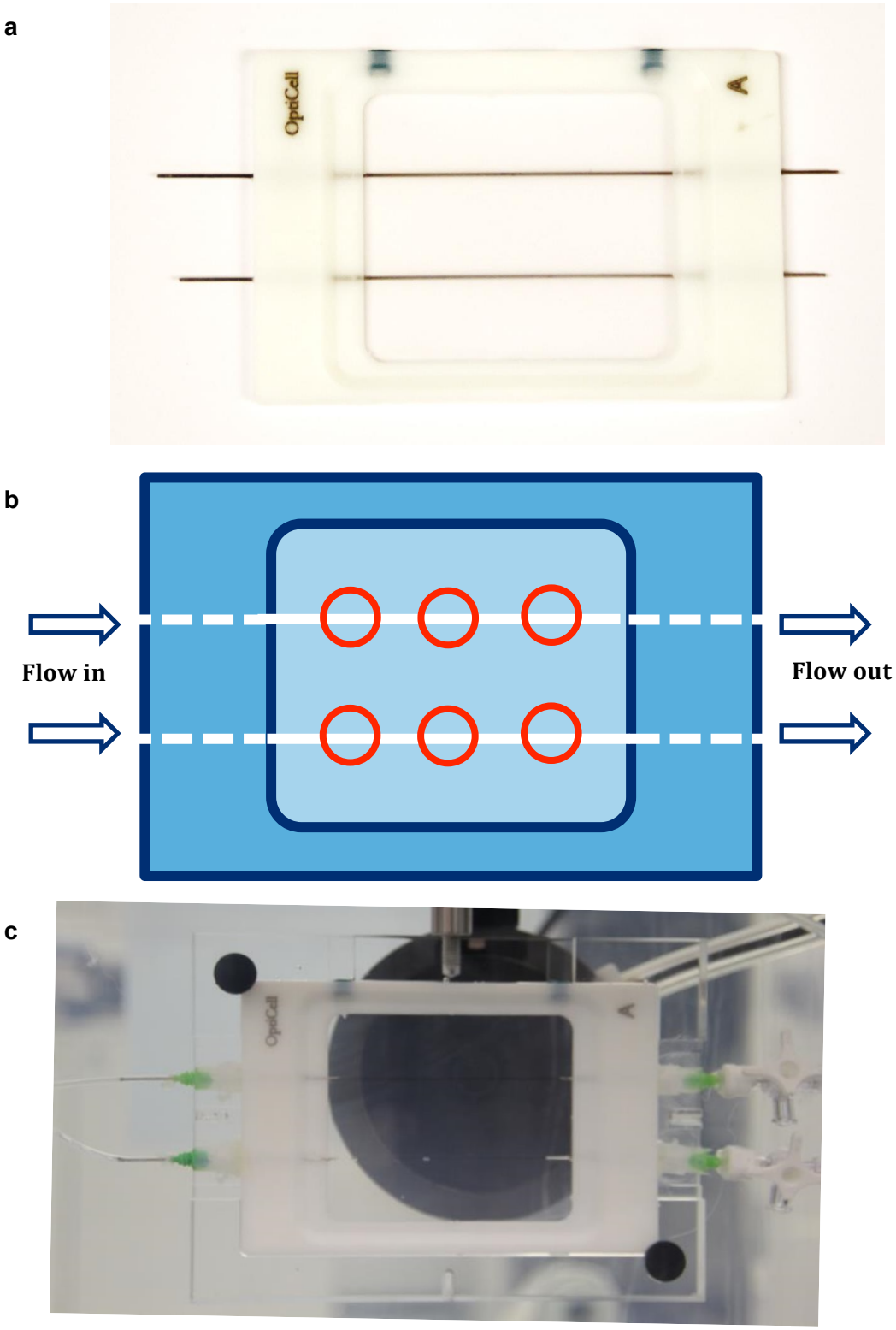

Figure 2-3: OptiCell tumour mimicking phantom
(a) Photograph to demonstrate the filling of an OptiCells with agar to form 2 flow channels (b) schematic of the final OptiCell setup including inlets and outlets (c) photograph of the OptiCell system while inside the ultrasound tank. Ultrasound setup remained the same as described in Figure 2-1.

An OptiCell® (ThermoScientific, 10374333) was drilled with 4 holes of diameter 1 mm such that 2 steel rods could be inserted lengthways through the OptiCell® 25 mm apart and 20 mm from the top and the bottom of the holder (see Figure 2-3 a). UltraPure™ Agarose-1000 (Life Technologies, 16550100) was mixed with water and microwaved to dissolve the powder. The agar was then degassed, while keeping temperature above 35°C, and injected into the OptiCell® containing the steel rods using an injection point. Another needle was inserted into the second injection point in order to allow gas to escape during the filling. Once filled with agar this second needle was removed and agar continued to be injected up to the maximum capacity of the OptiCell® (approximately 20 mL). The OptiCell® was then cooled in the fridge for 24 hours to allow the gel to set.

After varying the concentrations of agar, it was found that the optimum concentration was 1%. From a physical standpoint this concentration provided enough structural stability to prevent the OptiCell® failing when exposed to flow whilst not encumbering movement of drugs through the agar to such an extent that extravasation would not be visible. For biological relevance this concentration will allow cells to remain viable and should have a porosity of approximately 450 nm, a size that should accurately model the gaps within the endothelium of tumours[276,277].

Immediately before ultrasound treatment and approximately 24 hours after being refrigerated the steel rods were removed to reveal the flow channels. Tubing was connected to the flow channels by gluing 21 G x 31.75 mm blood collection needles (Beckton-Dickinson, 368837) using hot melt adhesive such that the tips of the needle just entered the agar filled volume. PVC tubing of

inner diameter 0.5 mm (Fisher, 13163503) was used as the inlet tubing and PVC tubing of inner diameter 2 mm was used as outlet tubing. The smaller inlet minimised the sample volume required whilst the larger outlet was used to reduce back-pressure within the system. Further blood collection needles were connected to the other end of the inlet tubing and glued to a T-junction (Beckton-Dickinson, 394601) connected to syringes, one containing the cavitation nuclei and the other containing deionised water. The outlet tubing was directly attached to a syringe. Each syringe was placed on an NE-1000 syringe pump with the inlet pump driving the liquid through the OptiCell® while the outlet pump withdrew the liquid, again, to reduce back-pressure within the system. By connecting the inlet to a T-junction it enabled the sample solution to be interchanged with water thus allowing washing of the flow channels without having to detach any of the components. Figure 2-3 b and Figure 2-3 c show a schematic and a photograph of the final set up. Once the adhesive had been allowed to set the OptiCell® was submerged in a tank containing filtered, degassed water at 37°C. The PCD was aligned to the flow channels within the OptiCell® and sample was flowed through at 1 mL/min. LabView software controlled the positioning of the flow channel to enable 3 positions to be treated along each channel 18.75 mm apart.

Flow phantom holder containing cells

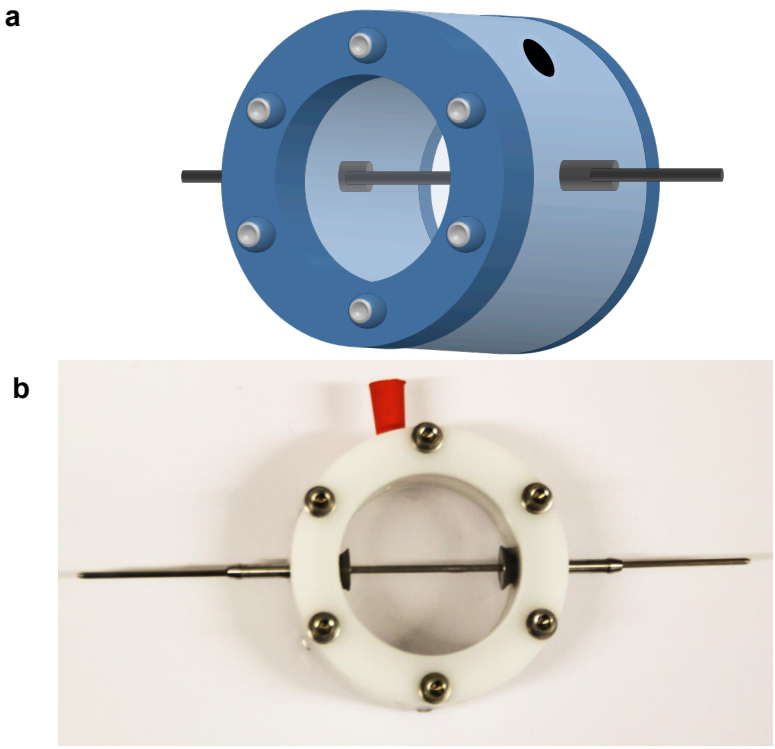

Figure 2-4: Tumour mimicking phantom containing cancer cells
(a) schematic of the phantom and (b) photograph of the cylindrical phantom holder. This was filled with $2x10^5$ CT-26 cells/mL in 1% agar. The steel rod was removed to create a flow channel of approximately 1.6mm diameter. Sample was flowed through at 1 mL/min and insonated as per Figure 2-1.

To measure cell death a custom made cylindrical phantom holder with diameter 40 mm and depth 15 mm containing a 1.6 mm diameter steel rod through the centre was filled with a mixture of cells and agarose as described by Bazan-Pregrino et al.[214]. 2% agarose was formulated in PBS (Life Technologies, 14190-094), allowed to cool to 37°C and mixed at a 1:1 ratio with CT-26 cells in Roswell Park Memorial Institute-1640 (RPMI, Sigma, R8758) and 10% foetal bovine serum (FBS) (Life Technologies, 10270106) to have a final concentration of $2x10^5$ cells/mL with an additional 4 µL/mL of propidium iodide (PI) (Sigma, P4864) to stain dead cells. This was immediately injected into the phantom holder and cooled in a fridge for 30

minutes before placing in an incubator for a further 24 hours. Figure 2-4 shows both a photograph and a schematic of the cell phantom holder.

The steel rods were removed and cavitation nuclei flowed through the resultant channel at 1 mL/min with the centre of the channel exposed to ultrasound with a frequency of 1.6 MHz, rarefactional pressure of 4 MPa, duty cycle of 5% and PRF of 10 Hz. Immediately after ultrasound treatment the agar within the phantom was dissected to give axial slices of 3 mm thickness. Fluorescence microscopy was used to view PI staining of DNA within cells to assess cell death.

2.3.3 Passive Acoustic Mapping (PAM)

A Verasonics system linked to a PC was used to input signals through a function generator, an RF amplifier and a matching network to a 0.5 MHz HIFU transducer in a tank of filtered water heated to 37°C, as described in Section 2.3.1. Within the HIFU a 128 element broadband linear array (Verasonics, L-11-4v) connected to the Verasonics system was used to record both passive cavitation and B-mode imaging. Matlab code, written by Carl Jensen, Christian Coviello and Callum Crake, then allowed a cavitation map to overlay the B-mode image in real time[247,248,278].

2.4 Particle and *in vitro* delivery characterisation

2.4.1 Size, ζ-potential, polydispersity and pH

Dynamic light scattering (DLS) is a technique that directs a laser through a suspension of particles and then measures the fluctuations of light scattered over time to determine the diffusivity. By assuming Brownian motion, the Stokes-Einstein equations (See Equation 2-1) can be used to determine the size distribution of the particles. It is only able to measure particles of a size less than 5 μm as above this Brownian motion is no longer an accurate model of the motion of particles.

Equation 2-1: Stokes-Einstein equation to determine the size of a particle by its diffusivity. D = diffusion coefficient; k = Boltzmann constant; T = temperature; μ = viscosity; R = hydrodynamic radius.

$$D = \frac{kT}{6\pi\mu R}$$

All measurements were performed using a Zetasizer Nano ZS (Malvern) and its supporting software. An incident beam of wavelength 633 nm was shone through 1 mL samples in 4 mL polystyrene cuvettes (Fisher, 11388773). The backscatter was measured at an angle of 173° and the correlation between speckle patterns over time was used to calculate particle velocity. The general purpose model performed both a cumulant and a distribution analysis to give both the mean diameter and the size distribution of the particles. Sizes quoted are determined by 'intensity' analysis – the intensity of the scattered light caused by particles of that size. Larger particles scatter more light and so greater weighting is given to them. This analysis mode is therefore the most stringent for the detection of micron scale contaminants and, consequently,

the absence of a micron-sized population provides compelling evidence for the nano-scale purity of samples. Z-average is the size of the particles if you were to fit a Gaussian curve to the particle size. It is much less sensitive to noise and can be used as a quality control. The polydispersity index is a value scaled from 0 to 1 relating to the standard deviation of the size distribution if it were to be Gaussian fitted. These calculations were repeated with 3 lots of a minimum of 11 sub runs for each sample.

ζ-potential is the charge at the surface of the electrical double layer, otherwise known as the slipping plane, surrounding a particle and is determined by the velocity of the particles when subjected to an electric field. The speed of particles was measured when a charge was applied to a flow channel containing the particles in the DLS. The Hückel equation (Equation 2-2) then enabled the ζ-potential to be calculated. Each of these measurements was performed in a 50 mM HEPES buffer totalling a volume of 750 µL. 3 lots of a minimum of 10 sub-runs were performed on each sample.

Equation 2-2: Hückel equation: U_E = electrophoretic mobility (velocity caused by an electric field); ε_r = dielectric constant; ε_0 = permittivity of free space; ζ = ζ-potential; µ = viscosity

$$U_E = \frac{2\varepsilon_r \varepsilon_0 \zeta}{3\mu}$$

ζ-potential is treated as an estimate for surface charge and is critical to a monodisperse colloidal suspension; the repulsion forces caused by the electrostatic charge of the particles must be significantly greater than the attractive Van der Waals forces to act as energy barrier to prevent the particles from colliding and aggregating. The ζ-potential must typically have a

charge of more than 30 mV or less than -30 mV in order for static repulsion to provide a stable dispersion[279]

The pH of solutions was measured using a pH-meter (Mettler Toledo).

2.4.2 Microscopy and TEM imaging

Bright field and fluorescent images were captured using a Nikon TI Eclipse fluorescence microscope with a mechanical stage. For fluorescent images a tetramethylrhodamine (TRITC) filter was used to image PI staining and a Fluorescein isothiocyanate (FITC) filter was used to image FITC labelled antibody. Large, composite images were stitched together using Nikon AR software. ImageJ software (Fiji) was subsequently used to adjust brightness and contrast equally across all images.

TEM copper grids coated with a formvar support film were either purchased (Agar Scientific, AGS162-6) or prepared in batches. To prepare the grids a microscope slide (Thermo Scientific, 10144633B) was briefly submerged in 0.6% formvar (Sigma, 09823) and then left to dry. A razor was used to cut around the edges of the slide and the formvar was released from the slide by breathing on the slide and then slowly submerging the slide in water. 400 mesh copper grids (TAAB, GM012) were then placed on the floating polymer with the rough surface downwards facing. Parafilm was used to remove the polymer layer containing the grids, which was allowed to dry on the original slides. The slides were carbon coated under an argon atmosphere using splutter coater (Quorem, Q150R ES) fitted with a carbon fibre cord. Grids were cut from the slide as needed.

Samples were prepared by leaving the grids on a 10 µL droplet for 10 minutes. The grids were dried using blotting paper before briefly transferring to a water droplet and drying again using absorbant paper and then air drying. Samples were imaged using a Tecnai 12 TEM (FEI) and the imaging software Digital Micrograph (Gatan).

2.4.3 Plate reader measurements

A FluoStar Omega plate reader (BMG) was used to measure fluorescence and absorbance of samples in a 96 well plate using the software provided with the plate reader. To create a fluorescence map the software was adjusted to measure pixels of 1.33 mm x 1.33 mm diameter.

2.4.4 SDS-PAGE to measure adsorbance of serum proteins onto particles

All solutions used to run sodium dodecyl sulphate polyacrylamide gel electrophoresis (SDS-PAGE) and subsequently stain with either Coomassie blue or silver staining can be seen in Table 2-2 and Table 2-3 respectively.

Varying concentrations of particles were incubated with pooled human serum (Sigma, H4522) for 1 hour at room temperature on a shaker. The solution was centrifuged at maximum speed for 20 minutes and 25 µL of the supernatant was mixed with 25 µL of loading buffer. The proteins were then denatured by heating to 100°C. A mini-PROTEAN® precast gel of 12% polyacrylamide consisting of 10 wells (Bio-Rad, 456-1044) was inserted into the cassette of a mini-PROTEAN® Tetra cell (Bio-Rad, 165-8000) and the bucket surrounding

the cassette was filled with running buffer. 20 µL of precision plus™ protein colour standard (Bio-Rad, 161-0374) was loaded into 1 well and the rest of the wells were loaded with 20 µL of denatured samples. The gel was then run at 140 V and 3 A until the CBB in the loading buffer visibly reached the bottom of the gel. The gel was then removed from its cassette and fixed in fixative enhancer solution for 20 minutes. The gel was washed twice in water for 10 minutes.

For Coomassie blue staining the proteins were then stained by incubating in Coomassie working solution for 2 hours at room temperature. The gel was incubated in destaining solution, with the destaining solution being replaced approximately every 20 minutes, until there was no background. Gels were then washed in water before being photographed.

For silver staining the gels were incubated in 50% silver staining solution and 50% development accelerator solution (Bio-Rad, 161-0449) until the gel had developed sufficiently. Placement in acetic acid for 15 minutes was followed by transfer into water before photographic capture.

Table 2-2 SDS-PAGE with coomassie blue staining solutions

Loading buffer	Destaining solution	Fixing solution	Coomassie blue working solution	Running buffer
2 mL 1 M Tris pH 6.8 (Bio-Rad, 161-0716)	30 mL methanol (Fisher, 10365710)	50 mL methanol	0.05g Coomassie brilliant blue R-250 (Bio-Rad, 161-0400)	100 mL 10x concentrate Tris/glycine/SDS (Bio-Rad, 161-0732)
2.7 mL glycerol (Sigma, G5516)	10 mL acetic acid (Fisher, 10034563)	10 mL acetic acid	45 mL methanol	900 mL water
4 mg Coomassie brilliant blue R-250 (Bio-Rad, 161-0436)	60 mL water	40 mL water	10 mL acetic acid	
1.6 g SDS (Fisher, 10593355)			45 mL water	
0.62 g DL-dithiothreitol (DTT, Sigma, D0632)				

Table 2-3: Silver staining solutions

Fixative enhancer solution	Staining solution
40 mL ethanol (Sigma, 24103)	5 mL silver complex solution
8 mL acetic acid	5 mL reduction moderator solution
8 mL fixative enhancer concentrate (Bio-Rad, 161-0461)	5 mL image development reagent
24 mL water	35 mL water

2.5 Routine cell passaging and culture

SKOV-3, HEPG2 and CT-26 cell lines (donated by the Department of Oncology, University of Oxford) were maintained at 37 °C with 5 % CO_2 in a humidity controlled incubator. Cells were passaged under sterile conditions in a class II laminar flow cabinet into tissue flasks of surface area 25 cm^2 (Corning, CLS431463), 75 cm^2 (Corning, CLS430641) or 150 cm^2 (Corning, CLS430825) containing 8, 13 or 25 mL of the appropriate growth media: HEPG2 (human liver hepatocellular cancer cells) and SKOV-3 (human ovary adenocarcinoma cells) were maintained in high glucose Dulbecco's modified Eagle's Media (DMEM) containing 2 mmol/L glutamine (Sigma, D5796) and 10 % FBS, while CT-26 (mouse colon cancerous fibroblast cells) were maintained in RPMI medium and 10% FBS.

Cells were passaged each time they reached approximately 90 % confluency by removing all old media, washing with warmed PBS and then adding 0.02 ml/cm^2 trypsin-EDTA (Sigma, 59418C). After approximately 5 minutes, once the cells appeared round under the microscope, the trypsin-EDTA was removed. The flasks were knocked and 10 mL of the appropriate media was used to transfer the cells into a centrifuge tube. Cells were spun at approximately 300g for 5 minutes (Eppendorf 5810R), resuspended in fresh media and pipetted into a new flask so as to have approximately 20 % confluency.

2.6 Animal studies

All animal experiments were performed in accordance with the terms of the UK Home Office guidelines and with the approval of the Medical Science Animal Ethics Committee, University of Oxford. Experiments were conducted under the Home Office Project Licence number 30/3186 and under the Personal Licence number I729DC1F9. Mice were supplied by Charles River Laboratories and housed at the Biomedical Services, John Radcliffe hospital. They were kept in individually ventilated caged (IVC) in temperature and humidity controlled rooms.

BALB/c mice were used for animal experiments using the murine cell line CT-26 and immunodeficient CD-1 nude mice were used for xenografts of SKOV3 and HEPG2 tumours.

Mice were weighed and tumours were sized at least 3 times a week. All tumour volumes reported are the multiplication of length, width and depth divided by 2 (as measured using callipers). Mice were euthanised if their weight remained below 90% of their initial weight for a period of longer than 3 days, if their tumour volume increased to above 1000 mm^3 or if they had ulceration that was not healing.

2.6.1 General Anaesthesia

Mice were anaesthetised by inhaling 1-2 L/min oxygen containing 2-5% isofluorane (purchased from biomedical services). Anaesthesia was performed for all procedures other than weighing and sizing of tumours.

2.6.2 Subcutaneous implantation of tumours

All mice underwent anaesthesia before implantation. The right flanks of BALB/c mice were shaved. A 27 gauge needle was used to subcutaneously (s.c.) implant the flanks of BALB/c mice with 100 µL of $2x10^6$ CT-26 cells/mL in PBS or CD-1 nude mice with 100 µL of $5x10^7$ SKOV-3 or HEPG2 cells/mL in a 1:1 solution of PBS and matrigel (SLS, 356237).

2.6.3 Ultrasound setup for tolerability studies

All tolerability studies were performed in conjunction with Robert Carlisle. BALB/c mice implanted with CT-26 cells were treated once the volume of tumours had reached approximately 100 mm^3. For treatment the tumour of a mouse was shaved and VEET was applied and washed away to remove any remaining hair. The mouse was anaesthetised and its tail vein cannulated. It was placed on a positioning board in a degassed water bath heated to 37°C and the PCD and HIFU were aligned on the tumour. The ultrasound setup was identical to that used in the *in vitro* studies.

25 µL of cavitation nuclei were injected with a further 5 25 µL doses injected at 2 minute intervals. Mice were subjected to ultrasound of maximum pressure 1.5 MPa, frequency 0.5 MHz and a duty cycle of 5% with a 0.5 Hz pulse repetition frequency (PRF). Ultrasound was applied for 30 seconds after each dose.

Blood samples of 20 µL were taken from the mice immediately after treatment and then 30 minutes, 3 hours, 24 hours and 4 days after treatment. They were

immediately added to 180 µL PBS, spun down and the supernatant recovered and stored at -20°C until analysis.

2.6.4 Ultrasound setup for virus delivery studies

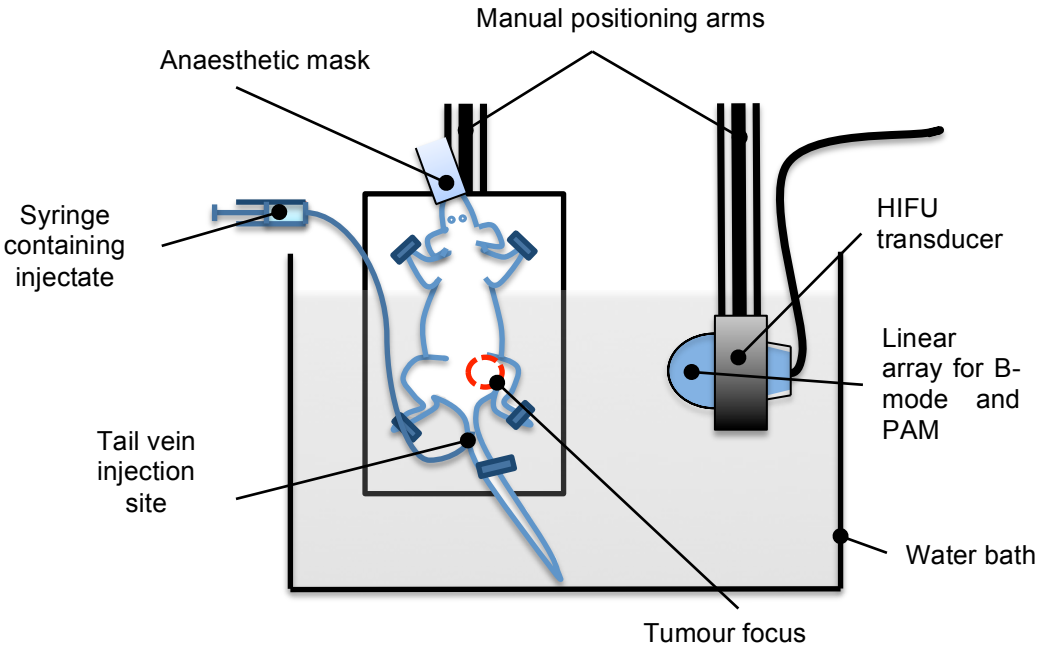

Figure 2-5: Schematic of the *in vivo* experiments
Mice were anaethetised, immersed in a water bath heated to 37°C and injected intravenously with PBS or vaccinia virus (VV) and cavitation nuclei. A transducer linked to a verasonics system was used to focus ultrasound at the tumour site and record both a B-mode image and the location and intensity of any cavitation response.

CD-1 nude mice were treated once the volume of their HEPG2 or SKOV-3 tumours had reached approximately 100mm^3. They were anaesthetised, cannulated and placed in a 37°C water bath as per the mice described in the previous section.

US with PAM was then used, as in Section 2.3.3, to insonate the tumour and map the cavitation events. A schematic of the *in vivo* setup can be seen in Figure 2-5. Once in place the HIFU was turned on before any administration of therapeutic to ensure there was no background cavitation.

There were 2 different dosing regimes for the administration of vaccinia virus (VV, supplied by Philippe Erbs of Transgene SA):

- *$1x10^5$ pfu VV*: 10 seconds after the beginning of ultrasound treatment 100 µL of VV and cavitation nuclei were administered. 2 minutes later a further 50 µL of the same solution was injected. 25 µL of cavitation nuclei were then subsequently administered at both 4 minute and 8 minute time points. 12 minutes after the initiation of treatment the ultrasound treatment was stopped and the mouse was removed from the water bath. Mice with large tumours were exposed to ultrasound at 4 different locations by moving the mouse at 3 minute intervals.

- *$1x10^6$ pfu VV*: 10 seconds after the beginning of ultrasound treatment 100 µL of VV and cavitation nuclei were administered. 4 minutes later they were injected with the same concentration of VV and cups. 2 further injection doses of 25 µL of 25 mg/mL cups were administered at both 6 minute and 8 minute time points. 10 minutes after the first injection dose the insonation was stopped and the mouse removed from the water bath.

20 days after treatment the mice were culled and their tumours and livers excised and stored at -20°C until they were assayed for luciferase or VV genome content.

Animal experiments involving the Verasonics probe were performed in conjunction with either Calum Crake or Christian Coviello and Robert Carlisle.

2.6.5 Luciferase expression *in vivo*

The VV was genetically engineered to express luciferase. To detect the infection of the virus, luciferase expression was measured 1 day, 2 days, 5 days, 10 days and 20 days after treatment. Mice were anaesthetised and had an intra peritoneal (i.p) injection of 100 µL of 15.8 mg/mL D-luciferin (Gold Biotechnology, LUCK). Mice were then kept under anaesthesia for a further 5 minutes before an IVIS 100 system (Xenogen) was used to image the biomluminescence in the mice. LivingImage software (Perkin Elmer) was used to view and measure the intensity of the bioluminescence.

2.6.6 Purification and quantitative polymerase chain reaction (qPCR)

Tumours and livers were thawed and lysis buffer (Promega, E397A) was added to the organs to have a concentration of 0.2 g tumour/mL and 0.4 g liver/mL. The organs were then disrupted mechanically using a homogeniser (IKA, T10 basic). DNA extraction and qPCR performed as described by Lyons et al.[280]. A 10-fold dilution series of VV was added to a homogenised PBS-treated tumour for a standard curve. A Gen Elute mammalian genomic DNA miniprep kit (Sigma, G1N350) was used to destroy virus capsids and purify the DNA. qPCR was performed using FAM / TAMRA labelled probe with the sequence [6FAM]ATCAAAATACAAGACGTCGCTTTTAGCAGCTAAAAGAA[TAM] and forward and reverse primers with sequences of AGATCATCGTATGGAGAGTCGTAAGAT and

TGACTACGTTGTTATGAGTGCTTGGTA purchased from Sigma. The qPCR mixture was composed of: 6.5 µL/well water, 12.5 µL/well master mix, 0.50 µL/well probe, 0.25 µL/well for primer and 0.25 µL/well reverse primer. 5 µL of the eluent from the DNA purification columns was then added to each well. QPCR run was performed using a StepOne Plus Real-Time PCR machine (Applied Biosystem) with settings as follows: an initial temperature ramp of 2 minutes at 50°C and 15 minutes at 95°C followed by 40 cycles interchanging between 30 seconds of 95°C and 2 minutes of 60°C. StepOne software was used to quantify the fluorescence in each well after each cycle enabling, with the standard curve, the number of VV genome copies in each organ to be quantified.

2.7 Biocompatibility studies

2.7.1 Human blood procurement and separation

Blood was collected into 4 mL heparin tubes (Vacuette, 95057-407) from donors within the laboratory. A maximum of 50 mL was taken from a person in a single instance and, over 6 months, the maximum permitted volume of blood to be taken from any participant was 250 mL from a female donor or 500 mL from a male donor.

To separate the blood into its constituent parts the tubes were centrifuged at 2000 g for 5 minutes. 1 mL of the supernatant was pipetted off as plasma ensuring not to disturb any of the pellet. This was immediately put on ice or stored at -80°C. To separate leukocytes the intermediate layer was pipetted from the centrifuged whole blood. 100 µL of red blood cell lysis (Roche,

11814389001) was added to each of the samples and made up to 1 mL with PBS, incubated at room temperature for 1 minute and then centrifuged at 7000 g for 5 minutes. This step was repeated until the pellet no longer had any red colouring. Subsequently the washes were repeated a further 3 times resuspeding each time in PBS. In the final washing step the leukocytes were resuspended in RPMI and the cells counted. Erythrocytes were removed from the centrifuged whole blood by pipetting 1 mL of solution from the bottom of the pellet.

2.7.2 Haemolysis assay

A haemolysis assay quantifies free haemoglobin release caused by the death and rupturing of erythrocytes. Red blood cells (RBC) and cell fragments pellet out when centrifuged whilst free haemoglobin remains in the supernatant and can be measured by absorbance at wavelength 541 nm.

Erythrocytes were washed 4 times by centrifugation at 2000 g for 5 minutes and the pellet was resuspended in PBS. In the final wash the erythrocytes were resuspended in PBS at a volume ratio of 1:10. Samples that had not been formulated in PBS were mixed at a ratio of 1:1 with 2xPBS as water induces erythrocyte cell death. 400 µL of particle solution was added to 100 µL of erythrocyte solution to then be aliquoted into 3 eppendorf tubes. Erythrocyte solutions were also added to deionised water, as a positive control, and PBS, as a negative control. All of the samples were incubated at 37 °C for 1 hour. The samples were then centrifuged at 10,000 g for 5 minutes. 100 µL of supernatant was pipetted into a 96-well plate where the

absorbance was measured at 541 nm. Equation 2-3 was used to calculate the proportion of erythrocyte cell death.

Equation 2-3: Calculation of erythrocyte cell death. Abs = absorbance; subscripts –ve and +ve refer to the negative and positive controls

$$Cell\ death\ (\%) = 100 \times \frac{Abs_{sample} - Abs_{-ve}}{Abs_{+ve} - Abs_{-ve}}$$

2.7.3 Leukocyte cell death and IL-6 ELISA

Leukocyte viability was assessed by 2 similar assays both using PI and flow cytometry. Carbon particles were tested by the following method: $1x10^6$ leukocyte cells were resuspended in 500 µL RPMI, 50 µL autologous plasma and 10 µL of sample. As a negative and a positive control 10 µL of either filtered deionised water or 2 µg/mL lipopolysaccharide (LPS) were added to the cells. The cells were incubated at 37 °C on a rotator wheel for 3 hours and then centrifuged at 2000 g for 5 minutes. 50 µL of the supernatant was stored at -80°C while the rest of the sample was redispersed and returned to the incubator for a further 21 hours with the caps slightly ajar to allow maintenance of CO_2 and oxygen levels. The samples were again centrifuged at 2000 g for 5 minutes and the supernatant removed to be stored at -80°C. The leukocytes were resuspended in 500 mL RPMI and analysed using a FACS Calibur machine (Becton Dickenson). PI was then added to the leukocyte sample at a concentration of 4 µg/mL and incubated for approximately 30 minutes on ice before they were again analysed using the FACS Calibur. CellQuest Pro software (Becton Dickenson) was used for data analysis.

Polymer cups were incubated with whole blood rather than a suspension of leukocytes in media. After an incubation of 20 minutes the leukocytes were isolated by incubation of the solution with red blood cell lysis buffer (Roche, 11814389001) for 5 minutes then centrifugation at 2000g for 5 minutes. The supernatant was discarded and the washing repeated until only a white pellet remained. The leukocytes were resuspended in RPMI and plasma and incubated at 37°C as before. The supernatant was taken at both a 3 hour and a 24 hour time point and the viability of the cells determined after 24 hours.

The IL-6 enzyme-linked immunosorbent assay (ELISA, Becton Dickinson, 550799) either used the samples from the leukocyte cell death experiment or plasma from the blood of mice that had been injected with particles. 10 µL of human plasma was diluted in 90 µL of sample diluent as was the murine plasma, which had already been diluted by a factor of 10 in PBS when acquired. The ELISA was performed as the kits instructions and the absorbance of each well was measured at 450 nm and 570 nm.

2.7.4 C3a and TNF-α ELISA

100 µL of plasma was incubated with 10 µL of a 5-fold dilution of nanoparticles on a blood wheel at 37 °C before centrifugation at 10,000 g for 5 minutes. 10 µL of the supernatant was removed and added to 2 µL of 50 mM ethylenediaminetetraacetic acid (EDTA, Sigma, EDS) pH 8. C3a and TNF-α concentrations in the plasma were measured using C3a and TNF-α ELISA kits (Beckton Dickenson, 550499 and 560478). Plasma was diluted 1 µL in 500 µL sample diluent for the C3a ELISA and 25 µL in 250 µL sample

diluent for the TNF-α ELISA. The protocols then proceeded as per the kits instructions.

2.7.5 MTS assay

A 96 well plate was seeded with 10,000 cells and 100 µL media, then left to incubate for 24 hours. 10 µL of a 5-fold dilution of the carbon nanoparticles were then incubated with the cells before incubating for a further 24 hours. The media was then replaced with a mixture of 1:4 (3-(4,5-dimethylthiazol-2-yl)-5-(3-carboxymethoxyphenyl)-2-(4-sulfophenyl)-2H-tetrazolium) (MTS, Promega, G3582) reagent and fresh DMEM. The 96 well plate was incubated for a further 30 minutes before the absorption at 492 nm was measured.

2.7.6 Alanine Aminotransferase (ALT) assay

Alanine aminotransferase (ALT) is an enzyme associated with hepatic necrosis and is used as a biomarker for liver toxicity. To test for its presence 10 µL of plasma diluted 1/10 in PBS from mice injected with cavitation nuclei and treated with ultrasound was transferred to a 96 well plate. 100 µL of ALT reagent (Thermo Scientific, TR71121) was then added to the 96 well plates and mixed. The absorbance of the wells was then measured at 340 nm over 30 minutes and compared to the readings in the blood before treatment.

2.8 Data processing and statistical analysis

Data was processed using Microsoft Excel or Mathworks Matlab. Graphpad Prism or OriginLab Origin were used to perform statistical analysis. One way analysis of variance (ANOVA) with Bonferroni pairwise comparison was used

to assess significance in data sets of more than 2 groups. Student's t-test was used to assess the significance between 2 independent groups. All figures display the mean and standard deviation of each group and significance is indicated by *, ** and *** representing p-values of less than 0.05, 0.005 and 0.0005 respectively. The statistical test used and the number of replicates within each group is specified in the figure legend.

3 Formulation, characterisation and biocompatibility of mesoporous carbon nanoparticles

3.1 Introduction

Chapter 1 discussed the potential of nano sized cavitation nuclei to improve the delivery of therapeutics by propelling both drugs and the nuclei into tumours[214,281]. A feature of the size of these nuclei is that they could co-localise with the therapeutic thus enabling them to continuously propel a drug further and further from the vasculature. This could potentially enable the whole tumour to be treated, as opposed to just the cells close to the periphery of blood vessels[68].

This chapter will focus on the formulation of particles of a size that would permit entry into the perivascular space of the blood supply supporting a tumour and have a shape that is capable of stabilising nano-sized gas bubbles on their surface to act as cavitation nuclei. As mentioned in Chapter 1 the ultrasound parameters would preferably have a mechanical index (MI) of less than 1.9[275,282].

Instead of a shelled nanobubble, we decided to explore a different concept of a particle capable of stabilizing nanoparticles on its surface, as shown schematically on Figure 3-1. The material of the nanoparticle would have to be sufficiently hydrophobic to encourage bubble growth upon exposure to ultrasound, but with adequate surface roughness to stabilize the nanobubble against dissolution in circulation.

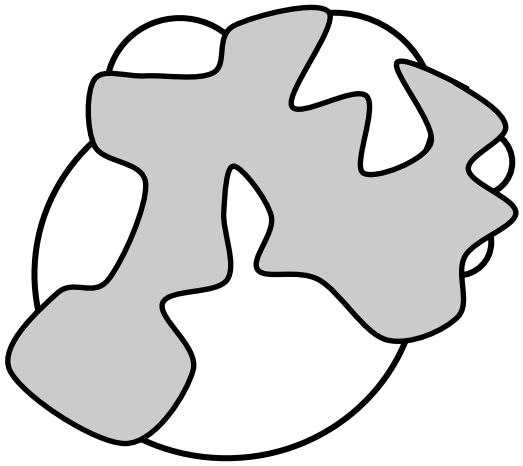

Figure 3-1: Schematic to illustrate the entrapment of nano-gas bubbles onto the surface of a solid particle
The rough surface of the particle would stabilise gas-bubbles without the need for a liposomal shell. This should enable them to more easily expand and contract in response to ultrasound than microbubbles of equivalent size.

It was hypothesised that mesoporous carbon particles of sizes between 100 and 200 nm could entrap nano-sized gas pockets onto their surface due to their rough surface. The radius of curvature of these bubbles will be greater than their actual diameter and, unlike their microbubble counterparts, they do not have a lipid layer surrounding the bubble providing increased viscous forces. Thus they should have a lower cavitation threshold than that of lipid stabilised bubbles with an equivalent radius of curvature[262,266].

Ideally the constituents of the cavitation nuclei would be pre-approved by the British Pharmacopeia. However, as carbon is not listed as an accepted material there will have to be extensive biocompatibility testing[283].

Carbon is an interesting case-study for assessing the impact of structure on toxicity because it has been used in a multitude of forms: buckyballs, carbon nanotubes and carbon black being the most frequently cited. Even with a similar shape multi-walled carbon nanotubes (MWCNT) stimulate both the classical and alternative complement pathways while single walled carbon nanotubes (SWCNT) only stimulate the classical pathway. However, SWCNT appear to cause more fibroblast cell death than their MWCNT counterparts[121,284]. SWCNT were also shown to induce the sequestration of pro-inflammatory cytokines tumour necrosis factor-α (TNF-α) and interleukin-1β (IL-1β) release whereas buckyball structures containing amino acids caused an increase of the cytokines IL-6, IL-8, and IL- 1β release but no increase in TNF-α[285,286]. In addition, buckyballs react with free radicals to mediate liver damage[287].The importance of shape was reinforces as SWCNT have been shown to cause similar lung toxicity to asbestos as their aspect ratio is increased[288].

Mesoporous carbon, under transition electron microscopy (TEM), looks to have a very similar composition to carbon black: a by-product of the partial combustion of hydrocarbons[289]. Carbon black toxicity testing has been performed in the past due to its use in rubber of tyres causing particulate release into the environment. Although carbon black has shown some inflammatory effects if inhaled, typically it has not shown significant toxicity if intravenously administered[285,290,291]. However, Brown et al. demonstrated that carbon black, in its ultrafine form, caused human monocytes to significantly increase production of TNF-α in comparison to carbon black in its micron form[292].

3.2 Chapter aims

The aim of this chapter is to:

- Develop a formulation strategy for the reproducible production of mesoporous carbon particles with a hydrodynamic diameter of 100-200 nm.
- Measure the cavitation response of the particles and compare to currently available micron-scale alternatives.
- Develop strategies for labelling the particles to allow the assessment of their pharmacokinetics and biodistribution
- Assess the tolerability of the particles *in vitro* and *in vivo*.

3.3 Methods and results

3.3.1 Size separation of particles in water

Commercially obtained mesoporous carbon (Sigma, 699632) was found to contain a disperse population of particulates with a wide range of sizes. Initial experiments were designed to test whether carbon nanoparticles (CNP) could be generated from this polydisperse mixture and whether CNP could be subsequently purified from contaminating micron-scale carbon particles (CMP).

Figure 3-2a gives an overview of the manufacturing procedure described here. 35 mL water was purified though a 0.2 μm filter (Sartorius, 16533) and added to 7 mg of carbon to fill a 50 mL sterile tube. This solution was then sonicated using a Microson^{TM} ultrasonic cell disruptor (Misonix) for 5 x 30 second bursts at 15 W (RMS) with 1 minute between each burst to avoid heating effects while still achieving disaggregation of agglomerates. Centrifugation at 2000 g for 5 minutes was then performed to create a pellet of the remaining agglomerates. The CNP containing supernatant was removed and the pellet discarded. This centrifugation step was repeated a second time at the same relative centrifugal force but for 30 minutes to ensure full removal of any remaining agglomerates. Figure 3-2b and Figure 3-2c show the size and polydispersity index (PDI) of the sample at each stage of the formulation by intensity analysis, as measured by dynamic light scattering (DLS) (as described in Chapter 2). A progressive shift away from micron scale particulates was achieved with each stage of the process, leading to the

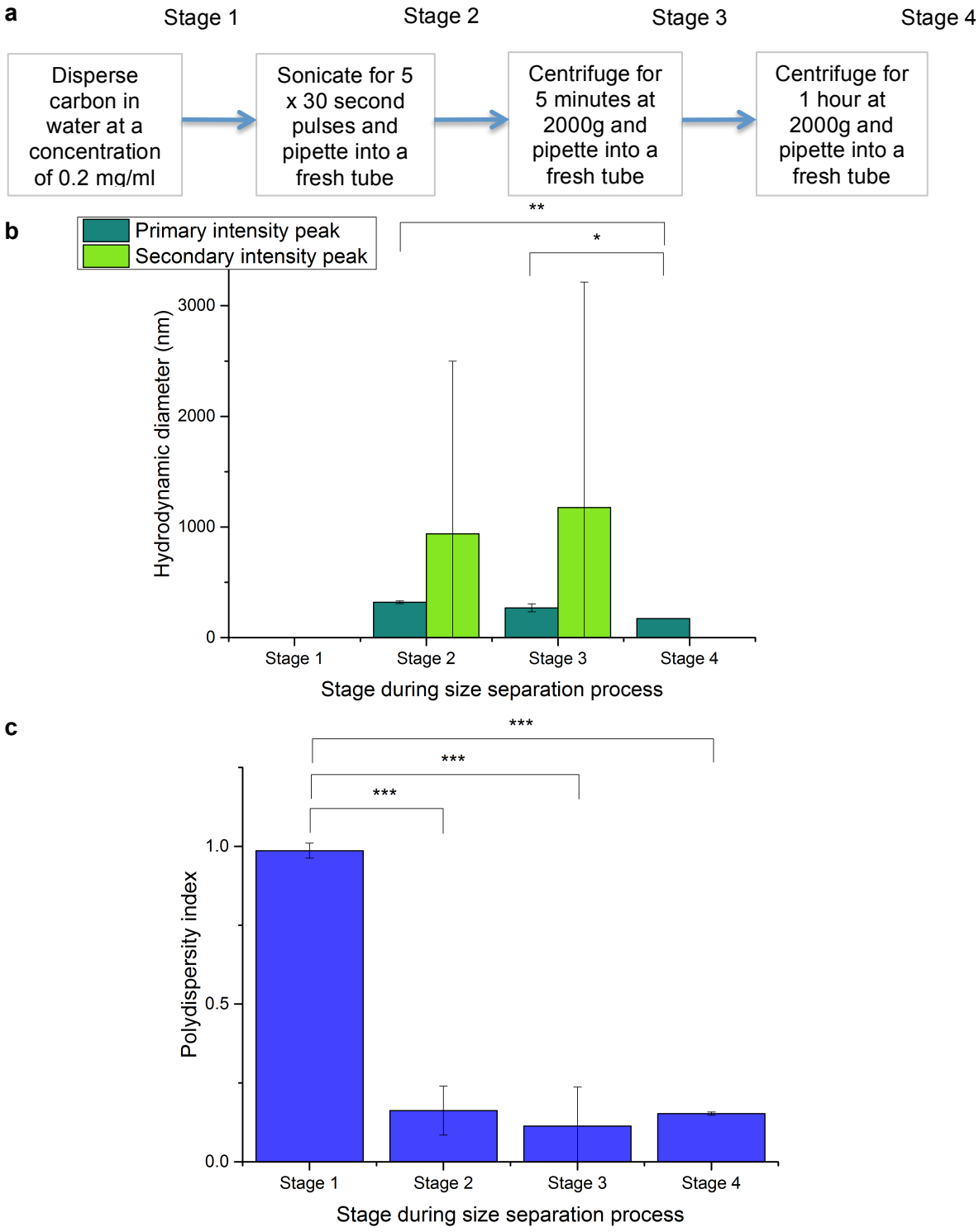

Figure 3-2: Validation of the size separation procedure of mesoporous carbon particles (a) An outline of the manufacturing process divided into 4 stages (b) hydrodynamic diameter after each stage of the process including secondary peaks. At Stage 1 the solution was too agglomerated for the DLS to give an estimate of the size of the particles. The final hydrodynamic diameter of the particles was 174 nm (c) Polydispersity index (PDI) of the particles during the manufacturing process with a final PDI of 0.154. Data represented as intensity. N = 3 separate formulation runs, standard deviation shown, ANOVA with Bonferroni post-test for significance. * = P<0.05, ** = P<0.005, *** = P<0.0005.

ultimate creation of a sample of pure 173 nm +/- 6 nm particles with a PDI of 0.168 +/- 0.014 which is indicative of a monodisperse sample. Before the particles were sonicated the DLS was unable to measure any size distribution but at Stages 2 and 3 there were secondary peaks recorded which is indicative of agglomerates in the solution. Only at the final stage was there reproducibly no longer any agglomerates detected in the solution. Absence of larger peaks when using the 'intensity' setting on DLS is a particularly stringent means of verifying that the sample is free from micron-scale contaminants.

In addition to analysis by DLS, TEM was used to validate the particle sizing and confirm sample purity (See chapter 2 for TEM imaging methodology). The images (Figure 3-3 a-d) show that although the overall shape of the particle is variable, they all have a multi-creviced structure, which may allow entrapment of gas. There is agreement with the DLS data with the majority of the particles having an average diameter of approximately 200 nm.

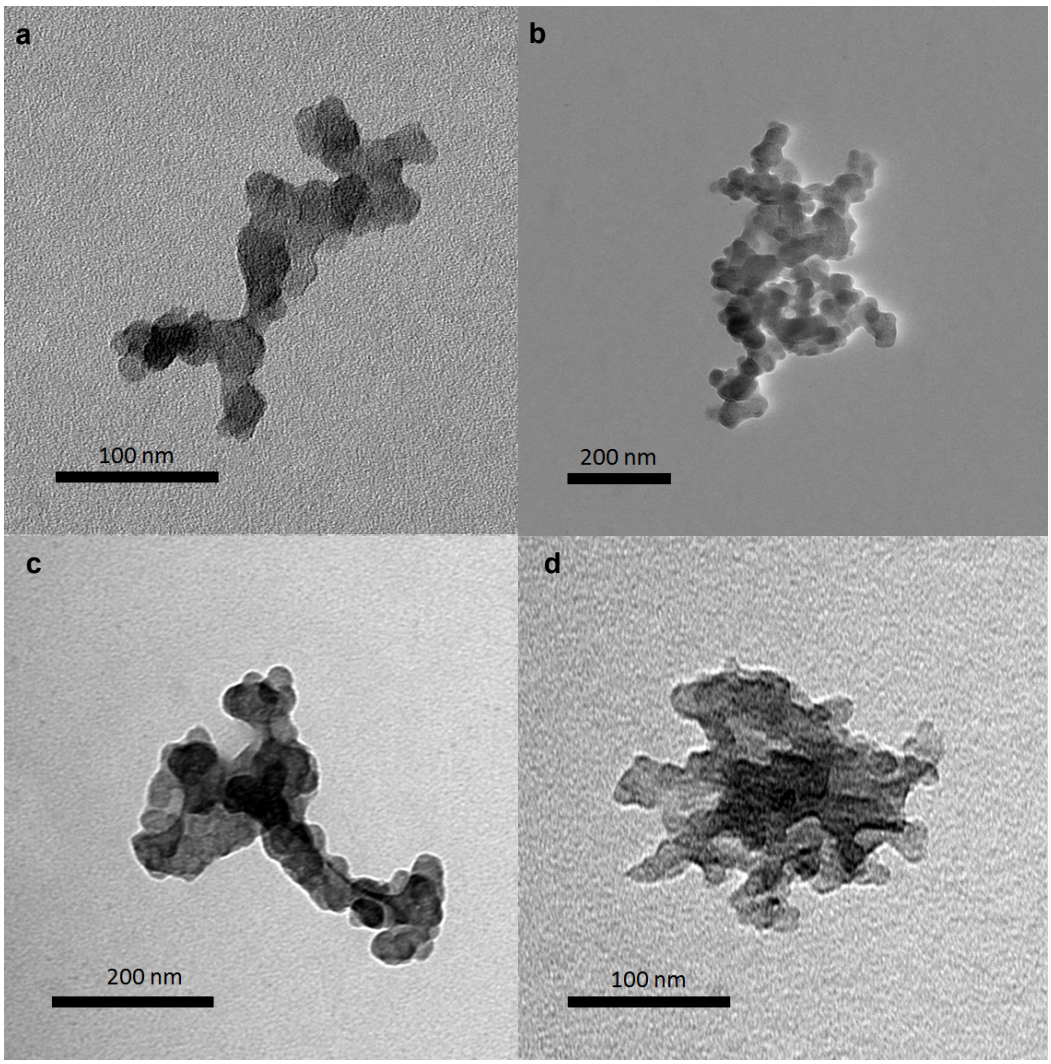

Figure 3-3: Examination of the mesoporous carbon particle morphology using transmission electron microscopy (TEM)
Droplets of sample were incubated on a carbon coated formvar copper grid, allowed to dry and imaged at magnifications of between 25,000 and 30,000x. (a)-(d) representative images of single mesoporous carbon particles.

3.3.2 Ultrasound characterisation of CNP solution

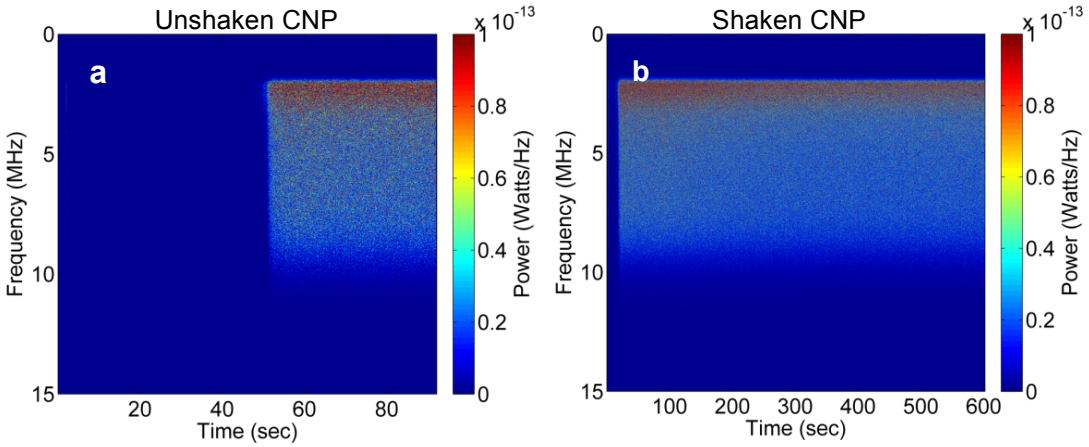

Figure 3-4: Demonstration of the CNP broadband emissions when exposed to ultrasound
Spectrogram images of the cavitation response of CNP when exposed to ultrasound of peak rarefactional pressure 1.5 MPa, frequency 0.5 MHz, duty cycle 5% and pulse repetition frequency (PRF) 0.5 Hz for an exposure time of 90 seconds. The spectrogram is divided into its compositional frequencies (MHz) and the power of each frequency (Watts/Hz) is calculated. The importance of gas bubbles entrained on the surface is shown by the difference between the ultrasound response of (a) unshaken CNP after centrifugation and (b) CNP shaken immediately after centrifugation.

The size-separated solution was dried, weighed and the final concentration of CNP measured to be 0.14 mg/mL, identifying a 30% loss of mass during the size separation process. This information subsequently enabled separated CNP sample and non-size separated carbon particles to be more accurately compared (on the basis of mass) for their ability to act as cavitation nuclei. Such testing was performed using the ultrasound setup as described in Chapter 2. Samples in a static chamber were insonated at 0.5 MHz driving frequency, 1.5 MPa peak rarefactional pressure, 5% duty cycle and 0.5 Hz pulse repetition frequency (PRF).

Both Figure 3-4 a and Figure 3-4 b show spectrograms - graphical representation of frequency content of acoustic emissions as a function of ultrasound exposure time - of the ultrasound response of CNP that had either been unshaken or shaken after the final size separation step. The particles

had been left for at least 10 minutes to allow large bubbles in the solution to disappear.

If the ultrasound caused stable oscillation of bubbles on the CNP surface, harmonics of the main 0.5 MHz excitation frequency above 2 MHz (i.e. 2.5 MHz, 3 MHz etc.) would have been visible as horizontal lines on the spectrograms. However, the generation of non-harmonic broadband emissions is indicative of inertial cavitation[206]. The importance of shaking the CNP was demonstrated by there being almost no signal for the first 50 seconds of treatment of the unshaken CNP. One hypothesis to explain this trend is that the nano-bubbles on the surface of the CNP oscillate and gradually coalesce until they reach a critical size at which they inertially cavitate and can then be detected, a process which appears to take about 50 seconds under these conditions. Alternatively, rectified diffusion, a process in which gas dissolved in the liquid diffuses into bubbles during the rarefactional phase of the ultrasound causing the bubbles to grow over time, may be the cause of the delayed ultrasound response[293]. In contrast, the process of shaking entrains larger initial nano-bubbles onto the surface from the outset, providing an immediate cavitation response. Although, CNP that had been shaken immediately cavitated but there was still a ‘priming’ effect whereby the cavitation intensity increased for the first 10 seconds of insonation. It is hypothesised, again, that this is due to bubbles on the surface of the CNP expanding to reach a size that more strongly resonates with the driving frequency.

Notably, the duration of this response far exceeds that provided by conventional ultrasound contrast agents, which are typically destroyed with the first 90 seconds at these ultrasound conditions. Indeed the cavitation response from CNP is not diminished even after 10 minutes ultrasound exposure.

The effect of size separation was studied by evaluating the ultrasound emissions caused by the insonation of CMP and the CNP produced from them – not taking into account the change in mass. Over 30 seconds the shaken CNP produced total energy emissions of 8.35 ± 0.51 $x10^{-7}$J compared to the energy emissions of shaken CMP of 6.49 ± 0.49 $x10^{-7}$J despite the reduced mass of carbon particles in the CNP. This could be explained by the disaggregation of CMP particles creating a larger total surface area of CNP.

3.3.3 *In vitro* tolerability

Having established that the CNP could provide a robust, sustainable cavitation response, their potential utility in biological systems was assessed, firstly by assessing their biocompatibility in such systems.

A haemolysis assay was used to assess the death of red blood cells (RBC) when incubated with a 2-fold serial dilution of the CNP or CMP (Figure 3-5). This assay (described in Chapter 2) uses the measurement of haemoglobin release as measured by absorbance at 541 nm caused by the loss of RBC membrane integrity. The degree of cell lysis was estimated by assuming a linear correlation between absorbance and cell death where no cell death was caused by incubation of RBC with PBS buffer while complete cell death was

caused by incubation with water. No significant ($p > 0.05$) decrease in RBC viability was observed at any concentration of either CNP or CMP.

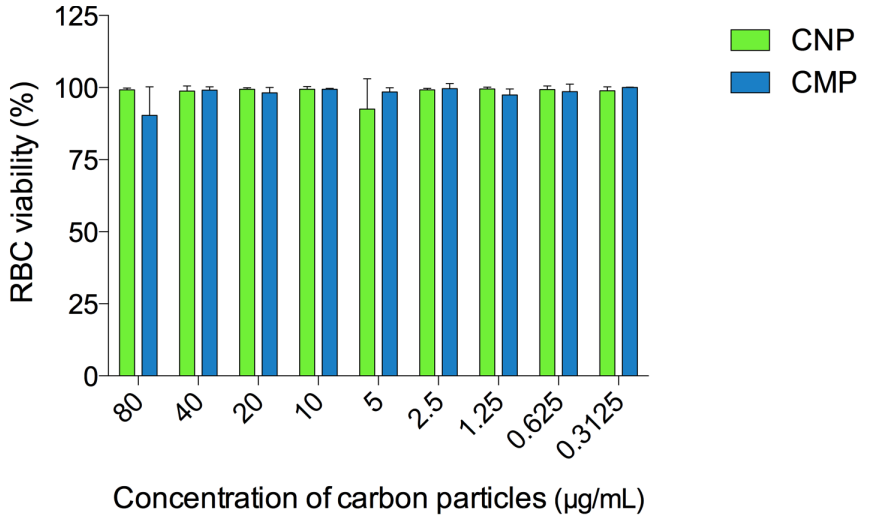

Figure 3-5: *In vitro* haemolysis assay to assess biocompatibility of mesoporous carbon particles
Human RBC were incubated with varying concentration of CNP and CMP mixed with RPMI at a ratio of 1:9 and resulting cell death was measured by the absorbance of the supernatant of the solution at wavelength 541 nm corresponding to haemoglobin. N = 3, standard deviation shown, a one way ANOVA with Bonferroni post-test analysis did not show any significant change in RBC viability at any concentration of CNP.

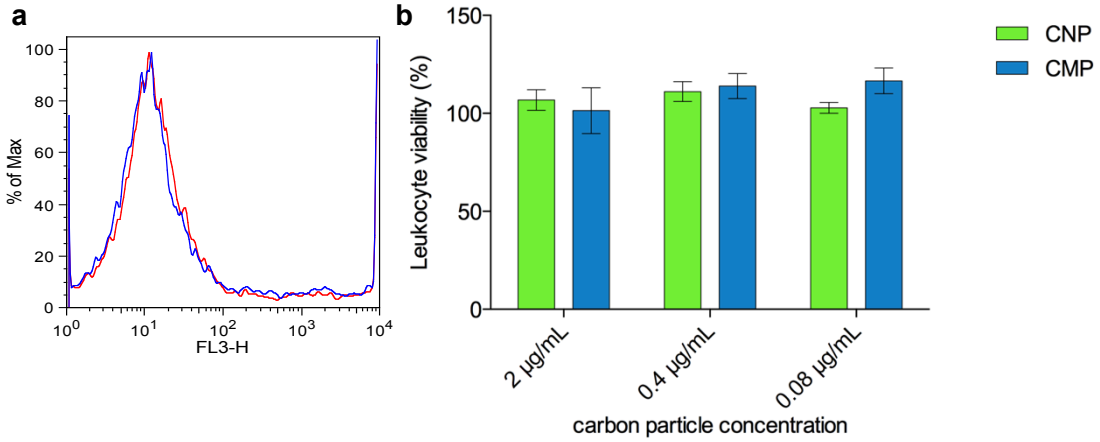

Figure 3-6: In vitro assessment of human leukocyte cell viability caused by incubation with CNP
$1x10^6$ leukocytes were incubated with 50 µL of plasma and varying concentrations of nanoparticles mixed with RPMI at a ratio of 1:9. Leukocytes were washed and resuspended in PBS to then be incubated with 2 µLof propidium iodide (PI). PI stains DNA but is membrane impermeable and consequently only stains cells with a compromised membrane. Flow cytometry was used to quantify the proportion of stained cells. (a) demonstration of the lack of change in PI staining of leukocytes incubated with PBS (red line) or 0.2 mg/mL CNP (blue line) (b) quantification of leukocyte cell viability when incubated with varying concentration of carbon nanoparticles mixed with RPMI at a ratio of 1:9. Mean values of N = 3 with standard deviation shown. One-way ANOVA with Bonferroni post-test analysis did not show a significant change in cell viability caused by any concentration of carbon particle ($p > 0.05$).

Flow cytometry and propidium iodide (PI) staining was used to assess the viability of leukocytes following incubation with the carbon particles for 24 hours. PI is a membrane impermeable dye, which fluoresces upon intercalation into DNA. When plasma and nuclear cell membranes are damaged PI can enter cells and produce a fluorescent signal. Flow cytometry allows the fluorescence of each individual cell in a population to be measured and so this assay provides information on the incidence and extent of cytotoxicity. Figure 3-6 a shows the there was no shift in fluorescence, as measured by flow cytometry, when leukocytes were incubated with CNP (blue line) and PBS (red line) superimposing. Figure 3-6 b is the quantification of leukocyte viability after incubation with carbon particles and shows that neither the CNP nor the CMP particles induced leukocyte death over the incubation period.

After 3 hours and 22 hours of the incubation of leukocytes and particles a sample of the supernatant was taken and IL-6 concentrations were measured using an enzyme-linked immunosorbent assay (ELISA, see Figure 3-7). Under stress conditions, monocytes, macrophages and T cells produce IL-6, a multi-functional cytokine that can be both pro- and anti-inflammatory[294]. Importantly, it stimulates an immune signalling cascade[294]. Lipopolysaccharide (LPS) was used as a positive control to have a final concentration of 10 ng/mL, which is consistent with previous ex vivo experiments used to stimulated IL-6 sequestration without causing cell death[295]. At the 3 hour time-point no significant difference in IL-6 release was detected between any of the samples above background ($p > 0.05$); there was a non-significant trend of higher CNP concentrations causing greater IL-6

production. In contrast, by 22 hours there was an increase of 2619 +/- 1429 pg/mL of IL-6 above background caused by incubation of the leukocytes with LPS. There was no trend in IL-6 concentration caused by increasing concentrations of CNP and CMP. Hence it can be concluded that carbon particles, either in CNP or CMP form, increase IL-6 release from leukocytes above the level which results from the ex vivo manipulation of these cells after 22 hours. The large error bars are due to single anomolous samples recording very high concentrations of IL-6. This may have been due to leukocytes being sensitised by the pipetting process during the separation and resuspension of leukocytes in media. To improve upon these results a sample size greater than 3 should have been used and greater care should have been taken in the treatment of the leukocytes.

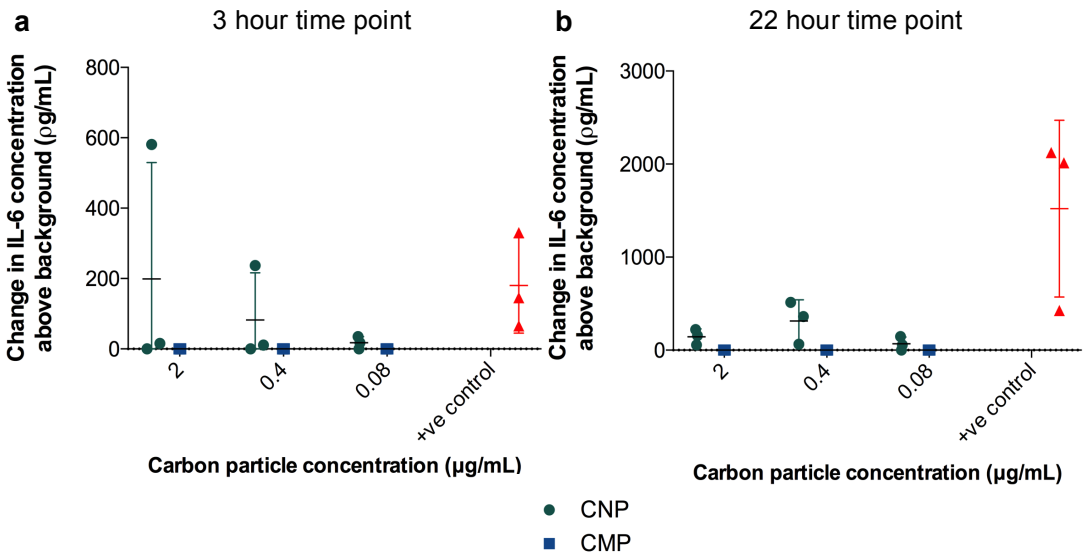

Figure 3-7: Measurements of the cytokine Interleukin-6 (IL-6) production over time caused by incubation of leukocytes and plasma with CNP and CMP
$1x10^6$ leukocytes were incubated with 50 µL of plasma and varying concentrations of particles mixed with RPMI at a ratio of 1:9. An ELISA was then used to measure the concentrations of IL-6 in the supernatant after (a) 3 hours and (b) 22 hours. Concentrations shown are values subtracted by background IL-6 production caused by incubation of leukocytes with buffer. Mean of N = 3 values, standard deviation shown, ANOVA with Bonferroni post-test comparison showed no significant change in IL-6 between any of the groups apart from between LPS and carbon particle groups after 22 hours, * = $P<0.05$.

Figure 3-8 shows the cell death of murine fibroblast carcinoma cell line CT-26 induced following incubation with a five-fold dilution series of carbon particles as quantified using the MTS assay (see chapter 2). MTS is a salt which, when reduced by metabolic enzyme activity within cells, produces a formazan dye that absorbs at 492 nm. The absorbance can thus determine metabolic rate and is used as a measure of cell viability. To increase the likelihood of a response higher concentrations of particles were used; at such high concentrations the size separation protocol was no longer completely effective meaning CMP remained in the solution (as determined by DLS). Despite the high number of particles no sample showed any reduction in cell viability compared to the negative control. A one-way ANOVA demonstrated that there was no significant difference in viability at any carbon particle concentration.

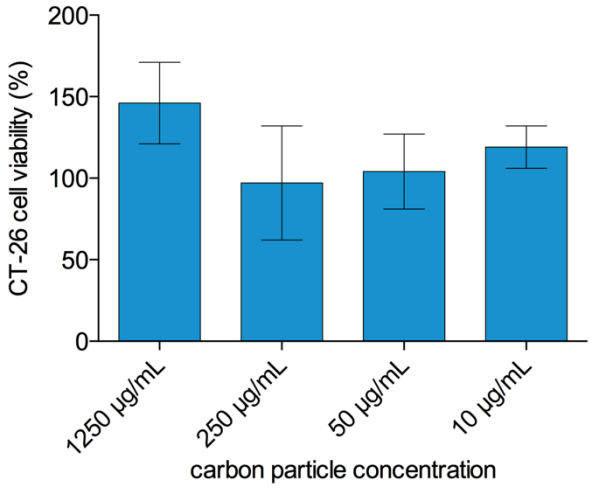

Figure 3-8: Cancer cell viability after incubation with mesoporous particles
Viability of CT-26 cells, a murine colon fibroblast cancer cell line, after incubation with varying concentration of carbon particles and RPMI mixed at a ratio of 1:9. Cell death was determined by the activity of cellular enzymes using an MTS assay (see 2.7.5) to calculate viability as a percentage of the viability of identically treated but non-exposed cells. Mean of N = 3 values, standard deviation shown, a one-way ANOVA with Bonferroni post-test did not show any significant change in CT-26 cell viability at any concentration of CMP.

Adsorbance of proteins onto the surface of the CNP when intravenously (i.v.) injected would both reduce the ultrasound responsiveness of the particles and lead to the raising of an immune response. An initial experiment was performed to detect the adsorbance of proteins within human serum onto the nanoparticles using sodium dodecyl sulphate polyacrylamide gel electrophoresis (SDS-PAGE) as described in Chapter 2. A 2-fold dilution of nanoparticles was incubated with 20% pooled human serum and, by measuring the amount of proteins in the supernatant after the centrifugation, it should be possible to identify the loss of proteins caused by adsorbance. An SDS-PAGE separates out protein bands within a mixture based on their molecular weight. Coomassie blue non-specifically stains gels to identify the locations of proteins bands on the gel. Experimental samples were compared to control samples with human plasma serum but no CNP.

The final gel can be seen in Figure 3-9 a. There appears to be no change in human serum proteins present in the gel which suggests the amount of proteins that adsorb onto the surface of the carbon particles is less than the detection limit of the coomassie blue stain (0.7 ng/mm^2).

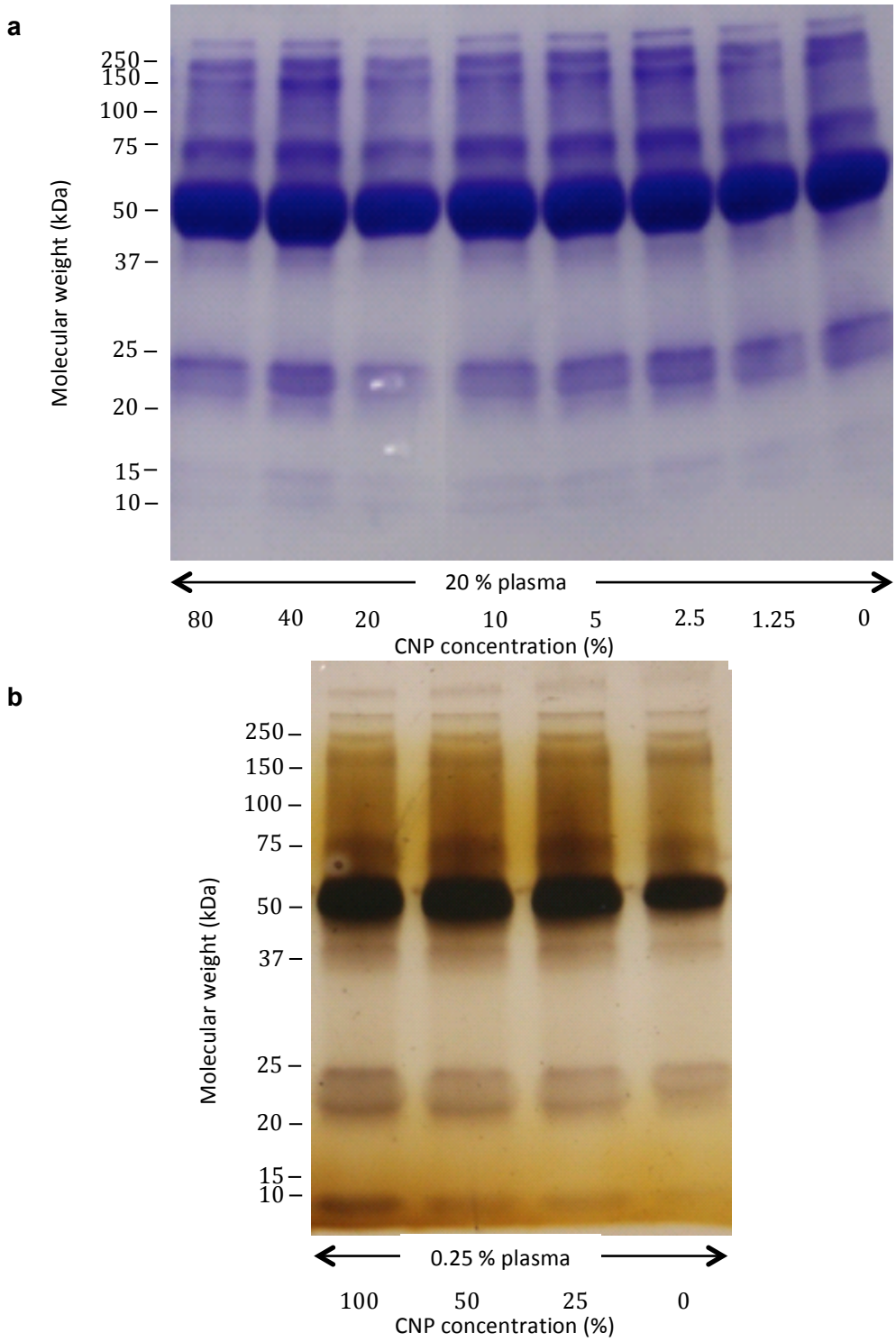

Figure 3-9: Measurement of human serum proteins physisorbtion onto CNP measured by SDS-PAGE

Plasma was incubated with varying dilutions of 0.2 mg/mL CNP for 1 hour at room temperature. The supernatant was then added to the wells of an SDS-PAGE. Protein bands, identified using a protein ladder, were stained with (a) comassie blue staining of CNP incubated with 20% plasma (b) silver staining of CNP incubated with either 0.5% or 0.25% human plasma.

As a result of the SDS-PAGE showing no detectable change in supernatant protein concentration Coomassie blue was exchanged for silver staining due to its heightened sensitivity of approximately 0.05 ng/mm[2296]. 0.2 mg/mL, 0.1 mg/mL or 0.25 mg/mL CNP was incubated with human serum to have a final serum concentration of 0.25% or 0.5%. This suggests there is negligible adsorbance of the serum proteins onto the CNP. Indeed, on the basis of literature and molecular weight marker lanes it is suggested that the three major bands evident on the gel represent albumin, haptoglobin and IgG light chains with molcular weights of 67 kDa 28 kDa and 100 kDa respectively[297]. As serum albumin is frequently a substantial portion of the protein corona surrounding particles it is reasurring that the level of this protein in the supernatent is not visibly diminished upon mixing with CNP[298]. The formation of a protein corona would probably detrimentally impact on the ability of the CNP to achieve favourable PK and maintain ultrasound response. However, the sensitivity of this study is limited. In the coomassie blue staining protocol approximately 45 mg albumin / mg CNP would need to be adsorbed to see a complete loss of the albumin band[299]. Although the silver staining protocol is more sensitive adorption of 0.56 mg albumin / mg CNP would still still be required to see a loss of the albumin band. Regarding the two other notable bands in the silver stained gel: CNP would have to adsorb 0.13 mg IgG / mg CNP or 0.01 mg haptoglobin / mg CNP to see a loss of the bands. Instead a pull-down assay should have been used to assess protein-particle interaction as it would have provided much greater sensitivity[300].

In summary physicochemical analysis demonstrated the efficacy and reproducibility of the method for producing CNP, whilst *in vitro* ultrasound

analysis demonstrated improved acoustic response with these CNP compared to the heavily aggregated parental CMP. Against expectations CNP and CMP demonstrated negligible RBC, leukocyte or cancer cell line toxicity in *ex vivo* studies and caused negligible protein adsorbance.

These studies indicated that in vivo study of these particles was warranted. The first step of such studies is to assess the pharmacokinetics and pharmacodynamics. However, labelling of the CNP is essential to assess their pharmacokinetics/pharmacodynamics (PK/PD). By characterising whether circulation would be extensive enough for the CNP to be useful and identifying the organs in which the CNP would accumulate a more focused raft of *in vivo* tolerability and efficacy assays could be used.

3.3.4 Labelling of carbon nanoparticles

A method of labelling the nanoparticles is highly desirable. This section presents the labelling strategy that was attempted on the CNP in order to assess the pharmacokinetics and clearance pathways of CNPs in vivo while maintaining their ultrasound responsiveness.

Graphite is oxidised when refluxed in strong acids. Nitric acid and sulphuric acid are the most frequently used acids for this purpose; nitric acid was chosen due to its lower propensity to leave contaminant residues[301]. Carboxyl groups would provide a simple conjugation method, by carbodiimide chemistry, to any molecule that contains an amine group.

Carbon particles were refluxed at 121°C in 70% nitric acid. At time points between the addition of the nitric acid and 1 hour, samples were diluted in

water and washed by centrifugation (see Chapter 2 for details). In the final step they were redispersed in 35 mL water to achieve a concentration of approximately 0.2 mg/mL and thus equivalent to initial experiments with CNP.

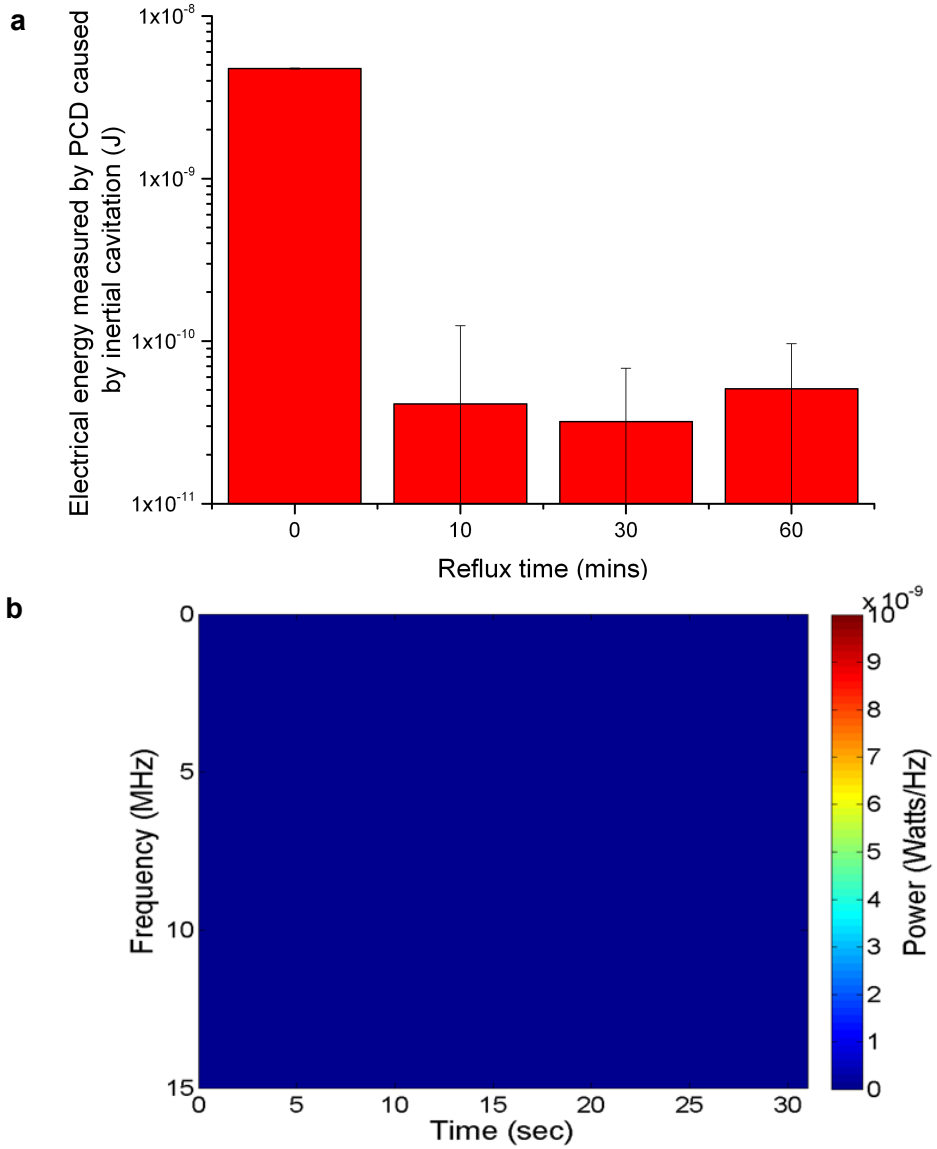

Figure 3-10: Ultrasound response of refluxed particles washed by centrifugation and redispersed in water

CNP that had been refluxed with 70% nitric acid for up to 1 hour, washed and then insonated with ultrasound of peak rarefecational pressure 1.5 MPa, frequency 0.5 MHz and duty cycle 5% with a 0.5 Hz PRF. (a) comparison of acoustic emissions of particles refluxed for varying lengths of time N = 1 performed in triplicate, standard deviation between each measurement. (b) representative spectrogram of the particles refluxed for 1 hour showing negligible cavitation either over time or across frequencies.

The ultrasound response of these particles, measured using the same conditions as those used in previous ultrasound measurement on unmodified particles (), can be seen in
Figure 3-10 a. The total energies were significantly depressed compared to the ultrasound response of particles that had not been treated with nitric acid dropping from 4.75 +/- 0.04 x 10^{-9} J to 4.11 +/- 8.31 x 10^{-11} J within 10 minutes of acid treatment. Brief incubation of the particles in nitric acid at room temperature followed by washing steps was sufficient to reduce the total acoustic emissions of CNP to 5% of the value achieved by their non-incubated counterparts. After 1 hour of oxidation this level dropped to almost 0.1%.
Figure 3-10 b displays the spectrogram of the ultrasound response of particles refluxed for 1 hour. There is clearly little to no ultrasound induced cavitation response detectable.

It was proposed that this was due to residual nitric acid on the surface of the particles reducing the surface tension of the solution and consequently destabilising gas bubbles on the CNP. In response, freeze-drying was chosen as a method to remove all nitric acid. Samples were taken following 0 hr, 2 hr, 4 hr, 8 hr or 24 hr reflux in nitric acid and washed using centrifugation before being lyophilised as described in Chapter 2. Briefly the freeze drying process is composed of 3 stages: the freezing step, which must be below the glass transition temperature of the solution to ensure the entire sample is frozen (set at -40°C), the primary drying step when the sublimation takes place and must be above the glass transition temperature (set at -20°C) and finally the secondary drying step where any remaining liquid is sublimated off (set at 20°C)[302].

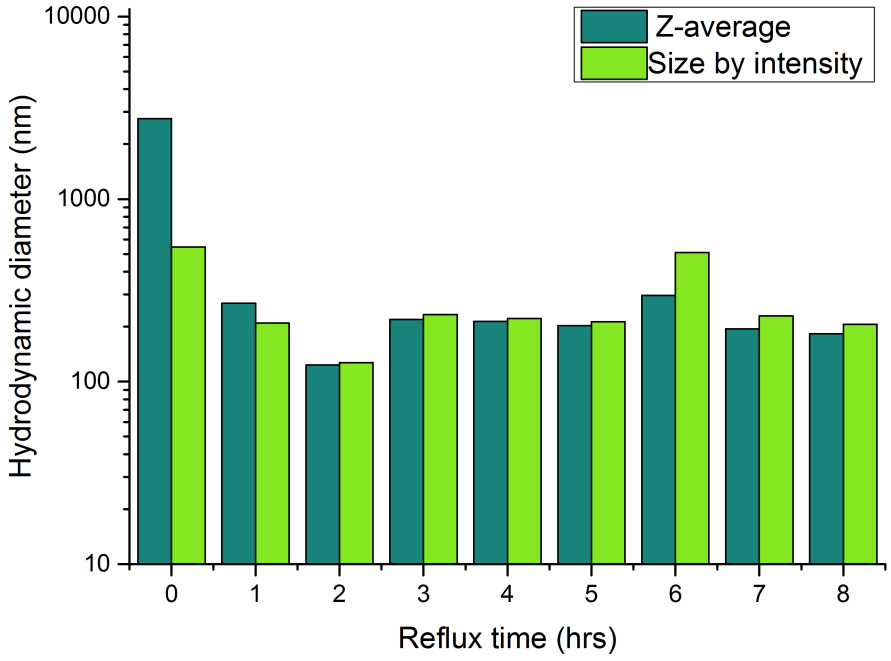

Figure 3-11: The impact of nitric acid reflux time on the size of the carbon particles
Carbon particles refluxed in 70% nitric acid for between 0 – 8 hrs were washed and freeze dried and redispersed in PBS. Their hydrodynamic diameter was measured using DLS. Both size by intensity and by z-average are shown as similar values indicate a monodisperse, Gaussian distribution of particles. N = 1, measurement performed in triplicate..

Samples were redispersed in 35 mL PBS and size separated as per the process described in Figure 3-2 a. Figure 3-11 shows the size distributions of the particles refluxed for varying lengths of time where size distribution is described using both the z-average and size by intensity: discrepancies between these 2 values suggest that the presence of agglomerates as the z-average indicates the mean diameter of particles assuming a monodisperse, Gaussian distribution while size by intensity can incorporate multiple peaks in the size distribution. Notably the 24 hour time point is not included due to the DLS being unable to analyse the sample. Figure 3-12 shows the ζ-potential of the particles between reflux times of 0 and 8 hours. The ζ-potential was also

measured at 24 hours but the signal-to-noise ratio was too great to give a clear result.

TEM was used to characterise the impact of nitric acid on the morphology of the AT-CNP at time points 0 hr, 4 hr, 8 hr and 24 hr (see Figure 3-13). The rough surface of the particles becomes smoothed and more spherical as the reflux time increases. A film also begins to develop around the particles, coating the cavities that were previously hypothesised to entrain gas bubbles and enable cavitation nuclei activity. Figure 3-13 d shows that the particles, after 24 hours of being refluxed in nitric acid, become very small and sparse which explains the difficulties DLS had in measuring the size and ζ-potential of the samples.

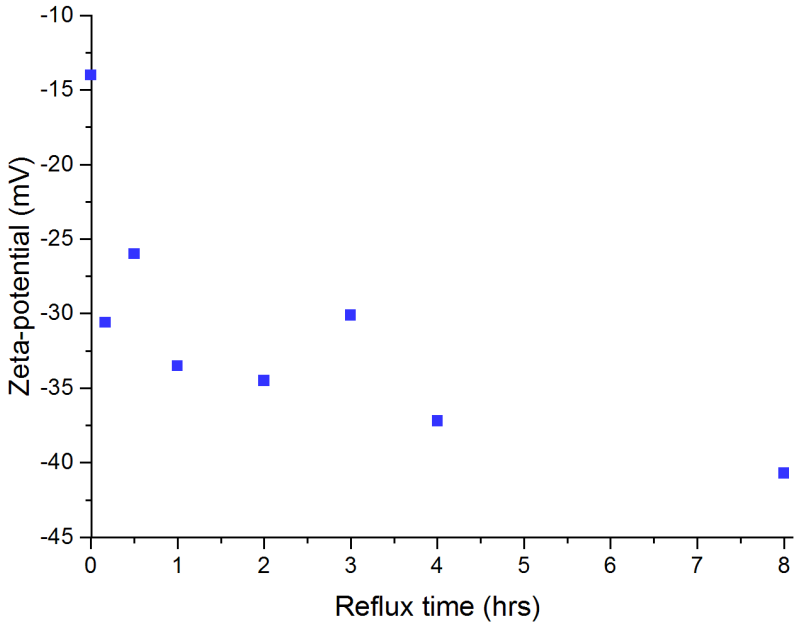

Figure 3-12: The impact of nitric acid reflux time on the ζ-potential of carbon particles
CNP were refluxed in 70% nitric acid for between 0 and 8 hours, washed by centrifugation and freeze dried. Their ζ-potential in 50 mM HEPES buffer pH 8 was measured using DLS. ζ-potential change is indicative of the oxidation of the carbon particle's surface to form carboxyl groups.

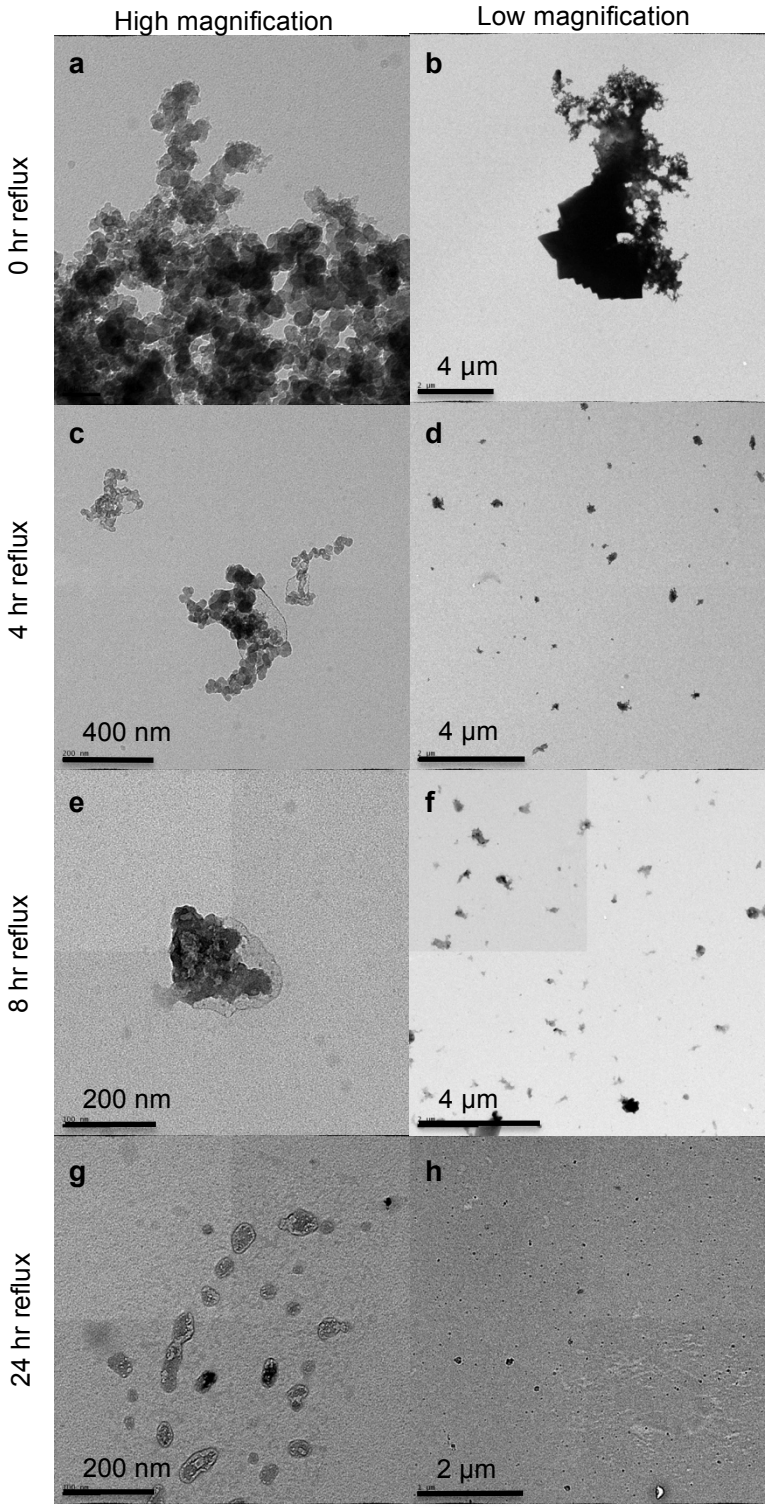

Figure 3-13: TEM images of nitric acid treated CNP (AT-CNP)
A 10 µL droplet of sample was incubated on a carbon coated formvar copper grids and imaged using TEM at a magnification of 11,200x to 23,000x to determine the change in morphology of the particles caused by varying reflux times (a) and (b) particles incubated in nitric acid at room temperature; (c) and (d) particles refluxed for 4 hrs; (e) and (f) particles refluxed for 8 hrs; (g) and (h) particles refluxed for 24 hrs.

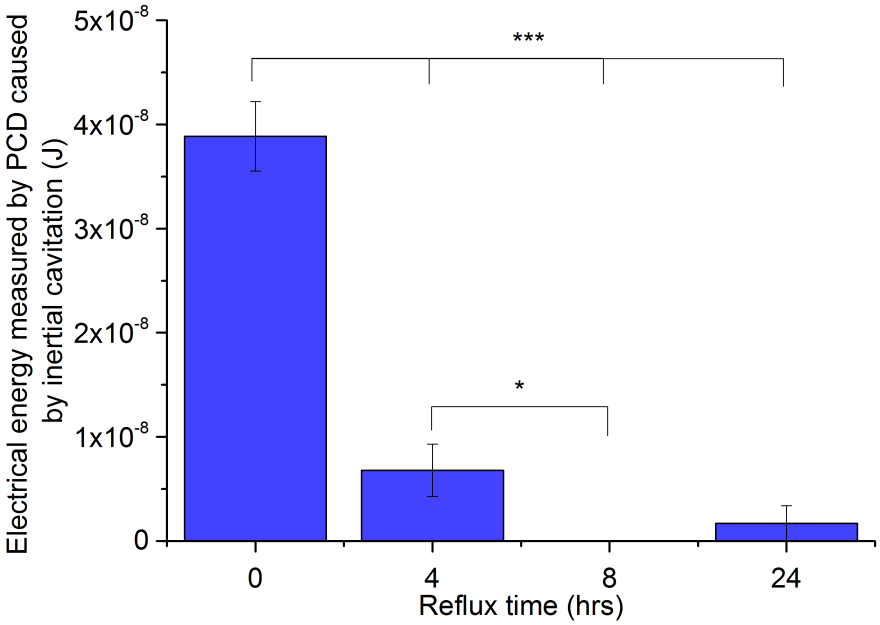

Figure 3-14: Sonosensitivity of the AT-CNP once freeze-dried and resuspended in water
Particles that had been acid treated for between 0 and 24 hours and subsequently washed, freeze dried and resuspended in water at a concentration of 0.2 mg/mL were insonated in a static chamber with ultrasound of peak rarefactional pressure 1.5 MPa, driving frequency 0.5 MHz, 5% duty cycle and PRF 0.5 Hz. Mean of N = 3 and standard deviation shown. One way ANOVA with Bonferroni post-test for significance. * = P<0.05, *** = P<0.0005.

To assess whether the changes to morphology did alter the sonosensitivity of AT-CNP, the ultrasound response of the particles was measured and can be seen in Figure 3-14. Particles that had only been incubated in nitric acid at room temperature and then freeze dried had very similar sonosensitivity to unmodified particles that had not been through the freeze drying process with total acoustic energies of 3.89 ± 0.33 $x10^{-8}$J and 4.17 ± 0.26 $x10^{-8}$J respectively. This suggests that the nitric acid was successfully removed by this method. As expected the longer the CNP were refluxed in nitric acid the lower the ultrasound responsiveness of the particles, probably due to the smoothing and film formation (as evident by TEM). A final acid treatment time of 1 hour was decided upon due to the change in ζ−potential (CNP = -14 mV, AT-CNP = -34 mV) indicating a substantial number of carboxyl groups on the surface providing the potential for particles to be adequately functionalised

while a short enough treatment time to minimise the loss of ultrasound responsiveness.

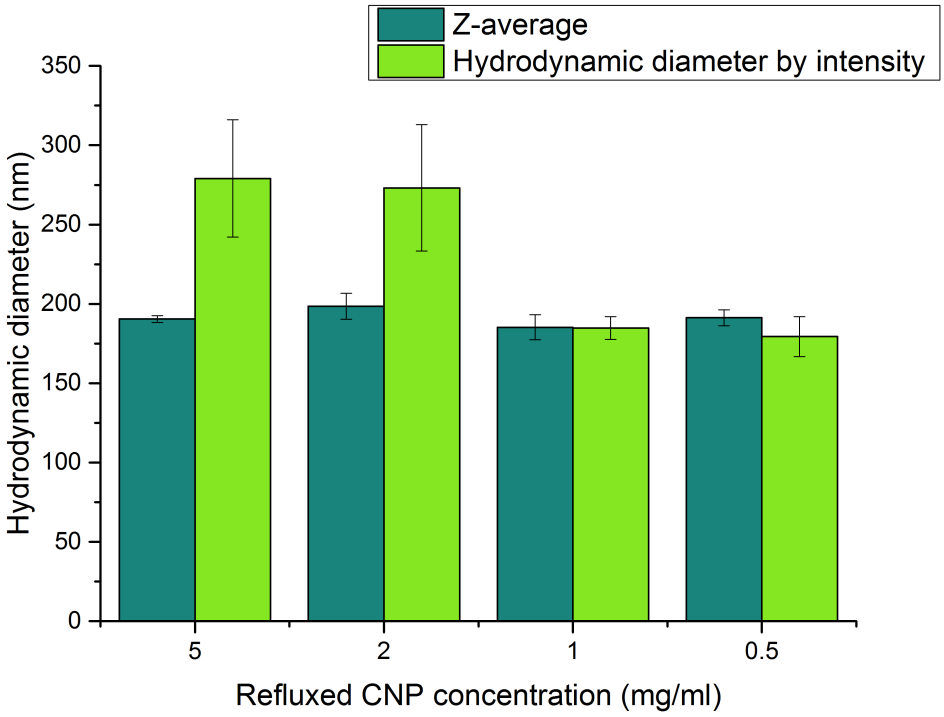

Figure 3-15: Identification of the maximum monodisperse AT-CNP concentration in PBS
CNP refluxed in 70% nitric acid for 1 hour were washed, freeze dried and resuspended in PBS to have concentrations between 0.5 and 5 mg/mL. Their hydrodynamic diameter was measured using DLS. Size by both intensity and by z-average are shown as similar values indicating a monodisperse, Gaussian distribution of particles. N = 1, measurement performed in triplicate, standard deviation between runs shown.

The increasingly negative ζ-potential permits the CNP to be monodisperse at higher concentrations. Particles were refluxed in nitric acid for 1 hour and samples of 583 µL, 1.459 mL, 2.917 mL and 7.292 mL were taken, washed, lyophilised and size separated as before. DLS measurements of z-average and size by intensity are shown Figure 3-15 of AT-CNP at concentrations between 0.2 mg/mL and 5 mg/mL in PBS. The maximum concentration was determined to be 1 mg/mL as at concentrations higher than this there was a discrepancy between the z-average and the diameter by intensity which is indicative of the presence of microparticles in the colloidal mixture. This 1

mg/mL concentration is 5 times greater than could be achieved by non-acid treated CNP. Loss in acoustic response upon acid treatment could potentially be compensated for by the ability to formulate and use higher concentrations.

Carbodiimide chemistry was chosen to conjugate a fluorescent dye to the carboxylated carbon particles[173]. The dye BODIPY® TR Cadaverine was chosen as it lacks a carboxyl group, thus enabling the particles and the dye to be directly mixed without risk of merely cross-linking fluorophore molecules.

To wash away remaining unreacted dye and carbodiimide reactants, 3 methods were tried: dialysis, gel filtration and centrifugation.

The particles could not be recovered by either dialysis nor gel matrix methods. However, centrifuging the particles at 14,000g for 30 minutes and resuspending in buffer enabled the successful recovery of the carbon particles without altering the final size distribution of the particles.

Figure 3-16 shows the fluorescence of a 2-fold dilution of the particles in human plasma and demonstrates the successful fluorescent labelling of the particles. It suggests that the carbon particle concentration could be calculated as a linear function of fluorescence (R^2 = 0.992) and the labelling was sensitive, i.e. to a concentration of approximately 5 µg/mL. If 200 µL of 1 mg/mL labelled CNP were to be injected into a mouse this would equate to CNP being measurable down to approximately 4% of the injected dose.

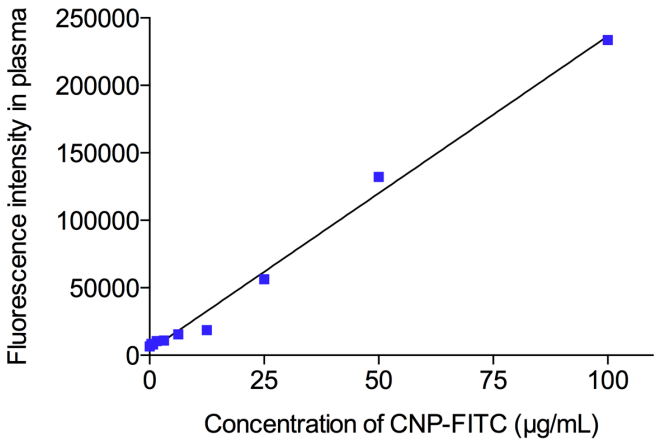

Figure 3-16: Linearity and limits of CNP fluorescently labelled
10 µL of a serial dilution of mesoporous carbon particles acid treated for 1 hour and conjugated to the fluorescent dye BODIPY® TR Cadaverine via carbodiimide chemistry was added to 90 µL of human plasma to identify the minimum detectable limit of the particles in the blood. The fluorescence was measured at an excitation wavelength of 584 nm and an emission wavelength of 520 nm. The coefficient of determination of a linear regression model fitter to the data indicated that there was a strong linear correlation between CNP-FITC and fluorescence (R^2 = 0.992).

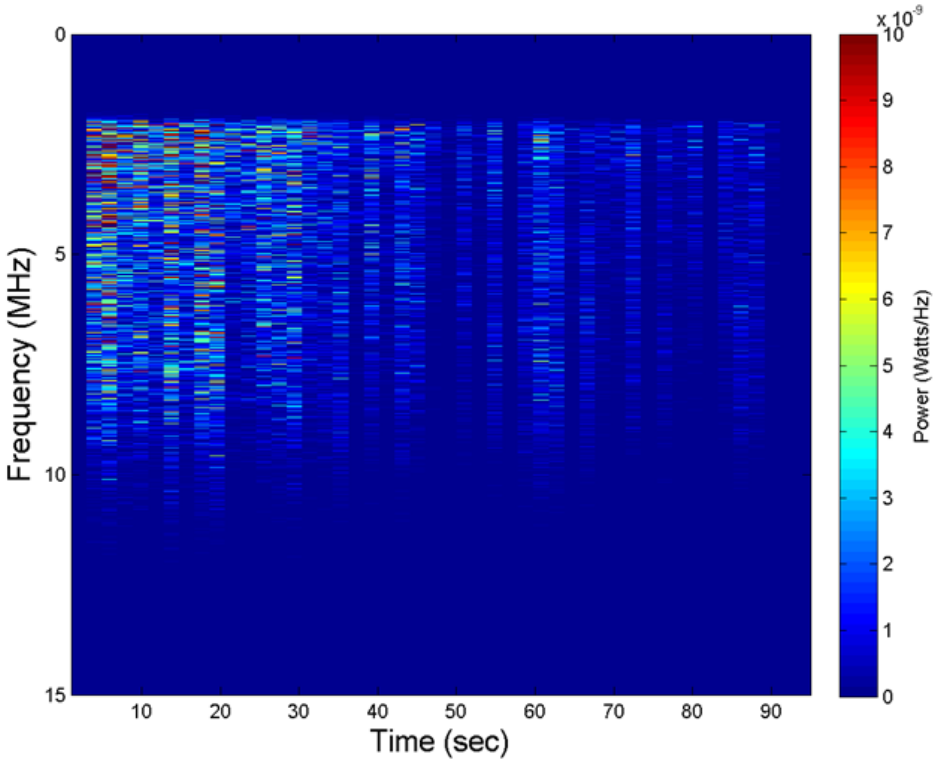

Figure 3-17: Ultrasound response of fluorescently labelled carbon particles
1 mg/mL of fluorescently labelled carbon particles were insonated in a static chamber using ultrasound of peak rarefactional pressure 1.5 MPa, frequency 1.5 MHz, 5% duty cycle and PRF 0.5 Hz. The power of the cavitation response is shown over time in the spectrogram.

Figure 3-17 displays a spectrogram of the ultrasound response of these fluorescently labelled CNP in a static chamber exposed to ultrasound of 0.5 MHz driving frequency, 1.5 MPa peak rarefactional pressure, 5% duty cycle and 0.5 Hz PRF. The total acoustic energy response was 3.15 $x10^{-9}$ J, substantially reduced from the energy response of the original size separated particles of 4.18 $x10^{-8}$ J and the refluxed and washed particles of 3.89 $x10^{-8}$ J.

As both the ultrasound response and the physiochemical properties of the CNP have been fundamentally altered by the process of labelling it was determined that PK/PD studies using fluorescently labelled cups would not be representative of non-labelled CNP.

Despite the limitation of being unable to track the PK profiles of non-labelled CNP and CMP, they were tested in *in vivo* studies to further probe the impact of particle size on ultrasound utility and safety.

3.3.5 *In vivo* biocompatibility

CT-26 cells, as used in the *in vitro* experiments, were subcutaneously implanted into BALB/c mice. Once the tumour had grown to a suitable size, each mouse was i.v. injected with a 25 µL dose of 0.2 mg/mL CNP or CMP. At 4 x 2 minute intervals a further 25 µL was injected. Half of these mice were subjected to ultrasound of peak rarefactional pressure 1.5 MPa, driving frequency 0.5 MHz and a duty cycle of 5% with a 0.5 Hz PRF totalling a treatment time of 30 seconds after each dose as per the ultrasound experiments performed in the static sample holder. The remaining mice were injected with CNP or CMP but were not treated with ultrasound.

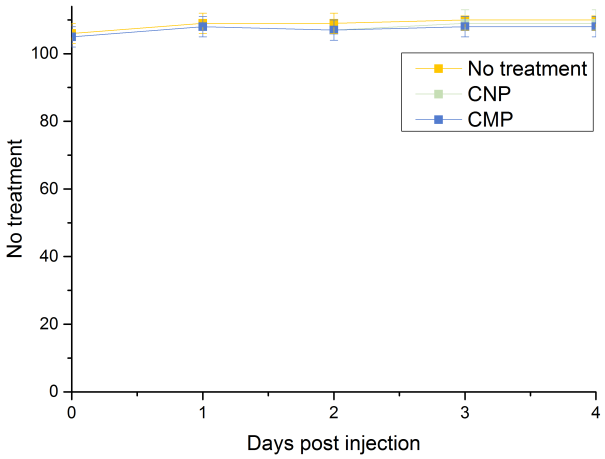

Figure 3-18: Changes in mice weights caused by intraveous (i.v.) injection of carbon particles
Mice were injected with 5 doses of 25 µL 0.2 mg/mL size separated or non-size separated carbon particles and their weights measured daily until they were sacrificed on day 4. N=4, standard deviation shown, Pair-wise t-test showed no significant difference between the weights of the mice in any group (P>0.05).

The mice were weighed each day after this treatment and blood samples were taken at time points 0, 30 minutes, 3 hours, 24 hours and 96 hours. After 4 days mice were sacrificed. Feeding habits of the mice were not perturbed, as evidenced by constant weight being maintained (see Figure 3-18), with no significant difference ($p > 0.05$) being detected between the weight of mice in the CNP and CMP groups compared to the non-treated controls at any time point.

Alanine aminotransferase (ALT) is an enzyme strongly associated with hepatic necrosis, which can be caused by nanoparticle toxicity[303]. Its presence is determined by the addition of a reagent that is reduced in the presence of ALT to produce a chemical which absorbs at 340 nm. Figure 3-19 shows there was no observable significant ($p > 0.05$) change in ALT levels in any of the sample groups and no change in ALT levels were seen over time compared to the sample taken 30 minutes prior to injection. This provides compelling evidence that the particles do not cause liver damage.

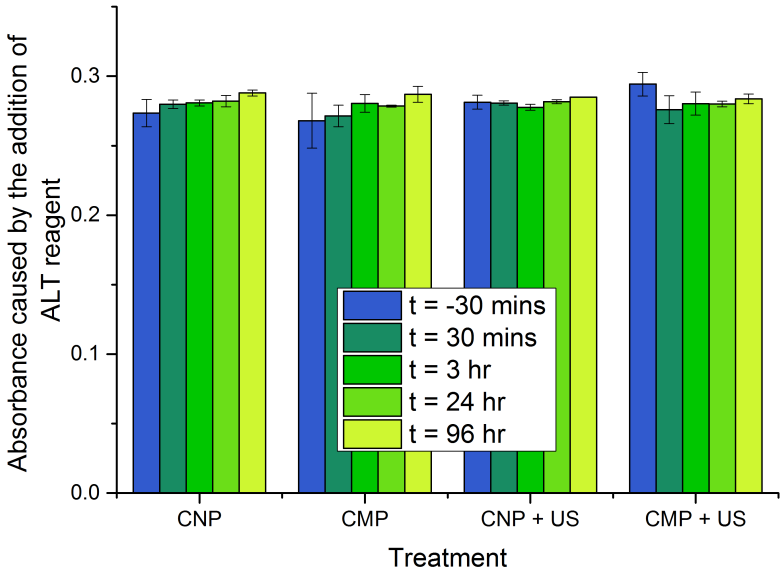

Figure 3-19: Changes in alanine aminotransferase (ALT) in mice plasma caused by i.v. injection of carbon particles with or without ultrasound treatment
100 µL ALT reagent was added to 10 µL plasma of obtained from mice before and after injection of 5 doses of 25 µL carbon particles and exposure to ultrasound of 0.5 MHz driving frequency, 1.5 MPa peak rarefactional pressure, 5% duty cycle and 0.5 Hz PRF. Absorbance was measured at 340 nm to observe differences in ALT concentrations. Mean of N = 4 values, standard deviation shown, ANOVA with Bonferroni post-test showed no significance (P>0.05).

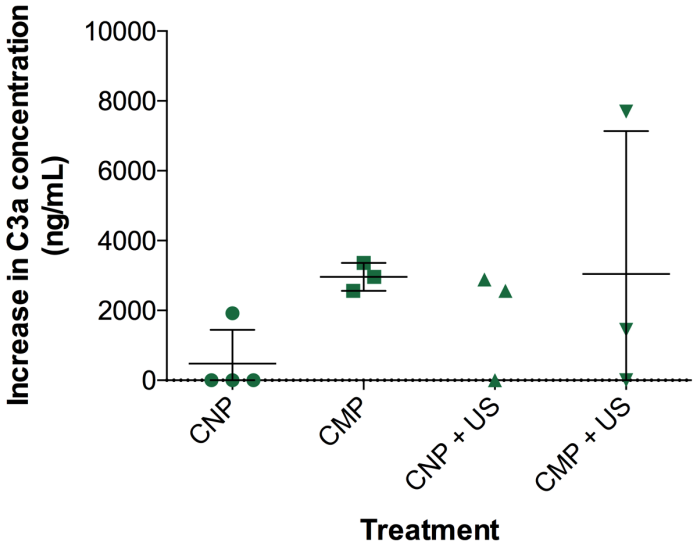

Figure 3-20: Change in plasma concentration of C3a in mice i.v. injected with carbon particles and exposed to ultrasound
Mice were i.v. injected with 5 doses of 25 µL carbon particles and exposed to ultrasound of 0.5 MHz driving frequency, 1.5 MPa peak rarefactional pressure, 5% duty cycle and 0.5 Hz PRF. The change in concentration of C3a between 30 minutes before treatment and 30 minutes after treatment is shown. N = 4, standard deviation shown, ANOVA with Bonferroni post-test showed no significance (P>0.05).

The complement response is part of the innate immune response. There are 3 pathways by which the complement response can be activated: the classical pathway, the alternative pathway and the lectin pathway[304]. The cleavage of complement component 3 (C3) to C3a and C3b is a result of the activation of these pathways. Plasma concentrations of C3a were thus used to assess the innate immune response to the particles[304]. Figure 3-20 shows the C3a concentrations, as measured by an ELISA, in the plasma of the mice 30 minutes subsequent to the treatment. The half-life of free C3a is just a few minutes and so its presence was not tested for at subsequent time points[305]. Equivalent and very low C3a concentrations were detected in the plasmas of all mice, indicating a negligible innate immune response to the particles. A single anomalous sample caused the mean C3a concentration of the "CNP + US" group to be high and have large standard deviation (data point not within the scale of the graph). The mouse may have been reacting to a stimulus other than the cups or the plasma may not have suitably mixed with EDTA to inhibit complement activation after taking the blood sample. Section 3.3.3 demonstrated that there was no measurable attachment of complement proteins onto the surface of the cups (despite limited assay sensitivity), which would often be the cause of activation of the complement system. Indeed, no group of mice had plasma C3a levels significantly greater than the level in pre-treated mice or the background negative control in the ELISA kit.

IL-6, as measured in the in vitro studies, was also measured in the plasma samples from the mice (see Figure 3-21). Again, statistical analysis of ANOVA with Bonferroni post-test statistical analysis showed that at no time point with CNP or CMP was the concentration of IL-6 in the plasma significantly greater

than the level in pre-treated mice ($p > 0.05$). This demonstrates the importance of morphology and administration route as Shvedova et al. demonstrated significant increases in IL-6 concentrations following delivery of carbon nanotubes by inhalation[306].

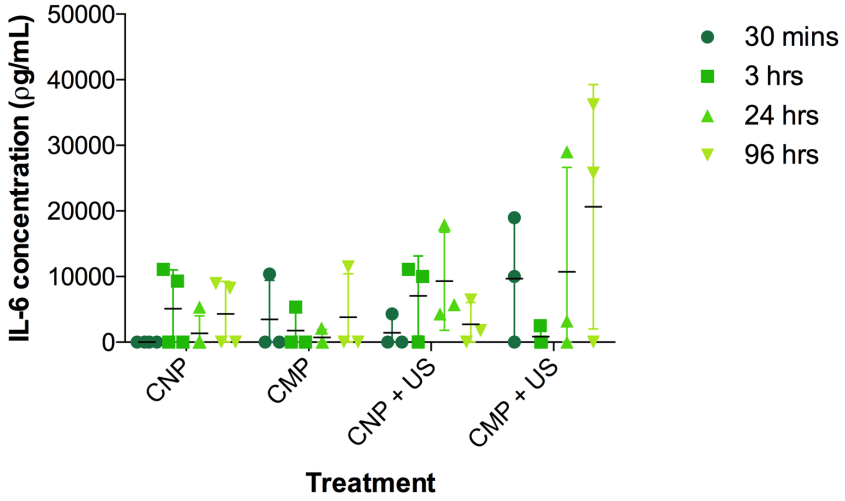

Figure 3-21: Concentration of IL-6 over time in the plasma of mice i.v. injected with carbon particles with or without ultrasound treatment
An ELISA was used to measure the concentrations of IL-6 in the plasma of mice over time that had been i.v. injected with carbon particles and ultrasound exposed. Ultrasound had a driving frequency of 0.5 MHz,1.5 MPa peak rarefactional pressure, 5% duty cycle and 0.5 Hz PRF. N = 4, standard deviation shown. ANOVA with Bonferroni post-test showed no significance (P>0.05).

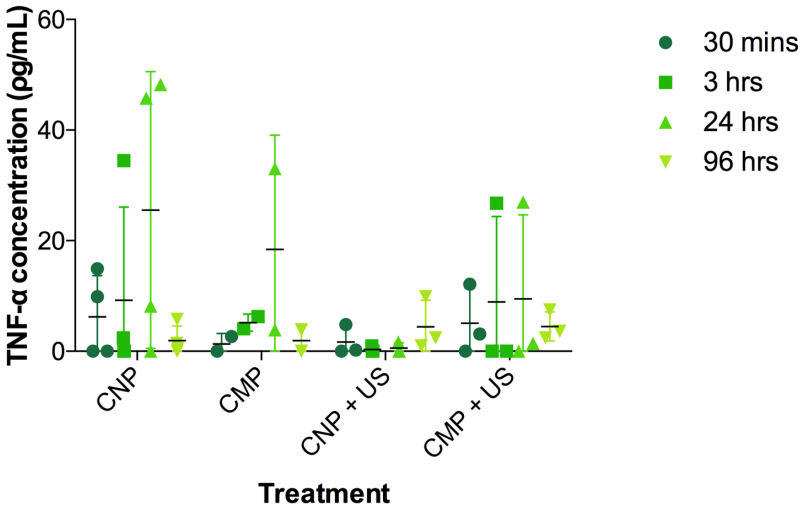

Figure 3-22: Concentrations of tumour necrosis factor (TNF-α) over time in the plasma of mice i.v. injected with carbon particles with or without ultrasound treatment
Mice were treated with 5 doses of 25 µL carbon particles or PBS. TNF-α concetrations were measured using an ELISA at time points between immediately before treatment and 4 days after treatment. Ultrasound had a driving frequency of 0.5 MHz,1.5 MPa peak rarefactional pressure, 5% duty cycle and 0.5 Hz PRF. N = 4, standard deviation shown, ANOVA with Bonferroni post-test for significance showed no significance (P>0.05).

TNF-α is a pro-inflammatory cytokine, associated with IL-6, which is able to activate multiple signal pathways to impact on cell proliferation, differentiation and apoptosis[307]. Concentrations of TNF-α in the plasma above 150 ρg/mL will induce lethal septic shock in mice. The concentrations of TNF-α induced by intravenous injection of carbon particles, with or without ultrasound, as determined using an ELISA, were very low (Figure 3-22)[308]. In agreement with the results reported by Brown et al. size separation of the carbon particles did not significantly reduce the TNF-α concentrations in the plasma in comparison to i.v. injections of CMP[292]. It is notable that both Figure 3-21 and Figure 3-22 have relatively large error bars. This is a consequence of the amounts of protein released being so low that they verge on the detection limit of the assays and so replicates often include a value of zero. This leads to error bars representing background noise. Higher plasma concentrations should have been used to ensure that both the IL-6 and TNF-α concentrations were within the detection limits of the ELISA.

3.4 Discussion

The data presented in this chapter demonstrates that mesoporous carbon particles can be size separated and reproducibly have a uniform size of less than 200 nm with a polydispersity of less than 0.2. The sonosensitivity of these nanoparticles was intensified by the disaggregation and size separation of agglomerated carbon particles despite a 30% loss of mass caused by the size separation. Solid particles of a size that may escape the vasculature supplying tumours while also acting as cavitation nuclei, have therefore been successfully formulated for the first time. Their extended cavitation response further supports the hypothesis that these particles could be capable of driving both themselves and a therapeutic into a tumour. This is unlike the current ultrasound cavitation nuclei used for the transportation of therapeutics. Microbubbles are destroyed in the process of inertial cavitation and are restrained to the vasculature[214]. Phase-changing nano-liposomes, the only alternative ultrasound-responsive agent that is of an equivalent size, are destroyed in the process of cavitation and thus will be unable to provide the same continuous delivery stimulus as it is hypothesised these solid particles are capable of[309]. The MI of the ultrasound parameters used was 2.1 which is just above that permitted in diagnostic ultrasound[222]. However, it has an I_{SPPA} of 75 W/cm^2, which is within diagnostic ultrasound limits[226].

The TEM images of the particles gives credence to the hypothesis that the rough hydrophobic surface is capable of entrapping gas on the surface and, due to the higher radius of curvature than that of a bubble of equivalent size, permits cavitation upon ultrasound exposure[275]. This hypothesis is also

supported by disruption of the particles into smaller aggregates increasing sonosensitivity as surface area is increased. As a result, a lower concentration CNP produced higher levels of cavitation than CMP. As CMP are broken down to CNP the size of the cavities are neither increasing nor decreasing but there will be a greater overall surface area and, consequently, the number of cavities capable of supporting nano gas pockets will increase.

In order to track the particles in vivo they were fluorescently labelled. A dye was chosen that could be conjugated to the particles in a single-step conjugation using carbodiimide chemistry. The fluorescence of the particles in plasma indicated that the conjugation had been successful while the sonosensitivity, although not at the very high levels associated with the particles before they were refluxed, still showed significant broadband emissions indicating that the particles could still instigate bubble nucleation and cavitation when subjected to ultrasound. The alterations to the surface improved the stability of the particles and enabled formulation of monodisperse solutions of the CNP at higher concentrations. However, the change in surface charge, as well as substantial modifications to their morphology caused by an intermediate acid treatment step, meant that this labelling technique was not suitable to measure the PK/PD of the particles.

Both *in vitro* and *in vivo* data suggests that the particles are biocompatible. They did not induce cell death of human leukocytes, human erythrocytes or a murine cancer cell line. IL-6 production both *in vitro* and *in vivo* was very low and there was no discernable pattern between concentrations of particles or time to indicate the particles caused anything more than a negligible effect.

ALT concentrations are neither time nor treatment dependent which suggests no change in concentration. Induction of C3a in mice caused by CNP was also minimal with no significant difference in levels of C3a in the plasma 30 minutes pre-injection and 30 minutes post-injection ($p > 0.05$). Finally, TNF-α concentrations remained low 30 minutes after injection. The mice weights remained constant indicating that their eating habits did not change and they were not in significant discomfort. Consequently we conclude that at the concentrations tested the particles do not induce cell death, stimulate an innate immune response, cause liver damage or stimulate the production of inflammatory cytokines linked to immune signalling cascades. However, it is also clear that the development of this technology may ultimately be hindered by difficulties faced in labelling CNP and tracking their PK and biodistribution. Such studies are essential in the clinical translation process and so this represents a substantial problem.

3.5 Conclusions

This chapter reports:

- Cavitation nuclei with a hydrodynamic diameter smaller than 200 nm have been successfully formulated.
- The particles were successfully modified to have carboxyl functional groups on their surface. They were then further conjugated to a fluorescent dye such that they could be tracked in vivo while still acting as cavitation nuclei. However, the labelling process did alter the surface properties of the particle and thus would potentially change the distribution and clearance pathways of the particles.
- These particles have been judged to be biocompatible because:
    - They did not induce death of either healthy human blood cells or cancer cells in vitro.
    - They did not stimulate the production of cytokines linked with inflammation and immune response either in vitro or in vivo.
    - They did not cause liver damage in vivo as measured by the presence of ALT.

4 Polymer cup formulation, characterisation and biocompatibility

4.1 Introduction

Work reported in Chapter 3 demonstrated that carbon nanoparticles (CNP) could be formulated to have a size that would potentially enable them to escape the tumour vasculature. The cavitation response of the CNP would indicate that bubbles without a lipid layer can be stabilised on nanoparticles and that the impetus derived from cavitation could potentially drive therapeutics out of the blood stream and into tumours. These findings raise the possibility that any nanoparticle could act as cavitation nuclei provided its morphology permits a gas bubble to be stabilised on its surface.

The absence of facile techniques to allow the detection or labelling of the CNP means that their pharmacokinetics (PK) and biodistribution would be hard to define. Modifying the surface charge of the CNP to enable labelling altered their cavitation response and would affect their biodistribution[310]. This, in addition to their irregular and unpredictable shape, means that it would be difficult to receive approval for their use as an injectable agent[311,312]. Consequently, alternative nanoparticles were considered that would have the

same gas-entrapping indentation present as in CNP, but with a more regular shape and a composition more amenable to labelling and detection.

Polymers tend to be very malleable and several polymer nanoparticles have now been approved for use in medical applications[81]. Lv et al. first demonstrated the formulation of polymer cups by seeded polymerisation[273]. In this process a polystyrene bead acts as a seed particle with the polymerisation of methyl merthacrylate (MMA) and hydroxyl ethyl methacrylate (HEMA) coating the bead via divinyl benzene (DVB) linkage. The reaction is initiated by potassium persulfate and heating. As the methacrylate chains polymerise they swell and pull the seed bead with them to leave a central cavity and, over a 5 hour reaction time, a hemispherical cup can be formed. Methyl methacrylate is a hydrophobic monomer and consequently the final particles, when dried, entrap gas on their surface[275,313].

4.2 Chapter Aims

The aims of this chapter are to:

- Formulate polymer cups to be stable in a solution which has clinical approval for use in intravenous injection (i.e. a clinically approved 'vehicle').
- Characterise the cavitation response of the cups when exposed to ultrasound.
- Characterise the biocompatibility of the cups both *ex vivo* and *in vivo.*

4.3 Methods and results

4.3.1 Physiochemical characterisation of polymer cups

Ultrasound responsive polymer cups were formulated as described by Kwan et al.[274]. The particles physical characteristics are shown in Figure 4-1. Figure 4-1 a and Figure 4-1 b provide images of the morphology of the 100 nm and 300 nm core particles as captured by TEM. They show a uniform population of polymeric particles of an equivalent size and shape. There was greater batch-to-batch variability of the 100 nm polymer core cups shown by TEM images; Figure 4-1 a shows an undulating surface while in other batches the cups appeared more similar to those shown in Figure 4-1 b. It is hypothesised that this variability is due to the higher surface to volume ratios of the 100 nm polymer beads resulting in a greater sensitivity to the reaction conditions. Each particle has a single indent of a size approximately equal to the core polystyrene particles used during formulation, hence the naming convention of polymeric cup. This would suggest that the final size of both the indent and total diameter of the particles could be easily manipulated using different sized polystyrene seed particles.

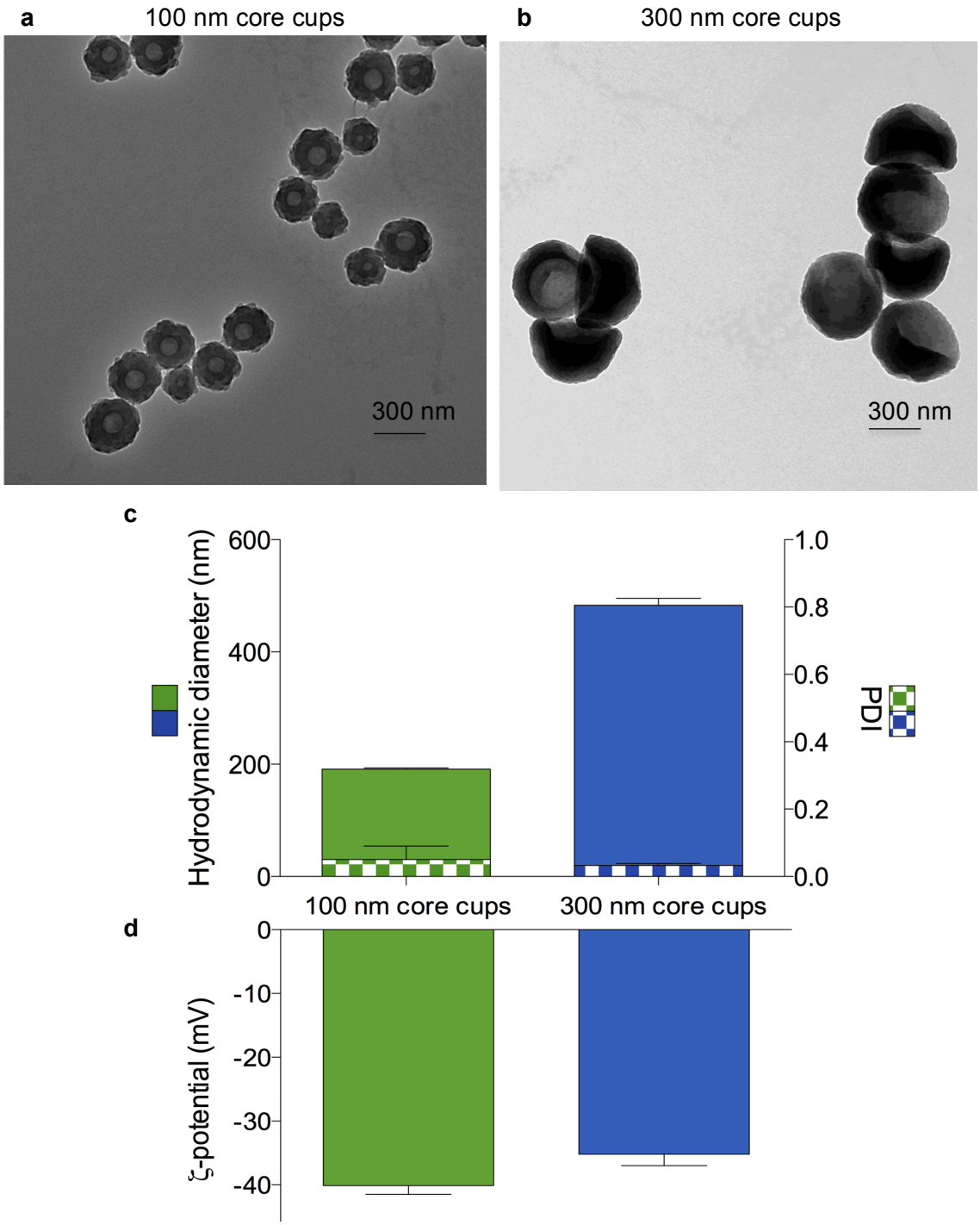

Figure 4-1: Physical characterisation of the polymer cups formed using either 100 nm or 300 nm core polystyrene cores

Transmission electron microscopy (TEM) and dynamic light scattering (DLS) were used to characterise the polymer cups. 10 µL of a solution of cups was incubated on a carbon coated formvar grid and imaged at magnifications of 6,800 (a) and (b) are TEM images of 100 nm and 300 nm core particles respectively. (c) hydrodynamic diameter (solid colour) and polydispersity index (PDI, chequered colour) of the cups (d) ζ-potential of the cups in 25 mM HEPES buffer NaOH pH 8. Error bars represent the standard deviation between 3 separately prepared batches of cups.

Sizing measurements by DLS (Figure 4-1 c) confirmed that using 100 nm polystyrene beads produced polymeric cups with a hydrodynamic diameter of 191 nm +/- 2nm and a polydispersity index (PDI) of 0.03 +/- 0.01, while 300 nm polystyrene particles created cups with a hydrodynamic diameter of 483 nm +/- 12 nm and a PDI of 0.05 +/- 0.04. This very narrow PDI is indicative of a very uniform product with little to no agglomeration. Figure 4-1 d shows that the 100 nm and 300 nm core particles have a ζ-potential of -40 +/- 1 mV and -35 +/- 2 mV respectively which would cause there to be strong static repulsion forces between the particles and consequently explain the very monodisperse non-aggregated nature of the samples.

In order to inject the cups into mice and ultimately humans they must be amenable to resuspension and storage in a clinically approved injectate solution. The stability of the cups was measured in the following clinically approved injectate solutions: glucose, saline, Ringer's, Ringers Lactate, plasma lysate and mannitol[283]. Stability was determined by mixing the cup solutions, which had been resuspended after air drying in water, at a 1:1 ratio with the injectate solutions and using DLS to measure the size and PDI of the resultant colloidal suspension 10 minutes later (Figure 4-2 a and Figure 4-2 b). Both 100 nm and 300 nm core cup formulations were unstable when resuspended in injectates containing salt i.e. saline, Ringer's, Ringers Lactate and plasma lysate as demonstrated by an increase in the hydrodynamic diameter. This may be due to the charge of the ions in the salt solutions causing the Debye length of the cups to become too short such that van der Waals forces overcome the static repulsion forces. This would lead to the destabilisation of the solution and subsequently agglomeration[279]. The size of

100 nm core cups remained constant in water, glucose and mannitol with hydrodynamic diameters measurements of 191 nm +/- 2nm, 190 nm +/- 1 nm and 192 nm +/-1 nm respectively. DLS measurements of 300 nm core cup in injectables showed them to be the less stable in mannitol than in glucose; in water or glucose the cups had a hydrodynamic diameter of 455 nm +/- 21 nm or 478 nm +/- 6 nm respectively whilst in mannitol their hydrodynamic diameter was measured to be 578 nm +/- 158 nm.

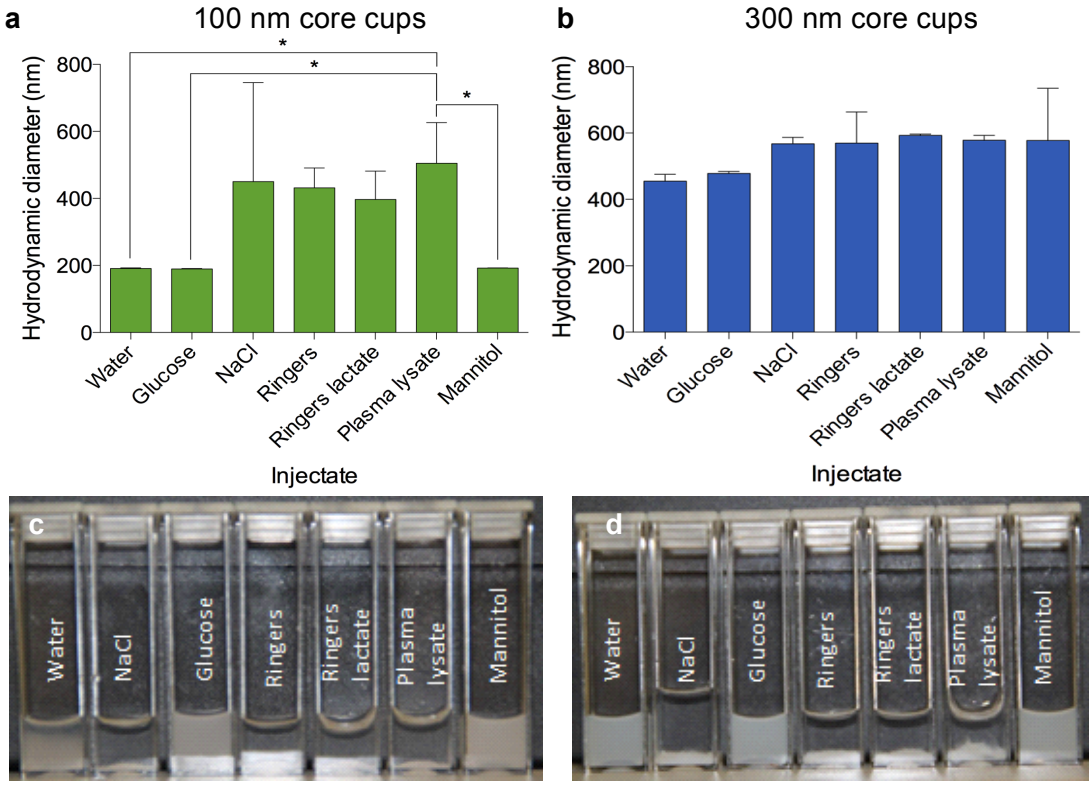

Figure 4-2: Stability of the cups in clinically approved injectable solutions
Stability of 100 nm core and 300 nm core cups in 6 clinically approved injectates was determined by measuring the size distribution using DLS approximately 5 minutes after mixing the cups with the injectate solution. Sizes reported are hydrodynamic diameter as measured by intensity. Error bars represent the standard deviation of the diameters, as measured by the DLS, of 3 different samples. (a) Size distribution of 100 nm polystyrene core cups (b) size distribution of 300 nm polystyrene core cups. (c) Photograph of the 100 nm polystyrene core cups 24 hours after mixing (d) photograph of the 300 nm polystyrene core cups 24 hours after mixing. N = 3, standard deviation shown, One-way ANOVA with Bonferroni post-test for significance. * = $P<0.05$.

The stability of the 100 nm core and 300 nm core cups in glucose and mannitol was confirmed by photographing the samples after 24 hours of incubation at room temperature (Figure 4-2 c and Figure 4-2 d respectively). Cups that had been mixed with injectates containing salt had clarified with dense white sediment appearing on the bottom of the cuvettes. In contrast, Brownian motion overcame gravitational forces in the cups suspended in glucose or mannitol as shown by the samples remaining uniformly opaque. Consequently it was decided that both cup formulations should, after the drying step, be resuspended and tested in glucose. All subsequent studies were performed with cups suspended in 200 µm filter sterilised 5% glucose.

4.3.2 Cavitation response of cups

Ultrasound testing was required to explore the hypothesis that shape rather than material is responsible for hydrophobicity at the nanoscale. This suggests that the depression within the cups would provide a surface onto which gas pockets would be trapped. In turn, this would lower the cavitation threshold (i.e. the minimum pressure required to achieve inertial cavitation events) of the solution in which the cups were suspended. Ultrasound testing was performed in a static chamber as described in Chapter 2.

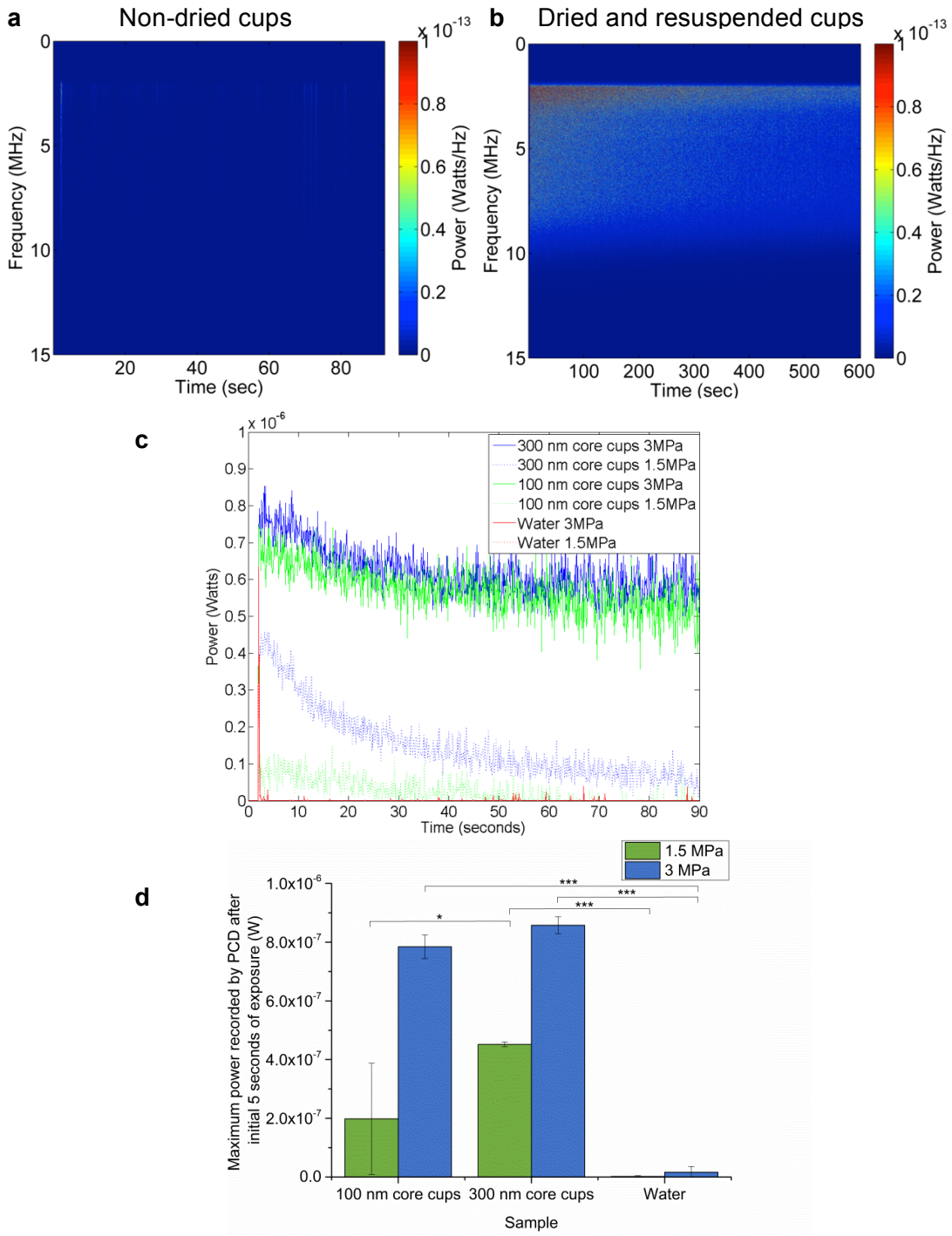

Figure 4-3: Cavitation response of either 100 nm or 300 nm polymer cups insonated with peak rarefactional pressure of 1.5 MPa or 3 MPa

Cups were insonated in a static chamber with a driving frequency of 0.5 MHz, 5% duty cycle and 10 Hz pulse repetition frequency (PRF). Demonstration of the importance of entraining a gas bubble within the cups is demonstrated by spectrograms of the ultrasound response to 1.5 MPa peak rarefactional pressure of (a) 300 nm core cups that had not been air dried and (b) 300 nm core cups that had been air dried and resuspended in water. (c) Power of the cavitation recorded by the PCD over 90 seconds when 100 nm and 300 nm core cups were exposed to ultrasound with peak rarefaction pressures of either 1.5 MPa or 3 MPa for 90 seconds (d) maximum power recorded by the PCD after an initial 5 seconds of exposure. Error bars indicate standard deviation between 3 samples. Significance determined by a one-way ANOVA with Bonferroni post-test. * = P<0.05, ** = P<0.005 and *** = P<0.0005.

Figure 4-3 a and Figure 4-3 b confirm the hypothesis that the cavitation is caused by gas entrapment on the surface of the cups. Undried or dried and resuspended 300 nm polystyrene core cups were insonated with ultrasound of driving frequency 0.5 MHz, pulse repetition frequency (PRF) 10 Hz, duty cycle 5% and a peak rarefactional pressure of 1.5 MPa: before being dried the cups produce only background levels of cavitation, but after drying and resuspension in glucose there was over a 100-fold increase in the energy of the cavitation recorded by the PCD over a 90 second period. Additionally Figure 4-3 b shows that the cups are capable of maintaining cavitation for over 10 minutes in the same way as was observed for CNP (Figure 3-4, Chapter 3).

Figure 4-3 c compares the ultrasound response recorded by a PCD of both cup formulations exposed to ultrasound for 90 seconds with the same ultrasound parameters as in Figure 4-3 a and Figure 4-3 b but with a peak rarefactional pressure of either 1.5 MPa or 3 MPa. It indicates that at 3 MPa both 100 nm and 300 nm core particles give a similar ultrasound response with a peak power of 8.5×10^{-7} W and 7.5×10^{-7} W respectively. However, at 1.5 MPa, the size of the cups clearly influences their cavitation response: 300 nm core cups continue to demonstrate cavitation but with a reduced peak power of 4.6×10^{-7} W with the ultrasound response decaying to less than 5×10^{-8} over the 90 second exposure while 100 nm core cups had a peak power of 1.5×10^{-7} W which decreased to 2×10^{-10} W – equivalent to background - over the exposure time. This experiment was repeated 3 times and Figure 4-3 d summarises the peak power recorded by the PCD for each experiment. It shows that 300 nm and 100 nm core cups, at 3 MPa, produce equivalent

levels of peak power and substantially (50-fold) and significantly ($p < 0.0005$) more than water alone. However, at 1.5 MPa, 300 nm core cups created significantly greater maximum power than both the 100 nm core cups ($p < 0.05$) and water ($p < 0.0005$) but the peak power produced by 100 nm core cups was not significantly ($p > 0.05$) greater than that of water.

4.3.3 *Ex vivo* tolerability of cups

Biocompatibilty profiling was performed on the 300 nm polystyrene core cups to assess how they interact with human blood. 100 nm core cups were not tested due to time constraints. It was determined that their similar ζ-potential and surface properties meant that comparable results would be expected between the two formulations of cups. In addition, the higher cavitation threshold of 100 nm core cups mean that they are unlikely to be used *in vivo* as the mechanical index required for cavitation would be too high.

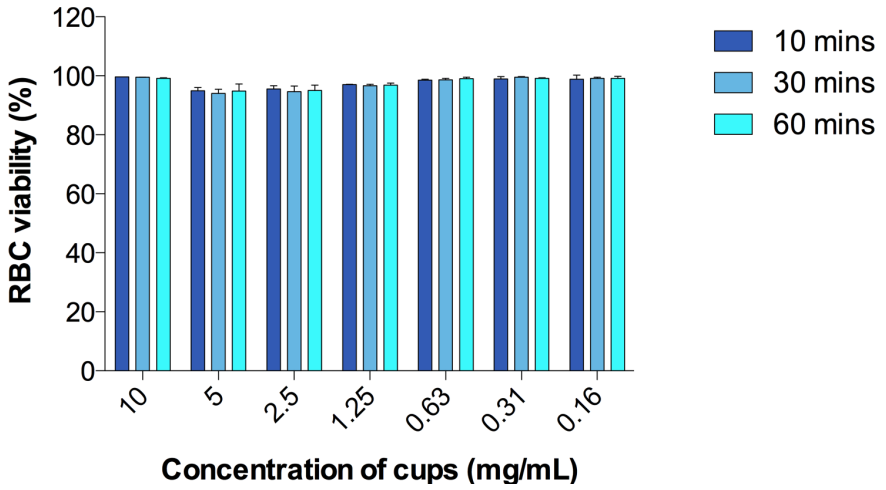

Figure 4-4: Haemolysis assay to assess biocompatibility of 300 nm core cups
Freshly isolated human red blood cells (RBC) were incubated at 37°C with varying concentration of cups in RPMI at a ratio of 1:9 for 10 minutes, 30 minutes or 1 hour. Cell death was measured by the absorbance of the supernatant of the solution at wavelength 541 nm corresponding to haemoglobin release. Concentrations of cups shown are the final concentration with RBC and RPMI. Error bars represent the standard deviation of N = 3 samples. A one-way ANOVA with Bonferroni pair-wise comparisons showed no significant change in RBC viability at any concentration, $P > 0.05$.

Graham calculated that within 5 minutes of intravenously injecting mice with polymer cups less than 30% of the cups remained in the bloodstream and within 20 minutes this figure had reduced to approximately 15%[314]. As a consequence blood biocompatibility profiling has limited the incubation time of the cups with the blood to between 5 minutes and 1 hour. Beyond such time points it is predicted levels of cups would be too low to have an effect.

A haemolysis assay using freshly isolated human red blood cells (RBC) incubated with a 2-fold dilution series of cups was performed and cell death was calculated as described in Chapter 2. Haemoglobin release, measured by absorbance of the supernatant, was used to evaluate RBC lysis. Figure 4-4 shows that there was no significant change to RBC viability caused by incubation with 300 nm core cups for up to 1 hour.

Whole blood was incubated with 300 nm core cups for 20 minutes. The leukocytes were then separated from the blood and incubated for a further 24 hours in plasma and RPMI at 37°C. Flow cytometry with propidium iodide (PI) staining was used to assess the impact of incubation with cups on leukocyte cell viability. This dye cannot permeate cells with intact plasma and nuclear membranes and so positive PI staining is indicative of cell death. Figure 4-5 demonstrates that the cups do not induce leukocyte cell death as, at no concentration of cups, did cell viability significantly ($p > 0.05$) deviate from that observed to be caused by incubation with the vehicle glucose buffer alone.

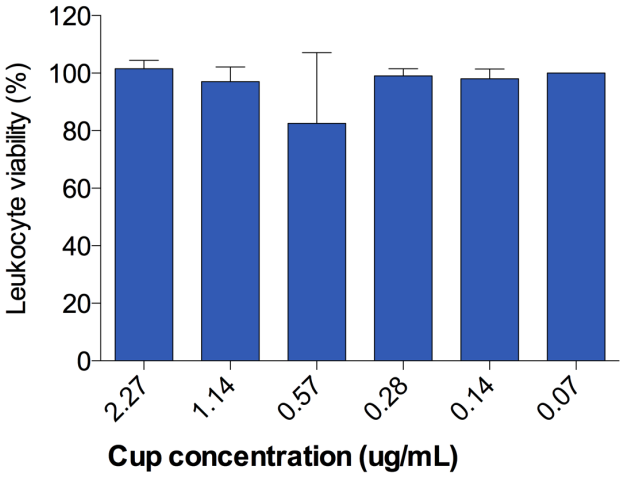

Figure 4-5: Change in human leukocyte cell viability after 24 hour incubation with varying concentrations of cups
100 µL whole fresh human blood was mixed with 10 µL of a 2-fold serial dilution of cups. The solution was incubated for 20 minutes before the leukocytes were isolated using centrifugation and red blood cell lysis buffer. The leukocytes were resuspended in RPMI and 5% human plasma and incubated for a further 24 hours. Propidium iodide (PI) staining of leukocytes was measured using flow cytometry and compared to the addition of buffer alone Concentrations of cups in the x-axis indicate the concentration of cups in solution during exposure. Error bars represent standard deviation between 3 samples. A one-way ANOVA with Bonferroni pair-wise comparisons showed no significant change in cell viability, $P > 0.05$.

An ELISA was used to investigate if the leukocytes responded to the cups by secreting interleukin-6 (IL-6), a cytokine linked with systemic inflammation. From the same leukocyte suspension used in Figure 4-5 an extraction was taken from the supernatant after 3 hours of incubation and the IL-6 concentrations measured. In a similar experiment but where the leukocytes had been isolated before incubation with the cups then resuspended in RPMI and plasma either 20 minutes or 60 minutes after incubation the IL-6 concentrations in the supernatant were measured after 24 hours. There was no correlation between cup concentration and IL-6 concentration in either assay (Figure 4-6 $P > 0.05$), and the very low levels detected did not differ significantly from those obtained in the vehicle only controls. As per the same experiments performed with CNP in Section 3.3.3 the spread of data around the background level lead to relatively large standard deviations. Higher

concentrations of plasma or a greater number of replicates may have increased the sensitivity of the assay or reduced the size of the standard deviations.

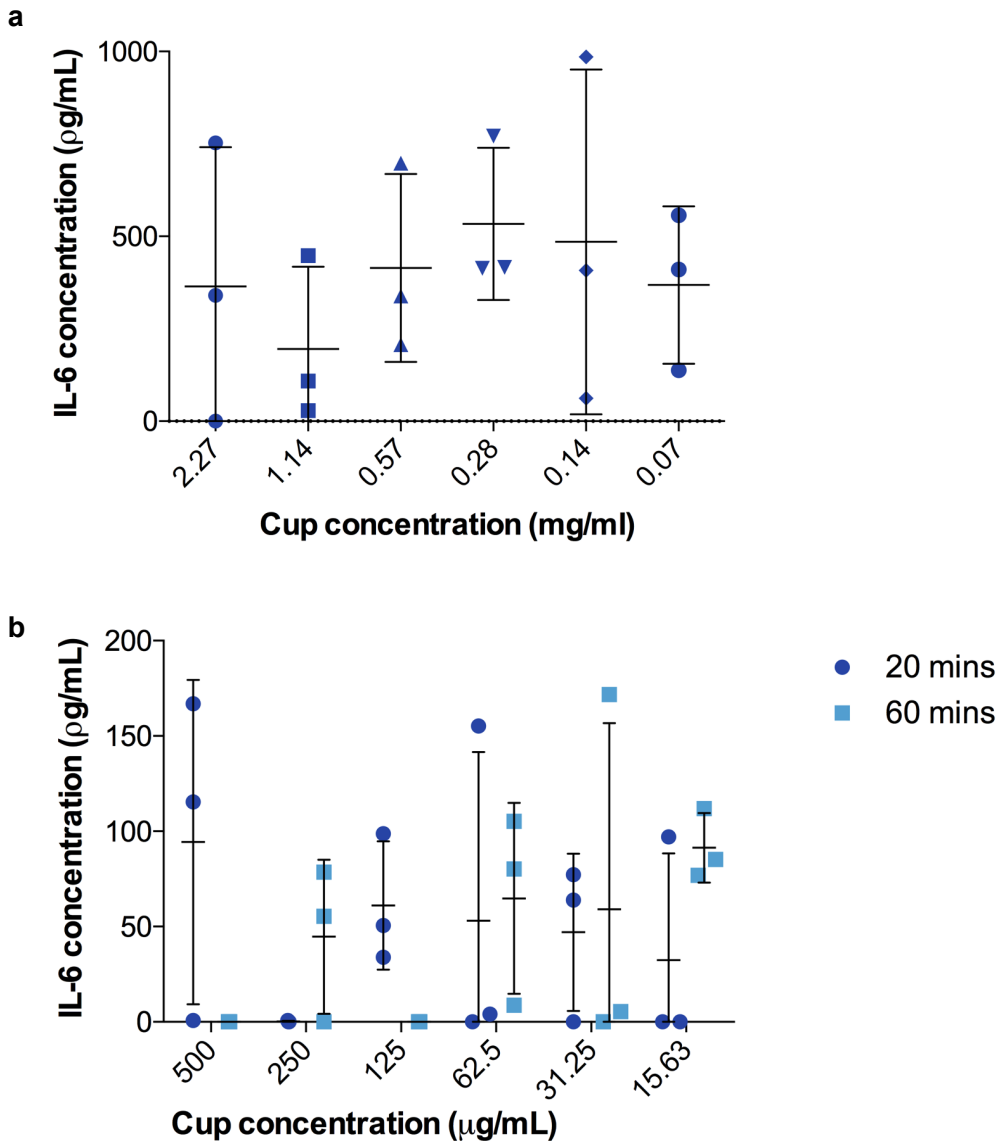

Figure 4-6: Interleukin-6 (IL-6) production caused by leukocyte incubation with 300 nm polystyrene core cups

Changes in the concentrations of IL-6 from background were measured in the supernatant of leukocytes that had been incubated with cups using an ELISA (a) leukocytes were isolated from whole blood after incubation with cups at a ratio of 1:10 and resuspended in RPMI containing 5% human plasma. IL-6 concentrations were measured 3 hours after incubation and (b) 4.7×10^5/mL human leukocytes in RPMI were mixed with 4.7% plasma and 0.9% 300 nm cups in water for either 20 minutes of 1 hour. Leukocytes were then resuspended in RPMI containing 5% plasma. An ELISA was used to measure the increase in the IL-6 concentration from background (from exposure to vehicle alone) after 24 hours. Concentrations displayed are the concentration of cups during exposure. Error bars indicate standard deviation of n=3 samples. A one-way ANOVA with Bonferroni pair-wise comparisons showed no significant change in cell viability, $P > 0.05$.

The same SDS-PAGE methodology as used with CNP and described in Chapter 2 was applied to look at the adsorbance of human serum proteins onto cups. A standard dilution of 300 nm core cups, with a maximum concentration of 6 mg/mL, was incubated with 0.25% human serum. Subsequent to running the SDS-PAGE the gel was stained using silver staining. The gel can be seen in Figure 4-7. There was a decrease in a protein band at approximately 150 kDa. This may be immunoglobulin G (IgG), although the reducing conditions of this gel should have broken IgG into its heavy and light chain components. No change was apparent in concentrations of albumin (molecular weight of 67 KDa), haptoglobin (100 kDa) and IgG light chains (28 kDa)[297]. From this it can be deduced that there is binding of a 150 kDa component, possibly IgG to the cups which is worthy of further investigation particularly with respect to a possible role in complement activation. As discussed in Section 3.3.3 a pull-down assay may have been more appropriate for this study.

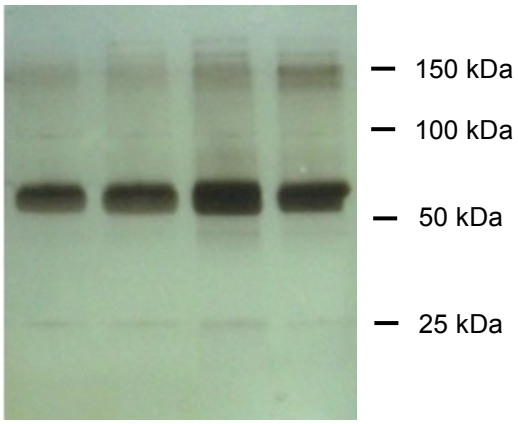

Figure 4-7: Adsorption of human serum onto the surface of cups measured using an SDS-PAGE

300 nm core cups of 5.4 mg/mL, 2.7 mg/mL or 1.35 mg/mL concentration were incubated with 0.25% pooled human serum for 1 hour. The supernatant of the solutions were added to the wells of an SDS-PAGE. Silver staining was used to identify and semi-quantitatively assess the protein levels that remained in the supernatant.

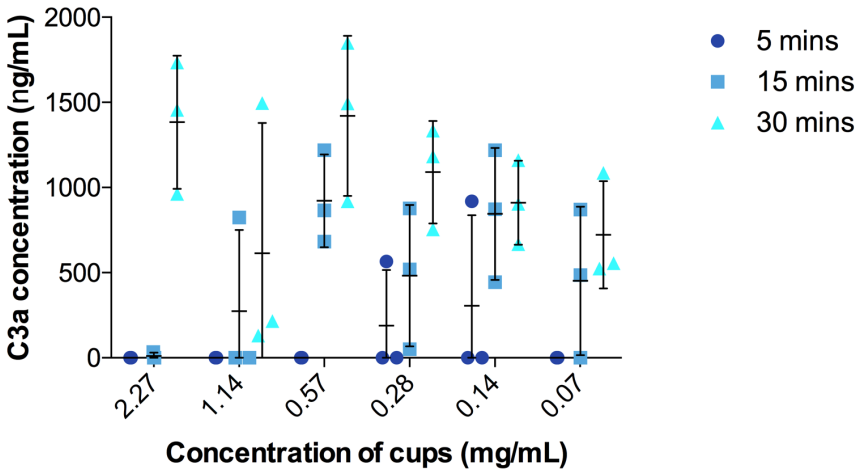

Figure 4-8: C3a concentrations in plasma after 30 minutes of incubation with polymer cups
Fresh non-EDTA human plasma was mixed with a serial dilution of 300 nm core cups to have a final plasma concentration of 9%. C3a concentration was measured, using an ELISA, after 30 minutes of incubation. Concentrations displayed are the final concentration of cups. Error bars indicate standard deviation of n=3 samples. A one-way ANOVA with Bonferroni pair-wise comparisons showed no significant change in C3a concentration between cup concentrations, P>0.05.

The classical pathway of the complement system is triggered by the binding of IgG or immunoglobin M (IgM) with an antigen. Consequently the adsorption of IgG onto the cups would be expected to result in complement activation. This activation could be measured by the concentrations of C3a as its presence is indicative of complement activation either by the classical or alternative pathways.

A 2-fold serial dilution of polymer cups was incubated with human plasma for 5, 15 or 30 minutes and the C3a concentration was measured using an ELISA. Figure 4-8 shows that there was no detectable C3a above background 5 minutes after incubation with cups and no clear trend between C3a concentration and cup concentration after 15 minutes of incubation. However, there was a possible, if not significant, correlation between cup concentration and C3a concentration after 30 minutes of incubation. 2.27 mg/mL cups caused an increase in the average C3a concentration of 1348 +/- 391 ng/mL.

This represents between 0.1% - 0.3% of the C3 in a mL of blood being cleaved to C3a[299]. Pre-clinical studies have presented concentrations of C3a above 20,000 ng/mL for vectors subsequently deemed safe for injection into humans, consequently, this complement activation is considered acceptable[315]. The large error bars remain a problem as per the same ELISA performed in Section 3.3.3. To improve upon this a greater number of samples could have been used.

4.3.4 *In vivo* tolerability of cups

$2x10^5$ of CT-26 cells were injected subcutaneously into the flank of BALB/c mice. 14 days later the mice were intravenously (i.v.) injected with either 200 µL of 25 mg/mL cups or 200 µL of PBS. Samples of blood were taken at 5, 15, 30 and 240 minutes at which time the mice were culled.

Plasma concentrations of IL-6 and C3a were determined using ELISAs. Similar to the *ex vivo* experiments there was no a significant increase in IL-6 concentrations within the plasma of the mice caused by injection of the cups ($p > 0.05$, Figure 4-9).

Ex vivo experiments suggested there may be an increase in C3a concentrations in the plasma of mice, however, the recorded C3a concentrations were not significantly increased in comparison to the PBS negative control (Figure 4-10).

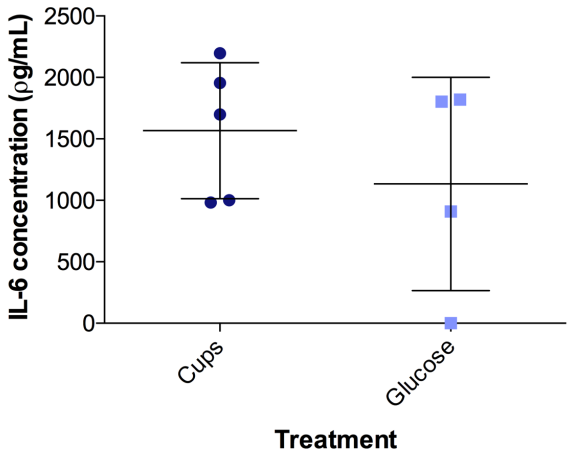

Figure 4-9: IL-6 concentrations in the plasma of mice 2 hours post i.v. injection of polymer cups
Mice were i.v. injected with 200 µL of either PBS or 25 mg/mL 300 nm cups. Blood samples were extracted after 2 hours and IL-6 concentration determined using an ELISA. The PBS group had 4 mice and the cups group had 5 mice. Error bars indicate standard deviation between groups. A t-test showed no significant change in IL-6 concentration between the two treatment groups, P>0.05.

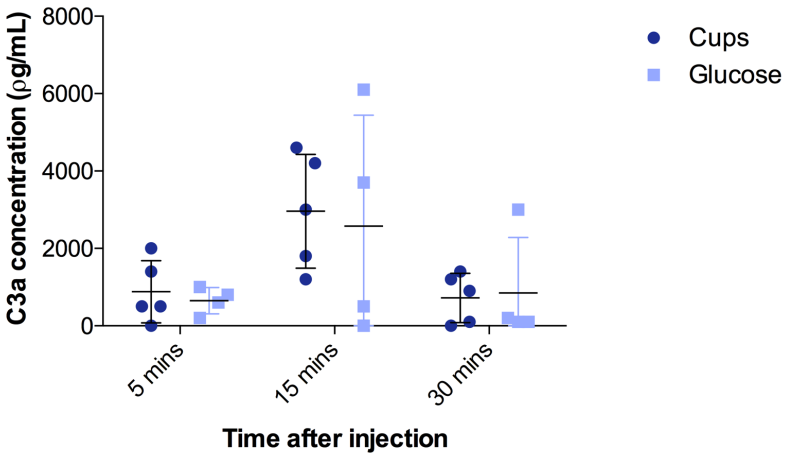

Figure 4-10: C3a plasma concentration over time caused by i.v. injection of polymer cups
Mice were i.v. injected with 200 µL of either PBS or 25 mg/mL 300 nm cups. Blood samples were taken 5 minutes, 15 minutes and 30 minutes post injection. C3a concentration in the plasma was measured using an ELISA. The PBS treatment group had 4 mice and the cup treatment group had 5 mice. Error bars indicate standard deviation between groups. A t-test between the PBS and cup treatment groups showed no significant change in C3a concentration at any time, P>0.05.

TNF-α concentration in the plasmas was also measured using an ELISA (Figure 4-11). The results match the IL-6 concentrations in that an injection of 25 mg/mL polymer cups produced similar concentrations to background, a t-test showed no significant difference between the treatment groups.

All of the ELISAs performed in this section had large standard deviations which resulted in no significance being able to be drawn from the treatment with cups. These error bars may have been due to inconsistencies in mixing of reagents and washing during the assay. Alternatively there is a risk that the injection may have caused an immune response in some of the mice if, for example, the needle was not sterile when cannulising the tail vein of the mice.

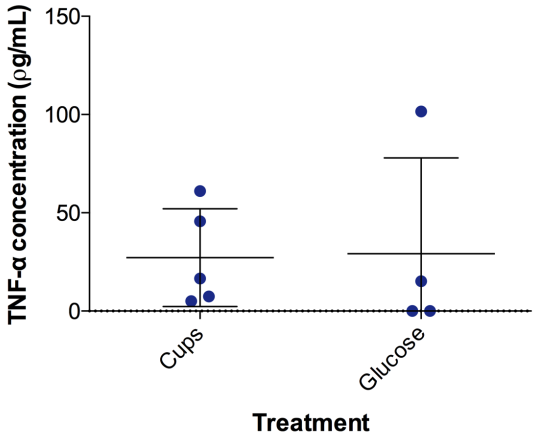

Figure 4-11: TNF-α concentrations in mice blood 2 hours after i.v. injection with polymer cups
Mice were i.v. injected with 200 µL of either PBS or 25 mg/mL 300 nm polystyrene core cups. TNF-α concentrations in the plasma of the mice treated were measured 2 hours after injection using an ELISA. The PBS treatment group had 4 mice and the cups treatment group had 5 mice. Error bars indicate standard deviation. A t-test showed no significant change in TNF-α concentration between the groups, $P>0.05$.

4.4 Discussion

Polymeric cups have been successfully formulated to have a uniform shape, with a very narrow size distribution of a size that could be predictably modified using different seed particles. The final hydrodynamic diameter of the cup formulations in this chapter were 191 nm and 483 nm and, as such, should be able to extravasate out of the vasculature into the perivascular space[67,68]. The facile chemistry used in the production of cups and the reproducibly monodisperse nature of the product indicate that they will be far more amenable to scale-up and GMP production than the CNP in Chapter 3.

The cavity inside the cups provided a surface onto which nano-gas pockets could be stabilised if the cups were air dried and then resuspended. These cups were able to act as cavitation nuclei in a reliable and sustained manner. The necessity of the drying step to provide a gas bubble on the surface of the cups was demonstrated by the negligible cavitation response of cups that had not been dried.

The effect of the peak rarefractional pressure of the ultrasound exposure on the cavitation response indicated that the cavitation threshold of the 300 nm core cups at ultrasound frequency of 0.5 MHz is approximately 1.5 MPa whilst the 100 nm core cups have a threshold of between 1.5 MPa and 3 MPa. At 3 MPa the energies generated by their cavitation events were approximately equivalent suggesting that once cavitating, the initial size of the gas pocket does not influence the violence of the ultrasound response. The decay pattern of the cavitation response with time extends well beyond the duration for

which currently approved microbubble formulations would continue to generate cavitation, i.e. more than 10 minutes compared to 10 seconds.

The ζ-potential of both 100 nm and 300 nm core cups was strongly negative which may contribute to the rapid clearance of the particles from the blood stream as confirmed by Graham[314]. Extended blood circulation is not essential for these particles as the intention is to actively target the particles within minutes of injection using ultrasound rather than rely on passive accumulation. In this case ultrasound treatment would immediately follow injection in order to utilise as high a blood concentration of cups as possible.

Studies performed ex vivo with freshly isolated human blood components were used to address questions regarding the haemocompatibility of the cups and therefore their suitability for i.v. injection. Both RBC and leukocyte viability remained approximately 100% at all tested concentrations of cups. Secretion of IL-6 and complement activation was not observed in either ex vivo or in vivo assays. Difference in human and mouse clearance profiles often relate to the influence of pre-exposure (and therefore pre-existing immunity) and difference in the size of hepatic sinusoidal fenestrae (approximately 107 nm in humans and between 130 and 170 nm in mice[316]). However, as a novel agent above 300 nm in size neither of these factors should apply in the case of cups. It would therefore be expected that, once the raised circulation time of humans is accounted for, a similar clearance in humans would be observed and there would be minimal complement activation or inflammation.

On the basis of these studies we conclude that these cups are sufficiently biocompatible to warrant further investigation and clinical development.

4.5 Conclusion

This chapter reports that:

- Seeded emulsion polymerisation can be used to successfully manufacture suspensions of monodisperse, sub-micron polymer cups. Seed polymerisation provides a simple method to reproducibly vary the size of both the particle and the cavity.
- Ultrasound responsiveness of the cups was achieved by the entrainment of gas pockets on the surface of the cups, as non-dried cups were not responsive.
- Haemolysis assays and leukocyte cell viability was observed to be unaltered by incubation with cups in *ex vivo* assays
- *Ex vivo* and *in vivo* experiments did not show significant increases in complement, IL-6 or TNF-α release.

5 Cavitation-enhanced delivery of an antibody *in vitro*

5.1 Introduction

Delivery is a key problem in current anti-cancer therapy. The irregular vasculature and fast growth of tumours can cause the distances between cancer cells and blood vessels to extend up to 180 μm compared to less than 90 μm for normal cells[136,317]. A mixture of high intra-tumoural pressure and a dense extracellular matrix means that drug delivery is no longer conveyed by convection but relies upon the diffusivity of the therapeutic agent[63]. By the Stokes-Einstein equation the diffusivity of a drug is inversely proportional to its radius. As new therapeutic agents begin to incorporate functionality to, for example, evade the immune system, reduce toxicity or become more specific their size has grown and, consequently, delivery has begun to further restrict effective treatment.

In the past 17 years there have been 15 antibody cancer therapies approved by the FDA, 5 of which were approved in the last 3 years[26]. The academic journal Science listed cancer immunotherapy, which typically uses antibodies to stimulate the immune system, as their breakthrough technology of 2013[16]. However, antibodies have a much greater size than their small molecule chemotherapy predecessors: doxorubicin has a molecular weight of 544 Da

while trastuzumab (trade name Herceptin), an anti-human epidermal growth factor receptor-2 (HER2) antibody, has a molecular weight more than 250 times greater (146 kDa). This restricts the antibody from penetrating far from the vasculature[22].

In addition to approved 'block-buster' drugs such as trastuzumab a raft of new checkpoint inhibitor antibodies (e.g. anti-cytotoxic T-lymphocyte-associated protein 4 (CTLA-4) and anti-programmed death ligand 1 (PD-L1)) are providing impressive results in clinical trials[318]. As the clinical dependence on antibody therapeutics grows, the problem of poor tumour penetration will become an even greater concern. Wang et al have used HIFU in an animal model to show that delivery of a fluorescently labelled antibody could be enhanced leading to improved therapeutic efficacy[240]. However, this study did not use artificial cavitation nuclei, and thus necessitated the use of ultrasound with a peak rarefactional pressure of 8.95 MPa at 1 MHz to cause cavitation events at the focus. These ultrasound parameters are well above the therapeutic levels of ultrasound permitted in the clinic and are likely to cause substantial mechanical damage in and around the tumour. As a consequence tumour volume growth was reduced not just in the antibody and HIFU group but also in the HIFU group alone. Key questions about the ultrasound parameters which are effective and safe enough for clinical translation remain to be answered, It is proposed that the use of nanoscale cavitation nuclei and passive acoustic mapping offers a more viable route to the ultimate goal of ultrasound assisted delivery of antibodies in cancer patients.

A tumour-mimicking flow phantom was used to assess this hypothesis. Agarose gels containing flow channels have been used in the past to model

blood vessels within a tumour in order to assess the effects of ultrasound on drug delivery[214,319]. Agar is an ideal material as it has similar acoustic properties to human tissue, its transparency enables optical analysis and its porosity can be varied with concentration in order to mimic the 'leaky' vasculature associated with the endothelium of tumours. Fluorescently labelled antibodies were used as the model therapeutic.

5.2 Chapter aims

The aim of this chapter is to:

- Test the acoustic response of carbon nanoparticles (CNP) and polymer cups and compare to SV.
- Measure changes to the acoustic response caused by incubation with human serum.
- Characterise the effect of ultrasound parameters on the different cavitation nuclei.
- Assess if cavitation of the nanoparticles enhances antibody delivery and optimise ultrasound parameters to enhance delivery whilst avoiding high mechanical indices.
- Assess whether the parameters required for enhanced delivery are likely to cause cell death.

5.3 Methods and results

The ultrasound apparatus used was identical to that described in Chapter 2 (Figure 2-3). In brief a 0.5 MHz high intensity focused ultrasound (HIFU) was linked to a function generator via a matching network and an RF power amplifier. Labview software was used to control outputs from the function generator. The voltages measured from a 7.5 MHz passive cavitation detector (PCD) aligned with the HIFU were filtered using a 2 MHz high pass filter and amplified before the data was stored on a data acquisition (DAQ) card. The same HIFU transducer could also be driven at 1.6 MHz, but in this case the 2 MHz high pass filter for the PCD was exchanged for a 5 MHz high pass filter in order to enable effective filtration of the second and third harmonics of the driving frequency.

5.3.1 Comparison of the ultrasound responsiveness of the cavitation nuclei

The cavitation responses of both CNP and polymer cups have been described in Chapters 3 and 4 respectively, however it is essential to compare these particles with the microbubble formulation, SV, due to the improved therapeutic extravasation that has already been demonstrated using SV and ultrasound[191]. Consequently, it will act as a benchmark with which to compare CNP and cups. The concentration of SV was calculated to match the approximate volume of CNP at its maximum concentration: 0.2 mg/mL equates to an approximate volume of $1x10^{-4}$ mL CNP/ mL vehicle (assuming the CNP are spheres with a hydrodynamic diameter of 174 nm as measured

by DLS). This meant that the SV was diluted to 5% of its initial concentration[320]. Cups were used at a concentration of 5.4 mg/mL, which was not matched to the other cavitation nuclei. This equates to approximately double the concentration by volume of either SV or CNP. The concentrations of all cavitation nuclei were maintained throughout this chapter.

Figure 5-1 directly compares the electrical power recorded by the PCD when the different cavitation nuclei were exposed to ultrasound in a static chamber as described in Chapter 2 over a 10 minute duration. The ultrasound had a driving frequency of 0.5 MHz, a peak rarefactional pressure of 3 MPa, a pulse repetition frequency (PRF) of 10 Hz and a duty cycle of 5%. All of the cavitation nuclei demonstrated a gradual reduction in the cavitation power recorded by the PCD over time with the exception of CNP, which showed an initial priming step before this trend. 100 nm core and 300 nm core polymer cups achieved equivalent amounts of power caused by cavitation (9.6 and 10.1 $x10^{-6}$ J respectively). However, unlike its solid nanoparticle counterparts, the cavitation events caused by the SV abruptly ceased after 100 seconds. This was a reproducible phenomena hypothesised to be due to cavitation of microbubbles in the near field of the holder shielding microbubbles further from the focus. As the microbubbles are destroyed the previously shielded nuclei begin to cavitate until there are no longer any nuclei in the holder. Further studies should be performed to validate this hypothesis.

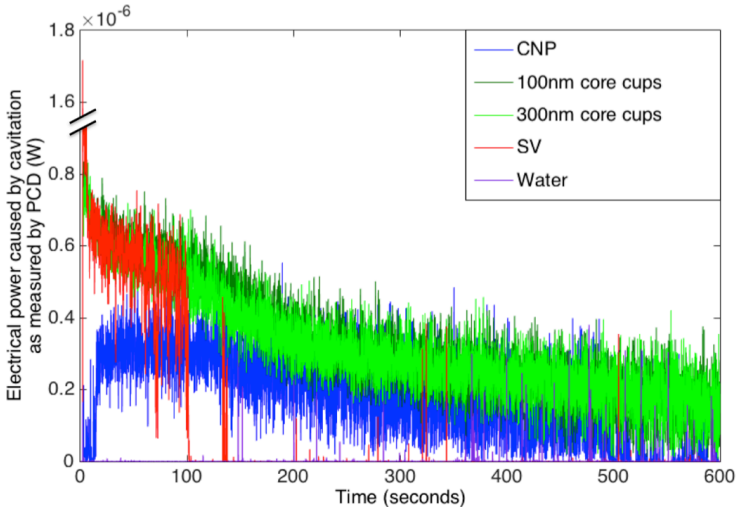

Figure 5-1: Comparison of the cavitation response of Sonovue (SV), carbon nanoparticles (CNP) and cups during 10 minutes of exposure to ultrasound
Samples in a static chamber were insonated with ultrasound of peak rarefactional pressure 3 MPa, driving frequency 0.5 MHz, 5% duty cycle and 10 Hz pulse repetition frequency (PRF). Electrical power was recorded by a 7.5 MHz passive cavitation detector (PCD).

The ultrasound parameters are critical to the number and strength of the cavitation events. To measure the cavitation response of each of the particles over a large parameter space the static chamber was replaced with the capillary flow channel as used by Kwan et al. and described in Chapter 2[275].

The intersection between the focal volume of the 0.5 MHz HIFU transducer and the capillary channel corresponds to a volume of 20 nL. A much smaller exposed volume than in the static chamber ensures that fewer particles will respond to each HIFU burst and consequently there will be a lower probability of the ultrasound response being skewed by a few anomalous particles. Additionally, a continuous flow of nuclei running through the focal point means each individual PCD recording can be considered independent.

The driving frequency, peak rarefactional pressure and pulse repetition frequency (PRF) of the ultrasound were varied to evaluate how the cavitation response of water, CNP, 300 nm polymer core cups and SV was dependent upon the ultrasound parameters (Figure 5-2)

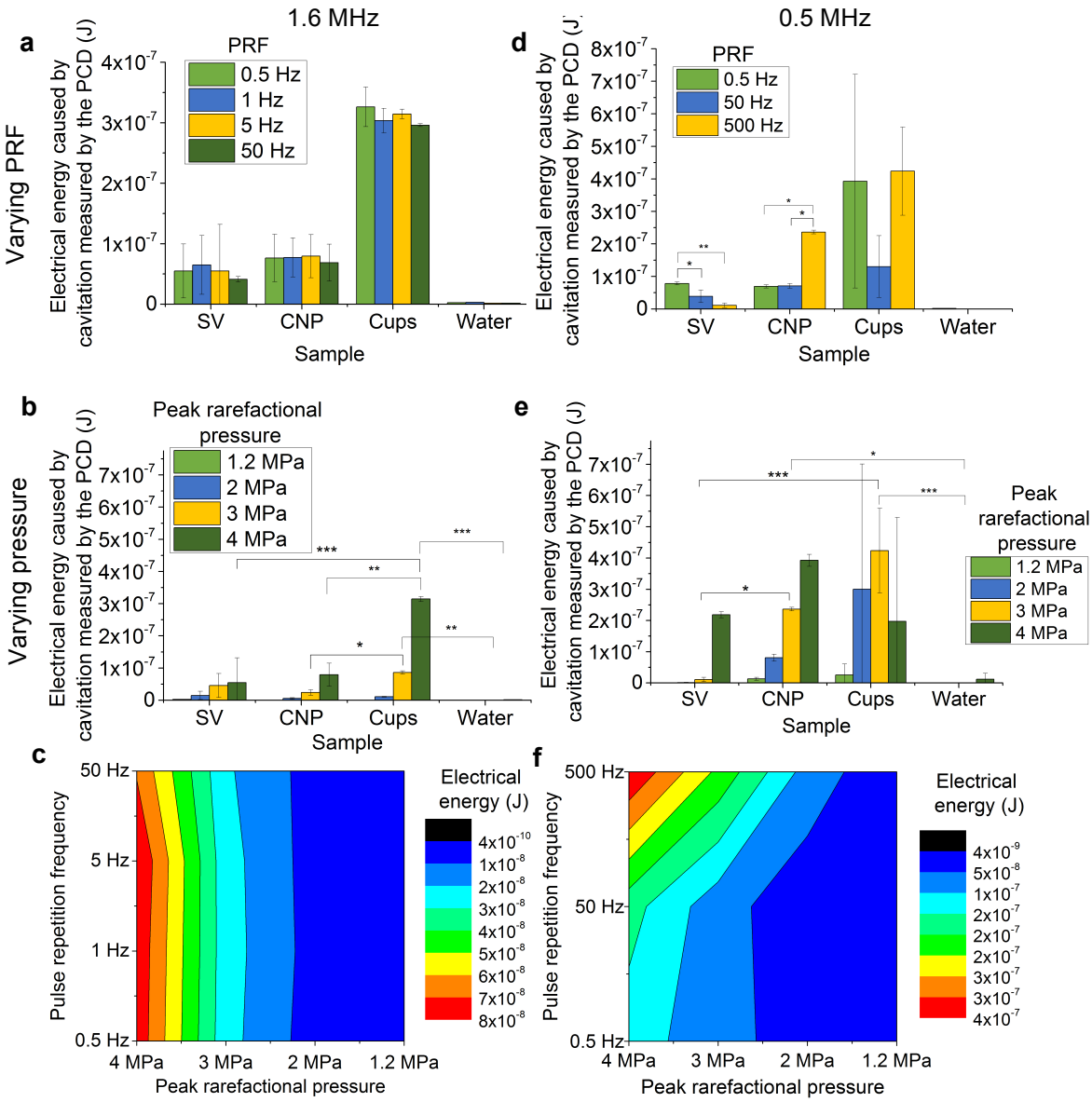

Figure 5-2: Impact of ultrasound parameters on the inertial cavitation response of the cavitation nuclei

Samples were flowed through capillary tubing at 0.3 mL/min and the ultrasound response measured over 30 second varying the parameters as follows (a) varying PRF and keeping frequency and peak rarefactional pressure constant at 1.6 MHz and 4 MPa (b) varying peak rarefactional pressure and keeping frequency and PRF constant at 1.6 MHz and 5 Hz (c) surface plot of cavitation response of CNP over the 2 variables of rarefactional pressure and PRF keeping driving frequency 1.6MHz (d) varying PRF and keeping frequency and peak rarefactional pressure constant at 0.5 MHz and 3 MPa (e) varying peak rarefactional pressure and keeping frequency and PRF constant at 0.5MHz and 500 Hz respectively (f) cavitation response of CNP at 0.5 MHz varying both PRF and rarefactional pressure. N = 3, standard deviation shown, ANOVA with Bonferroni post-test for significance. * = P<0.05, ** = P<0.005, *** = P<0.0005.

As expected, cavitation energy increased with an increase in the peak rarefactional pressure for all of the samples with the exception of 300 nm core polymer cups when insonated at 1.6 MHz driving frequency between 3 and 4 MPa; the lack of difference could be because above 3 MPa all of the cups are above their cavitation threshold. PRF was not a factor in cavitation response if the ultrasound had a driving frequency of 1.6 MHz, however, at 0.5 MHz it became much more critical to cavitation. A higher PRF caused CNP to cavitate more intensely while SV showed greater cavitation energies when the ultrasound had a lower PRF. Cavitation response of cups varied between the 3 different PRFs but did not do so significantly or with a clear trend. A frequency of 0.5 MHz tended to create greater cavitation energies than 1.6 MHz at higher pressures for all nuclei with the exception of 300 nm core cups. The SV did not give as strong a response in comparison to CNP and cups. At peak rarefactional pressure of 3 MPa, driving frequency of 0.5 MHz, PRF of 500 Hz and an ultrasound duration of 30 seconds SV produced 1.1 +/- 0.7 x 10^{-8} J energy while 300 nm core cups and CNP produced 2.3 +/- 0.1 x 10^{-7} J and 4.2 +/- 1.4 x 10^{-7} J, respectively, as had been seen in the static holder over the same duration (Figure 5-1). This may be due to the microbubbles being destroyed by a side-lobe of the HIFU beam before they could reach the focus of the PCD. The ultrasound response of CNP and cups was not significantly different when exposed to ultrasound with a driving frequency of 0.5 MHz ($p > 0.05$), however, at 1.6 MHz the cups gave a significantly stronger cavitation response than the CNP (ultrasound with peak rarefactional pressure of 3 MPa, a PRF of 5 Hz and exposure duration of 30 seconds

resulted in cavitation energy recorded by the PCD for CNP and cups of 2.4 +/- 0.8 $x10^{-8}$ J and 8.7 +/- 0.5 x 10^{-8} J; $p < 0.05$).

5.3.2 Adsorbance of human serum proteins onto the surface of the nanoparticles

As demonstrated in Chapters 3 and 4 both CNP and cups lower the cavitation threshold of the solution they are in by entrapping gas within crevices on their surfaces. Proteins also have the potential to adsorb onto the surface of the particles thus reducing the hydrophobicity of the surface and preventing the stabilization of gas pockets.

Chapter 3 and Chapter 4 showed no detectable adsorption of proteins in human serum onto CNP and minimal amounts of adsorption of a 150 kDa protein onto cups although the assays had limited sensitivity. To assess whether the presence of protein would alter the response of the cavitation nuclei to ultrasound following intravenous (i.v.) injection, the cavitation nuclei were incubated with human serum in a 1:1 ratio for 15 minutes before being flowed through a tissue mimicking phantom (as described in Chapter 2) at 1 mL/min. 3 locations on each flow channel were exposed to ultrasound of 0.5 MHz frequency, 10 Hz PRF and 5% duty cycle with a rarefactional peak pressure of 0.14, 0.5 or 1.2 MPa.

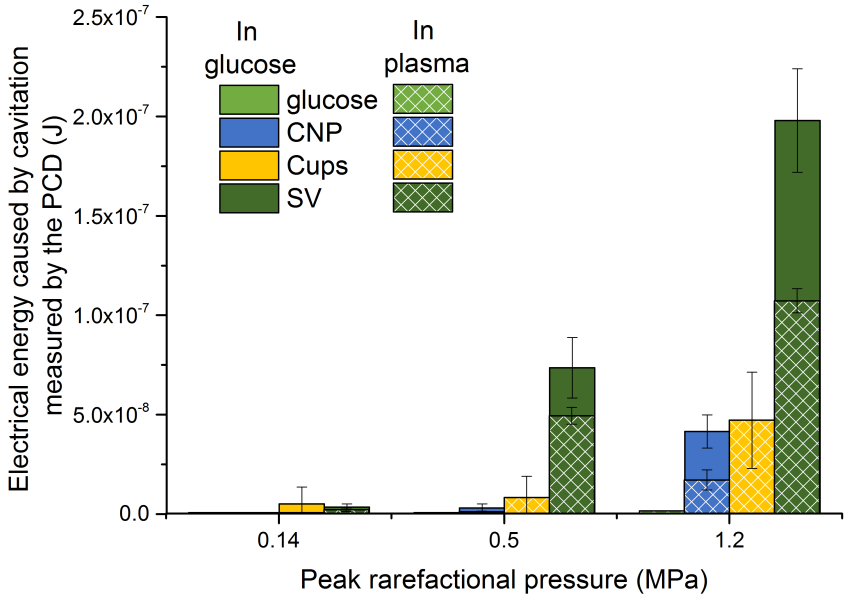

Figure 5-3: Ultrasound response of cavitation nuclei before and after incubation with human serum
Samples were incubated for 15 minutes in a 1:1 ratio and passed through a capillary flow channel at 0.3 mL/min. Ultrasound parameters were: 0.5 MHz driving frequency, 10 Hz PRF and 5% duty cycle. Peak rarefactional pressure was varied to characterise its impact upon the cavitation response. The serum incubated data is overlaid onto data from samples that were not incubated with any human serum. N=3, error bars indicate standard deviation.

Despite the lack of adsorption of proteins observed onto the CNP their ultrasound responsiveness was reduced by incubation with plasma (Figure 5-3). It is hypothesised that this is due to proteins adsorbing onto the CNP as the gas bubbles on their surface cavitate to temporarily reveal more of the surface of the particle. However, the ultrasound responsiveness of the 300 nm polystyrene core cups remained unaffected by the incubation with plasma. Notably, the cavitation energy measured by the PCD of SV showed a substantial drop in the presence of serum (at 1.5 MPa the cavitation response was reduced from 2.0 +/- 0.3 $x10^{-7}$ J to 1.1 +/- 0.1 $x10^{-7}$ J). Bonté and Juliano hypothesised that this is due to proteins in the plasma incorporating within the lipid bilayer of microbubbles to destabilise them[321]. However, in contrast to Figure 5-2, the SV caused a much stronger cavitation response than the CNP or the cups. This may be a consequence of the larger flow channel in Figure

5-3 causing fewer of the bubbles to be destroyed by shear stresses during flow. Indeed, the level recorded for SV in the larger flow channel was 270–fold greater than in was in the smaller flow channel in comparison to just 3–fold and 2–fold for the CNP and the cups at the same ultrasound parameters (there will be an increase in energy recorded for all nuclei due to the increased volume of particles within the focus).

5.3.3 Cell death caused by cavitation

Tissue mimicking phantoms used to this point did not include cells within the agarose matrix. This was a necessary step to increase the relevance and complexity of the model, and help answer important questions regarding the safety of cavitation instigation. An agarose tissue mimicking phantom containing CT-26 cells and propidium iodide (PI) was formulated as described in Chapter 2. Cavitation nuclei were flowed through the phantom and exposed to ultrasound of frequency 1.6 MHz, peak rarefactional pressure of 4 MPa, 10 Hz PRF and 5% duty cycle due to the low background cavitation response of glucose in comparison to the cavitation caused by 300 nm core cups. The agar was then sectioned and imaged. Cell death caused by the cavitation of the nuclei can be seen in Figure 5-4, which shows both the bright field and fluorescent images of these slices.

Glucose passed through the channel and exposed to ultrasound was used as a negative control for cell death while a section of cells and agar from a flow channel which had subsequently been refrigerated for 1 hour and left at room temperature for 48 hours in order to kill all the cells was used as a positive control. The mean fluorescence of pixels was calculated in a perpendicular

direction to flow (Figure 5-5). The distance of peak fluorescence (and, consequently maximum cell death) was predicted to be at the interface between flow and tissue mimicking phantom. Cell death was quantified as the difference in peak fluorescence intensity of the sample and the negative control divided by the difference in fluorescence of the positive and negative control. CNP and SV exposed to ultrasound did not appear to affect cell viability in the phantom (a 0% and 7% increase in cell death above the glucose control). However, channel deformation and an increase in the intensity of PI staining was evident for cups and there was an estimated 54% cell death at the interface between the flow channel and the tissue mimicking phantom. 0.5 mm from the interface this cell death was reduced to approximately 25%. This is a worst case scenario as PI is a marker of cell membrane permeability as it fluoresces when bound to DNA. Consequently the fluorescence shown by the microscopy images could be due to the transient effect of sonoporation rather than cell death.

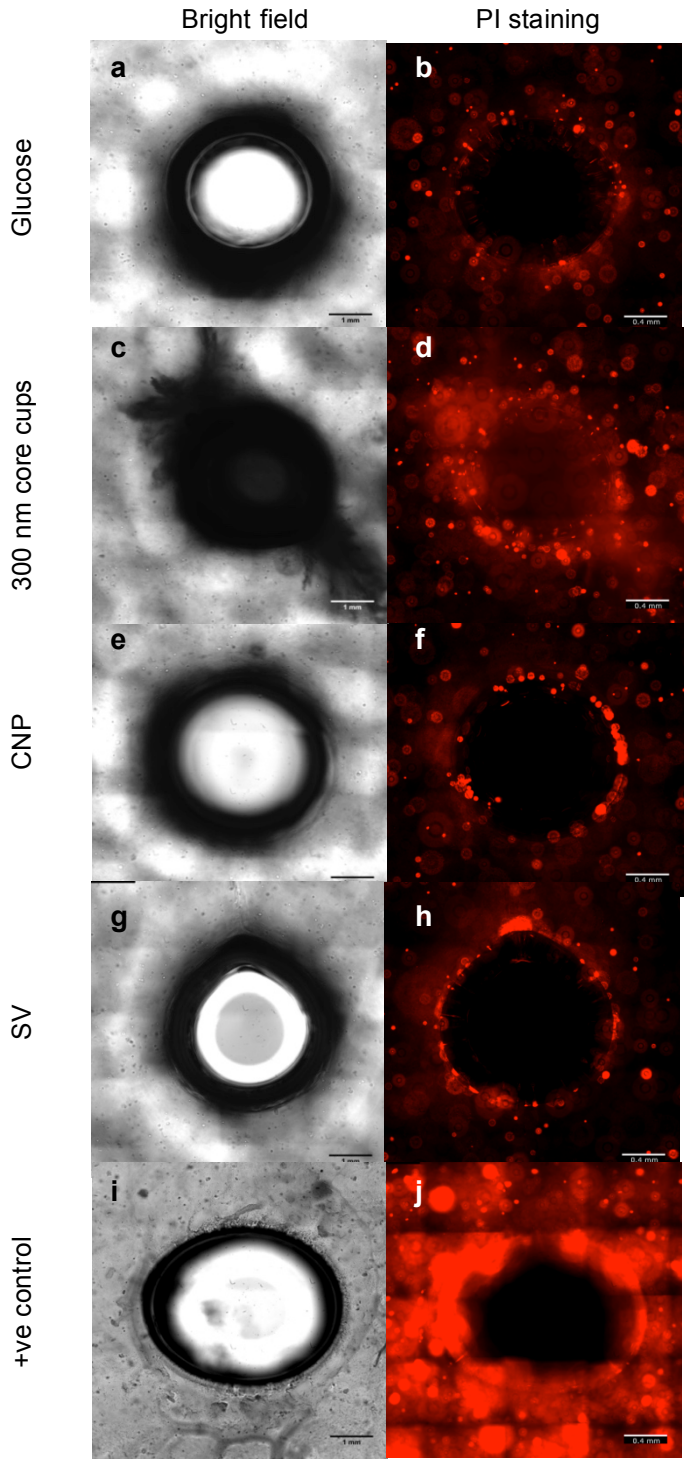

Figure 5-4: Cavitation induced cell death
Cavitation nuclei were passed through the flow channel of a tissue mimicking phantom, filled with 1% agar containing $2x10^5$ CT-26 cells and 4 µL/mL propidium iodide (PI), at 1 mL/min. The centre of the flow channel was then exposed to ultrasound of frequency 1.6 MHz, peak rarefactional pressure 4 MPa, 10 Hz PRF and 5% duty cycle. A central slice of each of the phantoms was imaged using fluorescence microscopy. Left hand column shows bright field images of the slice while right hand images shows fluorescence images using the Cy5 filter. Cavitation nuclei in the sample of a) and b) glucose alone c) and d) 300 nm core cups e) and f) CNP g) and h) SV and i) and j) positive control for cell death.

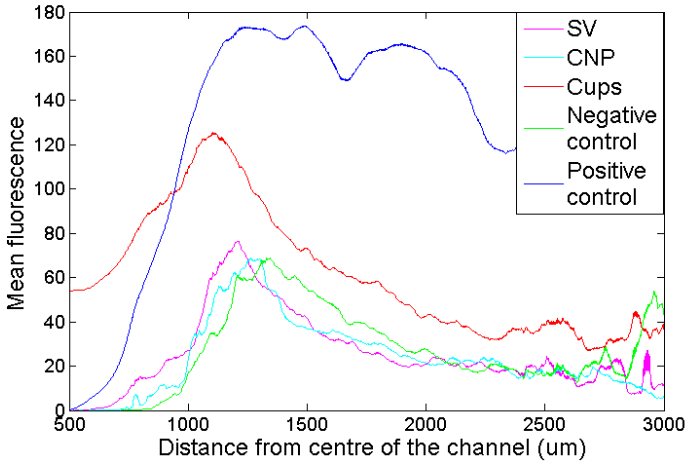

Figure 5-5: Mean fluorescence caused by PI staining of cavitation-induced cell death as a function of distance from the centre of the flow channel
Quantification of the fluorescence of the microscope images shown in Figure 5-4. MATLAB code was used to measure the mean fluorescence of pixels from the centre of the flow channel in a radial direction.

5.3.4 Extravasation of model drug

Having characterised the relative amounts of cavitation and cell damage produced by the cavitation nuclei upon exposure to ultrasound, their impact on the delivery of an antibody was investigated.

Transportation of a fluorescently labelled model antibody into the agar was measured following co-injection with cavitation nuclei into a tissue mimicking phantom and exposure to ultrasound.

5% glucose, 0.15 mg/mL CNP in glucose, 0.6 mg/mL cups in glucose or 1.5×10^7 SV bubbles/mL in PBS were mixed with 40 µL/mL FITC labelled antibody (Sigma, F9512 or Sigma, F0257). 3 mL of sample was passed through the phantom at a rate of 1 mL/min. Two focal points were selected 18.75 mm apart from each other with a third point that was not exposed to ultrasound in order to act as a negative control. Ultrasound had 10 Hz PRF and 5% duty cycle with either:

- 0.5 MHz driving frequency and peak rarefactional pressures of 1.2 MPa (due to this having already been demonstrated to improve delivery of an oncolytic virus using SV[191]) or 3 MPa (a pressure at which all cavitation nuclei were above their cavitation threshold (Figure 5-1))

  or

- 1.6 MHz driving frequency and peak rarefactional pressure of 2 MPa (an equivalent MI to a driving frequency of 0.5 MHz and peak rarefactional pressure of 1.2MPa) or 4 MPa (a pressure at which 300 nm core cups showed significant cavitation in comparison to SV and CNP (Figure 5-2, $p < 0.0005$ and $p < 0.005$ respectively)).

Each focal point was treated for 30 seconds. Flow channels were then washed with 6 mL water to remove antibody that had not been propelled into the agar. The ultrasound response of each of the cavitation nuclei at 0.5 MHz and 1.6 MHz is quantified in Figure 5-6 a and b respectively.

The data in Figure 5-3 and Figure 5-6 a both show the ultrasound response of the cavitation nuclei exposed to ultrasound of 0.5 MHz driving frequency, 1.2 MPa peak rarefactional pressure, 10 Hz PRF with a duration of 30 seconds. Both CNP and 300 nm core cups produced equivalent amounts of cavitational energy in both experiments ($4.2 +/ 0.8 \times 10^{-8}$ J vs $5.4 +/- 2.1 \times 10^{-8}$ J and $3.4 +/- 1.0 \times 10^{-8}$ J vs $3.6 +/- 1.2 \times 10^{-8}$ J respectively). However, the response of SV is substantially reduced ($2.0 +/- 0.3 \times 10^{-7}$ J vs $4.1 +/- 3.3 \times 10^{-8}$ J). As the only experimental difference is the addition of the antibody, it is possible this discrepancy could be due to an interaction between the antibody and the lipid bilayer of the microbubbles. This, again, confirms the inherent instability of microbubbles and their susceptibility to their environment.

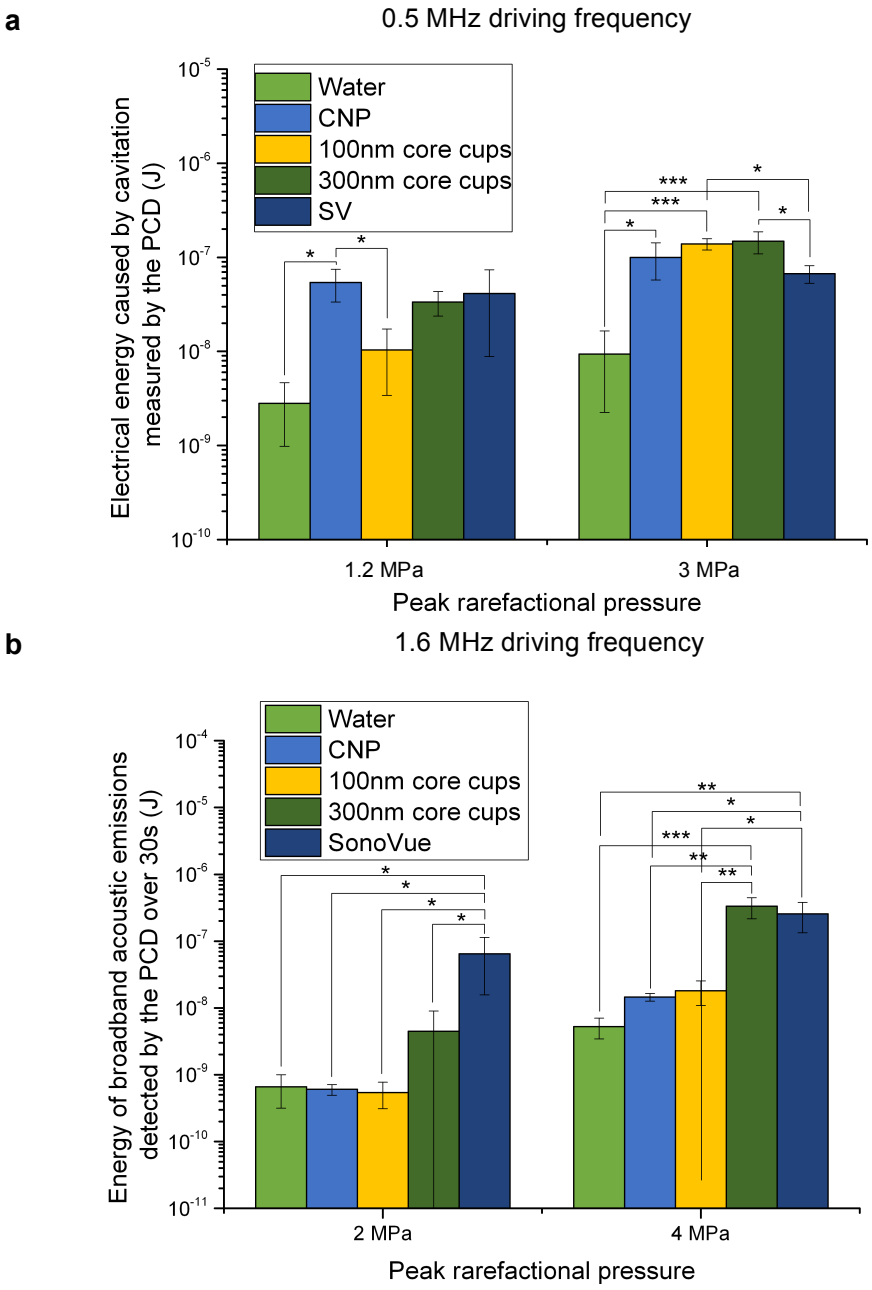

Figure 5-6: Ultrasound response of cavitation nuclei flowed through a flow phantom and insonated with a driving frequency of either 0.5 MHz or 1.6 MHz
Samples were flowed through the channel at 1 mL/min. Ultrasound parameters were (a) 0.5 MHz driving frequency, 5% duty cycle, 10 Hz PRF and peak rarefactional pressure of either 1.2 MPa or 3 MPa and (b) 1.6 MHz driving frequency, 5% duty cycle, 10 Hz PRF and peak rarefactional pressure of either 2 MPa or 4 MPa. N = 3, standard deviation shown, ANOVA with Bonferroni post-test for significance. * = P<0.05, ** = P<0.005, *** = P<0.0005.

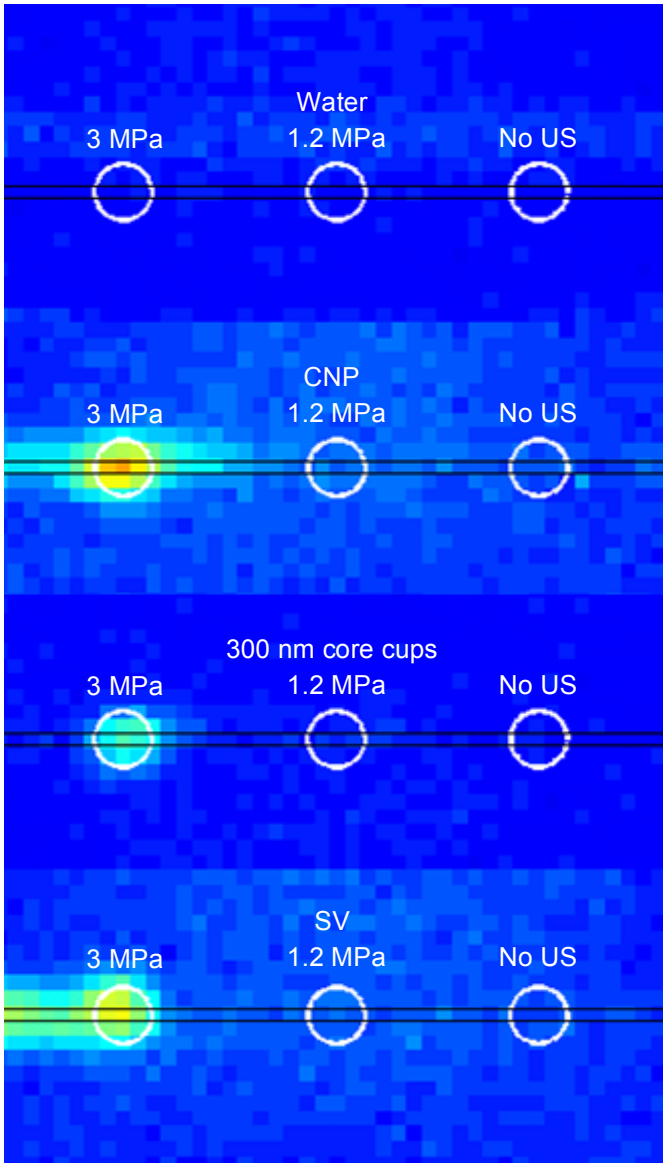

Figure 5-7: An example of a fluorescence map used to assess transport of FITC labelled antibody into a tumour mimicking phantom
Sample (glucose, CNP, 300 nm core cups or SV) was flowed through the channel at 1 mL/min. Focal points were treated with ultrasound of 0.5 MHz, 10 Hz PRF, 5% duty cycle and either 1.2 MPa or 3 MPa peak rarefactional pressure. Flow channels were then washed through with water to remove antibody that remained in the channel. Fluorescence of the phantom was mapped using a plate reader measuring using an excitation wavelength of 485 nm and emission wavelength of 520 nm.

Immediately post ultrasound exposure the phantoms were placed on a fluorescence plate reader and the distribution of the antibody was characterised. The resolution of the plate reader was approximately 1.33 mm by 1.33 mm. Representative maps can be seen in Figure 5-7. The increase in fluorescence at each of the focal points was calculated using Matlab software and compared to the region of the flow channel that had not been exposed to ultrasound in order to quantify these maps (Figure 5-8). Exposure to a peak rarefactional pressure of 3 MPa lead to both the CNP and SV nuclei causing significant amounts of extravasation in comparison to glucose alone (an increase in fluorescence of 2.0 times greater than without glucose alone in both cases ($p < 0.0005$). Notably 300 nm cups also provided an enhancement compared to glucose (1.4 +/- 0.1 but this was not significant, $p > 0.05$). At 1.5 MPa no significant changes in delivery were detected for any of the cavitation nuclei tested ($p > 0.05$). When considered in the context of the cavitation data in Figure 5-6 a it is apparent that the total energy of broadband acoustic emissions may not be the most accurate metric to help predict ultimate delivery. It is evident that cavitation was critical to penetration of the antibody into the agar, however, the degree of extravasation was not directly correlated to the intensity of the cavitation. This demonstrates the need to investigate the link between cavitation metrics and delivery achieved in more detail and the value of this phantom model in enabling such studies.

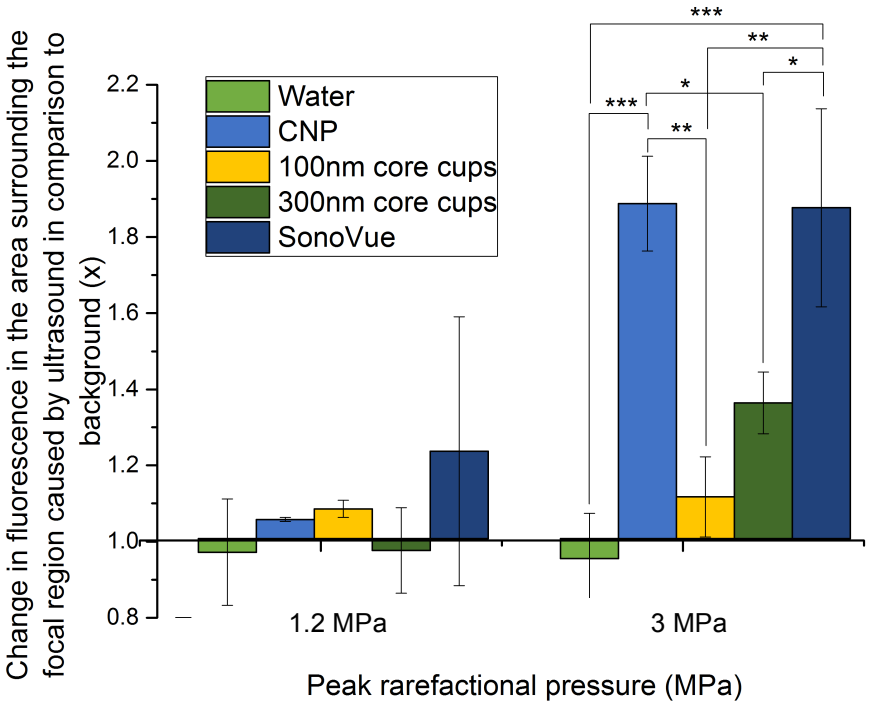

Figure 5-8: Quantified antibody extravasation caused by cavitation nuclei in flow phantom model insonated with 0.5 MHz ultrasound
Antibody delivery was measured using Matlab code to measure the increase in fluorescence intensity of 7 mm x 23 mm rectangle around the ultrasound focal point in comparison to a point on the same channel that had not been treated with ultrasound. N = 3, standard deviation shown, ANOVA with Bonferroni post-test for significance. * = P<0.05, ** = P<0.005, *** = P<0.0005.

The delivery of the antibody using ultrasound could also be measured using fluorescence microscopy. Figure 5-9 shows a representative example of each of the images from a fluorescence microscope showing the delivery of the antibody in addition to the bright field images of the same location. Extravasation caused by the combination of cavitation nuclei and ultrasound with a driving frequency of 1.6 MHz was measured by calculating the maximum distance at which the antibody could be detected from the flow channel. The difference in the method of quantification was caused by a change in the fluorescently labelled antibody, which did not provide sufficient fluorescence to be measurable by the plate reader. Matlab software was used to measure the fluorescence from the focal point of the ultrasound in a

perpendicular direction from the flow channel subtracted by the background diffusion from the channel.

Figure 5-10 shows a comparison between antibody delivery by 300 nm core cups exposed to 4 MPa peak rarefactional pressure and the background delivery in the same channel. Figure 5-10 b shows the maximum antibody extravasation distances caused by all of the cavitation nuclei at rarefactional pressures of both 2 MPa and 4 MPa. 300 nm core cups were the only cavitation nuclei at these ultrasound parameters to cause significant and reproducible extravasation of the antibody into the agar (0.38 +/- 0.23 mm, $p < 0.05$). This is in accordance with Figure 5-6 b, which showed that CNP and 100 nm core cups produced negligible cavitation at these parameters wherease 300 nm core cups achieved substantial cavitation response (3.3 +/ 1.2 x 10^{-7} J, $p < 0.0005$). Despite SV producing a significant cavitation response (2.6 +/- 1.2 x 10^{-7} J, $p < 0.005$) it caused negligible extravasastion of the antibody into the agar. This, again, confirms that cavitational energy alone is not a sufficient metric to predict delivery.

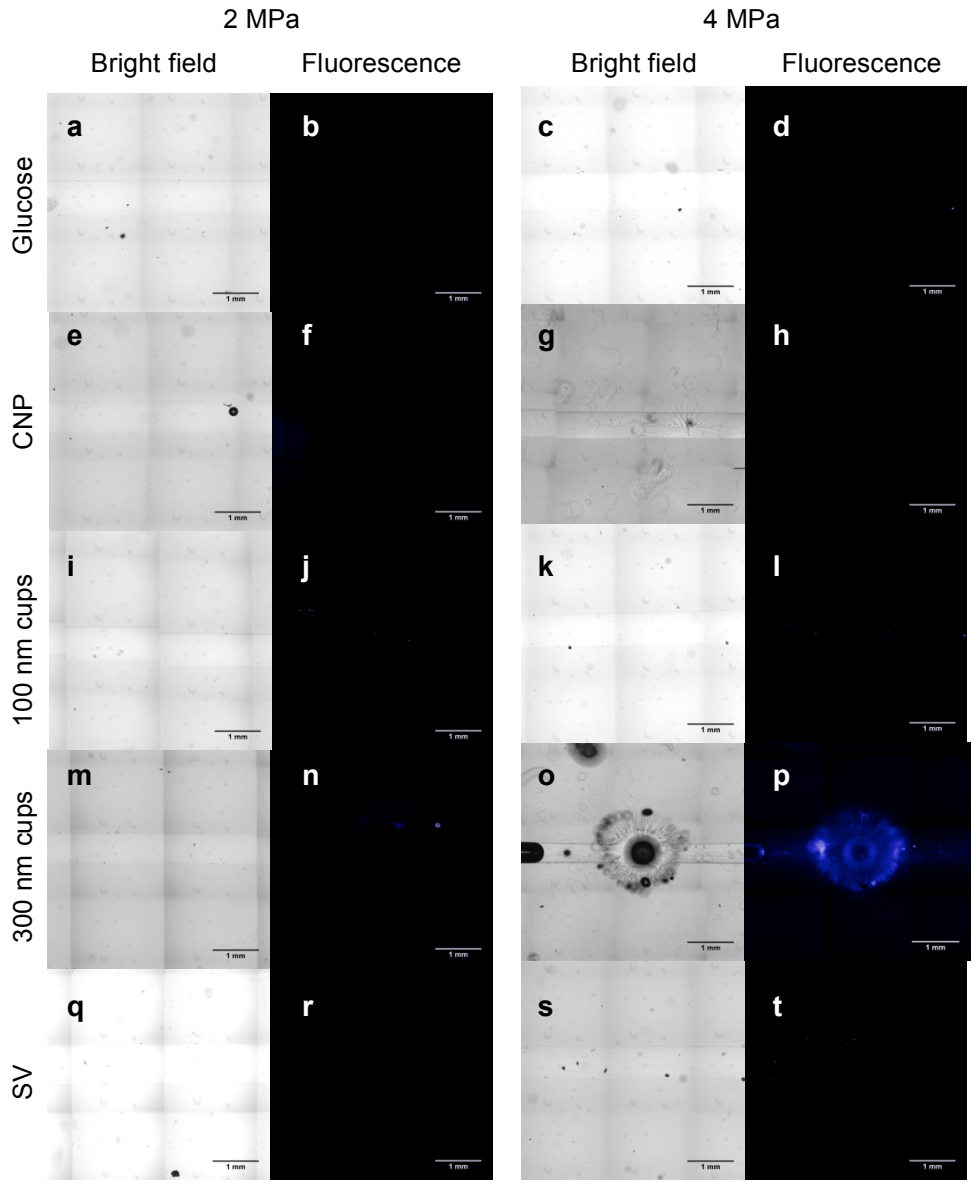

Figure 5-9: Examples of fluorescence and brightfield microscope images of cavitation mediated delivery of antibody after exposure to 1.6 MHz ultrasound
Samples were flowed through a tissue mimicking flow phantom and exposed to ultrasound with a driving frequency of 1.6 MHz, 10 Hz PRF, 5% duty cycle and peak rarefactional pressures of 2MPa (on the left hand side) and 4MPa (on the right hand side). Cavitation nuclei used were as follows (a)-(d) glucose (e)-(h) CNP (i)-(l) 100 nm core cups (m)-(p) 300 nm core cups and (q)-(t) SV.

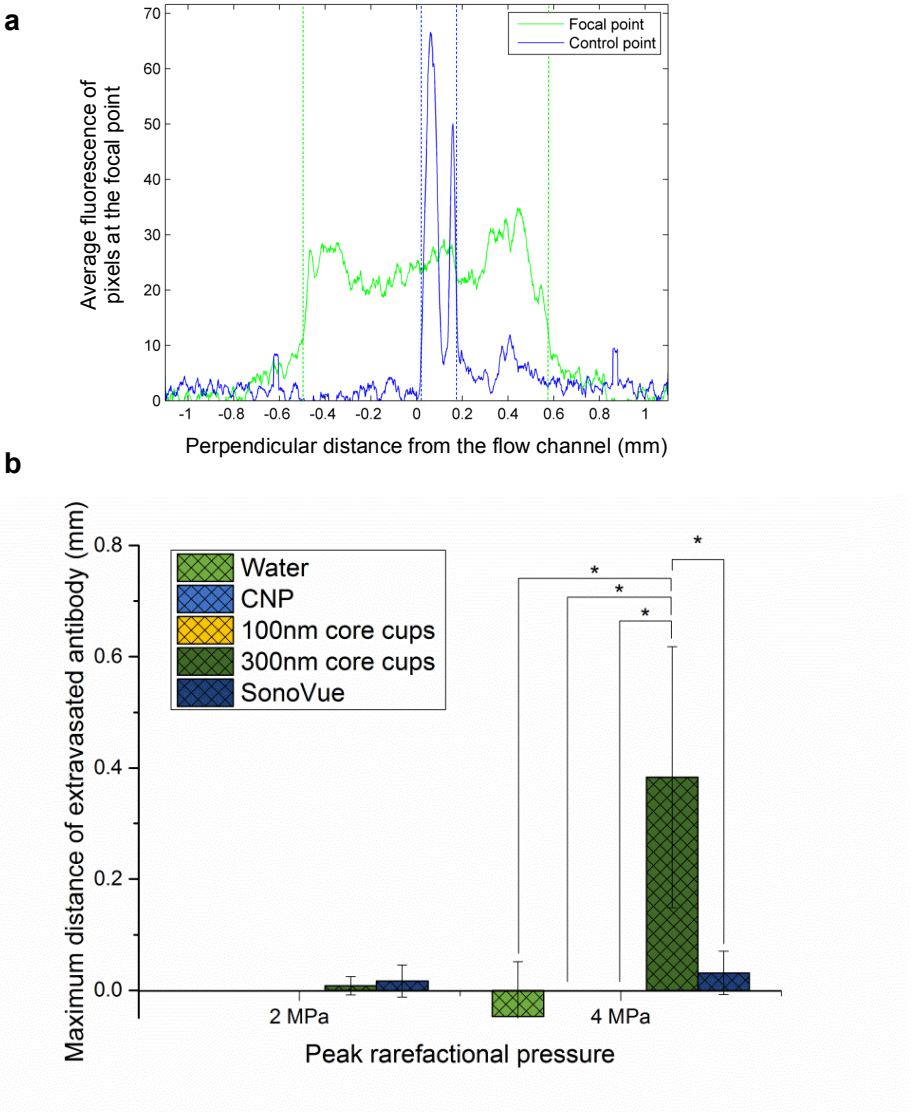

Figure 5-10: Extravasation distance of antibody caused by cavitation nuclei and 1.6 MHz ultrasound

Fluorescence microscope images (such as those shown in Figure 5-9) were analysed using custom Matlab code to quantify the extravasation distances of the fluorescently labelled antibody in an tissue mimicking flow phantom. Fluorescently labelled antibody had been flowed through the phantom with cavitation nuclei and insonated with ultrasound of driving frequency 1.6 MHz, 5% duty cycle, 10 Hz PRF and 2 MPa or 4 MPa peak rarefactional pressure (a) an example of fluorescence across the flow channel caused by the antibody being mixed with 300 nm core cups and insonating with a peak rarefactional pressure of 4 MPa (continuous green line) in comparison to a section of the same flow channel not treated with ultrasound (continuous blue line). Vertical dotted lines identify the distance the antibody has travelled both without (blue) and with (green) ultrasound. (b) Average maximum distances the antibody extravasated caused by each of the cavitation nuclei. N = 3, standard deviation shown, ANOVA with Bonferroni post-test for significance. * = $P<0.05$.

5.3.5 Ultrasound parameters influence on delivery

Experiments from Figure 5-6 to Figure 5-10 demonstrate that cavitation is a necessary condition to achieve enhanced delivery. However, the precise relationship between the cavitation events which occurred and the delivery which resulted required further investigation.

Consequently, a subsequent test was used to assess the effects of:

- **Duty cycle**: Exposure time was adjusted to keep the overall number of cycles constant but the duty cycle was varied.
- **Cycles per burst**: the duty cycle and the PRF were varied such that the number of cycles per burst was kept constant. Exposure time was also adjusted to keep the total number of cycles constant.
- **Total number of cycles**: exposure time was varied while all other parameters remained fixed.

It was hoped that varying each parameter in this way in isolation would help determine the impact of cycles per burst, PRF and total number of cycles on drug delivery. 300 nm core cups and fluorescently labelled antibody were injected through a tissue mimicking flow phantom at 1 mL/min and exposed to ultrasound that had a driving frequency of 1.6 MHz and a peak rarefactional pressure of 4 MPa. Studies were performed with 300 nm cups alone as they has demonstrated significant extravasation of the antibody at this frequency with a MI lower than any of the cavitation nuclei had at 0.5 MHz.

Table 5-1 lists the ultrasound parameters of each condition. Fluorescence microscopy mages were taken of each of the focal points and the extravasation distances were calculated as in Figure 5-10 a (data not shown).

Figure 5-11 shows the results of this test. It demonstrates that there is a minimum number of cycles per burst of between 1614 cycles per burst and 4035 cycles per burst is required to cause extravasation. PRF did not appear to have an effect on extravasation as long as the cycles per burst were kept constant. Finally total exposure time was important with a continual increase in delivery right up to the 30 second end point.

Table 5-1: Ultrasound parameters used to assess the impact of ultrasound parameters on the delivery of a model drug

Test	PRF (Hz)	Duty cycle (%)	Exposure time (s)	Cycles/burst	Total no. of cycles
Impact of cycles/burst	10	5	30	8070	2421000
	10	2.5	60	4035	2421000
	10	1	150	1614	2421000
	10	0.25	600	404	2421000
Impact of PRF	10	5	30	8070	2421000
	5	2.5	60	8070	2421000
	2	1	150	8070	2421000
	0.5	0.25	600	8070	2421000
Impact of total number of cycles	10	5	30	8070	2421000
	10	5	15	8070	1210500
	10	5	5	8070	403500
	10	5	1	8070	80700

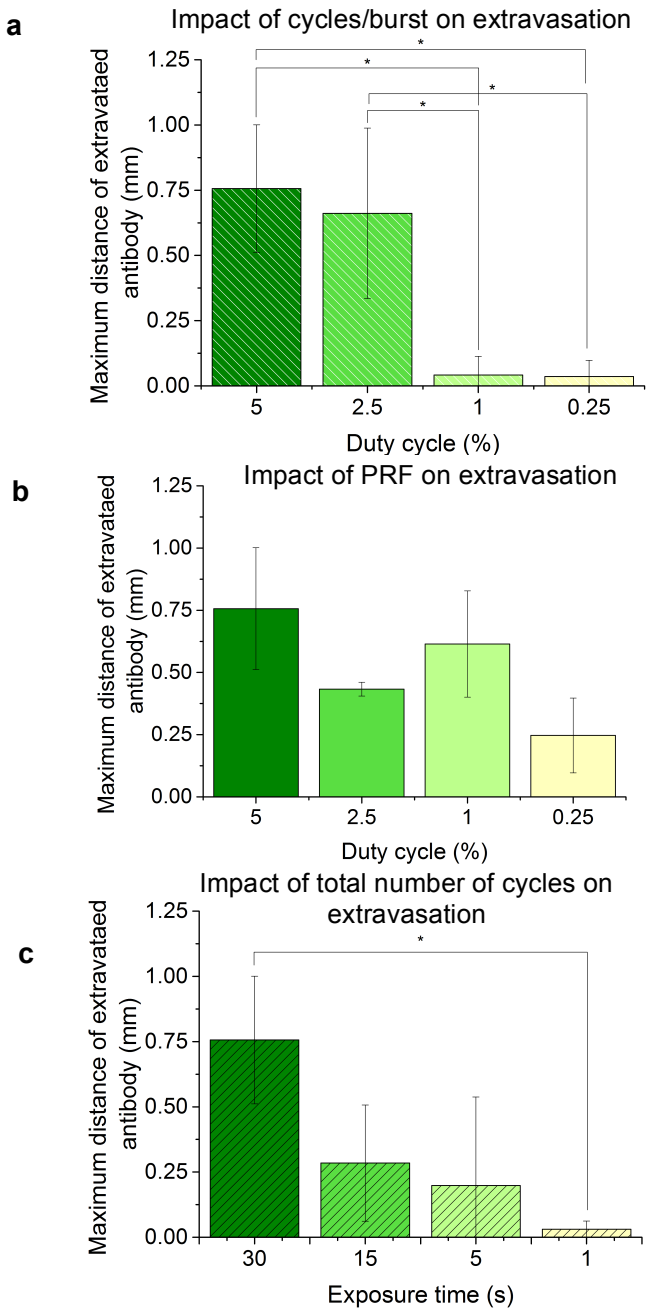

Figure 5-11: The impact of ultrasound parameters on the cavitation-mediated delivery of an antibody in tissue mimicking flow phantoms
300 nm polymer core cups mixed with a fluorescently labelled antibody were injected through flow phantoms at a rate of 1 mL/min. The flow channel was insonated with ultrasound of driving frequency 1.6 MHz and peak rarefactional pressure 4 MPa but with varying duty cycles, PRF and exposure times. Flow channels were washed through with water and the phantoms immediately imaged using a fluorescence microscope. Matlab code was used to calculate the maximum distance the antibody had extravasated from the channel. Ultrasound parameters changed were: (a) number of ultrasound cycles per burst (b) PRF and (c) total number of ultrasound cycles. N = 3, standard deviation shown, ANOVA with Bonferroni post-test for significance. * = $P<0.05$.

5.4 Discussion

Ultrasound-mediated cavitation offers a powerful means of achieving enhanced drug delivery using low cost, clinically available, non-invasive technology[322]. To date however the potential of ultrasound to enhance the delivery of antibody therapeutics has been rather under-researched[323]. Few studies have used cavitation and those which have done so have typically used much higher pressures without the use of cavitation nuclei[240,324]. The very few studies which have used cavitation nuclei have used microbubbles, which, as shown in this chapter, are rapidly destroyed by ultrasound (Figure 5-1) and are extremely sensitive to their environment (Figure 5-2 and Figure 5-3)[325].

The particles developed and described in chapters 3 and 4 of this thesis may provide a tool to progress this field of research. Both solid particle formulations show sustained cavitation activity in response to ultrasound exposure for over 10 minutes (Figure 5-1). In contrast the conventional microbubble formulation SV shows a response that is exhausted within 30 seconds. This difference is hypothesised to be due to the particles providing a surface onto which it is energetically favourable for the gas to restabilise onto after cavitation instead of dissolving[275]. This is unlike SV which, during the cavitation process, is destroyed.

The prolonged ultrasound response, in combination with the size of the particles, could offer the potential to continuously propel both a therapeutic agent and the cavitation nuclei far from the vasculature in tumours. The polymer cups also have the advantage that human serum does not diminish

their ultrasound response (Figure 5-3). This is not the case for SV and CNP, which suffer up to 3–fold decreases in activity upon serum addition.

As discussed in Chapter 1, diagnostic levels of ultrasound are restricted to a mechanical index (MI) of 1.9, spatial peak pulse average intensity (I_{SPPA}) of 190 W/cm^2 [226]. In these experiments all cavitation nuclei were able to enhance delivery of an antibody using ultrasound with a frequency of 0.5 MHz, MI of 4.2 and I_{SPTA} of 290 W/cm^2. Meanwhile, at a frequency of 1.6 MHz delivery was achieved using polymer cups and ultrasound with a MI of 3.2, I_{SPTA} of 520 W/cm^2. Despite these values being much higher than those permitted by the FDA for use as at diagnostic levels of ultrasound they are much lower than the parameters required to achieve delivery without cavitation (MI of 9.0 and I_{SPTA} of 2,600 W/cm^2 [240]). In addition, Figure 5-11 demonstrates that ultrasound parameters may be modified to reduce the peak rarefactional pressure but still cause similar levels of delivery e.g. by extending treatment times.

Analyses of the ultrasound exposure parameters used here demonstrated that PRF is a critical factor in the responsiveness of CNP at 0.5 MHz, however at 1.6 MHz this did not appear to be the case (Figure 5-2). At 1.6 MHz the variation of the PRF from 0.5 Hz to 50 Hz lead to the number of cycles per burst to range from 1614 to 16140, whereas the PRF range tested with the driving frequency of 0.5 MHz resulted in the cycles per burst range of 50, 500 and 50000. Consequently it is hypothesised that there may be a critical number of cycles per burst below which there may be an effect. For SV the higher PRFs lead to lower recorded cavitation responses. This could be due to the bubble being destroyed in the side lobes; higher PRFs and shorter

burst lengths would cause the SV to never fully replenish between bursts[326]. This may have the opposite effect for the CNP which are primed in the side lobes and consequently have a greater cavitation response with a higher PRF. Cups remain unaffected by PRF as they are neither destroyed nor enhanced by pre-application of ultrasound. At a driving frequency of 1.6 MHz the ultrasound is much less destructive to SV and does not have the same priming effect on CNP. As a consequence PRF did not appear to have an influence at these frequencies.

Driving frequency greatly influenced the cavitation threshold of particles. A lower frequency causes the expansion phase of a gas bubble to be longer thus leading to larger gas bubbles and, consequently, greater inertia of the surrounding liquid. This causes the cavitation threshold to be lower[327,328]. The morphology of CNP causes substantial variation in the size of bubbles on their surfaces. It is hypothesised that each bubble will have different cavitation threshold but at 0.5 MHz the extended rarefactional pressure phase of the ultrasound cycle would lead to an increased likelihood of bubbles coalescing to create larger gas bubbles with lower cavitation thresholds. As a consequence CNP would cavitate with much greater energy when treated with a driving frequency of 0.5 MHz rather than 1.6 MHz. Meanwhile cups, due to their uniform size, have a fixed cavitation threshold at the individual frequencies[275]. For nearly all cases a driving frequency of 0.5 MHz and peak rarefactional pressure of 3 MPa caused greater cavitational energy to be recorded by the PCD than ultrasound of a driving frequency of 1.6 MHz and peak rarefactional pressure of 4 MPa with the exception of the polymer cups (Figure 5-6).

CNP caused equivalent concentrations of antibody to extravasate out of the flow channel and into the agar as SV at 0.5 MHz and 3 MPa (Figure 5-8). Whereas at a driving frequency of 1.6 MHz and peak rarefactional pressure of 4 MPa 300 nm core cups caused significantly more extravasation than SV (Figure 5-10). Thus it has been shown that the solid particles are potential alternatives for SV for enhanced delivery of therapeutic agents.

Despite the phantom acting as a good model to measure cavitation-induced therapeutic delivery it does not take into account the practical aspects of selecting ultrasound parameters. For example, at a higher frequency there will be greater attenuation of the ultrasound wave within the body that will limit penetration, cause heating effects and limit the treated volume.

5.5 Conclusions

This chapter reports:

- Both CNP and cups are capable of instigating sustained ultrasound cavitation for over 10 minutes in comparison to SV, which is destroyed within 100 seconds.
- Incubation of the cavitation nuclei with human serum showed that protein adsorption did not alter the ultrasound responsiveness of polymer cups but the ultrasound responsiveness of SV and CNP was significantly reduced.
- A range of ultrasound parameters were assessed to identify the optimum conditions for cavitation and delivery:

  At a driving frequency of 0.5 MHz:

  - increasing PRF improved the ultrasound responsiveness of CNP, reduced the responsiveness of SV and did not influence cups.
  - 300 nm core cups and CNP have equivalent cavitation energies
  - CNP, polymer cups and SV were all capable of causing visible extravasation of a model therapeutic out of the flow channel

  At a driving frequency of 1.6 MHz

  - PRF does not impact upon either cavitation response nor resultant therapeutic delivery
  - 300 nm core cups are significantly more ultrasound-responsive than either CNP or SV and are also capable of causing significantly improved delivery of a therapeutic.
  - There is a critical number of ultrasound cycles per burst required to observe extravasation of a therapeutic out of a flow channel

  - No optimum treatment time was observed but by increasing exposure time therapeutic delivery was also increased
  - 300 nm core cups also caused cell membranes to permeabilise at the peak rarefactional pressures used to deliver the therapeutic although it uncertain whether this pertains to cell death or the temporal sonoporation effect.

- 300 nm core cups were the only cavitation nuclei used that were able to reproducibly have a strong cavitational response to ultrasound and enhance the delivery of a model drug at both 0.5 MHz and 1.6 MHz driving frequency .

6 *In vivo* assessment of submicron cavitation nuclei enhancing drug delivery

6.1 Introduction

Chapter 5 demonstrated the huge parameter space that requires investigation when trying to identify the optimal ultrasound exposure conditions needed for a particular cavitation agent. It is ethically and legally unsound to perform such wide-ranging studies in animals and so the in vitro phantom models used in Chapter 5 are an essential step in lessening the scale of subsequent animal studies. Experiments in Chapter 5 demonstrated that for carbon nanoparticles (CNP) and cups optimised ultrasound exposure parameters could be identified which could drive an antibody into tissue mimicking phantoms.

The knowledge gained from these phantoms can be further used to plan and execute in vivo studies. Notably, however, whilst fluorescence tracking offered a simple, quantifiable metric of delivery in the phantom model its utility in in vivo studies is much reduced due to sensitivity and signal to noise issues.

The ability of oncolytic viruses to produce transgenes and to self-amplify from within tumours makes them an attractive anti-cancer agent and also means they are an extremely useful tool in studying cavitation enhanced delivery[245,329].

Chapter 1 briefly outlined how viruses can be used as cancer therapeutics and the genetic engineering that has been performed on viruses to improve their specificity and cytotoxicity. In choosing which oncolytic virus to apply a range of parameters must be considered: immunogenicity, efficiency of infection, genome size, safety, ease of manipulation and ability to manufacture on a large scale[330,331]. Table 6-1 provides the genome size and approximate physical dimensions of some oncolytic viruses. For the reasons discussed in Chapter 1, as the size of the viruses being used increases so too does the does the scale of the tumour delivery problem, however, the genome size will allow greater flexibility to target and arm the virus[332].

Table 6-1: Genome size and physical size of oncolytic viruses

Virus	Genome size (kb)	Diameter (nm)	Ref.
Adenovirus	36-38	80-100	[40,333]
Herpes simplex virus-1	120-200	190 nm	[40,333]
Vaccinia virus	130-280	200 x 350 nm	[40,333]
Lentivirus	10	100-120	[334,335]
Seneca valley virus	7.3	27-30	[336]
Measles virus and Newcastle disease virus (paramxyoviridae family)	16-20	150-300 nm	[40,333]
Reovirus	22-27	75 nm	[40,333]
Poliovirus	7.2-8.4	30 nm	[40,333]
Vesicular stomatitis virus	13-16	60 x 180 nm	[40,333]

To date all previous studies demonstrating cavitation enhanced delivery of oncolytic viruses have utilised SonoVue (SV) bubbles, Such micron-sized cavitation agents are potentially sub-optimal (see Chapter 5) due to their inability to extravasate and sustain cavitation activity potentially hindering clinical translation[337,338]. Despite the limitations, Carlisle el al. demonstrated that cavitation was capable of improving the delivery of ~120 nm oncolytic adenovirus (Ad) with SV *in vivo*[191]. Insonation of the tumours increased the distance from the vasculature of transfected cells from less than 50 μm to more than 200 μm and average survival of the mice was extended. However, the delivery was not completely effective; large hypoxic regions of the tumour remained untreated and, despite the vastly extended survival times, there were no complete responses.

Hence, because oncolytic viruses represent a powerful new class of agents and because they can provide excellent delivery and distribution data they were chosen in preference to antibodies for the studies performed in Chapter 6. The virus to be used in these studies was supplied by Philippe Erbs of Transgene SA, France. To produce this vaccinia virus vector (denote VV from here on) the thymidine kinase gene and the ribonucleotide reductase gene were both deleted (TK-/RR-) from the Copenhagen strain of vaccinia virus. This attenuates the virus in non-dividing cells and improves its biodistribution[339,340]. In addition the virus had been modified to produce luciferase, an enzyme that catalyses a reaction with luciferin to produce bioluminescence. Consequently the activity of the virus could be quantified by injecting luciferin into mice and imaging the luminescence of the tumour. This enables virus infectivity to be monitored throughout a study without having to

cull mice at intermediate time points. This substantially reduces the numbers of mice needed for these studies.

The aim of this chapter is to determine whether sub-micron cavitation nuclei are capable of enhancing the delivery of a virus or whether the initial size of the SV bubble is critical to the mechanical forces required to propel large therapeutics out of the vasculature. Studies in Chapter 5 had demonstrated a substantial loss of cavitation activity upon mixing of CNP with plasma and so in vivo studies were performed with cups only. Notably, in contrast to CNP, cups are also amenable to labelling (See Chapter 2), a feature which permitted pharmacokinetic (PK) and biodistribution studies to be performed[274]. In addition in vitro experiments in Chapter 5 have demonstrated that cups can instigate cavitation to aid delivery of a therapeutic agent in response to ultrasound of either 0.5 MHz or 1.6 MHz driving frequency. This increases the likelihood of identifying parameters that can work in vivo.

This chapter will study the ability of sub-micron cavitation nuclei to deliver vaccinia virus (VV) into tumours. VV is a double stranded DNA virus which replicates in the cytoplasm rather than the nucleus of cells[341]. It is an attractive choice for cancer therapy for a number of reasons: (1) its use as a vaccine means it has been demonstrated to be safe - studies in 1968 showed 1 per 1,000,000 vaccinations resulted in death and 1 per 1,000 - 20,000 resulted in serious adverse events[342]. Furthermore, due to its extensive use vaccinia immune globulin has been developed and manufactured to manage adverse effects[343] (2) its large genome size means that genetic modifications to improve specificity and toxicity are not as restrictive as in other viruses (3) it

encodes its own transcription enzymes enabling it to replicate in the cytoplasm increasing the rate of lysis and spread and (4) it creates 2 virion forms: intracellular mature virus (IMV) and extracellular enveloped virus (EEV). IMV are immunogenic and are released as the cell lyses while EEV are IMV particles enveloped by lipids present in the host cell and are released before cell death. This means that the EEV particles are capable of traversing the blood stream without stimulating a strong immune response and being cleared[344]; clinical trials in which VV has been administered intratumourally have shown VV genome copies in non-treated metastases, signifying the ability of the virus to enter the blood stream[345]. However, once replicating within the target site they are still capable of eliciting immune-mediated cell death and vascular collapse[346].

With such benefits it is perhaps surprising that just 13 of the 300 ongoing, open clinical trials involving oncolytic viruses use VV as a vector (approximately 4%)[347]. Breitbach et al. suggested that the PK and tumoural penetration of VV was not restrictive[348]. However, a subsequent Phase I trial assessing i.v. administration in patients with colorectal cancer did not achieve any partial or complete responses[349]. It would appear that further development of VV vectors will focus on i.t. administration. Due to its many favourable features it may be expected that if systemic delivery of the virus were to be improved there would be substantial improvement in its overall anti-cancer efficacy and, therefore, more widespread clinical use would follow.

Testing the delivery of VV *in vivo* requires considered choice of the appropriate model[350]: Use of a xenograft model would allow VV to target

cancer cells similar to those which would be treated in humans. However, the immunocompromised mice required will not elicit the same rapid clearance of VV as would be expected in patients nor have the same immune response to cancer cells once infected. Due to the attenuation of VV in murine cancer cells the xenograft model was chosen[351].

As a preliminary study it was decided to test whether cavitation caused by a sub-micron particle (cups) could cause the enhanced delivery of VV in 2 human cell lines: SKOV-3, an ovarian adenocarcinoma cell line and HEPG2, a liver hepatocellular carcinoma.

Cups were i.v. co-injected with VV into mice and the tumours were exposed to ultrasound using a single-element high intensity focused ultrasound (HIFU) transducer. Passive acoustic mapping (PAM), as briefly described in Chapter 1, was then used to identify both the location and the intensity of cavitation by overlaying a 2-dimensional cavitation map over a B-mode image in real time[352]. The aim of this study was not just to enhance the delivery of VV but to also gain an insight as to how both the intensity of cavitation and its location impacts upon drug delivery.

6.2 Chapter Aims

The aim of this chapter is to:

- Identify any *in vivo* biocompatibility concerns caused by either the cups or the VV.
- Enhance the delivery of luciferase expressing VV using the nano cups formulated in Chapter 4.
- Examine whether ultrasound mediated delivery of VV provides a therapeutic benefit.
- Ascertain whether cavitation can be correlated with enhanced delivery using PAM.

6.3 Methods and results

6.3.1 Setup and PAM measurements

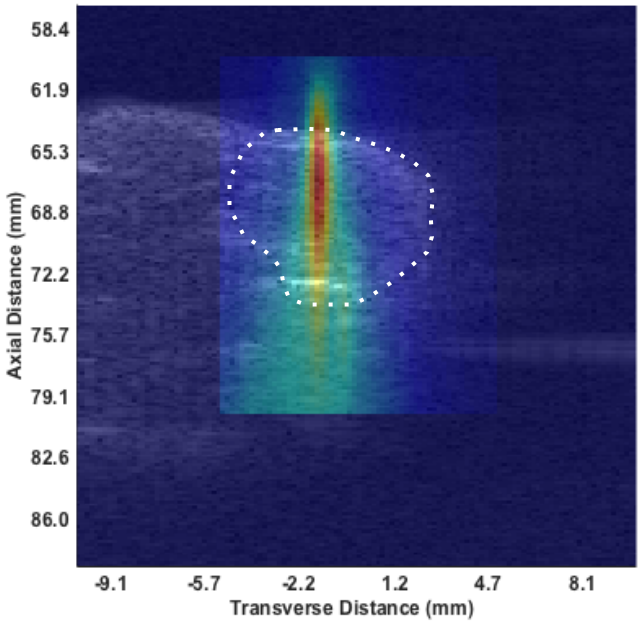

Figure 6-1: Example PAM image of a mouse injected with cavitation nuclei and treated with ultrasound
Mice implanted with SKOV-3 tumours were injected with 25 mg/mL cups and insonated with ultrasound of 0.5 MHz driving frequency, 1.5 MPa peak rarefactional pressure, 5% duty cycle and 0.5 Hz PRF. PAM images of sources of broadband acoustic emissions associated with inertial cavitation were created in real-time and overlayed onto a B-mode image. Figure shows a single frame of a reconstructed PAM image.

Mice were implanted with either HEPG2 or SKOV-3 cells. The concentration of the cups was increased from 5.4 mg/ml, as used in the previous chapter, to 25 mg/mL. This was due to better filtration of the cups allowing higher concentrations of monodisperse suspension to be formulated. Once tumours reached approximately 100 mm^3 they were treated with 25 mg/mL cups in 5% glucose, VV whilst tumours were insonated. A 0.5 MHz driving frequency was used as opposed to a 1.6 MHz driving frequency due to it having a larger focal volume, which means treatment of a whole tumour would require fewer treatment steps and a shorter duration. In addition, the pressure signal at

lower frequencies is less attenuated by the body, which will both permit treatment throughout the body and reduce heating effects. Figure 6-1 provides a sample image of PAM overlaying a B-mode image produced on the computer as treatment proceeded with a 0.5 MHz transducer.

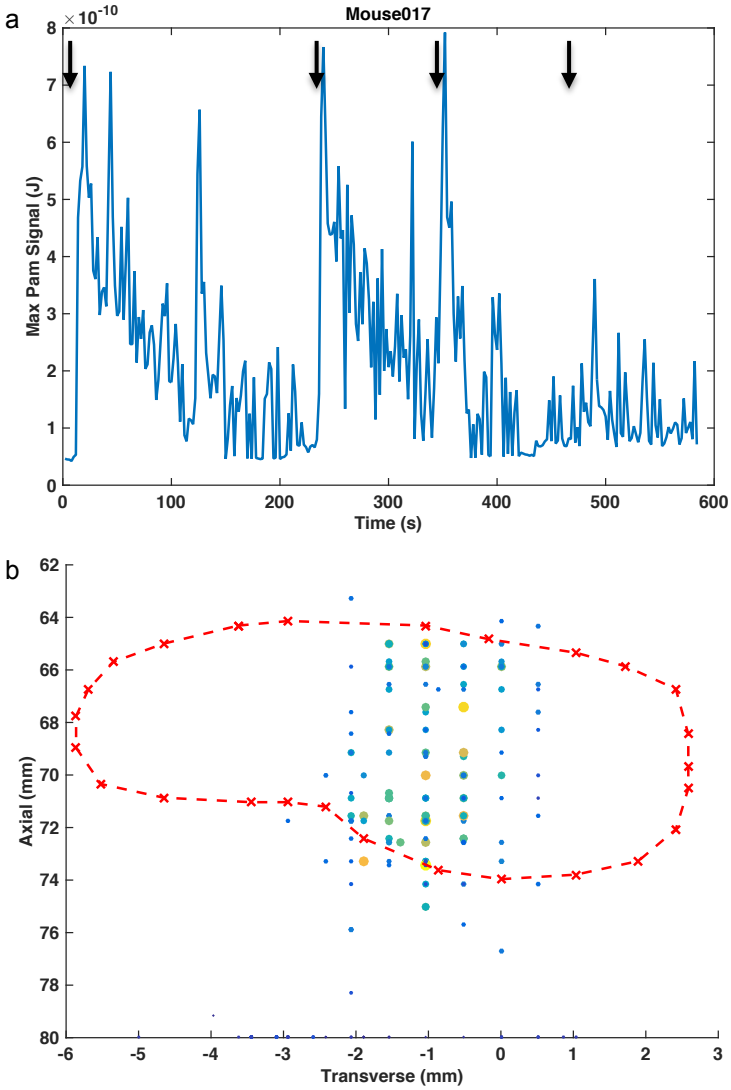

Figure 6-2: Example of how PAM data can be quantified after treatment
A mouse with a HEPG2 tumour was injected with cups and insonated with ultrasound of driving frequency 0.5 MHz, peak rarefactional pressure 1.5 MPa, 5% duty cycle and 0.5 Hz PRF. Data from the PAM was processed using code written by Christian Coviello and Calum Crake. (a) Peak cavitation power signals over the duration of the treatment (arrows show the times at which the mouse was dosed with cups) and (b) map of the location, intensity and frequency of the cavitation events in relation to the location of the tumour (marked by red dotted line). Points indicate the location of cavitation events: the size of the point indicates the frequency of cavitation while the colour from blue to orange indicates low to high peak power of cavitation at that site.

MATLAB code written by Dr. Christian Coviello and Calum Crake was used to identify the power of peak cavitation events over the duration of the treatment (Figure 6-2 a) and identify the location in relation to the tumour (Figure 6-2 b). This shows the utility of such passive acoustic mapping (PAM) and highlights that if cavitation can be directly related to enhanced extravasation it would enable the delivery of a therapeutic to be mapped. Such feedback on the success of delivery is not currently clinically available using a low cost, clinically available modality[353].

6.3.2 Assessment of tolerability and off-target infection

Mice were treated with a total dose of either $1x10^5$ pfu VV or $1x10^6$ pfu VV in a solution of 5% glucose with 25 mg/mL cups. Initial peak rarefactional pressure was set at 3 MPa, however, bruising was immediately evident in the mouse treated at these conditions. This could be the in vivo impact of the change in cell viability caused by equivalent amounts of cavitation observed in vitro (Figure 5-4). In response a pressure of 1.5 MPa was determined to be the lowest pressure that caused continuous cavitation in the presence of cups but did not result in broadband emissions in the absence of cups.

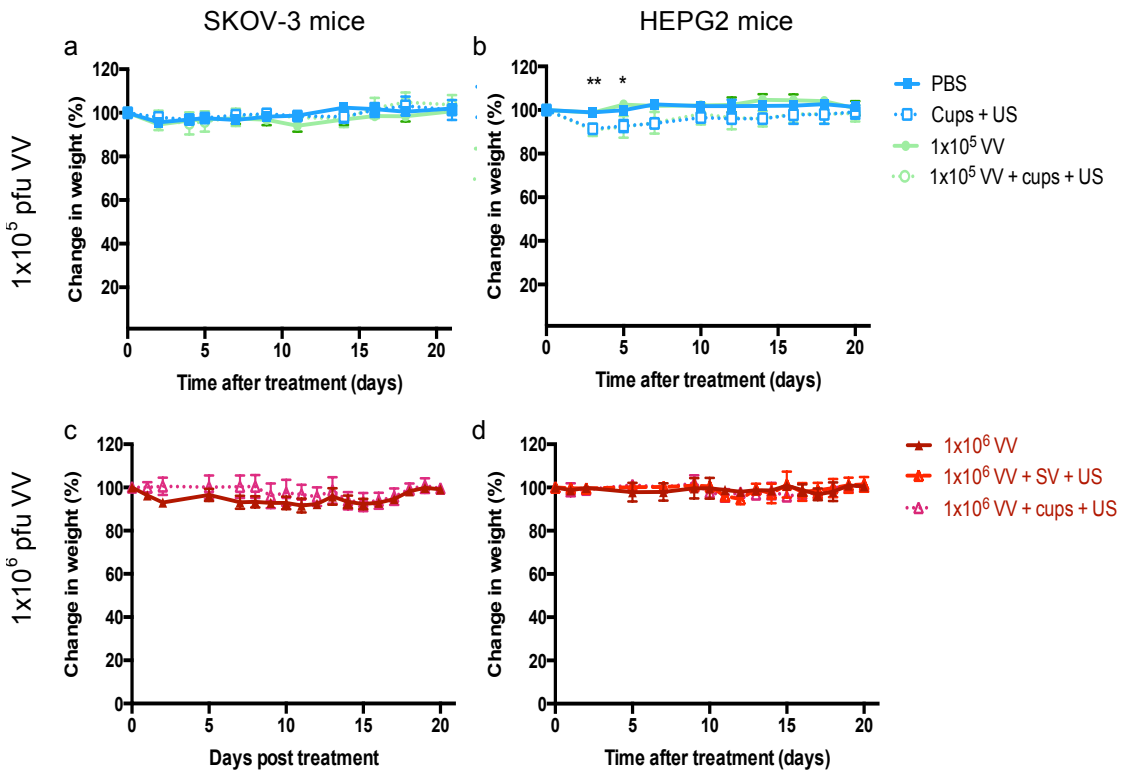

Figure 6-3: Change in weight of mice treated with 1x10^5 pfu and 1x10^6 pfu VV, cups and ultrasound
Mice were implanted with SKOV-3 or HEPG2 cells. Once the tumour had reached a size of approximately 100 mm^3 mice were i.v. injected with VV and cups or used as controls. Depending on the group tumours were insonated with ultrasound (US) of driving frequency 0.5 MHz, peak rarefactional pressure 1.5 MPa, duty cycle 5% and PRF 0.5 Hz or not (a) SKOV-3 mice injected with 1x10^5 pfu VV, (b) HEPG2 mice injected with 1x10^5 pfu VV, (c) SKOV-3 mice injected with 1x10^6 pfu VV and (d) HEPG2 mice injected with 1x10^6 pfu VV. Error bars indicate standard deviation of n=4 mice. A one-way ANOVA with Bonferroni pair-wise comparisons showed there to be a significant difference in the weights of HEPG-2 after treatment between the PBS control and 1x10^5 pfu VV + cups + US groups. * = P<0.05, ** = P<0.0005. There was no significant difference in the weights of mice implanted with SKOV-3 tumours or in the mice implanted with HEPG2 tumours and treated with 1x10^6 pfu VV.

The weights of the mice implanted with SKOV-3 or HEPG2 tumours showed no substantial or significant extended changes compared to controls (Figure 6-3), indicating minimal toxicity. The loss of weight in HPEG2 mice treated with VV, cups and ultrasound was transient and within the limits stipulated on the project licence with work was carried out under.

Capture by and infection of the liver is a well-recognised route for virus clearance in murine models[354]. Hepatic capture of virus typically involves 2 mechanisms 1) Kupffer cell mediated capture and elimination and, when this

is saturated 2) hepatocyte infection. Dose therefore plays a crucial role in the circulation, deposition and toxicity of viral vectors[355].

The effect of increasing the dose of VV in terms of liver clearance and potential tolerability concerns was made evident by luciferase expression in the mice 1 day after treatment. Figure 6-4 a shows that mice treated with $1x10^5$ pfu VV had luciferase liver expression below the sensitivity of the IVIS but a dose of $1x10^6$ pfu VV led to substantial amounts of luciferase expression in the liver (Figure 6-4 b). This suggests that by injecting $1x10^6$ pfu VV the Kupffer cells were saturated and the VV could infect hepatocytes. This may have implications for the acute toxicity of VV constructs, especially those used to deliver cytotoxic transgenes[346]. However, the cessation of liver luciferase expression at subsequent time points indicates that the engineering of VV to restrict replication to cancer cells is effective[339].

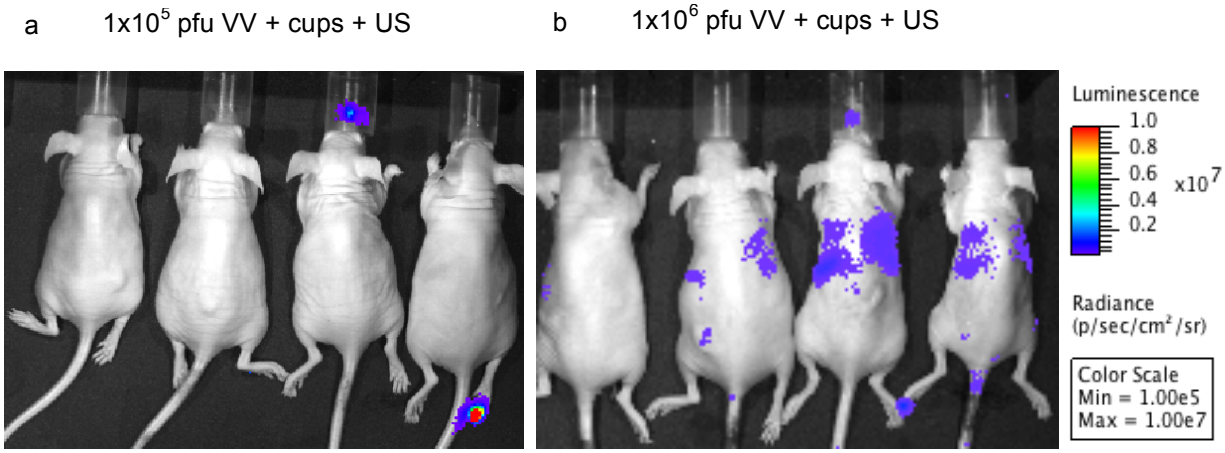

Figure 6-4: Luciferase expression in the livers of mice 24 hours after i.v. injected with $1x10^5$ or $1x10^6$ pfu VV
Bioluminescence of SKOV-3 mice 1 day after treatment with cups, ultrasound and either $1x10^5$ or $1x10^6$ pfu VV. Bioluminescence imaging of the mice was performed 5 minutes after an i.p injection of luciferin. (a) $1x10^5$ pfu VV treatment group and (b) $1x10^6$ pfu VV treatment group. Luciferase expression in the liver was too low to be recorded by the IVIS system at the $1x10^5$ pfu VV injection dose despite substantial VV activity being recorded from 5 days onward in the tumours of all mice.

The most obvious sign of toxicity was ulceration in SKOV-3 mice that had been i.v. injected with $1x10^6$ pfu VV and cavitation nuclei then treated with ultrasound. 5 out of the 8 mice treated in this way showed a skin lesion; the worst example of this ulceration caused 1 mouse to be culled 10 days into the treatment, in line with the licence under which this work was performed. This phenomenon did not occur in HEPG2 mice nor in mice with lower VV doses. This effect may represent an enhanced potency of virus replication in these tumours.

6.3.3 Cavitation-mediated delivery in mice treated with $1x10^5$ pfu VV, cups and ultrasound

Mice were implanted with either HEPG2 or SKOV-3 tumours. Once the tumours reached approximately $100mm^3$ the mice were treated with $1x10^5$ pfu VV and 25 mg/mL cups with or without ultrasound treatment. To assess whether ultrasound treatment alone impacts upon tumour growth control groups of PBS with or without ultrasound treatment were also included. 25 µL injections were administered through the tail vein every 2 minutes with the total treatment time lasting 10 minutes. Ultrasound parameters of 0.5 MHz driving frequency, 1.5 MPa peak rarefactional pressure, 5% duty cycle and 0.5 Hz PRF were used.

Bioluminescence created by luciferase expression was used as a metric to identify VV activity in the tumours as described in Chapter 2 and shown in Figure 6-4. Luciferase was measured 1, 2, 5, 10 and 20 days after treatment at which point the mice were culled. Figure 6-5 displays both the raw images

and the average luminescence of the tumours over time in both HEPG2 and SKOV-3 tumour models when treated with $1x10^5$ pfu VV and 25 mg/mL cups with or without ultrasound treatment.

In the SKOV-3 mice all ultrasound treated tumours showed strong luciferase expression from 2 days onwards while without ultrasound 2 of the mice never showed luciferase expression and the remaining 2 showed minimal expression (Figure 6-5 a). Without ultrasound treatment the luminescence peaked at day 5 (2.0 +/- 0.8 $x10^5$ photons/cm^2/s) while with ultrasound treatment the luminescence of the tumours also peaked at day 5 but with a bioluminescence of 2.2 +/- 1.6 $x10^8$ photons/cm^2/s (Figure 6-5 b).

Luciferase expression was not observed in any of the HEPG2 tumour bearing mice that received VV and cups but no ultrasound, while all 4 mice treated with VV, cups and ultrasound showed strong luciferase expression (Figure 6-5 c). Notably, VV encoded luciferase expression in the tumour did not diminish during the 20 days after treatment but remained at a plateau of $3x10^8$ photons/cm^2/s from 5 days after treatment until the 20 day endpoint (Figure 6-5 d), whereas in the SKOV-3 mice there was a gradual decline after 5 days. This may reflect differences in the amount of tumour cells remaining to provide sites of infection.

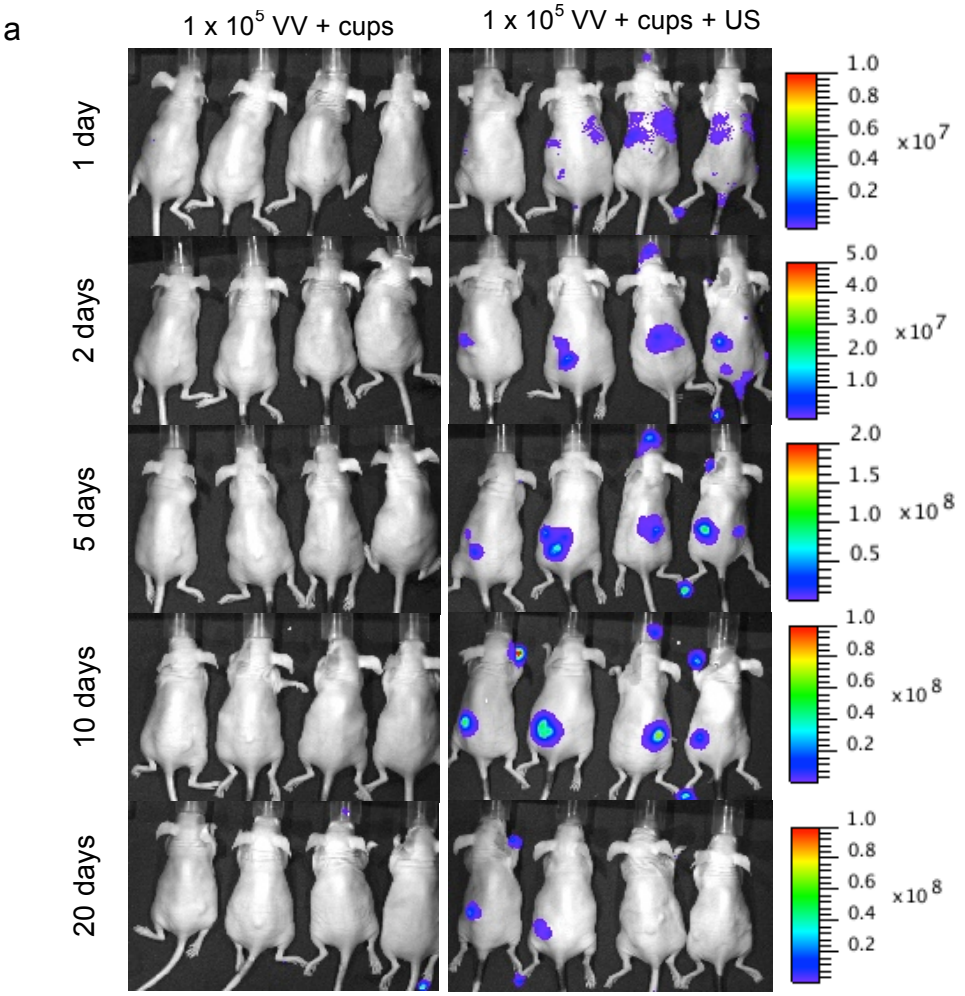
a
1 x 10^5 VV + cups
1 x 10^5 VV + cups + US
1 day
2 days
5 days
10 days
20 days
1.0
0.8
0.6
0.4
0.2
x10^7
5.0
4.0
3.0
2.0
1.0
x10^7
2.0
1.5
1.0
0.5
x10^8
1.0
0.8
0.6
0.4
0.2
x10^8
1.0
0.8
0.6
0.4
0.2
x10^8

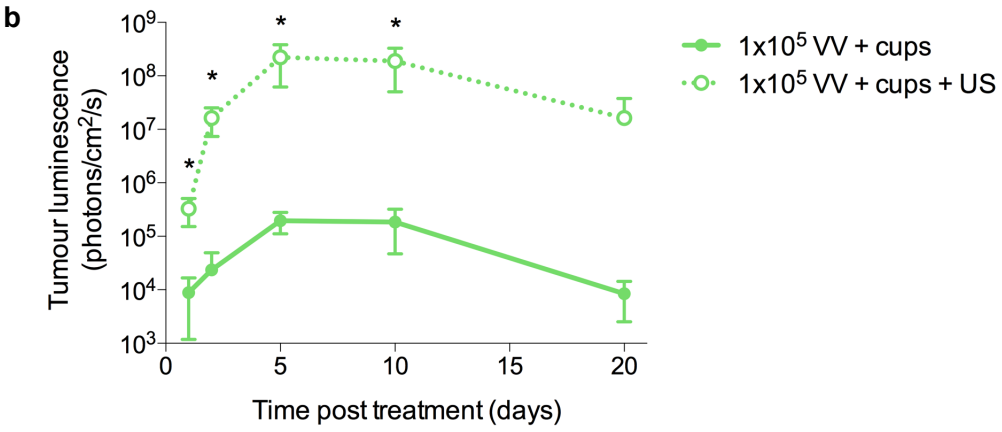
b
Tumour luminescence (photons/cm²/s)
10^9
10^8
10^7
10^6
10^5
10^4
10^3
*
*
*
*
0
5
10
15
20
Time post treatment (days)
1x10^5 VV + cups
1x10^5 VV + cups + US

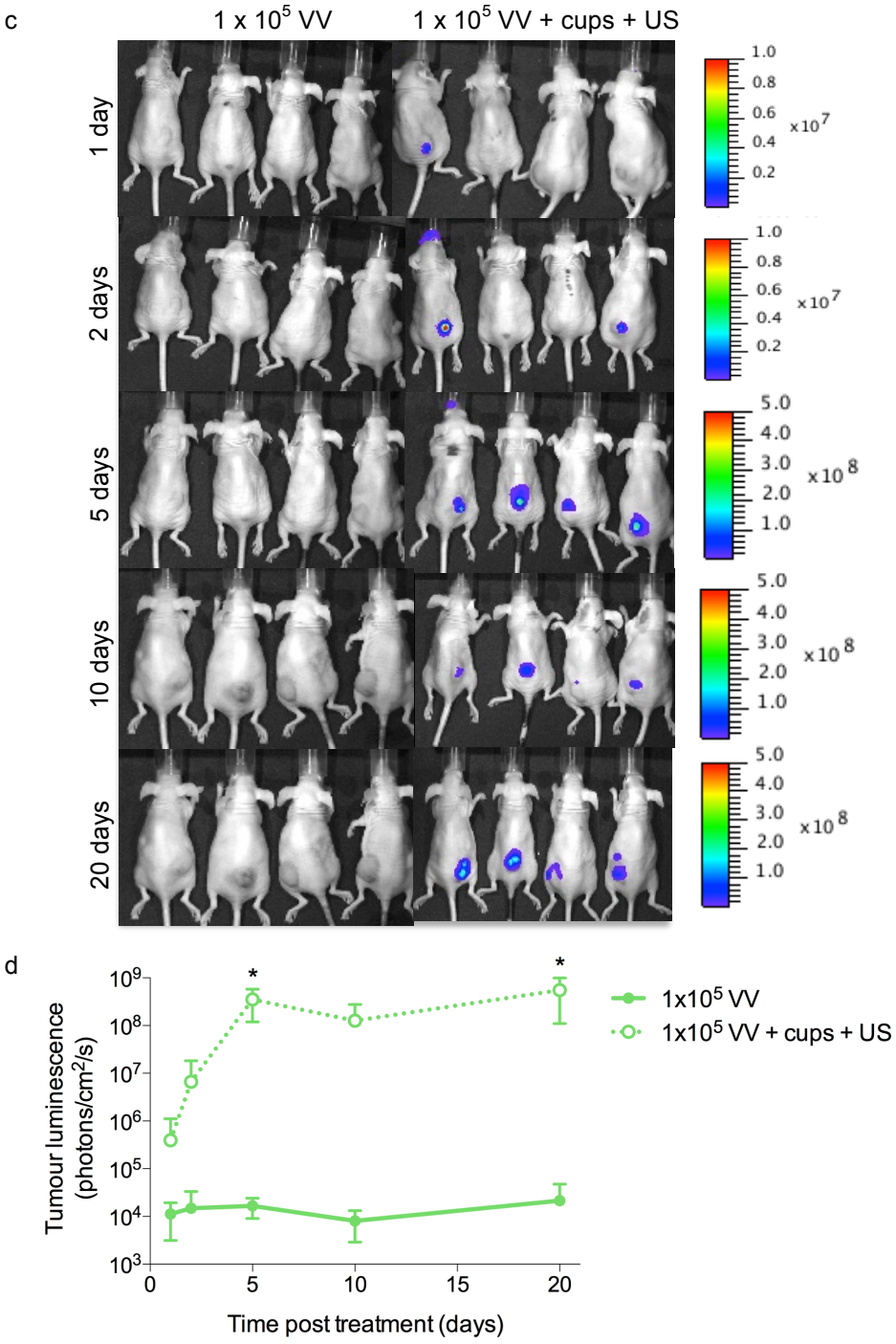

Figure 6-5: Measurements of luciferase expressions caused by the replication of VV after i.v. injection of mice with 1x10^{5}pfu VV

Mice were treated with VV and cups with or without ultrasound treatment. Bioluminescence imaging of the mice was performed 5 minutes after an i.p injection of luciferin to assess the activity of the VV by luciferase expression (a) raw luminescence images of mice implanted with SKOV-3 mice over time (b) effect of cups and ultrasound treatment on the mean luminescence of SKOV-3 tumours (c) raw luminescence images of mice implanted with HEPG-2 mice over time (d) effect of cups and ultrasound treatment on the mean luminescence of HEPG-2 tumours. Error bars indicate standard deviation of n=4 mice. T-test between groups showed cups and ultrasound significantly increased transgene expression of luciferase. * = P<0.05.

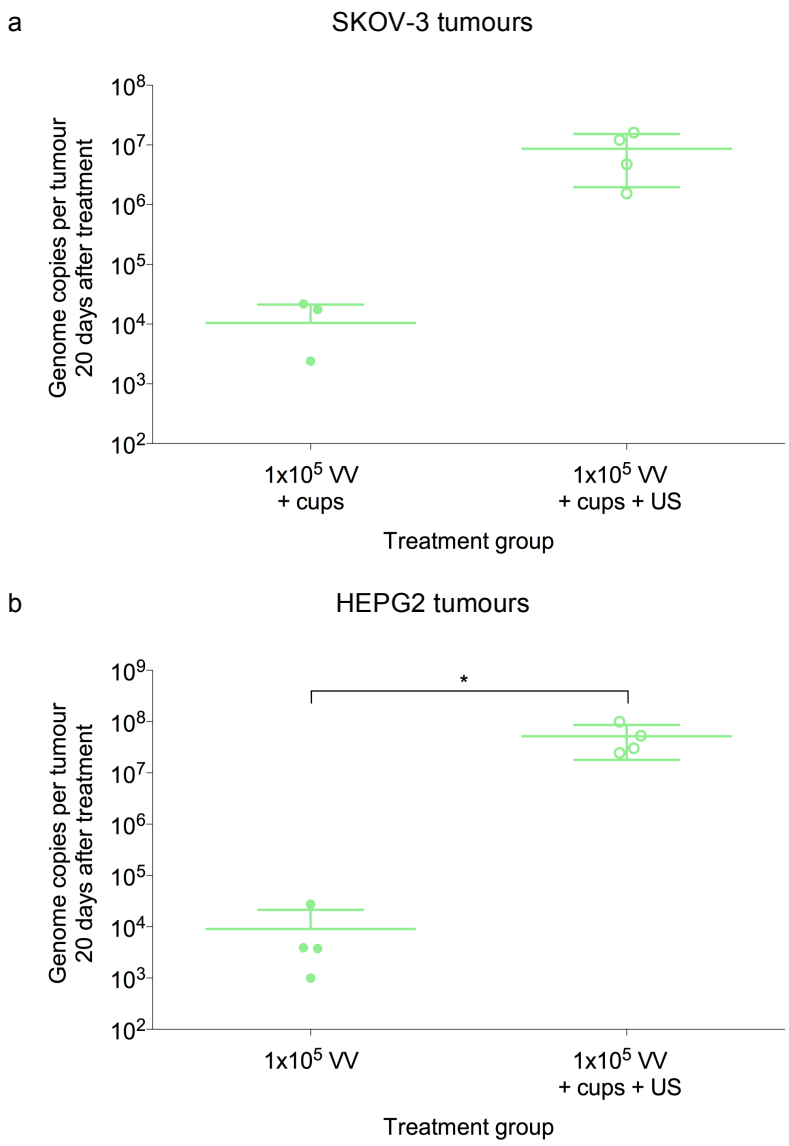

Figure 6-6: Genome copies of VV in the tumours of mice treated with 1x10^5 pfu VV with or without cups and ultrasound
Tumours were harvested 20 days (HEPG2 mice) or 21 days (SKOV-3 mice) after treatment and the DNA present in the cells was purified. qPCR was used to measure the amount of VV present in (a) SKOV-3 tumours and (b) HEPG-2 tumours. A two-way student t-test showed that there was significantly more VV copies were recovered from the tumours of mice that had been treated with VV, cups and ultrasound compared to control groups. * = P<0.05.

Figure 6-6 shows the number of VV genome copies recovered from tumours, as quantified using qPCR 20 days after treatment. This data was in accordance with the IVIS data. Figure 6-6 a shows that using cups and ultrasound to deliver VV in SKOV-3 mice, led to the recovery of 8.6 +/- 6.6 x10^6 VV copies in tumours 20 days after treatment, a substantial (over 750-

fold) increase compared to the number of copies recovered from the tumours of mice not treated with ultrasound (1.1 +/- 1.1 $x10^4$). In HEPG2 mice the average number of genome copies recovered from the tumours of mice treated with $1x10^5$ pfu VV without ultrasound treatment was equivalent to background measurements of VV (0.9 +/- 1.2 $x10^4$) while tumours that had been treated with ultrasound contained over 5,000-fold more VV genome copies in the tumour (5.2 +/- 3.4 $x10^7$, $p < 0.05$). Demers et al. suggested that to match i.t. injection 1,000-fold greater levels of virus had to be injected i.v., this data indicates that cups and ultrasound treatment may achieve the uplift required without necessitating such a dramatic increase in dose[356].

This study with a non-armed reporter VV was established to investigate delivery as such with just 4 mice per group it was not powered sufficiently to detect changes in tumour size or overall survival. Figure 6-7 shows that on average the size of SKOV-3 tumours in the control groups did not even double over the next 20 days, and as a consequence a differentiation in tumour size caused by the different treatments was unlikely. However, HEPG2 tumours grew much more aggressively and by 20 days tumours of mice treated with PBS had a volume approximately 9 times greater than their initial size. As may be predicted for such a small group sizes there was still not sufficient enough of an effect to demonstrate a difference in tumour sizes between treatment groups.

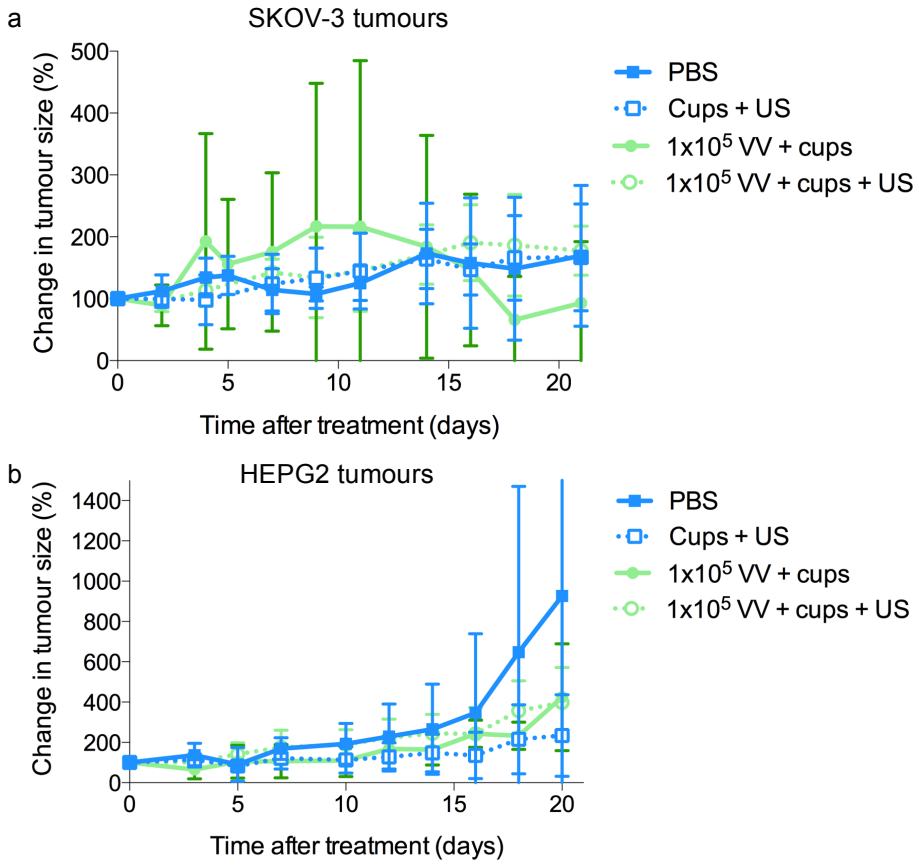

Figure 6-7: The impact of 1x10^5 VV injections and cups and ultrasound treatment on the growth of tumours
The size of the tumours of each of the treatment groups was measured every 2-3 days over either 20 or 21 days. The change in size was recorded as a percentage of their initial size (a) SKOV-3 tumours and (b) HEPG2 tumours. Error bars indicate standard deviation of n=4 mice. A one-way ANOVA with Bonferroni pair-wise comparison showed there was not a significant difference in tumour size between any of the groups (P>0.05).

A crucial aspect of the cavitation technology described here is that the cavitation events recorded during the treatment may predict the subsequent activity of the delivered therapy. Figure 6-8 shows there was no apparent relationship between the intensity of luciferase expression and cavitation response in the tumours (defined as maximum PAM signal over the duration of the treatment). However, greater overall cavitation energy recorded due to treatment may cause the time of maximum luciferase expression to be delayed. This may reflect that VV was more evenly distributed throughout the

tumour and so had a slower lag-phase before a sufficiently large infectious plaque could amplify-up to reach the detection limit[357].

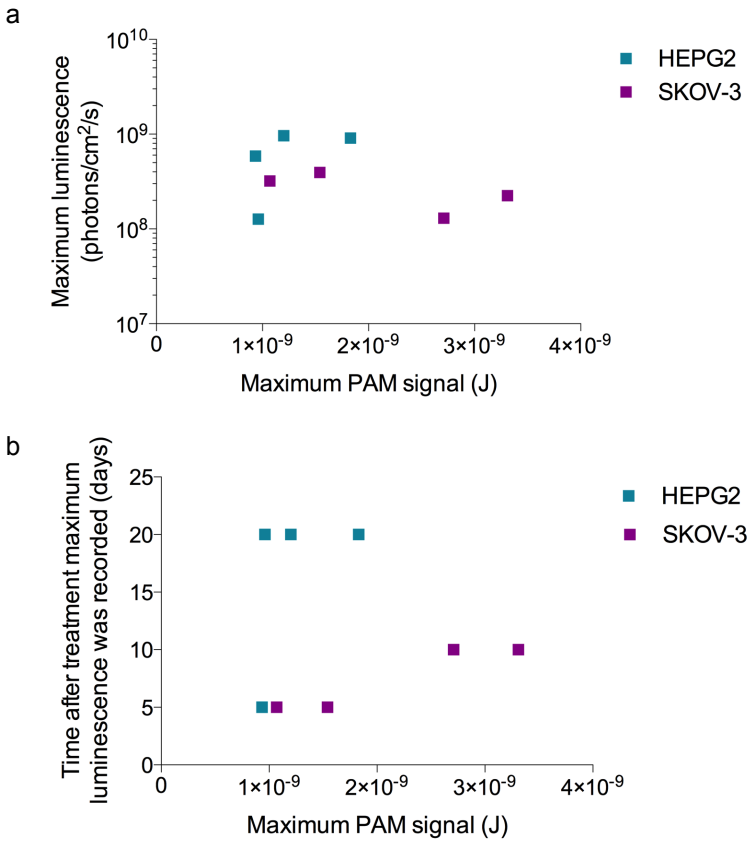

Figure 6-8: Testing the relationship between cavitation energy and luciferase expression in the tumours of mice treated with 1x10^5 VV, cups and ultrasound.
Mice implanted with either HEPG2 or SKOV-3 tumours were injected with 1x10^5 pfu luciferase expressing VV and cups with the tumours exposed to ultrasound. Cavitation was recorded by PAM and the cavitation energy calculated. Mice were injected with luciferin and their luminescence measured using an IVIS system after 1 day, 2 days, 5 days, 10 days and 20 days. (a) Comparison between cavitation energy and maximum luminescence recorded and (b) day of IVIS measurement that the maximum luminescence was recorded.

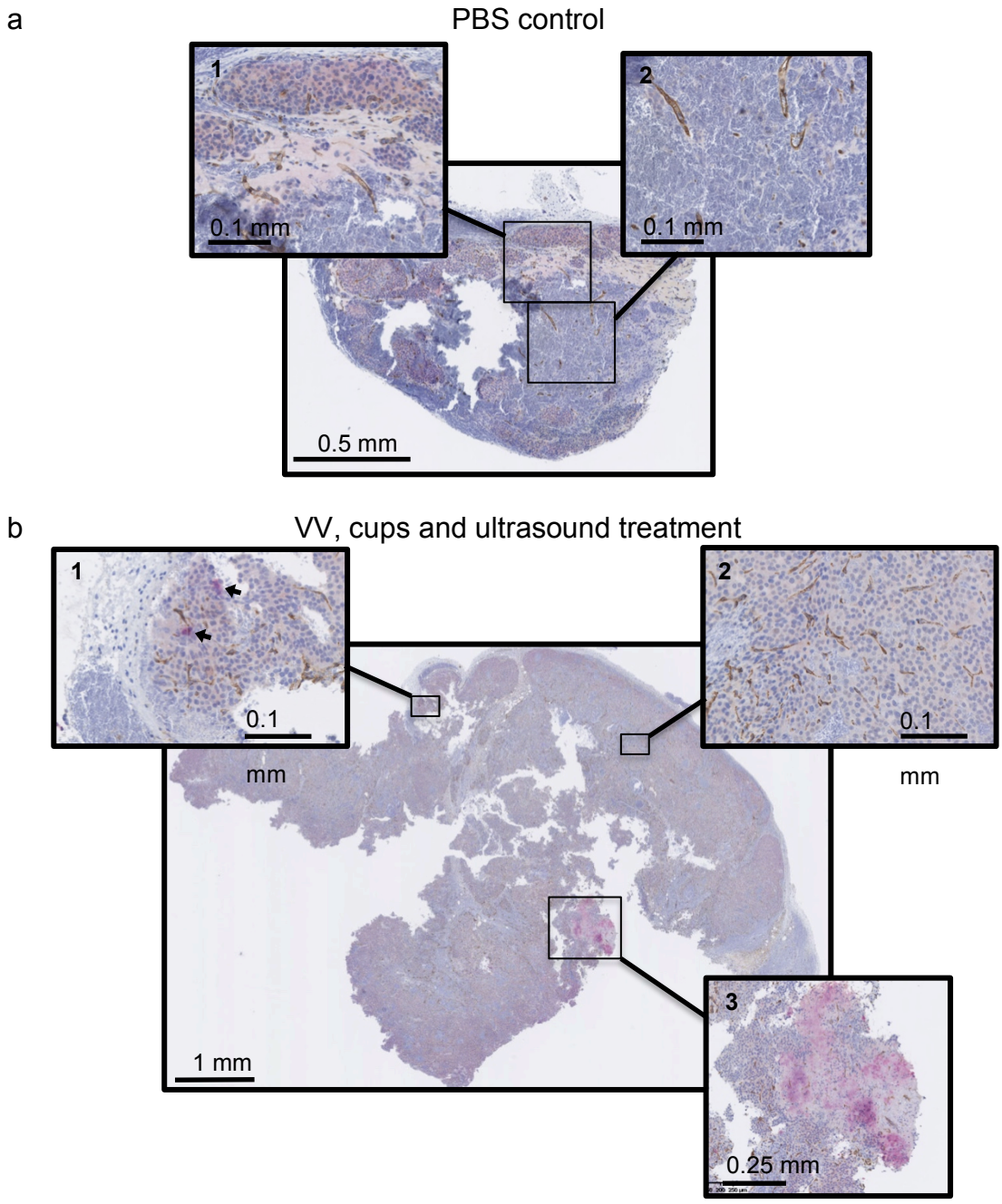

Figure 6-9: Immunohistochemical staining of a tumour treated with 1x10^5 pfu VV, cups and ultrasound
20 days after treatment the tumours of 2 of the HEPG2 tumour bearing mice were fixed in formalin. They were processed by Histologix Ltd to be paraffin embedded, sectioned and stained for vasculature (targeting CD31, brown), VV (pink) and cells (blue). Mice had been treated with (a) PBS to act as a negative control for the VV staining and (b) VV, cups and ultrasound.

Immunohistochemistry was performed on the tumours of mice 20 days after treatment with either PBS or VV, cups and ultrasound (Figure 6-9). A PBS control tumour was used to confirm that the VV staining procedure was

specific. A CD31 antibody was used to identify blood vessels within the tumour and assess whether the distribution of VV was localised with the vasculature. Analysis of the VV, cups and ultrasound treated tumour revealed that a large area of the tumour had been infected with the virus (see intense pink) leading to apparent cell death (Figure 6-9 b, panel 3). At this 20 day time point it is hard to assess whether such widely distributed infection at this site is the result of better initial delivery and seeding. It is evident that large areas of the tumour remained uninfected. Notably, some regions of the tumour close to the vasculature revealed small but intense VV staining, which may suggest secondary infections (marked with arrows in Figure 6-9 b, panel 1).

6.3.4 Cavitation-mediated delivery in mice treated with $1x10^6$ pfu VV, cups and ultrasound

To further probe the influence of cavitation on delivery and investigate the importance of VV dose, the experiment was repeated with $1x10^6$ pfu VV. Mice were implanted with SKOV-3 or HEPG2 cells. Once the tumour reached approximately 100 mm^3 mice were treated with either $1x10^6$ pfu VV alone or $1x10^6$ pfu VV with 25 mg/mL cups and ultrasound. Mice were treated as per the previous section but with a different dosing regime as described in Chapter 2. The change in dosing regime was intended to increase the overall cavitation energy as, anecdotally, the first dose caused the strongest and most sustained cavitation while the cavitation response of subsequent injections was more rapidly dampened. A third group was included in the mice implanted with SKOV-3 tumours, whereby $5x10^7$ SV microbubbles/mL (200 µL) was used as a replacement for the cups. This SV dose is the maximum

volume permissible to inject in these in vivo experiments and has previously demonstrated enhanced delivery of adenovirus[191,337].

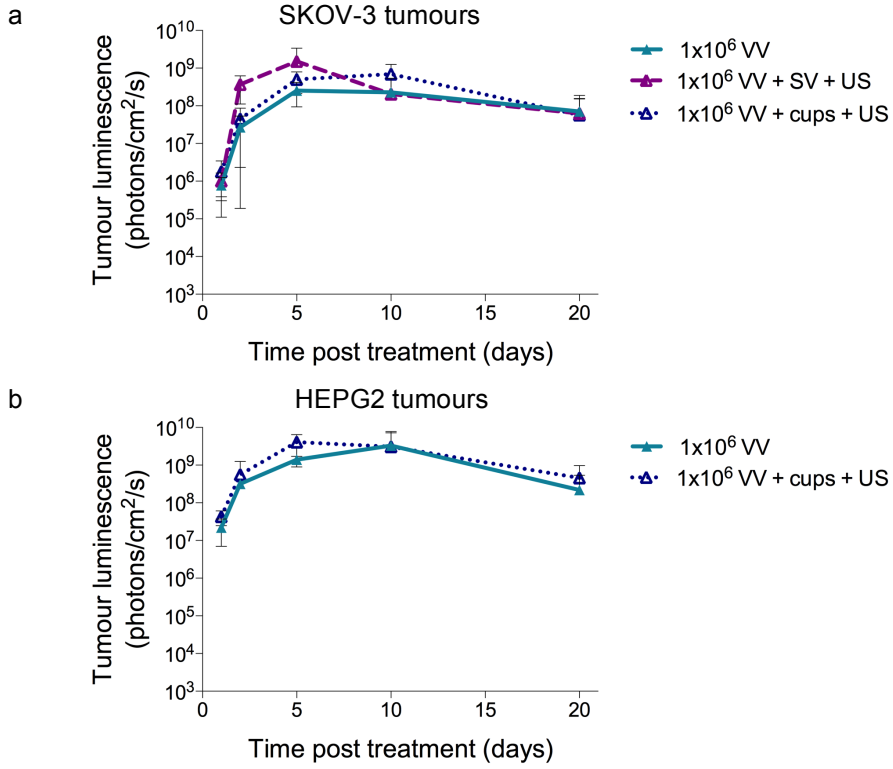

Figure 6-10: Luciferase expression caused by the infection of VV after i.v. injection with 1x10^6 pfu VV
Mice were treated with or without cups and ultrasound treatment. Bioluminescence imaging of the mice was performed 5 minutes after an i.p injection of luciferin to measure tumour activity by luciferase expression to identify the effect of cups and ultrasound treatment in on the mean luminescence in (a) SKOV-3 tumours and (d) HEPG-2 tumours. Error bars indicate standard deviation of n=4 mice. A one-way ANOVA with Bonferroni pair-wise comparison in mice with implanted with SKOV-3 tumours and a T-test in mice implanted with HEPG2 tumours showed there was no significant difference in transgene expression in the tumours between any of the treatment groups at any time point ($p > 0.05$).

Unlike in the 1x10^5 pfu VV dose study (Figure 6-5) there was not a significant difference in VV activity in the tumours caused by cavitation nuclei and ultrasound treatment as measured by luciferase expression (Figure 6-10, $p > 0.05$). Although treatment of 1x10^6 pfu VV, cups and ultrasound gave a measurement of 7.0 +/- 5.5 x 10^8 photons/cm^2/s, this ~3-fold increase compared to 2.5 +/- 1.6 x 10^8 photons/cm^2/s was not significant. The SV control group caused the greatest mean maximum luminescence of 1.5 +/-

1.9 x10^9 photons/cm^2/s but, again, this was not significant. The peak luminescence between the 1x10^5 and 1x10^6 pfu VV studies are not dissimilar – in SKOV-3 mice maximum bioluminescence in mice treated with 1x10^5 pfu VV, cups and ultrasound was 2.2 +/- 1.6 x10^8 photons/cm^2/s.

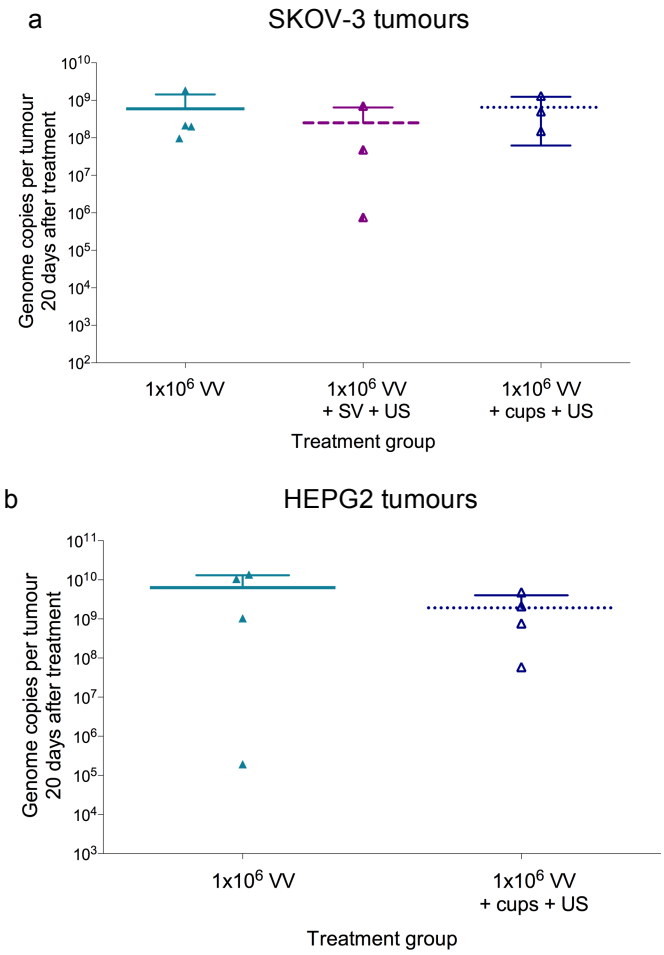

Figure 6-11: Genome copies of VV in the tumours of mice treated with 1x10^6 pfu VV with or without cups and ultrasound
Tumours were harvested 20 days after treatment the tumours were homogenised. qPCR was used to measure the amount of VV present in (a) SKOV-3 tumours and (b) HEPG2 tumours. A one-way ANOVA with Bonferroni pair-wise comparison in mice with implanted with SKOV-3 tumours and a T-test in mice implanted with HEPG2 tumours showed there was no significant difference in the number of genome copies caused by treatment with cavitation nuclei and ultrasound (P>0.05).

HEPG-2 luminescence was even more closely matched between the ultrasound treated and non-ultrasound treated groups with a maximum difference of just 1.2-fold detected at day 5 when $1x10^6$ pfu VV, cups and compared to 4.1 +/- 2.4 $x10^9$ photons/cm^2/s for the control group.

As in Figure 6-5 and Figure 6-6 the qPCR data concurred with the IVIS data; luciferase expression provided a good indicator for the number of VV genomes present in the tumours that were harvested (Figure 6-11). SKOV-3 tumours treated with VV alone had an average of 5.9 +/- 8.5 $x10^8$ copies, with SV and ultrasound the average was 2.5 +/- 3.9 $x10^8$ copies and with cups and ultrasound 6.5 +/- 5.9 $x10^8$ copies were recovered. Over 10-fold more VV was recovered from the tumours than in the previous experiment where mice were dosed with $1x10^5$ pfu VV, cups and ultrasound (8.6 +/- 6.7 x 10^6 VV copies).

The number of VV genome copies in HEPG-2 tumours treated with $1x10^6$ pfu VV alone or $1x10^6$ pfu VV, cups and ultrasound was 6.3 +/- 6.8 $x10^9$ and 1.9 +/ 2.1 $x10^9$ genome copies respectively. In comparison an average of 5.2 +/- 3.4 $x10^7$ were found in the HEPG2 tumours of mice injected with $1x10^5$ VV and cups then treated with ultrasound.

It is hypothesised that the cavitation enables the virus to create a purchase from which to infect the tumours, which at low doses is critical due to the virions being cleared so rapidly. However, once above the dose threshold at which the virus is capable of infecting tumour cells, cavitation does not significantly improve the number of cells infected.

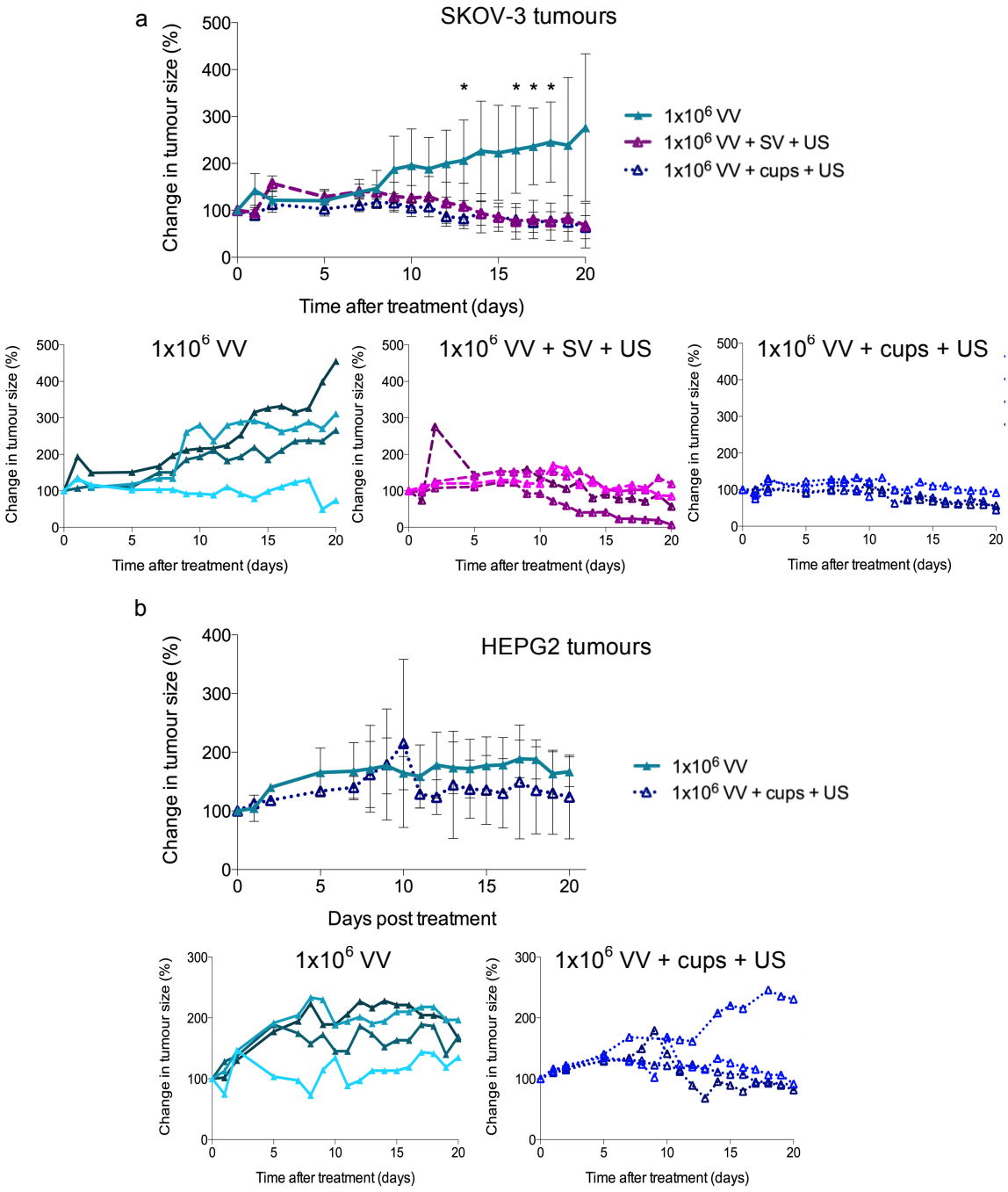

Figure 6-12: The impact of 1x10^6 VV and cups i.v. injection and ultrasound treatment on the growth of the tumours

The size of the tumours of each of the treatment groups was measured every 2-3 days for 20 days after treatment. Shown here are the change in the sizes from the time of treatment of (a) SKOV-3 tumours and (b) HEPG2 tumours. Below each graph are the sizes of the individual tumours in each group. Error bars indicate standard deviation of n=4 mice. A one-way ANOVA with Bonferroni pair-wise comparison in mice with implanted with SKOV-3 tumours showed there was a significant difference in tumour size between of mice that had been treated with cups and ultrasound in comparison to mice that were only treated with VV alone. * = P<0.05. However, a T-test in mice implanted with HEPG2 tumours showed no significance in the tumour sizes between the ultrasound and non-ultrasound treated mice.

Figure 6-12 a shows that despite the lack of a statistically significant increase in either VV activity or the number of VV genomes present in the tumour there was a significant difference in the growth of the SKOV-3 tumours ($p < 0.05$) caused by addition of cavitation nuclei and insonation. There was tumour size regression in all 4 of the mice treated with $1x10^6$ VV, cups and ultrasound whereas only 1 of the 4 mice that had not been treated with cavitation nuclei and ultrasound showed tumour regression. Cavitation caused by SV or cups in combination with VV caused equivalent SKOV tumour regression. These studies do not therefore demonstrate an advantage for SV in terms of efficacy. Although the superior stability in blood and duration of cavitation response from cups in vitro in comparison to SV (see Figure 5-1 and Figure 5-3) makes a compelling argument for their use.

In mice implanted with HEPG2 tumours there was not a significant difference in tumour size 20 days after treatment (Figure 6-12 b), however, 3 of the 4 mice treated with cavitation nuclei and ultrasound showed regression whereas without the ultrasound none of the mice showed any tumour regression. The 4^{th} mice that did not show regression had, initially, a small tumour of 78 mm^3. As a result an increase in the volume of the tumour to 180 mm^3 caused the results to be skewed. In addition, this mouse also had the lowest maximum cavitation power recorded (Figure 6-13). This suggests that there may be a minimum power cavitation threshold that must be achieved before a therapeutic benefit occurs.

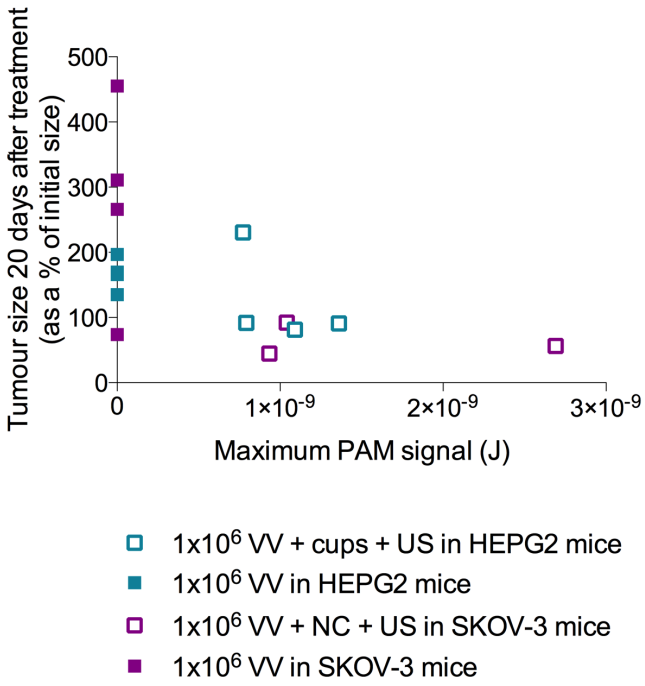

Figure 6-13: The effect of maximum power of cavitation on tumour growth
Mice implanted with either HEPG2 or SKOV-3 tumours were i.v. injected with $1x10^6$ pfu VV and 25 mg/mL of cups. Half of the mice were insonated with ultrasound of 0.5 MHz driving frequency, 1.5 MPa peak rarefactional pressure, 5% duty cycle and 0.5 Hz PRF. The power of cavitation events was recorded with a linear transducer array and calculated using Matlab code. It was then compared to the growth of the tumours 20 days after treatment (shown as a % of their initial size).

6.4 Discussion

In vitro studies had demonstrated that cups were able to deliver antibodies at both at 1.6 MHz and at 0.5 MHz. The lower of these two frequencies was chosen for use in vivo as has a greater treatment volume allowing faster treatment of the whole body is addition to lower attenuation thereby reducing heating effects and permitting areas of the body to be treated at a greater depth. Furthermore, use of this lower frequency facilitated real-time PAM of the location and intensity of cavitation events using a standard diagnostic array used for B-mode imaging during treatment. This therefore produced a complete system potentially capable of enhancing and monitoring delivery simultaneously.

The difference in liver expression caused by $1x10^5$ pfu VV and $1x10^6$ pfu VV demonstrates the importance of improved delivery. The maximum dose in clinical trials was limited to $1x10^9$ pfu VV due to higher doses causing hyperbilirubinemia – a condition linked to biliary obstruction and tumour swelling[345]. By combining the VV with cups and cavitation nuclei at the $1x10^5$ pfu VV dose there was infection detected in the tumours where, without the drug delivery system, levels were negligible. Furthermore at this dose there was no luciferase detected in the liver after 24 hours in contrast to the $1x10^6$ pfu VV dose. This suggests lower and less hepatotoxic doses could be used without sacrificing anti-tumour effects. Clinical trials have indicated that there appeared to be a threshold effect in systemic delivery of VV: biopsies showed the presence of VV genome copies in 87% of patients treated with $1x10^9$ pfu/dose or more of VV but no copies were detected in patients treated at

lower doses[348]. A dose of $1x10^5$ pfu VV appeared to be below the threshold of delivery in the HEPG2 implanted mice but the addition of cups and ultrasound to the treatment overcame this threshold.

At this dose there was no apparent correspondence between cavitation signal and the levels of VV luciferase expression but there did appear to be a relationship between the cavitation signal and the time at which the maximum expression of luciferase was observed. Better seeding of the VV may have caused the extended duration of expression as a result of greater ability to infect neighbouring cells. However, due to the threshold effect, this seeding may have dispersed the VV too sparsely.

The genetic component of oncolytic viruses opens up the possibility of using 'armed' agents that express therapeutic transgene. The studies performed here did not utilise such an 'armed' virus and so were only designed and powered to look at the question of delivery rather than therapy. It is not surprising therefore that a therapeutic benefit could not be detected at the $1x10^5$ pfu VV dose.

At the higher dose of $1x10^6$ pfu VV it was shown the cups and ultrasound could improve the therapeutic outcome of treatment, however, in contrast to the $1x10^5$ pfu VV concentration study, cavitation did not provide an increase in the luciferase expression. This may be due to the increased number of virus particles driven into the tumour by cavitation being relatively small in comparison to the total number of virion that had managed to infect tumour cells. Nevertheless, the location of the infection sites will remain critical. It is hypothesised that the cavitation will create a better spread of virus infection

through the tumour and, consequently, will increase the efficacy of the treatment. There was no clear correlation between VV concentration or luciferase expression with tumour regression. This suggests that the location of VV within the tumour could be critical. Although, as the lower dose of $1x10^5$ pfu VV showed, there must be a minimum amount of VV delivered into the tumours to be effective. This may be due to tumour regression not being entirely due to cell lysis caused by virus infection but by secondary inflammatory effects as well[44]. Therefore, better seeding of the virus would cause larger areas of the tumour to be treated.

In trying to draw a correlation between ultrasound response and therapeutic outcome it appeared that at $1x10^6$ pfu of VV there was one-to-one correlation between the presence or absence of a cavitation signal and the associated therapeutic benefit. 7 of the 8 mice treated with VV, cups and ultrasound showed regression of their tumours. The one mouse with a tumour which continued to grow had recorded the lowest peak cavitation signal of all of the mice.

The successful treatment of the tumours at $1x10^6$ pfu is remarkable considering 3 doses of $1x10^7$ pfu VV over a week showed 50% survival in an HEPG2 tumour model over 20 day period[358]. The virus used in this case was the Wyeth strain of VV with the TK gene deleted armed to produce granulocyte macrophage colony stimulating factor (GM-CSF) to both improve tumour selectivity and cause greater anti-tumour immunity.

6.5 Conclusions

This chapter reports that:

- Injection of the nanocups developed in Chapter 4 enabled sustained inertial cavitation activity in vivo upon exposure of the tumour to modest ultrasound pressures (1.5 MPa at 0.5 MHz)
- PAM enabled the monitoring and mapped the cavitation events over a B-mode image to provide information on whether cavitation was occurring within the tumour in real time.
- Delivery of VV and subsequent activity was dramatically improved with cavitation nuclei and ultrasound when mice were treated with $1x10^5$ pfu VV.
- A therapeutic benefit of cavitation nuclei and ultrasound was observed in mice i.v. injected with $1x10^6$ pfu VV where 7 of 8 mice treated with VV, cups and ultrasound showed tumour regression in comparison to just 1 in 8 of the mice treated with VV alone.
- Equivalent benefits were observed in mice treated with cups as with SV with both significantly improving the efficacy of the VV.

7 Conclusions and future work

7.1 Conclusions

The motivation of this thesis was to test different mechanisms by which the areas of tumours that are currently inaccessible to drugs can be treated more effectively. Cancer research has begun to move towards biological therapeutics, such as antibodies and oncolytic viruses, to replace or to combine with conventional small molecule chemotherapeutics[26,359]. However, the size of these agents means that distribution within tumours is particularly restricted, leading to poor therapeutic outcomes[22,191].

A number of different methods have been utilised to try and overcome the poor delivery of therapeutics into tumours and reduce the off-target toxic side effects of cancer drugs. Stimuli responsive therapeutic carriers release their cargo at the target site while improving the pharmacokinetics of the drug; such stimuli may be endogenous, such as pH, or external, such as temperature or pressure[192,259,360,361]. The most clinically advanced of these agents is Thermodox, a doxorubicin-loaded, thermosensitive liposome in Phase II and Phase III trials in combination with HIFU and radiowaves respectively[362]. However, by using biologics as therapeutics the drug is more specific to the tumour site and thus triggered release is less critical.

Ultrasound-induced cavitation has already been demonstrated to improve drug delivery in a range of pre-clinical models. Notably, to achieve this at

'diagnostic-like' ultrasound parameters a pre-existing gas bubble is required and to date most studies have relied on the use of the microbubble formulation, SonoVue (SV) to fulfil this role[135]. However, the instability of SV in the blood and its destruction during the cavitation process means that treatment times are limited. Nanodroplets are also capable of lowering the cavitation threshold and, in addition, remain more stable in the blood and can extravasate out of the vasculature[363]. Yet they are still destroyed during the process of cavitation.

The work presented in this thesis provides an alternative source of cavitation nuclei formulated to be both biocompatible and submicronic. The physiochemical, biological and ultrasound response characteristics of these nuclei were tested and compared to SV using in vitro and in vivo models. Notably, they were shown to maintain a submicron size range and respond to ultrasound for longer than shelled microbubbles.

Ultimately, the ability of these cavitation nuclei to respond to ultrasound and propel an oncolytic virus into and throughout tumours was demonstrated, resulting in dramatic improvements in the efficacy of the virus.

7.1.1 Formulation of cavitation nuclei in the sub-micron scale and validation of their biocompatibility

Two submicron particle formulations were developed that were able to lower the cavitation threshold of a solution to below that expected of lipid stabilised bubbles of the same size. These were named mesoporous carbon nanoparticles (CNP) and polymer cups. They both utilise crevices on their

surface to stabilise gas pockets. Upon exposure to ultrasound these bubbles act as cavitation nuclei to produce sustained cavitation. Cups, due to their uniform shape, had a very clear cavitation threshold below which negligible amounts of inertial cavitation were detected but above which there was strong, consistent cavitation. Conversely, CNP had a lower cavitation threshold than the polymer cups of equivalent size but produced less energy when the cups were above their cavitation threshold. As the peak rarefactional pressure increased, so too did the power of the cavitation caused by the CNP as a greater proportion of particles were raised above their cavitation threshold. In addition they showed a previously unreported 'priming effect' where there was an initial increase in the power of cavitation during insonation. It is hypothesised that this is caused by the multiple bubbles on the surface of a particle coalescing during the rarefactional periods of the ultrasound cycle until their cavitational threshold dropped to below the ultrasound peak rarefactional pressure. This cavitation behaviour is considerably different to microbubbles, which are destroyed rapidly by ultrasound exposure. Indeed, of all the classes of ultrasound responsive systems, such as microbubbles and acoustic vapourisation droplets, none demonstrate these characteristics or start and remain at the nanoscale following cavitation[364,365].

No proteins were observed to adsorb onto the CNP particles and the minor adsorbance of a protein of 150 kDa onto the surface of the cups did not correlate with complement activation, or a loss of cavitation energy. Both formulations were incubated with the different components of blood to characterise white and red blood cell lysis, complement activation and

stimulation of cytokine (IL-6 and TNF-α) release. Neither CNP nor polymer cups caused significant cell death or the stimulation of inflammatory cytokine production either *in vitro* or *in vivo*. However, there were large error bars when measuring the concentration of these cytokines and the complement protein C3a. Experiments would have benefitted from a larger sample size. Variability assessments should have been performed to calculate the number of mice that would have been required to see significant results. The weights, motility or socialisation of the mice injected with these cavitation nuclei were not affected by treatment.

7.1.2 Characterisation of ultrasound responsiveness of cavitation nuclei and optimisation of improved delivery of a therapeutic using cavitation nuclei and ultrasound *in vitro*

The cavitation nuclei formulated were directly compared to SV in tissue mimicking phantoms in order to assess the ability of cups and CNP to drive a fluorescently labelled antibody perpendicular to flow and into an agar based tissue mimicking phantom. It was shown that both cavitation nuclei could drive the antibody to equivalent distances as achieved with SV at driving frequencies of either 0.5 MHz or 1.6 MHz. Concurrent detection of acoustic emissions demonstrated that instigation of inertial cavitation was essential to the delivery.

Cups cavitated when exposed to driving frequencies of both 0.5 MHz and 1.6 MHz while CNP and SV only cavitated strongly when insonated at the lower driving frequency. Due to SV being destroyed by cavitation, high pulse repetition frequencies (PRF) caused them to be destroyed before they entered the focus and consequently caused the cavitation energy recorded to be low. Meanwhile high PRF improved the cavitation response of the CNP, potentially due to the CNP being 'primed' in the side lobes of the focal volume.

The impact of the ultrasound parameters on antibody delivery was assessed. It was found that the number of cycles per burst was critical to the delivery of the therapeutic. It is hypothesised that the convective eddies formed by cavitation are essential to the delivery of a therapeutic but this requires thousands of cycles until a uniform streaming effect is achieved. As would be expected, by extending the insonation time the overall drug delivery was increased. These studies helped identify polymer cups as the lead candidate for in vivo testing.

7.1.3 Demonstration of improved delivery of a therapeutic *in vivo*

Mice were implanted with 1 of 2 different human cancer cell lines and the resultant tumours were treated with polymer cups, vaccinia virus (VV) and ultrasound. Passive acoustic mapping was used to assess the intensity of the cavitation response as well as the location of the cavitation in reference to the tumour.

It was found that at low concentrations of VV ($1x10^5$ pfu) the activity of VV in the tumour was significantly improved by the combination of cavitation nuclei and ultrasound treatment (1,000 - 10,000 fold increase, $p < 0.05$). However, there was no resultant change in tumour growth. Immunohistochemistry revealed that large areas of the tumour remained uninfected 20 days after treatment even with the addition of cavitation-enhanced delivery. Secondary infections were apparent but the amplification of this non-armed reporter virus was not fast enough to counter the rapid growth of the tumour.

At higher concentrations of VV ($1x10^6$ pfu) the cavitation nuclei, in combination with ultrasound treatment, caused regression of the tumours in 7 of the 8 mice in comparison to just 1 of the 8 mice that were treated with VV alone. The impact of cavitation was evident in that the only tumour not to regress showed the lowest cavitation signal of all the mice. The cavitation enhanced delivery achieved with SV caused similar regression of the tumours as achieved with the cups but, due to the assessment of a successful response being binary, it was not possible to distinguish the relative success of the two types of cavitation nuclei.

7.2 Future work

This work has established that submicron, solid cavitation nuclei can improve the delivery of a therapeutic with the result being an improvement in the drug efficacy. Future work would include the direct comparison between SV and submicron cavitation nuclei in addition to the development of better understanding of the factors critical to an improvement in drug efficacy such as ultrasound parameters and cavitation nuclei concentration. A survival study

would provide further evidence that cavitation improves overall outcomes for the mice.

Groups of 4 or 5 mice are traditionally used in pilot animal studies. These preliminary experiments demonstrated that cup-induced cavitation significantly improved infection in tumours (Figure 6-5, $P < 0.05$) and significantly retarded tumour growth in the SKOV tumour model (Figure 6-12, $P < 0.05$). However, the HEPG2 model did not show significant tumour regression. Further studies powered using G*Power software (Dusseldorf University) could be performed in order to produce results that are more likely show statistical significance between the tumour growths of the two groups.

The low driving frequency of the ultrasound used in these in vivo experiments will have caused there to be cavitation outside of the tumour. It is hypothesised that there will be limited impact upon healthy tissue treated with the ultrasound, cups and drug provided the drug is cancer cell specific. This hypothesis must be tested in order to judge the safety of this technology.

It was theorised that cavitation improved the distribution of infected cells and thus enhanced the cytotoxicity and spread of the virus in tumours. In order to validate this hypothesis further histology needs to be performed to better understand both how cavitation affects the distribution of infected cells and whether this is the likely cause of the improved efficacy of the treatment.

The analysis of the relationship between cavitation response and delivery in vivo was crude due to the limited number of mice used and the inherent variability of in vivo studies. Passive acoustic mapping (PAM) provides a very rich source of data by which the impact of cavitation could be effectively

assessed. Culling some mice at an earlier time point would enable assessment on whether the location of delivery could accurately be identified by the PAM.

This work continues to be developed in a commercial and clinical setting. The ability to enhance the delivery and efficacy of currently approved drugs without the need to reformulate these drugs provides the approach with great potential. It is hoped the eventual ability to accurately interpret PAM to confirm whether complete treatment of a tumour has been achieved, will add further clinical utility.

References

1. Jemal, A. *et al.* Cancer Statistics, 2008. *CA Cancer J Clin* **58,** 71–96 (2008).
2. Bray, F., Ren, J. S., Masuyer, E. & Ferlay, J. Global estimates of cancer prevalence for 27 sites in the adult population in 2008. *Int J Cancer* **132,** 1133–1145 (2013).
3. Ferlay, J. *et al.* Estimates of worldwide burden of cancer in 2008: GLOBOCAN 2008. *Int J Cancer* **127,** 2893–2917 (2010).
4. Haber, D. A., Gray, N. S. & Baselga, J. The evolving war on cancer. *Cell* **145,** 19–24 (2011).
5. Vanneman, M. & Dranoff, G. Combining immunotherapy and targeted therapies in cancer treatment. *Nat Rev Cancer* **12,** 237–251 (2012).
6. Druker, B. J. & Lydon, N. B. Lessons learned from the development of an abl tyrosine kinase inhibitor for chronic myelogenous leukemia. *J Clin Invest* **105,** 3–7 (2000).
7. Flaherty, K. T. *et al.* Inhibition of mutated, activated BRAF in metastatic melanoma. *N Engl J Med* **363,** 809–819 (2010).
8. Allegra, C. J. *et al.* American Society of Clinical Oncology provisional clinical opinion: testing for KRAS gene mutations in patients with metastatic colorectal carcinoma to predict response to anti-epidermal growth factor receptor monoclonal antibody therapy. *J Clin Oncol* **27,** 2091–2096 (2009).
9. Tothill, I. E. Biosensors for cancer markers diagnosis. *Semin Cell Dev Biol* **20,** 55–62 (2009).
10. Luo, S., Zhang, E., Su, Y., Cheng, T. & Shi, C. A review of NIR dyes in cancer targeting and imaging. *Biomaterials* **32,** 7127–7138 (2011).
11. Baron, J. A. Screening for cancer with molecular markers: progress comes with potential problems. *Nat Rev Cancer* **12,** 368–371 (2012).
12. Reddy, L. H. Drug delivery to tumours: recent strategies. *J Pharm Pharmacol* **57,** 1231–1242 (2005).
13. Rai, A. J. *et al.* Proteomic approaches to tumor market discovery: Identification of biomarkers for ovarian cancer - ProQuest. *Arch pathol lab med* **126,** 1518–1526 (2002).
14. Larina, I. V., Evers, B. M. & Esenaliev, R. O. Optimal drug and gene delivery in cancer cells by ultrasound-induced cavitation. *Anticancer Res* **25,** 149–156 (2005).
15. Finn, O. J. Cancer immunology. *N Engl J Med* **358,** 2704–2715 (2008).
16. Couzin-Frankel, J. Cancer immunotherapy. *Science* **342,** 1432–1433 (2013).
17. Hu, Z. *et al.* Investigation of HIFU-induced anti-tumor immunity in a murine tumor model. *J Transl Med* **5,** 34 (2007).

18. Flier, J. S., Underhill, L. H. & Pastan, I. Multiple-drug resistance in human cancer. *N Engl J Med* **316,** 1388–1393 (1987).
19. Igney, F. H. & Krammer, P. H. Death and anti-death: Tumour resistance to apoptosis. *Nat Rev Cancer* **2,** 277–288 (2002).
20. Gottesman, M. M., Fojo, T. & Bates, S. E. Multidrug resistance in cancer: Role of ATP-dependent transporters. *Nat Rev Cancer* **2,** 48–58 (2002).
21. Goldstein, L. J. *et al.* Expression of multidrug resistance gene in human cancers. *J Natl Cancer Inst* **81,** 116–124 (1989).
22. Baker, J. H. E. *et al.* Direct visualization of heterogeneous extravascular distribution of trastuzumab in human epidermal growth factor receptor type 2 overexpressing xenografts. *Clin Cancer Res* **14,** 2171–2179 (2008).
23. Primeau, A. J., Rendon, A., Hedley, D., Lilge, L. & Tannock, I. F. The distribution of the anticancer drug Doxorubicin in relation to blood vessels in solid tumors. *Clin Cancer Res* **11,** 8782–8788 (2005).
24. Feng, S. S. & Chien, S. Chemotherapeutic engineering: Application and further development of chemical engineering principles for chemotherapy of cancer and other diseases. *Chem Eng Sci* **58,** 4087–4114 (2003).
25. Adams, G. P. & Weiner, L. M. Monoclonal antibody therapy of cancer. *Nat Biotech* **23,** 1147–1157 (2005).
26. FDA approved antibody-based therapeutics. *The Immunology Link* at <http://www.immunologylink.com/FDA-APP-Abs.html>
27. *FDA Approved drugs by therapeutic area*.
28. Duraiswamy, J., Kaluza, K. M., Freeman, G. J. & Coukos, G. Dual Blockade of PD-1 and CTLA-4 Combined with Tumor Vaccine Effectively Restores T-Cell Rejection Function in Tumors. *Cancer Res* (2013).
29. Dong, H. *et al.* Tumor-associated B7-H1 promotes T-cell apoptosis: a potential mechanism of immune evasion. *Nat Med* **8,** 793–800 (2002).
30. Wolchok, J. D. *et al.* Nivolumab plus ipilimumab in advanced melanoma. *N Engl J Med* **369,** 122–133 (2013).
31. Powles, T. *et al.* MPDL3280A (anti-PD-L1) treatment leads to clinical activity in metastatic bladder cancer. *Nature* **515,** 558–562 (2014).
32. Kong, Y.-C. M. & Flynn, J. C. Opportunistic autoimmune disorders potentiated by immune-checkpoint inhibitors anti-CTLA-4 and anti-PD-1. *Front Immunol* **5,** 206 (2014).
33. Brahmer, J. R. *et al.* Safety and activity of anti-PD-L1 antibody in patients with advanced cancer. *N Engl J Med* **366,** 2455–2465 (2012).
34. Tannock, I. F., Lee, C. M., Tunggal, J. K., Cowan, D. S. M. & Egorin, M. J. Limited penetration of anticancer drugs through tumor tissue. *Clin Cancer Res* **8,** 878–884 (2002).
35. Jain, R. K. *et al.* Angiogenesis in brain tumours. *Nat Rev Neurosci* **8,** 610–622 (2007).
36. Schmidt, M. M. & Wittrup, K. D. A modeling analysis of the effects of molecular size and binding affinity on tumor targeting. *Mol Cancer Ther* **8,** 2861–2871 (2009).
37. Thurber, G., Schmidt, M. & Wittrup, K. Factors determining antibody distribution in tumors. *Trends Pharmacol Sci* (2008).

38. Caul, E. O. & Appleton, H. The electron microscopical and physical characteristics of small round human fecal viruses: an interim scheme for classification. *J Med Virol* **9,** 257–265 (1982).
39. Philippe, N. *et al.* Pandoraviruses: amoeba viruses with genomes up to 2.5 Mb reaching that of parasitic eukaryotes. *Science* **341,** 281–286 (2013).
40. Cattaneo, R., Miest, T., Shashkova, E. V. & Barry, M. A. Reprogrammed viruses as cancer therapeutics: targeted, armed and shielded. *Nat Rev Micro* **6,** 529–540 (2008).
41. Russell, S. J., Peng, K.-W. & Bell, J. C. Oncolytic virotherapy. *Nature biotechnology* **30,** 658–670 (2012).
42. Stojdl, D. F. *et al.* Exploiting tumor-specific defects in the interferon pathway with a previously unknown oncolytic virus. *Nat Med* **6,** 821–825 (2000).
43. Coffey, M. C., Strong, J. E., Forsyth, P. A. & Lee, P. W. Reovirus therapy of tumors with activated Ras pathway. *Science* **282,** 1332–1334 (1998).
44. Breitbach, C. J. *et al.* Targeted inflammation during oncolytic virus therapy severely compromises tumor blood flow. *Mol Ther* **15,** 1686–1693 (2007).
45. Liu, T. C., Galanis, E. & Kirn, D. Nature Clinical Practice Oncology | Clinical trial results with oncolytic virotherapy: a century of promise, a decade of progress | Article. *Nat Clin Pract Oncol* **4,** 101–117 (2007).
46. Freytag, S. O. *et al.* Phase I study of replication-competent adenovirus-mediated double suicide gene therapy for the treatment of locally recurrent prostate cancer. *Cancer Res* **62,** 4968–4976 (2002).
47. Hwang, T.-H. *et al.* A mechanistic proof-of-concept clinical trial with JX-594, a targeted multi-mechanistic oncolytic poxvirus, in patients with metastatic melanoma. *Mol Ther* **19,** 1913–1922 (2011).
48. Lichty, B. D., Breitbach, C. J., Stojdl, D. F. & Bell, J. C. Going viral with cancer immunotherapy. *Nat Rev Cancer* **14,** 559–567 (2014).
49. Patel, M. R. & Kratzke, R. A. Oncolytic virus therapy for cancer: the first wave of translational clinical trials. *Transl Res* **161,** 355–364 (2013).
50. Sheridan, C. First oncolytic virus edges towards approval in surprise vote. *Nat Biotech* **33,** 569–570 (2015).
51. Dolgin, E. Oncolytic viruses get a boost with first FDA-approval recommendation. *Nat Rev Drug Discov* **14,** 369–371 (2015).
52. Kaufman, H. L. *et al.* Primary overall survival (OS) from OPTiM, a randomized phase III trial of talimogene laherparepvec (T-VEC) versus subcutaneous (SC) granulocyte-macrophage colony-stimulating factor (GM-CSF) for the treatment (tx) of unresected stage IIIB/C and IV melanoma. *ASCO Meeting Abstracts* **32,** 9008a (2014).
53. Liu, B. L. *et al.* ICP34.5 deleted herpes simplex virus with enhanced oncolytic, immune stimulating, and anti-tumour properties. *Gene Ther* **10,** 292–303 (2003).
54. Senzer, N. N. *et al.* Phase II clinical trial of a granulocyte-macrophage colony-stimulating factor–encoding, second-generation oncolytic herpesvirus in patients with unresectable metastatic melanoma. *J Clin Oncol* **27,** 5763–5771 (2009).

55. Subr, V. *et al.* Coating of adenovirus type 5 with polymers containing quaternary amines prevents binding to blood components. *J Control Release* **135,** 152–158 (2009).
56. Willmon, C. *et al.* Cell carriers for oncolytic viruses: Fed Ex for cancer therapy. *Mol Ther* **17,** 1667–1676 (2009).
57. Di, Y., Seymour, L. & Fisher, K. Activity of a group B oncolytic adenovirus (ColoAd1) in whole human blood. *Gene Ther* **21,** 440–443 (2014).
58. Miller, A. *et al.* Reporter gene imaging identifies intratumoral infection voids as a critical barrier to systemic oncolytic virus efficacy. *Mol Ther* **1,** (2014).
59. Baban, D. F. & Seymour, L. W. Control of tumour vascular permeability. *Adv Drug Deliver Rev* **34,** 109–119 (1998).
60. Boucher, Y. & Jain, R. K. Microvascular pressure is the principal driving force for interstitial hypertension in solid tumors: implications for vascular collapse. *Cancer Res* **52,** 5110 (1992).
61. Jain, R. K. The next frontier of molecular medicine: Delivery of therapeutics. *Nat Med* **4,** 655–657 (1998).
62. Byrne, J. D., Betancourt, T. & Brannon-Peppas, L. Active targeting schemes for nanoparticle systems in cancer therapeutics. *Adv Drug Deliver Rev* **60,** 1615–1626 (2008).
63. Magzoub, M., Jin, S. & Verkman, A. S. Enhanced macromolecule diffusion deep in tumors after enzymatic digestion of extracellular matrix collagen and its associated proteoglycan decorin. *FASEB J* **22,** 276–284 (2008).
64. Haley, B. & Frenkel, E. Nanoparticles for drug delivery in cancer treatment. *Urol Oncol Semin O I* **26,** 57–64 (2008).
65. Modi, S., Prakash Jain, J., Domb, A. J. & Kumar, N. Exploiting EPR in polymer drug conjugate delivery for tumor targeting. *Curr Pharm Design* **12,** 4785–4796 (2006).
66. Fang, J., Nakamura, H. & Maeda, H. The EPR effect: Unique features of tumor blood vessels for drug delivery, factors involved, and limitations and augmentation of the effect. *Adv Drug Deliver Rev* **63,** 136–151 (2011).
67. Hobbs, S. K. *et al.* Regulation of transport pathways in tumor vessels: role of tumor type and microenvironment. *P Natl Acad Sci USA* **95,** 4607–4612 (1998).
68. Matsumura, Y. & Maeda, H. A new concept for macromolecular therapeutics in cancer chemotherapy: mechanism of tumoritropic accumulation of proteins and the antitumor agent smancs. *Cancer Res* **46,** 6387–6392 (1986).
69. Iyer, A. K., Khaled, G., Fang, J. & Maeda, H. Exploiting the enhanced permeability and retention effect for tumor targeting. *Drug Discov Today* **11,** 812–818 (2006).
70. Auffan, M. *et al.* Towards a definition of inorganic nanoparticles from an environmental, health and safety perspective. *Nat Nanotechnol* **4,** 634–641 (2009).
71. Laginha, K. M., Verwoert, S., Charrois, G. J. R. & Allen, T. M. Determination of doxorubicin levels in whole tumor and tumor nuclei in murine breast cancer tumors. *Clin Cancer Res* **11,** 6944–6949 (2005).

72. Seymour, L. W. *et al.* Influence of molecular weight on passive tumour accumulation of a soluble macromolecular drug carrier. *Eur J Cancer* **31,** 766–770 (1995).
73. Yang, X. C. *et al.* Drug delivery using nanoparticle-stabilized nanocapsules. *Engew Chem Int Edit* **123,** 497–501 (2011).
74. Kircheis, R. *et al.* Coupling of cell-binding ligands to polyethylenimine for targeted gene delivery. *Gene Ther* **4,** 409 (1997).
75. Parveen, S., Misra, R. & Sahoo, S. K. Nanoparticles: a boon to drug delivery, therapeutics, diagnostics and imaging. *Nanomedicine: Nanotechnology, biology and medicine* **8,** 147–166 (2011).
76. Brewer, E., Coleman, J. & Lowman, A. Emerging technologies of polymeric nanoparticles in cancer drug delivery. *J Nanomater* **2011,** 1 (2011).
77. Etheridge, M. L. *et al.* The big picture on nanomedicine: the state of investigational and approved nanomedicine products. *Nanomedicine* **9,** 1–14 (2013).
78. Townley, H. E., Rapa, E., Wakefield, G. & Dobson, P. J. Nanoparticle augmented radiation treatment decreases cancer cell proliferation. *Nanomedicine: Nanotechnology, biology and medicine* **8,** 526–536 (2012).
79. Nohynek, G. J. & Dufour, E. K. Nano-sized cosmetic formulations or solid nanoparticles in sunscreens: A risk to human health? *Arch Toxicol* **86,** 1063–1075 (2012).
80. Nohynek, G. J., Antignac, E., Re, T. & Toutain, H. Safety assessment of personal care products/cosmetics and their ingredients. *Toxicol Appl Pharm* **243,** 239–259 (2010).
81. Dobrovolskaia, M. A. & McNeil, S. E. Immunological properties of engineered nanomaterials. *Nat Nanotechnol* **2,** 469–478 (2007).
82. Naahidi, S. *et al.* Biocompatibility of engineered nanoparticles for drug delivery. *J Control Release* **166,** 182–194 (2013).
83. Choi, C. H. J., Alabi, C. A., Webster, P. & Davis, M. E. Mechanism of active targeting in solid tumors with transferrin-containing gold nanoparticles. *P Natl Acad Sci USA* **107,** 1235–1240 (2010).
84. Hauck, T. S., Anderson, R. E., Fischer, H. C., Newbigging, S. & Chan, W. C. W. In vivo quantum-dot toxicity assessment. *Small* **6,** 138–144 (2010).
85. Schipper, M. L. *et al.* A pilot toxicology study of single-walled carbon nanotubes in a small sample of mice. *Nat Nanotechnol* **3,** 216–221 (2008).
86. Shukla, R., Bansal, V., Chaudhary, M. & Basu, A. Biocompatibility of gold nanoparticles and their endocytotic fate inside the cellular compartment: A microscopic overview. *Langmuir* **21,** 10644–10654 (2005).
87. Sahu, S. C. & Casciano, D. A. *Nanotoxicity*. (John Wiley & Sons, 2009).
88. O'Brien, M. E. R. *et al.* Reduced cardiotoxicity and comparable efficacy in a phase III trial of pegylated liposomal doxorubicin HCl (CAELYX/Doxil) versus conventional doxorubicin for first-line treatment of metastatic breast cancer. *Ann Oncol* **15,** 440–449 (2004).
89. Díaz, B. *et al.* Assessing methods for blood cell cytotoxic responses to

inorganic nanoparticles and nanoparticle aggregates. *Small* **4,** 2025–2034 (2008).
90. Han, V., Serrano, K. & Devine, D. V. A comparative study of common techniques used to measure haemolysis in stored red cell concentrates. *Vox Sang.* **98,** 116–123 (2010).
91. Minetti, M., Agati, L. & Malorni, W. The microenvironment can shift erythrocytes from a friendly to a harmful behavior: pathogenetic implications for vascular diseases. *Cardiovasc. Res.* **75,** 21–28 (2007).
92. Yu, T., Malugin, A. & Ghandehari, H. Impact of Silica Nanoparticle Design on Cellular Toxicity and Hemolytic Activity. *ACS Nano* **5,** 5717–5728 (2011).
93. Mossman, B., Light, W. & Wei, E. Asbestos: mechanisms of toxicity and carcinogenicity in the respiratory tract. *Annu Rev Pharmacol* **23,** 595–615 (1983).
94. Champion, J. A. & Mitragotri, S. Role of target geometry in phagocytosis. *P Natl Acad Sci USA* **103,** 4930–4934 (2006).
95. Chithrani, B. D., Ghazani, A. A. & Chan, W. C. W. Determining the size and shape dependence of gold nanoparticle uptake into mammalian cells. *Nano Lett* **6,** 662–668 (2006).
96. Geng, Y. *et al.* Shape effects of filaments versus spherical particles in flow and drug delivery. *Nat Nanotechnol* **2,** 249–255 (2007).
97. Díaz, B. *et al.* Assessing Methods for Blood Cell Cytotoxic Responses to Inorganic Nanoparticles and Nanoparticle Aggregates. *Small* **4,** 2025–2034 (2008).
98. Renwick, L. Impairment of alveolar macrophage phagocytosis by ultrafine particles. *Toxicol Appl Pharm* **172,** 119–127 (2001).
99. Kuo, J.-H. S., Jan, M.-S. & Chiu, H. W. Mechanism of cell death induced by cationic dendrimers in RAW 264.7 murine macrophage-like cells. *J Pharm Pharmacol* **57,** 489–496 (2005).
100. Fenoglio, I., Croce, A., Di Renzo, F., Tiozzo, R. & Fubini, B. Pure-silica zeolites (porosils) as model solids for the evaluation of the physicochemical features determining silica toxicity to macrophages. *Chem Res Toxicol* **13,** 489–500 (2000).
101. Xiao, K. *et al.* The effect of surface charge on in vivo biodistribution of PEG-oligocholic acid based micellar nanoparticles. *Biomaterials* **32,** 3435–3446 (2011).
102. Dobrovolskaia, M. A., Aggarwal, P., Hall, J. B. & McNeil, S. E. Preclinical studies to understand nanoparticle interaction with the immune system and its potential effects on nanoparticle biodistribution. *Mol Pharm* **5,** 487–495 (2008).
103. Gessner, A., Lieske, A., Paulke, B. R. & Muller, R. H. Influence of surface charge density on protein adsorption on polymeric nanoparticles: analysis by two-dimensional electrophoresis. *Eur J Pharm Biopharm* **54,** 165–170 (2002).
104. Li, S.-D. & Huang, L. Pharmacokinetics and biodistribution of nanoparticles. *Mol Pharm* (2008). doi:10.1021/mp800049w
105. Choi, H. S. *et al.* Renal clearance of quantum dots. *Nat Biotech* **25,** 1165–1170 (2007).
106. Chen, L. T. & Weiss, L. The role of the sinus wall in the passage of erythrocytes through the spleen. *Blood* **41,** 529–537 (1973).

107. Awasthi, V. D., Garcia, D., Goins, B. A. & Phillips, W. T. Circulation and biodistribution profiles of long-circulating PEG-liposomes of various sizes in rabbits. *Int J Pharm* **253,** 121–132 (2003).
108. Ferrari, M. Cancer nanotechnology: opportunities and challenges. *Nat Rev Cancer* **5,** 161–171 (2005).
109. Lin, Y. *et al.* Advances toward bioapplications of carbon nanotubes. *J Mater Chem* **14,** 527–541 (2004).
110. Calvo, P. *et al.* Long-circulating PEGylated polycyanoacrylate nanoparticles as new drug carrier for brain delivery. *Pharm Res* **18,** 1157–1166 (2001).
111. Moonsub Shim, Nadine Wong Shi Kam, Robert J Chen, Yiming Li, A. & Dai, H. Functionalization of carbon nanotubes for biocompatibility and biomolecular recognition. *Nano Lett* **2,** 285–288 (2002).
112. Shiraishi, K. *et al.* Hydrophobic blocks of PEG-conjugates play a significant role in the accelerated blood clearance (ABC) phenomenon. *J Control Release* **165,** 183–190 (2013).
113. Soppimath, K. S., Aminabhavi, T. M., Kulkarni, A. R. & Rudzinski, W. E. Biodegradable polymeric nanoparticles as drug delivery devices. *J Control Release* **70,** 1–20 (2001).
114. LaVan, D. A., McGuire, T. & Langer, R. Small-scale systems for in vivo drug delivery. *Nat Biotech* **21,** 1184–1191 (2003).
115. Wang, M. & Thanou, M. Targeting nanoparticles to cancer. *Pharmacol Res* **62,** 90–99 (2010).
116. Maldiney, T. *et al.* Effect of core diameter, surface coating, and PEG chain length on the biodistribution of persistent luminescence nanoparticles in mice. *ACS Nano* **5,** 854–862 (2011).
117. Szebeni, J. *et al.* Liposome-induced complement activation and related cardiopulmonary distress in pigs: factors promoting reactogenicity of Doxil and AmBisome. *Nanomedicine* **8,** 176–184 (2012).
118. Delfino, R. J., Sioutas, C. & Malik, S. Potential role of ultrafine particles in associations between airborne particle mass and cardiovascular health. *Environ Health Persp* **113,** 934–946 (2005).
119. Varga-Szabo, D., Pleines, I. & Nieswandt, B. Cell adhesion mechanisms in platelets. *Arterioscler. Thromb. Vasc. Biol.* **28,** 403–412 (2008).
120. in *Nanotoxicity* (eds. Sahu, S. C. & Casciano, D. A.) (John Wiley & Sons, 2009).
121. Tian, F., Cui, D., Schwarz, H., Estrada, G. G. & Kobayashi, H. Cytotoxicity of single-wall carbon nanotubes on human fibroblasts. *Toxicol in Vitro* **20,** 1202–1212 (2006).
122. Cabral, H. *et al.* Accumulation of sub-100 nm polymeric micelles in poorly permeable tumours depends on size. *Nat Nanotechnol* **6,** 815–823 (2011).
123. Onoue, S., Yamada, S. & Chan, H. K. Nanodrugs: pharmacokinetics and safety. *Int J Nanomedicine* **9,** 1025–1037 (2014).
124. Jain, T. K., Reddy, M. K., Morales, M. A., Leslie-Pelecky, D. L. & Labhasetwar, V. Biodistribution, Clearance, and Biocompatibility of Iron Oxide Magnetic Nanoparticles in Rats. *Mol Pharm* **5,** 316–327 (2008).

125. Chen, Z. *et al.* Acute toxicological effects of copper nanoparticles in vivo. *Toxicol Lett* **163,** 109–120 (2006).
126. Wang, J. *et al.* Acute toxicity and biodistribution of different sized titanium dioxide particles in mice after oral administration. *Toxicol Lett* **168,** 176–185 (2007).
127. Liu, D., Mori, A. & Huang, L. Role of liposome size and RES blockade in controlling biodistribution and tumor uptake of GM1-containing liposomes. *Biochimica et Biophysica Acta (BBA)-Biomembranes* **1104,** 95–101 (1992).
128. Wang, J. *et al.* The role of micelle size in tumor accumulation, penetration, and treatment. *ACS Nano* **9,** 7195–7206 (2015).
129. Derfus, A. M., Chan, W. C. W. & Bhatia, S. N. Probing the cytotoxicity of semiconductor quantum dots. *Nano Lett* **4,** 11–18 (2004).
130. Yu, T., Malugin, A. & Ghandehari, H. Impact of silica nanoparticle design on cellular toxicity and hemolytic activity. *ACS Nano* (2011). doi:10.1021/nn2013904
131. Scown, T. M. *et al.* High doses of intravenously administered titanium dioxide nanoparticles accumulate in the kidneys of rainbow trout but with no observable impairment of renal function. *Toxicol Sci* **109,** 372–380 (2009).
132. Evgin, L. *et al.* Complement inhibition prevents oncolytic vaccinia virus neutralization in immune humans and cynomolgus macaques. *Mol Ther* **23,** 1066–1076 (2015).
133. Chiocca, E. A. *et al.* Oncolytic virus therapy of multiple tumors in the brain requires suppression of innate and elicited antiviral responses. *Nat Med* **5,** 881–887 (1999).
134. Alves-Rosa, F. *et al.* Treatment with liposome-encapsulated clodronate as a new strategic approach in the management of immune thrombocytopenic purpura in a mouse model. *Blood* **96,** 2834–2840 (2000).
135. Pitt, W. G., Husseini, G. A. & Staples, B. J. Ultrasonic drug delivery--a general review. *Expert Opin Drug Deliv* **1,** 37–56 (2004).
136. Carlisle, R. & Coussios, C.-C. Mechanical approaches to oncological drug delivery. *Ther Deliv* **4,** 1213–1215 (2013).
137. Connolly, D. T. *et al.* Tumor vascular permeability factor stimulates endothelial cell growth and angiogenesis. *J Clin Invest* **84,** 1470–1478 (1989).
138. Rosenstein, M., Ettinghausen, S. E. & Rosenberg, S. A. Extravasation of intravascular fluid mediated by the systemic administration of recombinant interleukin 2. *J Immunol* **137,** 1735–1742 (1986).
139. Lejeune, F. J. Clinical use of TNF revisited: improving penetration of anti-cancer agents by increasing vascular permeability. *J Clin Invest* **110,** 433–435 (2002).
140. Chauhan, V. P. & Stylianopoulos, T. Delivery of molecular and nanoscale medicine to tumors: Transport barriers and strategies. *Annu Rev Chem Biomol Eng* **2,** 281–298 (2011).
141. Kanesa-thasan, A. *et al.* Comparison of image-guided intratumoral versus intravenous delivery of therapeutic nanoparticles for the treatment of hepatocellular carcinoma. *J Vasc Interv Radiol* **24,** S142 (2013).

142. Bazan-Peregrino, M., Carlisle, R. C., Purdie, L. & Seymour, L. W. Factors influencing retention of adenovirus within tumours following direct intratumoural injection. *Gene Ther* **15,** 688–694 (2008).
143. McGuire, S. & Yuan, F. Quantitative analysis of intratumoral infusion of color molecules. *Am. J. Physiol. Heart Circ. Physiol.* **281,** H715–21 (2001).
144. Goel, R., Shah, N., Visaria, R., Paciotti, G. F. & Bischof, J. C. Biodistribution of TNF-alpha-coated gold nanoparticles in an in vivo model system. *Nanomedicine* **4,** 401–410 (2009).
145. Johannsen, M., Thiesen, B., Wust, P. & Jordan, A. Magnetic nanoparticle hyperthermia for prostate cancer. *Int J Hyperther* **26,** 790–795 (2010).
146. Ballou, B. *et al.* Sentinel lymph node imaging using quantum dots in mouse tumor models. *Bioconjugate Chem* **18,** 389–396 (2007).
147. Johannsen, M. *et al.* Morbidity and quality of life during thermotherapy using magnetic nanoparticles in locally recurrent prostate cancer: Results of a prospective phase I trial. *Int J Hyperther* **23,** 315–323 (2007).
148. Shvedova, A. A. *et al.* Unusual inflammatory and fibrogenic pulmonary responses to single-walled carbon nanotubes in mice. *Am J Physiol Lung Cell Mol Physiol* **289,** L698–L708 (2005).
149. Hoet, P. H., Brüske-Hohlfeld, I. & Salata, O. V. Nanoparticles – known and unknown health risks. *J Nanobiotechnol* **2,** 12 (2004).
150. Gabizon, A. *et al.* Prolonged circulation time and enhanced accumulation in malignant exudates of doxorubicin encapsulated in polyethylene-glycol coated liposomes. *Cancer Res* **54,** 987 (1994).
151. Maeda, N. *et al.* Anti-neovascular therapy by use of tumor neovasculature-targeted long-circulating liposome. *J Control Release* **100,** 41–52 (2004).
152. Graham, S. M. *et al.* Inertial cavitation to non-invasively trigger and monitor intratumoral release of drug from intravenously delivered liposomes. *J Control Release* **178,** 101–107 (2014).
153. Tailor, T. D. *et al.* Effect of pazopanib on tumor microenvironment and liposome delivery. *Mol Cancer Ther* **9,** 1798 (2010).
154. Kirpotin, D. B. *et al.* Antibody targeting of long-circulating lipidic nanoparticles does not increase tumor localization but does increase internalization in animal models. *Cancer Res* **66,** 6732–6740 (2006).
155. Li, K. C. P., Pandit, S. D., Guccione, S. & Bednarski, M. D. Molecular imaging applications in nanomedicine. *Biomed Microdevices* **6,** 113–116 (2004).
156. Davis, M. E., Chen, Z. G. & Shin, D. M. Nanoparticle therapeutics: an emerging treatment modality for cancer. *Nat Rev Drug Discov* **7,** 771–782 (2008).
157. Pirollo, K. F. & Chang, E. H. Does a targeting ligand influence nanoparticle tumor localization or uptake? *Trends Biotechnol* **26,** 552–558 (2008).
158. Savić, R., Eisenberg, A. & Maysinger, D. Block copolymer micelles as delivery vehicles of hydrophobic drugs: Micelle–cell interactions. *J Drug Target* **14,** 343–355 (2015).
159. Danhier, F., Feron, O. & Préat, V. To exploit the tumor

microenvironment: Passive and active tumor targeting of nanocarriers for anti-cancer drug delivery. *J Control Release* **148,** 135–146 (2010).
160. Hood, J. D. *et al.* Tumor regression by targeted gene delivery to the neovasculature. *Science* **296,** 2404 (2002).
161. Nagase, H. & Woessner, J. F. Matrix metalloproteinases. *J Biol Chem* **274,** 21491 (1999).
162. Ruoslahti, E.others. Specialization of tumour vasculature. *Nat Rev Cancer* **2,** 83–90 (2002).
163. Ruoslahti, E. Specialization of tumour vasculature. *Nat Rev Cancer* **2,** 83–90 (2002).
164. Jubeli, E., Moine, L., Vergnaud-Gauduchon, J. & Barratt, G. E-selectin as a target for drug delivery and molecular imaging. *J Control Release* **158,** 194–206 (2012).
165. Creixell, M. *et al.* Preparation of epidermal growth factor (EGF) conjugated iron oxide nanoparticles and their internalization into colon cancer cells. *J Magn Magn Mater* **322,** 2244–2250 (2010).
166. Tailor, T. D. *et al.* Effect of pazopanib on tumor microenvironment and liposome delivery. *Mol Cancer Ther* **9,** 1798–1808 (2010).
167. Wang, X. *et al.* Folate receptor targeting silica nanoparticle probe for two-photon fluorescence bioimaging. *Biomed Opt Express* **1,** 453–462 (2010).
168. Wiiger, M. T., Gehrken, H. B., Fodstad, Ø., Mælandsmo, G. M. & Andersson, Y. A novel human recombinant single-chain antibody targeting CD166/ALCAM inhibits cancer cell invasion in vitro and in vivo tumour growth. *Cancer Immunol. Immunother.* **59,** 1665–1674 (2010).
169. Brannon-Peppas, L. & Blanchette, J. O. Nanoparticle and targeted systems for cancer therapy. *Adv Drug Deliver Rev* **64,** 206–212 (2012).
170. Oerlemans, C. *et al.* Polymeric Micelles in Anticancer Therapy: Targeting, Imaging and Triggered Release. *Pharm Res* **27,** 2569–2589 (2010).
171. Sapsford, K. E. *et al.* Functionalizing nanoparticles with biological molecules: developing chemistries that facilitate nanotechnology. *Chem Rev* **113,** 1904–2074 (2013).
172. *The molecular probes handbook: A guide to fluorescent probes and labeling technologies*. (2010).
173. Hermanson, G. T. *Bioconjugate Techniques*. (Academic Press, 2008).
174. Sun, X., Zhang, G., Patel, D., Stephens, D. & Gobin, A. M. Targeted cancer therapy by immunoconjugated gold–gold sulfide nanoparticles using Protein G as a cofactor. *Ann Biomed Eng* **40,** 2131–2139 (2012).
175. Nobs, L., Buchegger, F., Gurny, R. & Allémann, E. Current methods for attaching targeting ligands to liposomes and nanoparticles. *J Pharm Sci* **93,** 1980–1992 (2004).
176. Mosqueira, V., Legrand, P., Morgat, J. L. & Vert, M. Biodistribution of long-circulating PEG-grafted nanocapsules in mice: Effects of PEG chain length and density. *Pharm Res* **18,** 1411–1419 (2001).
177. Chertok, B., Moffat, B. A., David, A. E., Yu, F. & Bergemann, C. Iron oxide nanoparticles as a drug delivery vehicle for MRI monitored

magnetic targeting of brain tumors. *Biomaterials* **29,** 487–496 (2008).
178. Li, L. *et al.* Triggered content release from optimized stealth thermosensitive liposomes using mild hyperthermia. *J Control Release* **143,** 274–279 (2010).
179. Hernot, S. & Klibanov, A. L. Microbubbles in ultrasound-triggered drug and gene delivery. *Adv Drug Deliver Rev* **60,** 1153–1166 (2008).
180. Guo, X. & Szoka, F. C., Jr. Chemical approaches to triggerable lipid vesicles for drug and gene delivery. *Acc Chem Res* **36,** 335–341 (2003).
181. Andresen, T. L., Jensen, S. S. & Jorgensen, K. Advanced strategies in liposomal cancer therapy: problems and prospects of active and tumor specific drug release. *Prog Lipid Res* **44,** 68–97 (2005).
182. Helmlinger, G., Yuan, F., Dellian, M. & Jain, R. K. Interstitial pH and pO2 gradients in solid tumors in vivo: High-resolution measurements reveal a lack of correlation. *Nat Med* **3,** 177–182 (1997).
183. Gatenby, R. A. & Gillies, R. J. Why do cancers have high aerobic glycolysis? *Nat Rev Cancer* **4,** 891–899 (2004).
184. Chen, Y. *et al.* Manganese oxide-based multifunctionalized mesoporous silica nanoparticles for pH-responsive MRI, ultrasonography and circumvention of MDR in cancer cells. *Biomaterials* **33,** 7126–7137 (2012).
185. Brewer, E., Coleman, J. & Lowman, A. Emerging Technologies of Polymeric Nanoparticles in Cancer Drug Delivery. *J Nanomater* **2011,** 1–10 (2010).
186. Gaber, M. H., Hong, K., Huang, S. K. & Papahadjopoulos, D. Thermosensitive Sterically Stabilized Liposomes: Formulation and in Vitro Studies on Mechanism of Doxorubicin Release by Bovine Serum and Human Plasma. *Pharm Res* **12,** 1407–1416 (1995).
187. Koning, G. A., Eggermont, A. M. M., Lindner, L. H. & Hagen, ten, T. L. M. Hyperthermia and Thermosensitive Liposomes for Improved Delivery of Chemotherapeutic Drugs to Solid Tumors. *Pharm Res* **27,** 1750–1754 (2010).
188. Hyperthermia in Cancer Treatment. *http://www.cancer.gov/about-cancer/treatment/types/surgery/hyperthermia-fact-sheet* (2011).
189. van der Zee, J. *et al.* Comparison of radiotherapy alone with radiotherapy plus hyperthermia in locally advanced pelvic tumours: a prospective, randomised, multicentre trial. *Lancet* **355,** 1119–1125 (2000).
190. Evjen, T. Sonosensitive liposomes for ultrasound-mediated drug delivery. (University of Tromso, 2011). doi:10.1016/j.ejpb.2010.04.012>http://dx.doi.org/10.1016/j.ejpb.2010.04.012
191. Carlisle, R. *et al.* Enhanced tumor uptake and penetration of virotherapy using polymer stealthing and focused ultrasound. *J Natl Cancer I* **105,** 1701–1710 (2013).
192. Mylonopoulou, E. & Peregrino, M. B. Exploitation of cavitation-enhanced heating for release of doxorubicin from thermosensitve liposomes by therapeutic ultrasound. *J Acoust Soc Am* **128,** 2418 (2010).
193. Woo, J. A short history of the development of ultrasound in obstetrics

and gynecology. *History of Ultrasound in Obstetrics and Gynecology, Part* **1,** 1–23 (2002).
194. Miller, D. L. *et al.* Overview of therapeutic ultrasound applications and safety considerations. *J Ultras Med* **31,** 623–634 (2012).
195. Qian, Z. W. *et al.* Noninvasive thermometer for HIFU and its scaling. *Ultrasonics* **44,** e31–e35 (2006).
196. Coleman, A. J. & Saunders, J. E. A review of the physical properties and biological effects of the high amplitude acoustic fields used in extracorporeal lithotripsy. *Ultrasonics* **31,** 75–89 (1993).
197. Ng, K. Y. & Liu, Y. Therapeutic ultrasound: Its application in drug delivery. *Med Res Rev* **22,** 204–223 (2002).
198. Fenster, A. & Downey, D. B. 3-D ultrasound imaging: A review. *IEEE Eng Med Biol* **15,** 41–51 (1996).
199. Blomley, M. J., Cooke, J. C., Unger, E. C., Monaghan, M. J. & Cosgrove, D. O. Microbubble contrast agents: a new era in ultrasound. *BMJ* **322,** 1222–1225 (2001).
200. Burri, M. V., Gupta, D., Kerber, R. E. & Weiss, R. M. Review of novel clinical applications of advanced, real-time, 3-dimensional echocardiography. *Transl Res* **159,** 149–164 (2012).
201. O'Neill, D. P. *et al.* A three-state mathematical model of hyperthermic cell death. *Ann Biomed Eng* **39,** 570–579 (2011).
202. Graham, S. J. *et al.* Quantifying tissue damage due to focused ultrasound heating observed by MRI. *Magn. Reson. Med.* **41,** 321–328 (1999).
203. Maxwell, A. *et al.* Disintegration of tissue using high intensity focused ultrasound: two approaches that utilize shock waves. *Acoustics Today* **8,** 24–34 (2012).
204. Illing, R. O. *et al.* The safety and feasibility of extracorporeal high-intensity focused ultrasound (HIFU) for the treatment of liver and kidney tumours in a Western population. *Br J Cancer* **93,** 890–895 (2005).
205. de Smet, M., Heijman, E., Langereis, S., Hijnen, N. M. & Grüll, H. Magnetic resonance imaging of high intensity focused ultrasound mediated drug delivery from temperature-sensitive liposomes: an in vivo proof-of-concept study. *J Control Release* **150,** 102–110 (2011).
206. Leighton, T. G. *The Acoustic Bubble*. (Academic Press, 1997).
207. Neppiras, E. A. Acoustic cavitation series: part one. *Ultrasonics* **22,** 25–28 (1984).
208. Leighton, T. G. *The acoustic bubble*. **10,** (Academic Press, 1997).
209. Salgaonkar, V. A., Datta, S., Holland, C. K. & Mast, T. D. Passive cavitation imaging with ultrasound arrays. *J Acoust Soc Am* **126,** 3071 (2009).
210. Hynynen, K. The threshold for thermally significant cavitation in dog's thigh muscle in vivo. *Ultrasound Med Biol* **17,** 157–169 (1991).
211. Guzman, H. R., McNamara, A. J., Nguyen, D. X. & Prausnitz, M. R. Bioeffects caused by changes in acoustic cavitation bubble density and cell concentration: a unified explanation based on cell-to-bubble ratio and blast radius. *Ultrasound Med Biol* **29,** 1211–1222 (2003).
212. Huber, P. E. & Pfisterer, P. In vitro and in vivo transfection of plasmid DNA in the Dunning prostate tumor R3327-AT1 is enhanced by

focused ultrasound. *Gene Ther* **7,** 1516–1525 (2000).
213. Zhou, Y., Yang, K., Cui, J., Ye, J. Y. & Deng, C. X. Controlled permeation of cell membrane by single bubble acoustic cavitation. *J Control Release* **157,** 103–111 (2011).
214. Bazan-Peregrinoa, M., Arvanitisa, C. D., Rifaia, B., Seymour, L. W. & Coussios, C.-C. Ultrasound-induced cavitation enhances the delivery and therapeutic efficacy of an oncolytic virus in an in vitro model. *J Control Release* **157,** 235–242 (2012).
215. Shohet, R. V. *et al.* Echocardiographic destruction of albumin microbubbles directs gene delivery to the myocardium. *Circulation* **101,** 2554–2556 (2000).
216. Evjen, T. J. Sonosensitive liposomes for ultrasound-mediated drug delivery. (2011).
217. Mitragotri, S. Healing sound: the use of ultrasound in drug delivery and other therapeutic applications. *Nat Rev Drug Discov* **4,** 255–260 (2005).
218. Chernysh, I. N., Everbach, E. C., Purohit, P. K. & Weisel, J. W. Molecular mechanisms of the effect of ultrasound on the fibrinolysis of clots. *J Thromb Haemost* n/a–n/a (2015). doi:10.1111/jth.12857
219. Harpaz, D. Ultrasound enhancement of thrombolytic therapy: observations and mechanisms. *Acute Card Care* **3,** 81–89 (2000).
220. Miller, D. L. & Quddus, J. Sonoporation of monolayer cells by diagnostic ultrasound activation of contrast-agent gas bodies. *Ultrasound Med Biol* **26,** 661–667 (2000).
221. Coleman, A. J. & Saunders, J. E. A survey of the acoustic output of commercial extracorporeal shock wave lithotripters. *Ultrasound Med Biol* **15,** 213–227 (1989).
222. Safety Group of the British Medical Ultrasound Society. *Guidelines for the safe use of diagnostic ultrasound equipment*. (The British Medical Ultrasound Society, 2010).
223. Paliwal, S. & Mitragotri, S. Ultrasound-induced cavitation: applications in drug and gene delivery. *Expert Opin Drug Deliv* **3,** 713–726 (2006).
224. Apfel, R. E. & Holland, C. K. Gauging the likelihood of cavitation from short-pulse, low-duty cycle diagnostic ultrasound. *Ultrasound Med Biol* **17,** 179–185 (1991).
225. Dalecki, D., Child, S. Z., Raeman, C. H. & Cox, C. Hemorrhage in murine fetuses exposed to pulsed ultrasound. *Ultrasound Med Biol* **25,** 1139–1144 (1999).
226. Phillips, R. & Harris, G. *Information for manufacturers seeking marketing clearance of diagnostic ultrasound systems and transducers*. (Food and drug administration, 2008).
227. Dalecki, D. Mechanical bioeffects of ultrasound. *Annu. Rev. Biomed. Eng.* **6,** 229–248 (2004).
228. Haar, ter, G. Safety and bio-effects of ultrasound contrast agents. *Medical and Biological Engineering and Computing* **47,** 893–900 (2009).
229. Hancock, H. A. *et al.* Investigations into pulsed high-intensity focused ultrasound–enhanced delivery: Preliminary evidence for a novel mechanism. *Ultrasound Med Biol* **35,** 1722–1736 (2009).
230. Husseini, G. A. & Pitt, W. G. Ultrasonic-activated micellar drug delivery

for cancer treatment. *J Pharm Sci* **98,** 795–811 (2009).
231. Zeghimi, A., Escoffre, J. M. & Bouakaz, A. Role of endocytosis in sonoporation-mediated membrane permeabilization and uptake of small molecules: a electron microscopy study. *Phys Biol* **12,** 066007 (2015).
232. Prausnitz, M. R. & Langer, R. Transdermal drug delivery. *Nat Biotech* **26,** 1261–1268 (2008).
233. Ferrara, K. W. Driving delivery vehicles with ultrasound. *Adv Drug Deliver Rev* **60,** 1097–1102 (2008).
234. Taniyama, Y. *et al.* Local delivery of plasmid DNA into rat carotid artery using ultrasound. *Circulation* **105,** 1233–1239 (2002).
235. Iwanaga, K. *et al.* Local delivery system of cytotoxic agents to tumors by focused sonoporation. *Cancer Gene Ther* **14,** 354–363 (2007).
236. Rifai, B., Arvanitis, C. D., Bazán-Peregrino, M. & Coussios, C.-C. Cavitation-enhanced delivery of macromolecules into an obstructed vessel. *J Acoust Soc Am* **128,** EL310–15 (2010).
237. Yuh, E. L. *et al.* Delivery of systemic chemotherapeutic agent to tumors by using focused ultrasound: study in a murine model. *Radiology* **234,** 431–437 (2005).
238. Stieger, S. M. *et al.* Enhancement of vascular permeability with low-frequency contrast-enhanced ultrasound in the chorioallantoic membrane model. *Radiology* **243,** 112–121 (2007).
239. Bazán-Peregrino, M., Arvanitis, C. D., Rifai, B., Seymour, L. W. & Coussios, C.-C. Ultrasound-induced cavitation enhances the delivery and therapeutic efficacy of an oncolytic virus in an in vitro model. *J Control Release* **157,** 235–242 (2012).
240. Wang, S. *et al.* Pulsed high intensity focused ultrasound increases penetration and therapeutic efficacy of monoclonal antibodies in murine xenograft tumors. *J Control Release* **162,** 218–224 (2012).
241. Lee, T., Baac, H. W., Ok, J. G., Youn, H. S. & Guo, L. J. Controlled generation of single microbubble at solid surfaces by a nanosecond pressure pulse. *Phys Rev Applied* **2,** 1–10 (2014).
242. Shen, Z. Y. & Hu, B. Low-frequency low-intensity ultrasound with contrast agent for the treatment of subcutaneous tumors in mice. *Sci Res Essays* **6,** 5579–5585 (2011).
243. Böhmer, M. R. *et al.* Focused ultrasound and microbubbles for enhanced extravasation. *J Control Release* **148,** 18–24 (2010).
244. Bekeredjian, R. *et al.* Ultrasound targeted microbubble destruction increases capillary permeability in hepatomas. *Ultrasound Med Biol* **33,** 1592–1598 (2007).
245. Bazán-Peregrino, M. *et al.* Cavitation-enhanced delivery of a replicating oncolytic adenovirus to tumors using focused ultrasound. *J Control Release* **169,** 40–47 (2013).
246. Carlisle, R. & Coussios, C. C. Mechanical approaches to oncological drug delivery. *Ther Deliv* (2013).
247. Jensen, C. R. *et al.* Spatiotemporal monitoring of high-intensity focused ultrasound therapy with passive acoustic mapping. *Radiology* **262,** 252–261 (2012).
248. Choi, J. J., Carlisle, R. C., Coviello, C., Seymour, L. & Coussios, C.-C. Non-invasive and real-time passive acoustic mapping of ultrasound-

mediated drug delivery. *Phys Med Biol* **59,** 4861–4877 (2014).
249. Alter, J., Sennoga, C. A., Lopes, D. M., Eckersley, R. J. & Wells, D. J. Microbubble stability is a major determinant of the efficiency of ultrasound and microbubble mediated in vivo gene transfer. *Ultrasound Med Biol* **35,** 976–984 (2009).
250. Xing, Z. *et al.* The fabrication of novel nanobubble ultrasound contrast agent for potential tumor imaging. *Nanotechnology* **21,** 1–8 (2010).
251. Wheatley, M. A., Forsberg, F., Dube, N., Patel, M. & Oeffinger, B. E. Surfactant-stabilized contrast agent on the nanoscale for diagnostic ultrasound imaging. *Ultrasound Med Biol* **32,** 83–93 (2006).
252. Liu, J. *et al.* Nanoparticles as image enhancing agents for ultrasonography. *Phys Med Biol* **51,** 2179–2189 (2006).
253. Oeffinger, B. E. & Wheatley, M. A. Development and characterization of a nano-scale contrast agent. *Ultrasonics* **42,** 343–347 (2004).
254. Rapoport, N. *et al.* Ultrasound-mediated tumor imaging and nanotherapy using drug loaded, block copolymer stabilized perfluorocarbon nanoemulsions. *J Control Release* **153,** 4–15 (2011).
255. Williams, R. *et al.* Characterization of submicron phase-change perfluorocarbon droplets for extravascular ultrasound imaging of cancer. *Ultrasound Med Biol* **39,** 475–489 (2013).
256. Wang, X. *et al.* Perfluorohexane-encapsulated mesoporous silica nanocapsules as enhancement agents for highly efficient high intensity focused ultrasound (HIFU). *Adv Mater* **24,** 785–791 (2012).
257. Figueiredo, M. & Esenaliev, R. PLGA nanoparticles for ultrasound-mediated gene delivery to solid tumors. *J Drug Deliv* **2012,** 1–20 (2012).
258. Sheeran, P. S., Luois, S. H., Mullin, L. B., Matsunaga, T. O. & Dayton, P. A. Design of ultrasonically-activatable nanoparticles using low boiling point perfluorocarbons. *Biomaterials* **33,** 3262–3269 (2012).
259. Couture, O. *et al.* In vivo targeted delivery of large payloads with an ultrasound clinical scanner. *Med Phys* **39,** 5229–5237 (2012).
260. Couture, O. *et al.* Ultrasound internal tattooing. *Med Phys* **38,** 1116–1123 (2011).
261. Shapiro, M. G. *et al.* Biogenic gas nanostructures as ultrasonic molecular reporters. *Nat Nanotechnol* **9,** 311–316 (2014).
262. Borkent, B. M., Dammer, S. M., Schönherr, H., Vancso, G. J. & Lohse, D. Superstability of surface nanobubbles. *Phys Rev Lett* **98,** 1–4 (2007).
263. Uddin, M. H., Tan, S. Y. & Dagastine, R. R. Novel characterization of microdrops and microbubbles in emulsions and foams using atomic force microscopy. *Langmuir* **27,** 2536–2544 (2011).
264. Zhang, X. H., Khan, A. & Ducker, W. A. A nanoscale gas state. *Phys Rev Lett* **98,** 1–4 (2007).
265. Brenner, M. P. & Lohse, D. Dynamic equilibrium mechanism for surface nanobubble stabilization. *Phys Rev Lett* **101,** 1–4 (2008).
266. Ljunggren, S. & Eriksson, J. C. The lifetime of a colloid-sized gas bubble in water and the cause of the hydrophobic attraction. *Colloid Surfaces A* **129-130,** 151–155 (1997).
267. Eggen, S. *et al.* Ultrasound improves the uptake and distribution of liposomal Doxorubicin in prostate cancer xenografts. *Ultrasound Med*

Biol **39,** 1255–1266 (2013).
268. Matsumura, Y. & Maeda, H. A new concept for macromolecular therapeutics in cancer chemotherapy: Mechanism of tumoritropic accumulation of proteins and the antitumor agent smancs. *Cancer Res* **46,** 6387–6392 (1986).
269. Choudhury, N. On the Manifestation of Hydrophobicity at the Nanoscale. *J Phys Chem B* **112,** 6296–6300 (2008).
270. Keller, J. B. & Miksis, M. Bubble oscillations of large amplitude. *J Acoust Soc Am* **68,** 628–633 (1980).
271. Brenner, M. & Lohse, D. Dynamic Equilibrium Mechanism for Surface Nanobubble Stabilization. *Phys Rev Lett* **101,** 214505 (2008).
272. *Cavitation at the Nano Scale*. (International Congress on Acoustics).
273. Lv, H. *et al.* Facile fabrication of monodisperse polymer hollow spheres. *Langmuir* **24,** 13736–13741 (2008).
274. Kwan, J. *et al.* Ultrasound-propelled nanocups for drug delivery. *Small* (2015).
275. Kwan, J. *et al.* Ultrasound-induced inertial cavitation from gas-stabilizing nanoparticles. *Phys Rev Lett* **92,** 1–5 (2015).
276. Yang, L., Li, C., Chen, L. & Li, Z. An agarose-gel based method for transporting cell lines. *Curr Chem Genomics* **3,** 50–53 (2009).
277. Pernodet, N., Maaloum, M. & Tinland, B. Pore size of agarose gels by atomic force microscopy. *Electrophoresis* **18,** 55–58 (1997).
278. Crake, C. *et al.* Passive acoustic mapping of magnetic microbubbles for cavitation enhancement and localization. *Phys Med Biol* **60,** 785 (2015).
279. Everett, D. H. *Basic principles of colloid science*. (Royal Society of Chemistry, 1988).
280. Lyons, M. *et al.* Adenovirus type 5 interactions with human blood cells may compromise systemic delivery. *Mol Ther* **14,** 118–128 (2006).
281. Eggen, S. *et al.* Ultrasound Improves the Uptake and Distribution of Liposomal Doxorubicin in Prostate Cancer Xenografts. *Ultrasound Med Biol* (2013).
282. Holland, C. K. & Apfel, R. E. An improved theory for the prediction of microcavitation thresholds. *IEEE Trans Ultrason Ferroelect Freq Contr* **36,** 204–208 (1989).
283. British Pharmacopoeia Commision. *British Pharmacopoeia*. (Stationary Office).
284. Salvador-Morales, C. *et al.* Complement activation and protein adsorption by carbon nanotubes. *Mol Immunol* **43,** 193–201 (2006).
285. Shvedova, A. A. Unusual inflammatory and fibrogenic pulmonary responses to single-walled carbon nanotubes in mice. *AJP: Lung Cellular and Molecular Physiology* **289,** L698–L708 (2005).
286. Rouse, J. G., Yang, J., Barron, A. R. & Monteiro-Riviere, N. A. Fullerene-based amino acid nanoparticle interactions with human epidermal keratinocytes. *Toxicol in Vitro* **20,** 1313–1320 (2006).
287. Gharbi, N. *et al.* [60]Fullerene is a powerful antioxidant in vivo with no acute or subacute toxicity. *Nano Lett* **5,** 2578–2585 (2005).
288. Wick, P. *et al.* The degree and kind of agglomeration affect carbon nanotube cytotoxicity. *Toxicol Lett* **168,** 121–131 (2007).
289. Donnet, J.-B. *Carbon Black*. (CRC Press, 1993).

290. Dick, C. A. J., Brown, D. M., Donaldson, K. & Stone, V. The role of free radicals in the toxic and inflammatory effects of four different ultrafine particle types. *Inhal Toxicol* **15,** 39–52 (2003).
291. Bottini, M., Bruckner, S., Nika, K., Bottini, N. & Bellucci, S. Multi-walled carbon nanotubes induce T lymphocyte apoptosis. *Toxicol Lett* (2006).
292. Brown, D. M. *et al.* Calcium and ROS-mediated activation of transcription factors and TNF-alpha cytokine gene expression in macrophages exposed to ultrafine particles. *Am J Physiol Lung Cell Mol Physiol* **286,** L344–L353 (2004).
293. Crum, L. A. Acoustic cavitation series: part five rectified diffusion. *Ultrasonics* **22,** 215–223 (1984).
294. Naugler, W. E. & Karin, M. The wolf in sheep's clothing: the role of interleukin-6 in immunity, inflammation and cancer. *Trends Mol Med* **14,** 109–119 (2008).
295. Heagy, W. *et al.* Lower levels of whole blood LPS-stimulated cytokine release are associated with poorer clinical outcomes in surgical ICU patients. *Surg Infect (Larchmt)* **4,** 171–180 (2003).
296. Merril, C. R., Goldman, D. & Van Keuren, M. L. Simplified silver protein detection and image enhancement methods in polyacrylamide gels. *Electrophoresis* **3,** 17–23 (1982).
297. Lundblad, R. L. Considerations for the use of blood plasma and serum for proteomic analysis. *J Gastroenterol* **1,** (2005).
298. Tenzer, S. *et al.* Rapid formation of plasma protein corona critically affects nanoparticle pathophysiology. *Nat Nanotechnol* **8,** 772–781 (2013).
299. *Normal laboratory values: MKSAP(R) 14*. (American College of Physicians).
300. Tan, X. *et al.* Functionalization of graphene oxide generates a unique interface for selective serum protein interactions. *ACS Appl Mater Interfaces* **5,** 1370–1377 (2013).
301. Shin, Y.-R., Jung, S.-M., Jeon, I.-Y. & Baek, J.-B. The oxidation mechanism of highly ordered pyrolytic graphite in a nitric acid/sulfuric acid mixture. *Carbon* **52,** 493–498 (2013).
302. Abdelwahed, W., Degobert, G., Stainmesse, S. & Fessi, H. Freeze-drying of nanoparticles: Formulation, process and storage considerations. *Adv Drug Deliver Rev* **58,** 1688–1713 (2006).
303. Ramaiah, S. K. A toxicologist guide to the diagnostic interpretation of hepatic biochemical parameters. *Food Chem Toxicol* **45,** 1551–1557 (2007).
304. Kirschfink, M. & Mollnes, T. E. Modern complement analysis. *Clin Diagn Lab Immun* **10,** 982–989 (2003).
305. Mueller-Ortiz, S. L. *et al.* Targeted disruption of the gene encoding the murine small subunit of carboxypeptidase N (CPN1) causes susceptibility to C5a anaphylatoxin-mediated shock. *J Immunol* **182,** 6533–6539 (2009).
306. Shvedova, A. A. *et al.* Inhalation vs. aspiration of single-walled carbon nanotubes in C57BL/6 mice: inflammation, fibrosis, oxidative stress, and mutagenesis. *Am J Physiol Lung Cell Mol Physiol* **295,** L552–L565 (2008).
307. Hehlgans, T. & Pfeffer, K. The intriguing biology of the tumour

necrosis factor/tumour necrosis factor receptor superfamily: players, rules and the games. *Immunology* **115,** 1–20 (2005).
308. Calandra, T. *et al.* Protection from septic shock by neutralization of macrophage migration inhibitory factor. *Nat Med* **6,** 164–170 (2000).
309. Rapoport, N. Y., Nam, K. H., Gao, Z. & Kennedy, A. Application of ultrasound for targeted nanotherapy of malignant tumors. *Acoust Phys* **55,** 594–601 (2009).
310. He, C., Hu, Y., Yin, L., Tang, C. & Yin, C. Effects of particle size and surface charge on cellular uptake and biodistribution of polymeric nanoparticles. *Biomaterials* **31,** 3657–3666 (2010).
311. Eifler, A. C. & Thaxton, C. S. in *Biomedical Nanotechnology* **726,** 325–338 (Humana Press, 2011).
312. Crist, R. M. *et al.* Common pitfalls in nanotechnology: lessons learned from NCI's Nanotechnology Characterization Laboratory. *Integr Biol (Camb)* **5,** 66–73 (2013).
313. Dalton, P. D., Flynn, L. & Shoichet, M. S. Manufacture of poly(2-hydroxyethyl methacrylate-co-methyl methacrylate) hydrogel tubes for use as nerve guidance channels. *Biomaterials* **23,** 3843–3851 (2002).
314. Graham, S. in *Ultrasound-triggered drug release from liposomes using nanoscale cavitation nuclei* (eds. Coussios, C. C. & Carlisle, R.) 1–250 (2015).
315. Cichon, G. *et al.* Complement activation by recombinant adenoviruses. *Gene Ther* **8,** 1794–1800 (2001).
316. Wisse, E., Jacobs, F., Topal, B., Frederik, P. & De Geest, B. The size of endothelial fenestrae in human liver sinusoids: implications for hepatocyte-directed gene transfer. *Gene Ther* **15,** 1193–1199 (2008).
317. Minchinton, A. I. & Tannock, I. F. Drug penetration in solid tumours. *Nat Rev Cancer* **6,** 583–592 (2006).
318. Antonia, S. J., Larkin, J. & Ascierto, P. A. Immuno-oncology combinations: A review of clinical experience and future prospects. *Clin Cancer Res* **20,** 6258–6268 (2014).
319. Mo, S. Cavitation-enhanced tumour targeting virotherapy by ultrasound. (University of Oxford, 2013).
320. Schneider, M. Characteristics of SonoVuetrade mark. *Echocardiography* **16,** 743–746 (1999).
321. Bonté, F. & Juliano, R. L. Interactions of liposomes with serum proteins. *Chem Phys Lipids* **40,** 359–372 (1986).
322. Mo, S., Coussios, C.-C., Seymour, L. & Carlisle, R. Ultrasound-enhanced drug delivery for cancer. *Expert Opin Drug Deliv* **9,** 1525–1538 (2012).
323. Lai, C.-Y., Fite, B. Z. & Ferrara, K. W. Ultrasonic enhancement of drug penetration in solid tumors. *Front. Oncol.* **3,** (2013).
324. Khaibullina, A. *et al.* Pulsed high-intensity focused ultrasound enhances uptake of radiolabeled monoclonal antibody to human epidermoid tumor in nude mice. *Journal of Nuclear Medicine* **49,** 295–302 (2008).
325. Heath, C. H., Sorace, A., Knowles, J., Rosenthal, E. & Hoyt, K. Microbubble therapy enhances anti-tumor properties of cisplatin and cetuximab in vitro and in vivo. *Otolaryngology -- Head and Neck Surgery* 0194599812436648 (2012). doi:10.1177/0194599812436648

326. Choi, J. J. & Coussios, C.-C. Spatiotemporal evolution of cavitation dynamics exhibited by flowing microbubbles during ultrasound exposure. *J Acoust Soc Am* **132,** 3538–3549 (2012).
327. Hill, C. R. Ultrasonic exposure thresholds for changes in cells and tissues. *J Acoust Soc Am* **52,** 667–672 (1972).
328. *Physical Principles of Medical Ultrasonics*. *Physical Principles of Medical Ultrasonics* i–xv (John Wiley & Sons, Ltd, 2004). doi:10.1002/0470093978.fmatter
329. Okunaga, S., Takasu, A., Meshii, N. & Imai, T. Ultrasound as a method to enhance antitumor ability of oncolytic herpes simplex virus for head and neck cancer. *Gene Ther* (2015).
330. Thomas, C. E., Ehrhardt, A. & Kay, M. A. Progress and problems with the use of viral vectors for gene therapy. *Nat Rev Genet* **4,** 346–358 (2003).
331. Chiocca, E. A. Oncolytic viruses. *Nat Rev Cancer* **2,** 938–950 (2002).
332. Wein, L. M., Wu, J. T. & Kirn, D. H. Validation and analysis of a mathematical model of a replication-competent oncolytic virus for cancer treatment implications for virus design and delivery. *Cancer Res* **63,** 1317–1324 (2003).
333. Hunt, M. *Virology*. (University of South California School of Medicine, 2015).
334. Tolmachov, O., Al-Allaf, F. A. & Tolmachova, T. *Currrent issues in molecular virology - Viral genetics and biotechnological applications*. (InTech, 2011).
335. Fleury, S. *et al.* Multiply attenuated, self-inactivating lentiviral vectors efficiently deliver and express genes for extended periods of time in adult rat cardiomyocytes in vivo. *Circulation* **107,** 2375–2382 (2003).
336. Hales, L. M. *et al.* Complete genome sequence analysis of Seneca Valley virus-001, a novel oncolytic picornavirus. *J Gen Virol* **89,** 1265–1275 (2008).
337. *SonoVue: European Medicines Agency*. (2004).
338. Kress, S. *Medical Review: SonoVue*. *Center for drug evaluation and research* (2014).
339. Puhlmann, M. *et al.* Vaccinia as a vector for tumor-directed gene therapy: biodistribution of a thymidine kinase-deleted mutant. *Cancer Gene Ther* **7,** 66–73 (2000).
340. Tartaglia, J. *et al.* NYVAC: a highly attenuated strain of vaccinia virus. *Virology* **188,** 217–232 (1992).
341. Bland, J. O. W. & Robinow, C. F. The inclusion bodies of vaccinia and their relationship to the elementary bodies studied in cultures of the rabbit's cornea. *J Pathol Bacteriol* **48,** 381–403 (1939).
342. Lane, J. M., Ruben, F. L., Neff, J. M. & D, M. J. Smallpox vaccine: Adverse event rates, 1968. *www.bt.cdc.govagentsmallpoxvaccine-safetypdfadverse-events-chart.pdf*
343. Wittek, R. Vaccinia immune globulin: current policies, preparedness, and product safety and efficacy. *Int J Infect Dis* **10,** 193–201 (2006).
344. Roberts, K. L. & Smith, G. L. Vaccinia virus morphogenesis and dissemination. *Trends Microbiol* **16,** 472–479 (2008).
345. Park, B. H., Hwang, T., Liu, T. C., Sze, D. Y. & Kim, J. S. Use of a targeted oncolytic poxvirus, JX-594, in patients with refractory primary

or metastatic liver cancer: a phase I trial. *Lancet Oncol* **9,** 533–542 (2008).
346. Kirn, D. H. & Thorne, S. H. Targeted and armed oncolytic poxviruses: a novel multi-mechanistic therapeutic class for cancer. *Nat Rev Cancer* **9,** 64–71 (2009).
347. Clinical Trials search. *clinicaltrials.gov* at <http://clinicaltrials.gov/ct2/home>
348. Breitbach, C. J. *et al.* Intravenous delivery of a multi-mechanistic cancer-targeted oncolytic poxvirus in humans. *Nature* **477,** 99–102 (2011).
349. Park, S. H. *et al.* Phase 1b trial of biweekly intravenous Pexa-Vec (JX-594), an oncolytic and immunotherapeutic vaccinia virus in colorectal cancer. *Mol Ther* **23,** 1532–1540 (2015).
350. Chin, L. *et al.* Recapitulating human cancer in a mouse. *Nat Biotech* **31,** 392–395 (2013).
351. Kim, J. H. *et al.* Systemic armed oncolytic and immunologic therapy for cancer with JX-594, a targeted poxvirus expressing GM-CSF. *Mol Ther* **14,** 361–370 (2006).
352. Collin, J., Coviello, C., Lyka, E., Leslie, T. & Coussios, C. Real-time three-dimensional passive cavitation detection for clinical high intensity focused ultrasound systems. *J Acoust Soc Am* **133,** 3263–3263 (2013).
353. Grüll, H. & Langereis, S. Hyperthermia-triggered drug delivery from temperature-sensitive liposomes using MRI-guided high intensity focused ultrasound. *J Control Release* **161,** 317–327 (2012).
354. Lieber, A. *et al.* The role of Kupffer cell activation and viral gene expression in early liver toxicity after infusion of recombinant adenovirus vectors. *J. Virol.* **71,** 8798–8807 (1997).
355. Tao, N. *et al.* Sequestration of adenoviral vector by Kupffer cells leads to a nonlinear dose response of transduction in liver. *Mol Ther* **3,** (2001).
356. Demers, G. W. *et al.* Pharmacologic indicators of antitumor efficacy for oncolytic virotherapy. *Cancer Res* **63,** 4003–4008 (2003).
357. Bailey, K. *et al.* Mathematical model for radial expansion and conflation of intratumoral infectious centers predicts curative oncolytic virotherapy parameters. *PLOS ONE* **8,** e73759 (2013).
358. Heo, J. *et al.* Sequential therapy with JX-594, a targeted oncolytic poxvirus, followed by sorafenib in hepatocellular carcinoma: preclinical and clinical demonstration of combination efficacy. *Mol Ther* **19,** 1170–1179 (2011).
359. Miest, T. S. & Cattaneo, R. New viruses for cancer therapy: meeting clinical needs. *Nat Rev Micro* **12,** 23–34 (2014).
360. Schroeder, A. *et al.* Ultrasound triggered release of cisplatin from liposomes in murine tumors. *J Control Release* **137,** 63–68 (2009).
361. Yan, L. *et al.* A pH-responsive drug-delivery platform based on glycol chitosan-coated liposomes. *Small* n/a–n/a (2015). doi:10.1002/smll.201501412
362. *www.celsion.com*.
363. Min, H. S. *et al.* Liver-specific and echogenic hyaluronic acid nanoparticles facilitating liver cancer discrimination. *Advanced*

Functional Materials **23,** 5518–5529 (2013).
364. Hitchcock, K. E. *et al.* Ultrasound-enhanced rt-PA thrombolysis in an ex vivo porcine carotid artery model. *Ultrasound Med Biol* **37,** 1240–1251 (2011).
365. Vlaisavljevich, E., Durmaz, Y. Y., Maxwell, A., Elsayed, M. & Xu, Z. Nanodroplet-mediated histotripsy for image-guided targeted ultrasound cell ablation. *Theranostics* **3,** 851–864 (2013).

8 Appendix

8.1 Peer reviewed journal articles

J. Kwan, **R. Myers**, C.Coviello, S. Graham, A. Shah, E. Stride, R. Carlisle and C.-C. Coussios. “Ultrasound-propelled nanocups for drug delivery”, Small (2015).

J. Kwan, S. Graham, **R. Myers**, R. Carlisle, E. Stride and C.-C. Coussios. “Ultrasound-induced inertial cavitation from gas stabilizing nanoparticles”, Physical Review E 92:23019 (2015).

S. Mo, R. Carlisle, R. Laga, **R. Myers**, S. Graham, R. Cawood, K. Ulbrich, L. Seymour and C.-C. Coussios. “Increasing the density of nanomedicines improves their ultrasound-mediated delivery to tumours”, Journal of Controlled Release 210: 10-18 (2015).

S. Graham, R. Carlisle, J. Choi, M. Stevenson, A. Shah, **R. Myers**, K. Fisher, M.-Bazan Peregrino, Leonard Seymour and Constantin-C. Coussios. “Inertial cavitation non-invasively trigger and monitor intratumoral release of drug from intravenously delivered liposomes” Journal of Controlled Release 178(28): 101-107 (2014).

8.2 Presentations

R. Myers, S. Graham, J. Kwan, A. Shah, S. Mo, R. Carlisle and C.C. Coussios: “Evaluation of sub-micron ultrasound-responsive particles as a drug delivery strategy”. Acoustical Society of America. Providence, RI, USA (8^{th} May 2014)

R. Myers, S. Graham, R. Carlisle, C. Coviello, A. Cifor, P. Probert-Smith, J. Schnabel, A. Noble, L. Seymour, C.-C. Coussios: "Targeted drug delivery with real-time monitoring by ultrasound". UK Therapeutic Ultrasound Interest Group. Oxford, United Kingdom (8th July 2013).

R. Myers, S. Graham: "Carbon nanoparticles as cavitation nuclei for targeted drug delivery". Oxford, United Kingdom (7nd July 2013).

R. Myers, S. Graham, C.-C. Coussios, R. Carlisle: "Targeted nano-encapsulated virus released by ultrasound". Centre for Doctoral Training in Healthcare Innovation. Oxford, United Kingdom (22nd March 2013).

8.3 Posters

R. Myers, S. Graham, J. Kwan, A. Shah, S. Mo, R. Carlisle and C.C. Coussios: "Evaluation of sub-micron ultrasound-responsive particles as a drug delivery strategy". *Acoustical Society of America.* Providence, RI, USA (7th May 2014).

R. Myers, S. Graham, R. Carlisle and C. Coussios: "Formulation and toxicity of mesoporous carbon". Medical Engineering Council Annual Meeting. Ascot, United Kingdom (3-4th September 2013).

R. Myers, S. Graham, H. Schiffter, C. Coussios: "Active targeting of sonosensitive nanoparticles for cancer therapy". Centre for Doctoral Training in Healthcare Innovation Symposium. Oxford, United Kingdom (12th March 2012).

8.4 Conflict of Interest

The author is a paid employee of OxSonics Ltd., a company that is developing the technology described within this thesis.